Numerical Modeling of Multiphase Flows with Applications to the Automotive Industry

by

Chenguang Li

A thesis
presented to the University of Waterloo
in fulfillment of the
thesis requirement for the degree of
Doctor of Philosophy
in
Mechanical Engineering

Waterloo, Ontario, Canada, 2015

Author's Declaration

I hereby declare that I am the sole author of this thesis. This is a true copy of the thesis, including any required final revisions, as accepted by my examiners.

I understand that my thesis may be made electronically available to the public.

Abstract

Multiphase flows have become an issue of deep concern in the automotive industry. Two specific problems of concern to the ABC Group and Ford Motor Company have shown that the current multiphase models available in commercial software are not able to satisfy the requirements of the automotive industry for numerical simulations: namely, the need to solve complex industrial problems and the need to provide accurate solutions for these problems. The first problem of concern involves degassing in coolant surge tanks. Bubbles mixed in the coolant constitute a risk factor that influences the cooling performance, and the degree of mixing needs to be strictly controlled. Therefore, simulating the degassing rate accurately is of critical importance for the design of a coolant surge tank. The second case of concern focuses on a multiphase-flow-induced vibration and noise problem in a dynamic valve. This problem relates directly to the noise, vibration and harshness (NVH) performance of a hybrid vehicle. The dynamic motion of a dynamic valve, which is controlled by a balance between the spring force and the pressure force of the diesel-air multiphase flow acting on the valve, results in a complicated generation and propagation of mechanical and fluid-dynamic noise. This is a complex problem that combines multiphase flows and fluid-structure interaction (FSI). Motivated by these two problems posed by our industrial collaborators, this research has been conducted specifically in order to improve both the predictive accuracy of and degree of complexity of problems that can be addressed by the multiphase flow models presently available in commercial software. Moreover, the improvements obtained here are used to solve the two industrial problems described above. Towards this purpose, the ANSYS-FLUENT software is utilized for the current research because of its overall computational capabilities, its ease of use, and its widespread application in the automotive industry. However, to address the two aforementioned problems, it was necessary to improve the modeling capabilities of the ANSYS-FLUENT software. For this purpose, a number of model improvements were implemented in this study. Firstly, a multiphase flow model in ANSYS-FLUENT was improved through the utilization of user-defined functions (UDFs). Secondly, UDFs were also implemented to generalize the solution procedures in the FSI model. Thirdly, a Scheme command file was used to the

FSI model to provide a significantly improved solution algorithm based on an implicit solver that is capable of addressing problems requiring the strong coupling between the flow solver and the FSI solver.

Validations of the key methodologies (viz., the multiphase flow, the dynamic meshing capability and the FSI) of the integrated modeling system were carried out before being applied to the two specific problems of concern described above. Firstly, a bubbly turbulent flow in a vertical pipe was simulated and then compared with the experimental measurements in order to validate the improved multiphase flow model. The new multiphase flow model is based on the original Eulerian model (sometimes referred to as the two-fluid model in the literature) in ANSYS-FLUENT, but this model incorporates a number of new interfacial force models which were implemented using a UDF. The "wall peak" observed in the radial distribution of the gas volume fraction and the shift of this peaks towards the core (center) of the flow (to give a "core peak") as the volume fraction of the gas increases are captured correctly in our simulations, in contrast to the simulation results reported by other researchers. The immiscible model was also tested and found to be able to capture the major features of the bubbly flow in the vertical pipe.

A turbulent flow over a square cylinder with a prescribed motion was used as the second benchmark test case. The purpose of this test was to validate the capability and accuracy of the dynamic (or moving) mesh model in ANSYS-FLUENT. Two methods (namely, smoothing and layering) were used to generate the dynamic mesh. Both of these dynamic meshing methods yielded good performance in terms of the mesh quality. The predicted shedding of the Karman vortex street behind the cylinder and the "lock-in" phenomena over a small range of reduced velocities agreed well with the experimental measurements. The layering method for dynamic mesh generation was found to give a higher computational efficiency than the smoothing method.

Validation of the FSI model was more complicated than that of multiphase flow model, as models for FSI depend critically on the specific physical characteristics of the problem and these characteristics dictate whether a weak coupling or strong coupling is required

for the solution. To validate the model for a weak-coupling FSI problem, a turbulent flow over and past an autonomous-oscillating square cylinder was used as the benchmark test case. The vortex-induced vibration occurring behind the square cylinder for this case constitutes the classic weak-coupling FSI problem. A UDF was implemented to simulate the FSI using a dynamic mesh. A layering method was used to generate the dynamic mesh. The predicted shedding of the Karman vortex street behind the cylinder and the "lock-in" phenomenon over a small range of reduced velocities was found to agree well with the experimental measurements. For a strong-coupling FSI validation, we used a laminar flow in a heart valve as a benchmark test case. This valve has a free rotating leaflet controlled by periodic variations of the unsteady inlet velocity. To address this case, a new implicit solution methodology was proposed and implemented using a command file (written in Scheme) in order to solve this large-displacement problem. Simulation results indicate that the periodic motion of the leaflet was predicted fairly accurately even when friction was ignored. The resulting implicit FSI model demonstrates the capability of the new modeling tool in solving strongly coupled FSI problems similar to that associated with the operation of a dynamic valve.

The improved and validated multiphase flow model was applied firstly to a simulation of the degassing problem in a coolant surge tank. Grid sensitivity tests and time step sensitivity tests were conducted in order to determine optimal values for various parameters to be used in the simulation. Parametric tests, including inlet velocity tests, bubble diameter tests and liquid viscosity tests were undertaken. A degassing rate was proposed and defined as a metric for the degassing process. Geometries for a single-chamber and three connected chambers were simulated. It was found that bubbles are degassed stage by stage owing to the buoyancy effect. The degassing rate is a dynamic variable related to many physical properties, such as the inlet velocity, the liquid viscosity and the bubble size. A larger inlet velocity, a greater liquid viscosity, and a smaller bubble size result in a lower degassing rate. The effect the drag force models is not obvious although the drag force is the most important interfacial force influencing the degas rate. The effect of the lift force models is even weaker than that of drag force for determination of the phase interaction.

It is concluded that our proposed integrated modeling system provides reasonably good results for the degassing process in a surge tank.

Finally, the multiphase-flow-induced vibration and noise problem in a dynamic valve was simulated using our proposed integrated modeling system. For a two-phase flow through the valve, the simulations showed that the deformation and breakup of gas bubbles in the gap between the poppet and the valve seat generate vibrations that arises primarily from the force imbalance between the spring and the two-phase fluid-flow-induced forces on the poppet. A spectral analysis of the transient pressure force on the poppet revealed the presence of a strong cyclical behavior consisting of two major components. There was a low-frequency peak located at about 87 Hz and associated with the frequency of the poppet vibration (and which we interpret to be the source of the mechanical noise) and a high-frequency peak located at about 450–970 Hz which is associated with compressibility effects and the unsteady vortex motions in the spring chamber. The poppet vibration and noise are influenced by various factors such as the flow condition, the spring system properties, and the geometry of the valve. Larger bubbles and a lower inlet velocity result in larger displacements in the poppet in a non-equilibrium condition and induce a greater loading on the spring due to the higher pressures. These pressures in turn amplify the poppet vibration and noise. The detailed simulations and subsequent analysis of the complex interactions that occur in the turbulent multiphase fluid motion through a moving poppet valve allowed deeper physical insights and an improved understanding of both the source and properties of the vibration and noise generated in this complicated dynamic system.

Acknowledgements

I owe my first and deepest gratitude to my supervisors Professors Fue-Sang Lien and Eugene Yee. Professor Lien brought me here to Waterloo five years ago. What he provided me with was not only the precious chance to pursue a PhD at the University of Waterloo, but also a door to a wonderful new world. I am grateful for his teaching, supervision, advice, and attitude to research, which have helped shape my academic and professional career. Also, I am deeply grateful to Professor Yee for his guidance, patience and support. I am very fortunate for being able to work with such a passionate scientist, whose commitment to science will be always be an influence to me.

It is my pleasure to express my gratitude to my mother country, the People's Republic of China, for its financial support. Thanks also to my current university, the University of Waterloo.

I am grateful to the Ford Motor Company and ABC Group Inc., who together have provided me with the chance to investigate research problems with strong relevance to industry. My thanks as well to Dr. Mike Dong from the Ford Motor Company, and Dr. Meishen Li and Dr. Hao Wu from the ABC Group, for their helpful technical support.

I would also like to thank everyone in my group for the friendly and warm environment they have created. Thank to Huangrui Mo, who shared his beautiful thesis template and provided related technical support. I would like to give a special mention to Dr. Kun-Jung Hsieh, as I have very much appreciated his patient explanations and sincere advice whenever I encountered problems.

Lastly, I would like to express my sincere thanks to my parents, family, and friends for their genuine interest, optimism, and encouragement throughout this process. Of particular significance, I extend my special appreciation to my mother, for her boundless patience, love, and support. It would have been impossible to complete this work without her confidence, encouragement, and understanding.

Table of Contents

List of Figures

List of Tables

Nomenclature

Roman Characters

Symbol	Description	Unit
A	cross-sectional area in Equation (3.5), (3.6), and (4.6);	m^2
	amplitude in Equation (4.14)	m
$\mathbf{A}$	area vector of a face	m^2
B	bulk modulus	Pa
$\mathbf{c}$	vector from the centroid of a cell to the centroid of adjacent cell that shares a face	
C	coefficient	
d	diameter	m
d_H	long axis of a deformed bubble	m
D	side length of the square cylinder	m

D_ω	cross-diffusion term	
Eo	Eötvös number	
Eo_d	Eötvös number based on the long axis of a deformed bubble	
f	force	N
$\mathbf{f}$	vector from the centroid of a cell to the centroid of its faces	
f_D	drag function	
$\mathbf{F}$	force in Equations (3.8) to (3.42);	N
	net force or torque in Equations (3.95) to (3.103)	N or N m
$\mathbf{g}$	gravitational acceleration	m s^{-2}
G	generation of turbulence kinetic energy due to the mean velocity gradients	
G_k	production of turbulence kinetic energy	
h	specific enthalpy	J
H	height of a mesh layer	m
$\overline{\overline{I}}$	unit tensor	
k	kinetic energy	
k_S	spring stiffness	N s^{-1}
K	exchange coefficient	

$\overline{\overline{L}}$	inertia tensor	kg m^2
m	mass	kg
M	torque	N m
$\mathbf{M}$	moment	N m
M_w	molecular weight	
n	sample number	
$\mathbf{n}_W$	wall normal vector	
p	pressure	Pa
p_{op}	operating pressure	Pa
q	heat flux	W m^{-2}
Q	intensity of the heat exchange	W m^{-3}
Q_V	volume flow rate	m^3 s^{-1}
r	distance to the rotation axis	m
R	universal gas constant	
Re_b	bubble Reynolds number	
R_p	radius of a pipe	m
R_t	transformation (rotation) matrix	
S	sample value	

S_e	equivolume skew	
S_ij	strain-rate tensor	
S_Φ	source term of Φ	
t	time	s
u	velocity magnitude	m s^{-1}
$\mathbf{v}$	velocity	m s^{-1}
$\dot{\mathbf{v}}$	acceleration	m s^{-2}
V	volume in Equation (3.1) and (3.1);	m^3
	translational velocity or angular velocity in Equation (3.94) to (3.102)	m s^{-1}
$\dot{V}$	acceleration of the translational motion or rotation	m s^{-2}
x_i	averaged nodal position of node i	
(x, y, z)	Cartesian coordinates	
y_W	distance to the wall	m
Y_k	dissipation of the kinetic energy	

Greek Characters

Symbol	**Description**	**Unit**
α	volume fraction	

α_S	split factor	
α_C	collapse factor	
β	temperature transmission factor	
Γ	diffusion coefficient	
δ	acceleration increment	rad s^{-2}
Δt	time step	s
ε	turbulent dissipation	
ε_a	absolute error	
ε_r	relative error	
θ	angular displacement	rad
$\dot{\theta}$	angular velocity	rad s^{-1}
$\ddot{\theta}$	angular acceleration	rad s^{-2}
λ_{RT}	Rayleigh–Taylor instability wavelength	m
μ	dynamic viscosity	Pa s
μ_e	effective viscosity	Pa s
μ_t	turbulent viscosity	Pa s
ρ	density	kg m^{-3}
σ	surface tension	N m^{-1}

σ_r	respective turbulent Prandtl number	
$\bar{\bar{\tau}}$	stress-strain tensor	
Φ	general scalar	
ω	specific rate of dissipation	
ω_s	angular velocity of the structure	rad s^{-1}
$\dot{\omega}_s$	angular acceleration of the structure	rad s^{-2}

Subscripts

Symbol	**Description**
0	initial state
b	bubble
B	body coordinates
cap	cap bubbles regime
dis	distorted bubble regime
dri	driving
D	drag force
g	gas
gl	from the gas phase to the liquid phase

hor	horizontal, direction perpendicular to the gravity
i	cell index
ide	ideal
ini	initial
inl	inlet
l	liquid
lg	from the liquid phase to the gas phase
L	lift force
m	mixture
max	maximum
min	minimum
n	time step index in Equation (3.92) to (3.102);
	normal in Equation (4.22)
net	net (force or moment)
nor	normalized
ope	operating
opt	optimal
out	outlet

ref	reference
req	required
sto	Stokes regime
sup	superficial
t	tangent
TD	turbulence dispersion force
v	vortex
var	variation
ver	vertical, direction parallel to the gravity
vis	viscous regime
VM	virtual mass force
WL	wall lubrication force
ω	vorticity

Superscripts

Symbol	**Description**
k	iteration index

Abbreviations

Acronym	Description
1D	One-Dimensional
2D	Two-Dimensional
3D	Three-Dimensional
ALE	Arbitrary Lagrangian-Eulerian
CCD	Charged-Coupled Device
CFD	Computational Fluid Dynamics
CFL	Courant-Friedrichs-Lewy
CSD	Computational Structure Dynamics
EMD	Empirical Mode Decomposition
FAD	Favre-Averaging Drag
FFT	Fast-Fourier Transform
FSI	Fluid-Structure Interaction
HHT	Hilbert-Huang Transform
HSA	Hilbert Spectral Analysis
IEC	International Electrotechnical Commission
IMF	Intrinsic Mode Function

ISA	Instrument Society of American
MUSIG	Multiple Size Group
NVH	Noise, Vibration and Harshness
QA & QC	Quality Assurance and Quality Control
RMS	Root Mean Square
RPI	Rensselaer Polytechnic Institute
UDF	User-Defined Function
VIV	Vortex-Induced Vibration
VOF	Volume of Fraction

Chapter 1

Introduction

Multiphase flow is a common phenomenon in the automotive industry. Vehicle liquids, such as fuel and coolant, possess unstable physical properties and are subject to large ranges of pressure and temperature variations. These liquids may mix with air, readily forming a liquid–gas flow. However, a liquid–gas flow is generally harmful in the automotive industry. In some cases, the performance of vehicles degrades as the physical properties of the fuel or coolant do not operate at their optimal conditions owing to the presence of a liquid-gas flow. The presence of cavitation and unsteadiness in the flow causes corrosion, vibration and noise problems. These pressing issues require a solution for high-quality products pursued by the automotive industry. In consequence, a deeper understanding of the complex phenomenology associated with liquid–gas flows is critically important to the automotive industry.

1.1 Motivations

Multiphase flow is a complicated phenomenon with a research history shorter than 100 years. The theoretical, experimental, and numerical research to date has contributed

limited depth and clarity to the understanding of this phenomenon. Based on the needs of the automotive industry, two aspects of numerical models on multiphase flows need further development: namely, accuracy and capability. Two examples are presented in the following sections to illustrate these two requirements in the solution of complex problems.

1.1.1 Coolant Degassing Problem (Requirement for Accuracy)

The cooling system used in vehicles (Figure 1.1) employs a circulating coolant and is designed to keep the engine operating under a tolerable temperature. The surge tank, also named degas bottle, plays an important role in the cooling system. Because the cooling system operates as a closed system, the surge tank primarily serves as a coolant reservoir to compensate for coolant contraction or expansion under large temperature variations. The secondary function of a surge tank is degassing. Gas dissolved in the coolant will induce cavitation in the pumps of the cooling system and degrade the coolant performance.

Various surge tanks are used in the automotive industry. Some surge tanks have only a single chamber, but others have multiple chambers (Figure 1.2). Generally, the structure of a surge tank is designed to satisfy the requirements for degassing. For example, vertical structures aid degassing. Some surge tanks work under atmospheric pressure, but others are pressurized and equipped with a control valve. In this thesis, the physical object is a pressurized surge tank with many chambers, as this type of surge tank has better degassing performance and is used more widely.

The flow in a surge tank is very complex due to its multi-chamber structure (Figure 1.2). Liquid–gas multiphase flow will progress through each chamber in a specified order, accompanied by degassing caused by the buoyancy effect. The gas in the coolant system is a mixture of coolant vapor and air. High acceleration associated with vehicles in motion could agitate the coolant in the surge tanks. As a result, air is very easily mixed with the coolant.

Liquid–gas flow is the most complicated multiphase flow. Depending on the velocities and volume fractions of the two phases, the flow can be classified into different regimes leading to different flow properties (which will be introduced in Section 2.1). Low velocities and gas volume fractions tend to form bubbly flow in which bubbles easily follow the liquid. However, when the velocities and volume fractions are high enough to form a slug flow, the buoyancy effect dominates the bubble motion, which in turn aids degassing. Moreover, the liquid's physical properties, such as surface tension and viscosity, also affect the degassing performance.

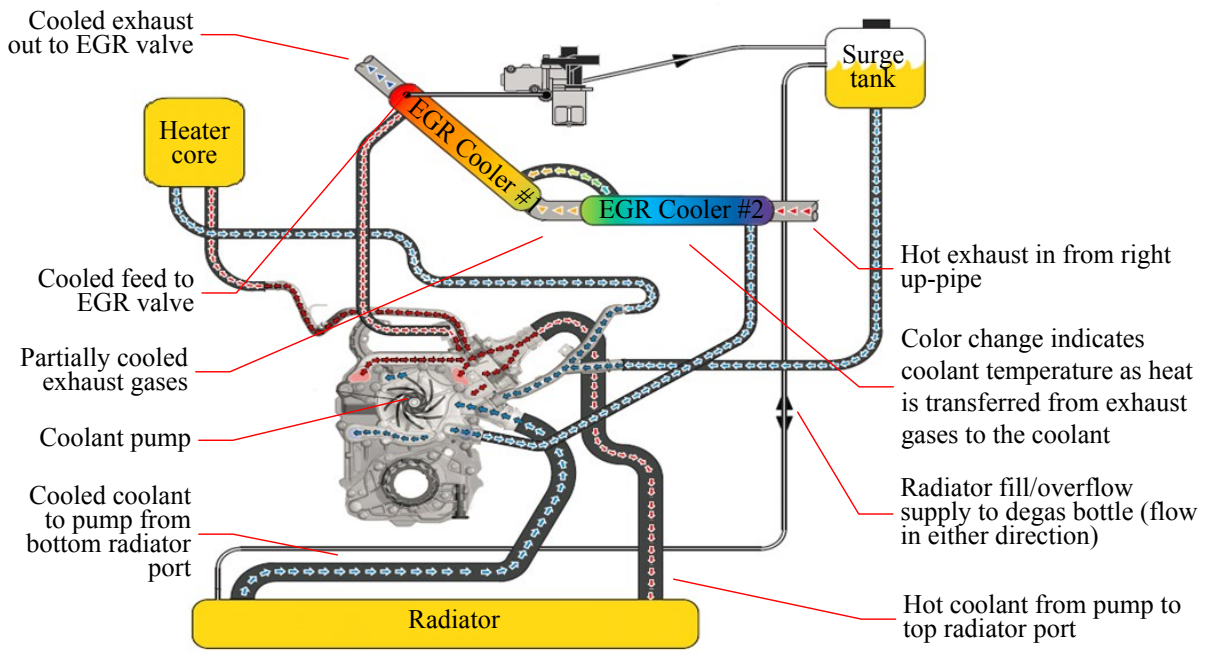

Figure 1.1: Schematic diagram of a cooling system [61].

In view of this, the degassing performance depends on many elements including the surge tank structure, the vehicle motion, the inlet velocity, the gas volume fraction, the coolant physical properties, etc. A deeper understanding of the degassing process is required by designers to ensure safe and efficient operation of an engine served by the surge tank. Experiments are difficult to perform, owing to the small dimension of the surge tank

as well as the sensitivity of liquid–gas flows to any contact measurement. Also with the time requirement of the collaborative project with ABC Group Inc., therefore, numerical method is adopted in the present work. An accurate model for the bubble motion is the key to accurately predict the degassing rate performance of a surge tank.

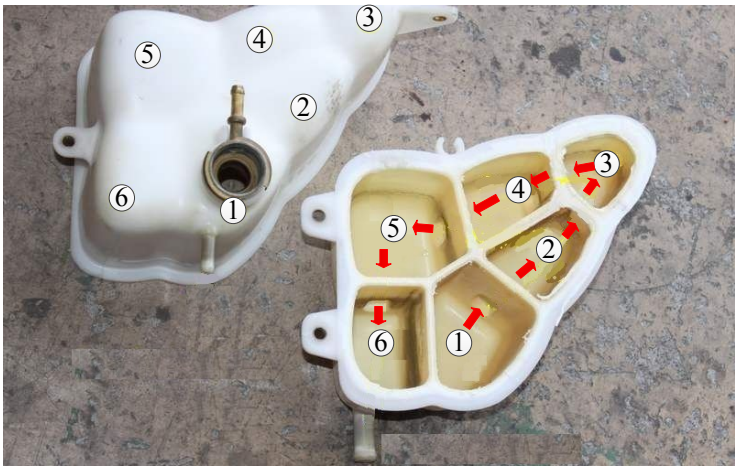

Figure 1.2: Structure of a surge tank [57].

1.1.2 Dynamic-valve Vibration and Noise Problems (Requirement for Capability)

Valves are widely used in material transport systems. The gap size of a valve can be adjusted to satisfy different operating conditions. A dynamic valve is special, as its gap is controlled automatically by the operating condition, usually related to the pressure acting on the poppet valve. Obviously, the flow field in a dynamic valve becomes very unsteady due to the dynamic motion of the poppet valve. Moreover, when liquid–gas (two-phase) flows are involved, the flow field can become very complex. The liquid–gas flow interacting with the poppet valve can potentially generate more pressure fluctuations. As a result, vibration and noise can be generated from the operation of the dynamic valve and this vibration and noise can propagate into the cabin.

The problem of dynamic-valve vibration has never been carefully researched before, but was first encountered by the automotive industry during the development of hybrid vehicles. A whistle noise problem was reported by drivers in so many maintenance cases that lowering the noise, vibration and harshness (NVH) index (an important performance metric of a car) became one of the major issues related to hybrid vehicles. Ford Motor Company confirmed that the noise accompanied by vibration was generated by a dynamic valve in the fuel system.

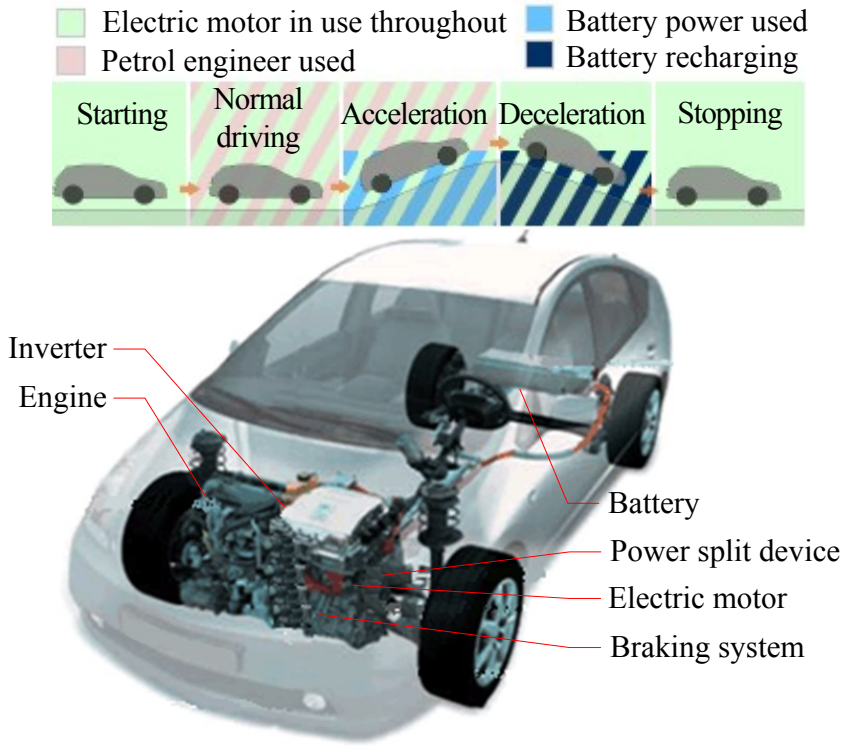

Figure 1.3: Key components of hybrid vehicles [20].

This issue occurs in hybrid vehicles owing to their special architecture. In hybrid vehicles, both the conventional engine and the battery are essential to provide power. They work together or alternately to maximize their strengths, giving a hybrid car better fuel efficiency. Electrical power is used when the car needs less mechanical power, and

the conventional engine and the electric power work together when the car accelerates (Figure 1.3). Hence, if the work condition switches from heavy duty to low duty, the conventional engine automatically stops working; at this moment, the whistle noise occurs. The dynamic valve is a component of the fuel system that works with the engine. Its noise is overwhelmed by the noise from the working engine until the hybrid car switches to electrical power alone. The fuel system does not stop working as soon as the engine stops, so the noise from the dynamic valve is audible over the noise of the electric motor.

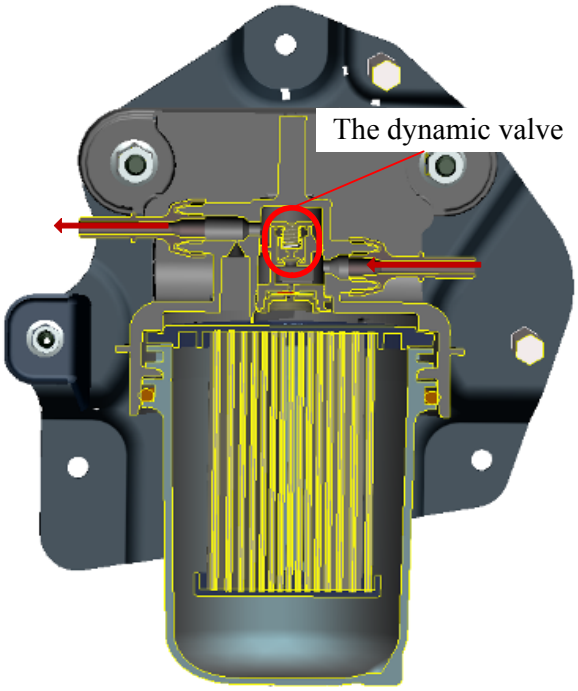

Figure 1.4: Fuel path of the fuel filter in the fuel system [27].

The physical mechanisms responsible for the generation of the vibration and whistle noise are still poorly understood to date owing to various complexities such as the varying operating conditions, the movable structures, and the presence of multiphase flows in the dynamic valve. Figure 1.4 shows the location of the dynamic valve within the fuel system. Unused fuel from the engine returns to the tank through the dynamic valve, which controls

the flow rate of the returning fuel by varying the gap size. The structure of the dynamic valve is shown in Figure 1.5. The poppet is a movable component with a spring pressing it onto the valve seat. The fluid flowing through it exerts an upward pressure on the poppet seal. The gap size is determined by the position of the poppet, which in turn is controlled by the balance between the fluid pressure and the spring force. The fluctuating pressure due to the varying operating conditions of the car causes the poppet to vibrate. Generally, the vibration occurs at a low frequency. However, if a liquid–gas flow is involved, the vibration can reach a high enough frequency to induce noise. In the present work, the flow is a mixture of diesel, diesel vapor and air. When the mixture goes through the gap, the pressure can decline suddenly due to the rapid escape or breaking of bubbles, causing a continual high-frequency vibration of the poppet. This serious impact of multiphase flow was validated by Ford using a simple test: if the flow involved only water, no noise was heard.

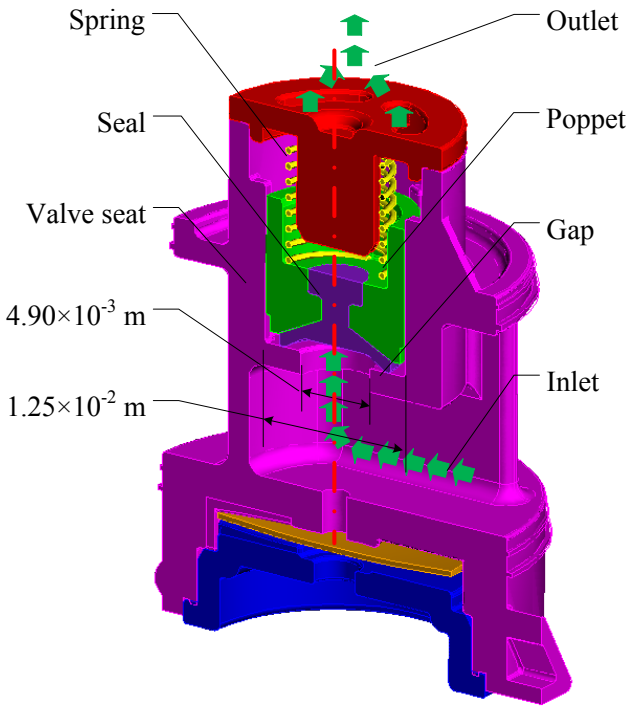

Figure 1.5: Geometry of the dynamic valve.

This vibration and noise problem caused by the dynamic valve lowers the NVH performance of a hybrid vehicle directly and significantly. Hybrid vehicles usually have higher prices than conventional vehicles, resulting in higher customer expectations. However, a noise problem always makes the driver uncomfortable and even misleads the driver to assume a malfunction. Therefore, this noise problem is an urgent obstacle in the development and acceptance of hybrid vehicles.

Understanding the physical mechanisms that generate vibration and noise in a multiphase fluid–structure interaction (FSI) system is foundational to eliminate the noise. Numerical simulation is used in the present work because experiments are difficult to perform, owing to the small dimension of the dynamic valve. To satisfy the time requirement of the collaborative project with Ford, the research is limited to the simulation of the flow field in the dynamic valve instead of both the flow field and the acoustic field. The most important challenge is to build a realistic model applicable to combined multiphase flow and FSI.

1.2 Objectives and Proposal

Elucidating the physical mechanism of liquid–gas flow is foundational to solving the surge tank and the dynamic-valve issues described in the previous section. Numerical simulation is adopted in the present work because experiments are difficult to perform owing to the small dimension of flow domains in a surge tank or a dynamic valve.

Briefly, the major objectives in this thesis are

(1) to develop an accurate numerical model for the simulation of multiphase flow, and to evaluate the parameters associated with the degassing process in a surge tank;

(2) to develop a reliable numerical model for the simulation of multiphase FSI problems, and to elucidate the fundamental mechanisms associated with noise generation in the

dynamic valve.

Obviously, this topic is very challenging for the reasons summarized below:

(1) the degassing process is very complex and related to many elements that are difficult to quantify;

(2) solving the valve vibration and noise problem requires multiphase flow modeling, a good-quality dynamic (or moving) mesh, and a strongly-coupled FSI algorithm. These key techniques require careful validation against related benchmark problems before this tool can be used to achieve the second objective above. However, without significant validation and modifications none of the existing software programs can be used to simulate this problem;

(3) the simulation of multiphase flow requires intensive computational resources. The model built in the present work must be efficient for use in the automotive industry;

(4) coupling these techniques together, particularly when advanced multiphase and turbulence models are included, makes convergence of the overall solution procedure very difficult;

(5) no experimental data are available to validate the CFD simulations.

After considering the above factors and experimenting with various CFD packages (such as ANSYS-CFX, ANSYS-FLUENT and STAR-CCM+), ANSYS-FLUENT was chosen as the simulation tool because it offers the best overall capabilities to solve the present complex problem, flexibility for users to modify or improve models through ANSYS-FLUENT's user-defined functions (UDFs), and accessibility on SHARCNET (www.sharcnet.ca). However, the present FSI problem in a multiphase flow cannot be solved well by the original models in ANSYS-FLUENT (Version 13.0) for two reasons. Firstly, the interfacial force models in the multiphase model are incomplete and/or need improvement. For example, the wall lubrication force is excluded. Secondly, in ANSYS-FLUENT, FSI problems are solved using a dynamic mesh, which is limited in that the motion of the structure

(i.e., the poppet in a dynamic valve) is determined by Newton's second law of motion with forces acting on the structure obtained by the surrounding flow field at the previous time step. This method may cause the solution procedure to diverge for strongly coupled large-displacement problems, where the motion of the structure is very sensitive to the surrounding flow field, particularly in the case when the flow field changes significantly between two consecutive time steps. Hence, large-displacement FSI problems involving multiphase flows are very challenging to solve for any commercial software and in-house CFD codes. In the following, six steps are proposed to improve and validate the individual components of the entire model and then to investigate the degassing phenomenology in a surge tank and the fundamental noise generation mechanisms in a dynamic valve:

(1) use UDFs to enhance the liquid–gas multiphase flow models, which are deficient in ANSYS-FLUENT;

(2) use the "Scheme" command file, which can be embedded into ANSYS-FLUENT, to rearrange the simulation procedure;

(3) carefully choose several benchmark test problems, for which experimental data are available to compare with simulation results, to verify the capability and accuracy of each key technique;

(4) apply the new model to a degassing problem in a coolant surge tank and analyze an indication to measure the degassing performance as well as the influence of various parameters;

(5) integrate all the key techniques and apply them to simulate the liquid–gas flows in the dynamic valve provided by Ford and analyze the surface pressure fluctuations inside the valve and their interactions with the nearby flow field to identify the sources of the noise;

(6) propose degassing improvement and noise reduction strategies by, e.g., optimizing the shape of the poppet valve to reduce noise.

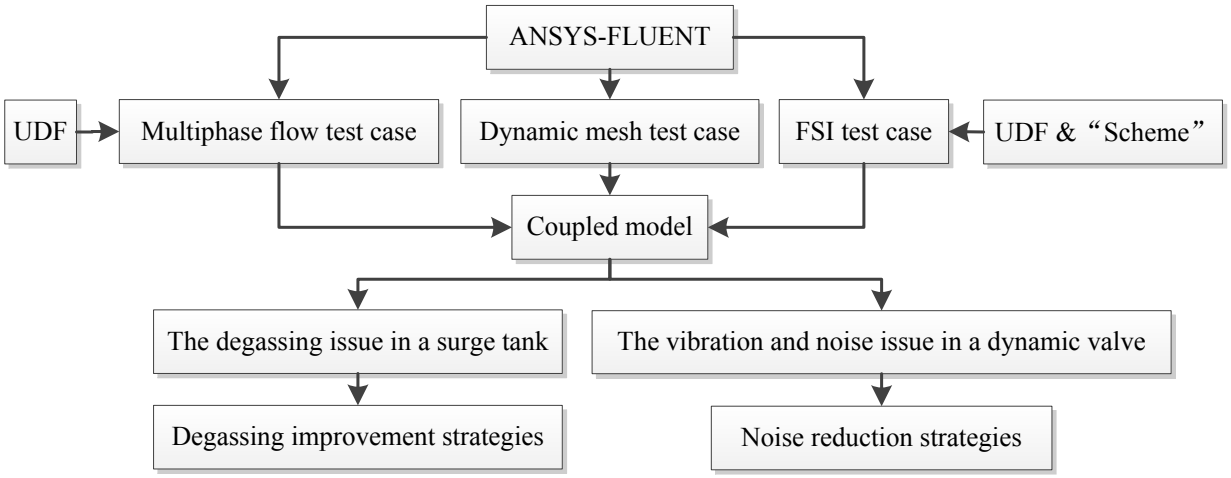

Figure 1.6: Flow chart of the research proposal.

The proposal of this work, involving the above six steps and their inter-connections, is illustrated in Figure 1.6. Due to the absence of experimental data on surface pressure and/or flow field measurements inside the surge tank and the dynamic valve, particularly for multiphase flows, three groups of benchmark test problems (multiphase turbulent flow modeling, dynamic mesh and FSI) will be investigated to validate the numerical tool. After the three benchmark test groups have been successfully validated against the experimental data from the open literature, an improved version of ANSYS-FLUENT will be developed to incorporate more advanced multiphase flow and FSI models. The new model will be used to study the flow field in a coolant surge tank provided by ABC Group in Toronto. Detailed CFD parameters, such as grid size, time step, and interfacial forces will be optimized. Degassing rate and parametric effect on it will be analyzed in a specified geometry. These results will provide the underlying (supporting) reference for the design and performance prediction of coolant surge tanks. The new modeling system will also be applied to a dynamic valve from a hybrid vehicle provided by Ford in Dearborn, USA. The distribution of noise sources in terms of surface pressure fluctuations inside the valve and its relation to the multiphase flow parameters (such as the bubble diameter and inlet velocity) will be analyzed based on the unsteady CFD solutions, followed by a spectral analysis. The

findings of the present research will help motor companies, such as Ford, to devise a noise-reduction plan for hybrid vehicles at the early stages of design. Since noise problems in fuel systems have never been an issue for regular vehicles, where noise from a gasoline engine always exceeds that from the fuel system, it is anticipated that the outcome of the present research will be novel, and its impact on cost-savings for the automotive industries (including OEMs and component suppliers) will be significant.

1.3 Thesis Organization

This thesis is organized as follows:

Chapter 2 reviews previous research on multiphase models, FSI models, and combined multiphase–FSI models. The existing problems in the previous research are highlighted.

Chapter 3 presents mathematical and numerical models employed in this work, as well as improvements and modifications made to them.

Chapter 4 validates new models with improvements and modifications in three key techniques. Numerical and experimental results are compared among various models.

Chapter 5 presents results from the new model applied to a degassing problem in a coolant surge tank. A definition for the degassing rate is proposed and used for model verification and comparison of results. A parametric test analyzes the influence of various parameters on the degassing performance.

Chapter 6 applies the new model to the dynamic-valve vibration and noise problem. Numerical results illuminate the physical mechanism of noise generation in a multiphase FSI system. The mechanism is verified using experimental noise samples.

Chapter 7 presents a final summary, contributions, and recommendations for future work.

Chapter 2

Literature Review

In this chapter, previous research on the key techniques for the simulation of multiphase flow and fluid–structure interaction (FSI), as well as the simulation of fluid–structure interaction involving multiphase flows, are reviewed. Subsequently, a review of research on the coolant degassing problem and valve vibration and noise is presented. Limitations of current methodologies and models are summarized.

2.1 Multiphase Flow

Multiphase flows (i.e., liquid–gas flows in which a liquid is the primary phase and a gas is the secondary phase) are common in many applications pertinent to the energy, chemistry, petroleum, metallurgy, and cryogenic industries. In the case of pre-mixed combustion, in which air and fuel are mixed before entering the combustion chamber, the mixing rate plays an important role as far as the combustion efficiency is concerned. Other cases exist (e.g., medical syringes) where liquid–gas flows should be strictly avoided. Generally speaking, multiphase flow exists depending on the working conditions. Depending on the applications, the existence of multiphase flow can be detrimental to a device's normal

operation (such as in pumps, cavitation induced by liquid–gas flow will damage the pump structures). Hence, it is very important to understand the details of flow properties and, in some cases, interactions of the flow with the surrounding structures.

Research on liquid–gas flows has a history shorter than 100 years. Due to the deformable interface and the compressibility of the gas, these types of flows are among the most complex multiphase flows, particularly under turbulent conditions. In experimental research, difficulties arise from the high sensitivities of liquid–gas flows to disturbances from equipment in the environment. Most of the reported research work concerns flows in vertical or horizontal pipes, which are very simple geometries. The difficulties are even more evident in the corresponding efforts to model these complex flows using computational fluid dynamics (CFD). The coupling between the two phases, and the dynamic break up and coalescence phenomena of gas bubbles in a liquid are very difficult to describe by conservation laws, especially when only very limited experimental data are available for model calibration.

Many classification methods have been proposed for liquid–gas flows. Depending on the relative velocities between the liquid and gas phases, the behavior of a liquid–gas flow can vary considerably. As such, the flow regimes can be bubbly flow, slug flow, or annular flow (Figure 2.1) [52]. Also, other classifications of liquid–gas flows exist depending on whether the two phases are the same composite and/or whether interactions (through interfacial forces) between the phases are taken into account and/or whether the gas phase is compressible or incompressible.

With the advancement of computing power, particularly on parallel platforms, more multiphase models have been developed. Some models track explicitly the interface between the two phases (e.g., models in the literature that were referenced in Section 2.2), while others do not, like the volume of fluid (VOF) method [43]. When the interface is not tracked directly, it can be re-constructed, e.g., linearly [89] based on the volume fraction of gas (or the color function C). For example, in the case of a water–air flow, let us assume that the value of C in a control volume is either 0 or 1, representing water or air,

respectively. When C is between 0 and 1, the interface exists in that control volume and can be re-constructed by using, for example, the Piece Linear Interface Calculation (PLIC) method [89].

With respect to the modeling of liquid–gas flows, depending on the simulation methodology used for the gas phase, these models can be divided into two main categories, namely the Euler–Euler approach and the Euler–Lagrange approach.

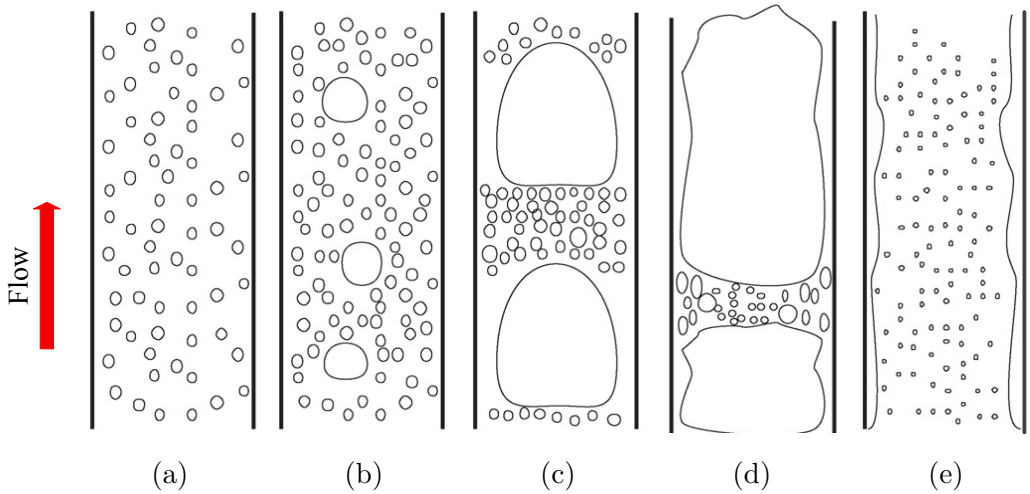

Figure 2.1: Flow regimes in a upward vertical pipe [52]: (a) bubbly flow; (b) cap bubbly flow; (c) slug flow; (d) churn-turbulent flow; and, (e) annular flow.

2.1.1 Euler–Euler Approach

In the Euler–Euler approach [4, 49], separate phases are treated as interpenetrating fluids described in the Eulerian framework. This approach includes the one-fluid model and the two-fluid model. In ANSYS-FLUENT, the one-fluid models include the VOF model and the mixture model, and the two-fluid model is referred to as the Eulerian model. All multiphase models in the Euler–Euler approach are based on the same basic concept which characterizes the distribution of each phase of the fluid by tracking the volume fraction of

each phase throughout the entire computational domain.

The one-fluid model solves only one set of momentum transport equations. For the physical problem investigated in the present work, the inability of the one-fluid model to solve for the interfacial effects in a liquid–gas flow is a major limitation. In the two-fluid model, the velocity differences and interfacial forces among the different phases are explicitly accounted for in each cell (or control volume). This differs from a one-fluid model where the different phases are treated as a mixture of all phases with the same properties (i.e., same viscosity, density, velocity, pressure, and turbulence quantities). In the VOF model, the resulting velocity field from a single momentum equation is shared among the phases. In the mixture model, the relative velocity between the two phases can be reconstructed based on the mixture velocity obtained from its own transport equation. In the mixture momentum equation, an additional term involving the drift velocity (defined as the difference between the phase velocity and mixture velocity, and is related to the relative velocity) can be derived. To complete the formulation, a simple drag model based on the mixture velocity is required to calculate the relative velocity.

In the two-fluid model, the interfacial effect is modeled using several forces: the drag force $\mathbf{F}_D$, lift force $\mathbf{F}_L$, virtual mass force $\mathbf{F}_{VM}$, turbulence dispersion force $\mathbf{F}_{TD}$, and wall lubrication force $\mathbf{F}_{WL}$. The continuity and momentum equations are solved for each phase individually. In fact, the gas phase exists in the liquid phase in the form of bubbles. As a consequence, it seems unreasonable to consider the gas phase as a continuum. In the two-fluid model, this problem is solved by considering the gas as a continuum only to solve for its volume fraction and velocity, but the influence of the bubble size is included in models of the interfacial forces which involve the bubble hydraulic diameter.

The Euler–Euler approach has been widely used to solve multiphase problems. Pfleger et al. [82] simulated rectangular bubble columns on a laboratory scale using the two-fluid model. Only the drag force was considered in their interfacial force model. The bubble columns were simulated as a mono-dispersed flow with a constant bubble diameter. The vertical bubble velocity distributions at different heights under both laminar and turbulent

conditions were compared (for the latter, both the single-phase model and the with a dispersion turbulence model were utilized), clearly showing that the effect of turbulence on bubbly flows was very important. In comparison with the experimental results, the standard single phase model was shown to perform quite well. Following the work by Pfleger et al. [82], Bannari et al. [10] included the drag force, lift force, virtual mass force, and turbulent dispersion force models in the momentum equations in their simulations. Díaz et al. [26] also adopted a similar model, but without considering the turbulent dispersion force. They found that the effect of the virtual mass force on the solutions was insignificant. However, the lift force negatively affected the result at high gas volume fractions, likely due to the lift coefficient in the model being far from "universal" and requiring further calibration. Selma et al. [92] and Gupta et al. [41] also simulated the rectangular bubble columns, particularly focusing on the influence of the diameter distribution and the break-up and coalescence behaviors of bubbles on the phenomena, instead of how many of the interfacial forces need to be included in the two-fluid model in order to accurately represent the flow.

Based on the multiphase flow database compiled by Lucas et al. [66, 67, 65] and Prasser et al. [86] for water–air bubble flows in a vertical pipe, Frank et al. [33, 36, 34] improved the two-fluid multiphase flow models in ANSYS-CFX. In their work, four interfacial forces, namely the drag force, the lift force, the wall lubrication force and the turbulent dispersion force, were used simultaneously in the simulations. Not only was a mono-disperse flow simulated, but a poly-disperse flow involving 21 bubble groups with different bubble diameters and superficial velocities (defined in Section 4.1.2) was also modeled using the inhomogeneous MUSIG (multiple size group) model. The radial distributions of the volume fraction of air at selected column heights were compared to the experimental results, and good agreement was achieved.

Table 2.1 compares simulations in the above literature according to the physical problems, interfacial forces considered, and turbulence models adopted. Most authors applied the multiphase flow model to simple but classical cases, such as bubble column flow and bubbly pipe flow, which are easy to validate by comparison with experimental results. Drag

force, lift force, virtual mass force, wall lubrication force, and turbulence dispersion force are five interfacial forces modeled in this field (see Section 3.2.1). It is generally accepted that the drag force is the most important one. However, researchers have different opinions as to whether to add the other four interfacial forces to the conservation equations (more discussion on this issue can be found in Section 3.2.1). Researchers chose different turbulence models, but more effort has been focused on how to solve for the interactions between the turbulence and the phases. Three different methodologies used in ANSYS-FLUENT for modeling turbulence in a multiphase flow (namely, the dispersed model, the mixture model, and modeling the turbulence separately for each fluid phase) will be described in Section 3.3.

Nevertheless, many other methods exist to model turbulence. In the single-phase model, while the continuous phase is modeled as turbulent (or laminar, depending on the physical problem), the dispersed gas phase is always modeled as laminar. The "dispersed turbulence model" [82, 4] and the Sato model [86, 35] follow from the same assumption: turbulence of the dispersed gas phase is fully influenced by the continuous liquid phase, while turbulence of the continuous phase is solvable from the turbulence equations with the addition of the influence from the dispersed phase through the incorporation of additional source terms. In these models, the dispersed bubbly phase used a zero-equation turbulence model (the eddy viscosity has the same value for the two phases). The above three models differ in how they model the influence of the dispersed phase on the continuous phase. The "dispersed turbulence" method models this effect by a source term in the continuity equation of the liquid phase. In the Sato model, this influence is manifested as extra viscosity induced by bubbles when calculating the eddy viscosity of the liquid phase. But the dispersed turbulence model in ANSYS-FLUENT introduces this influence by adding a source term to the turbulence equations and adding the turbulence dispersion force to the momentum transport equation for the liquid phase.

Table 2.1: Comparison of different multiphase simulations available in the literature.

Literature	Physical problem	Interfacial forces	Turbulence model	Turbulence for multiphase
Pfleger et al. [82]	Rectangular bubble column	$\mathbf{F}_D$; $\mathbf{F}_D$, $\mathbf{F}_{TD}$	Standard $k-\epsilon$	Mixture; dispersed
Bannari et al. [10]	Rectangular bubble column	$\mathbf{F}_D$, $\mathbf{F}_L$, $\mathbf{F}_{VM}$	Standard $k-\epsilon$	Mixture
Díaz et al. [26]	Rectangular bubble column	$\mathbf{F}_D$, $\mathbf{F}_L$, $\mathbf{F}_{VM}$	Standard $k-\epsilon$	Dispersed
Selma et al. [92]	Rectangular bubble column; stirred-tank reactor	$\mathbf{F}_D$, $\mathbf{F}_L$, $\mathbf{F}_{VM}$	Standard $k-\epsilon$	Mixture
Gupta and Roy [41]	Rectangular bubble column	$\mathbf{F}_D$, $\mathbf{F}_L$, $\mathbf{F}_{VM}$	RNG $k-\epsilon$	Mixture
Prasser et al. [86]	Bubbly flow in a vertical pipe	$\mathbf{F}_D$, $\mathbf{F}_L$, $\mathbf{F}_{WL}$, $\mathbf{F}_{TD}$	SST	Sato
Frank et al. [35]	Bubbly flow in a vertical pipe	$\mathbf{F}_D$, $\mathbf{F}_L$, $\mathbf{F}_{WL}$, $\mathbf{F}_{TD}$	SST	Sato

Overall, the Euler–Euler approach is not too difficult to realize even if the secondary phase includes a large amount of bubbles. Increasingly, interfacial forces are commonly incorporated in the momentum transport equations. However, very little work has been attempted to add distinct bubble groups with various diameters and to consider the break-up and coalescence behaviors of the bubbles (that is why the comparison in Table 2.1 does not focus on this aspect). In the Euler–Euler approach, bubbles with different diameters must be treated as different phases, and the number in each group needs to be solved by additional equations, such as PBE (Population Balance Equation) [92]. The computational requirement obviously poses a constraint when a wide range of bubble diameters needs to be considered in the simulation. Although the effects of bubble break-up and coalescence can be modeled, the exact processes cannot be simulated due to a lack of clear interfaces between the two phases supported by a sufficiently fine grid resolution. Generally speaking, the Euler–Euler approach is ideal to simulate the macroscopic behavior of a group of bubbles with a small variation in the bubble size.

2.1.2 Euler–Lagrange Approach

The Euler–Lagrange approach is usually used for solving multiphase flows with discrete phases, such as bubbly flow. It is also called the discrete particle model (DPM). The continuous phase is solved by the Navier–Stokes equations, while the dispersed phase is described using a Lagrangian methodology. The disperse phase can exchange momentum, mass, and energy with the fluid phase. The interaction between bubbles in the dispersed phase can be modeled based on the collision and break-up theory. Depending on the interaction models, this approach consists of the soft sphere model proposed by Tsuji et al. [105] and the hard sphere model proposed by Hoomans et al. [44].

In general, the motion of bubbles can be simulated at the mesoscopic level with higher detail than the Euler–Euler approach. Since the bubbles are treated discretely, any diameter distribution of the discrete phase can be solved without a serious increase in the computational resources. However, this approach still has many limitations. Firstly, the

methodology ignores the influence of bubbles on the fluid; viz., neglecting the volume of the discrete phase potentially influences the simulation results of the continuous phase and limits the application of the Euler-Lagrange approach to those cases that involve only a low (small) discrete-phase volume fraction. Secondly, the methodology focuses on the positions of bubbles, so the pressure and velocity distributions are not available. Thirdly, especially for the hard-sphere model, motion details, such as the process of bubble break-up and droplet collision, are not modeled or solved. However, the changing of bubble size and number due to break-up or coalescence can be modeled. In the present study, the gas volume fraction is above 10 %, and the pressure solution is very important to the calculation of the force on the poppet; therefore, the Euler–Lagrange approach is not appropriate for addressing this problem.

2.2 Fluid–Structure Interaction

Fluid–structure interaction (FSI) is one of the most difficult problems encountered in many research areas, such as building erosion in wind engineering, weapons development, and medical engineering of artificial organs. The interaction occurs between some moving or deformable structure(s) and an internal or surrounding fluid flow. Both computational fluid dynamics (CFD) and computational structural dynamics (CSD) modeling and computational issues, including their coupling, will need to be considered when solving FSI problems.

Fluid–structure interaction can be classified into one-way coupling and two-way coupling [13]. In one-way coupling, only one effect, either from fluid to structure or structure to fluid, is significant, while the opposite effect is weak and therefore ignored. In two-way coupling, reciprocal effects between the fluid and structure are both very strong and, in consequence, the effects of the fluid on the structure and the structure on the flow both need to be resolved.

Two-way coupling is further divided into strong coupling and loose coupling [106]. For strong coupling problems, the interaction between the fluid and structure is very tight so that the flow and structure fields must be solved simultaneously (i.e., in the same time step) in conjunction with the kinematic interface continuity condition. In loose coupling problems, the flow and structure fields are solved according to a pre-defined order spanning two consecutive time steps. For example, the flow field is solved first, and the structure field is then determined at the next time step with the flow field (just obtained) used as boundary conditions at the fluid–structure interface. This method is computationally more efficient but is only suitable for problems in which only the one-way action of either the fluid on the structure or the structure on the fluid is strong.

Two different approaches can be used to solve FSI problems: namely the monolithic approach and the staggered approach. The former solves the equations governing both the fluid and structure fields within one solver, and obviously it is a two-way coupling. The latter solves the fluid and the structure equations separately using two different solvers [106]. If the two solvers exchange solutions in the same time step, the process is known as an implicit algorithm; alternatively, in an explicit algorithm the exchange is done in different time steps. The staggered approach could accommodate one-way coupling or two-way coupling. Loose coupling problems can be solved by the staggered approach without encountering divergence problems. In contrast, the solutions of the fluid and the structure fields for strong coupling problems must be synchronized at every time step. Good results could be obtained from a monolithic approach. But if the staggered approach is adopted, it must be solved using an implicit algorithm.

Generally speaking, problems with a small structural displacement, such as deformation, can be solved as loose coupling problems. However, problems with a large structural displacement, such as the motion of the structure, is usually considered as strong coupling problems.

Many models have been developed to solve FSI problems. Here, only methods for strong coupling problems are reviewed. For flexible-body problems, in which the structure

field solutions are required, CSD equations need to be solved. Related research has been focused on how to solve a coupled system of CFD and CSD equations. For some problems involving rigid or flexible bodies but concerned only with the position of the interface between the fluid and structure, the FSI problem could be simplified as a fluid mechanics problem with dynamic boundary conditions. In the present work, the motion of the poppet valve is controlled by the balance of the pressure from the adjacent fluid and the spring force following Hooke's law. We further assume the deformation of the poppet valve is very small compared to its displacement and, therefore, can be ignored for the present research. Furthermore, many equations already need to be solved for multiphase flows and, as a consequence, FSI methods that do not add additional equations for structure are more realizable and computational feasible.

Dumont et al. [30, 31] and Dahl et al. [23] simulated the leaflet motion in a heart valve with one and/or two leaflets using the dynamic mesh method in FLUENT. The leaflet motion in a heart valve is considered as a large-displacement problem, which might incur convergence problems if the staggered coupling approach is employed. As a remedy, a fully implicit scheme is preferred to solve the motion of the valve leaflet. In the solution iterations, the gradient of torque and the angular acceleration are calculated from values of the previous time step in order to estimate the angular acceleration at the current time step. Due to the variation of gradient of torque with the angular position of the leaflet, selection of initial values at the first iteration of every time step becomes an issue. Dumont et al. [30] first proposed a predictive method by equating the torque for the first iteration at the current time step to the value of the angular acceleration obtained in the previous time step. The torque gradient in the second iteration was increased by a constant value (prescribed empirically by the user) based on the angular acceleration obtained in the previous time step. They obtained good results in comparison with the experiment. However, this method has a number of problems. Firstly, the method requires two iterations to determine the initial torque gradient, but there is no guarantee that the procedure even results in the correct value owing to the fact that in the second iteration even the sign of the prescribed constant used for the correction is unknown (viz., it is unknown whether

the correction to the initial torque gradient needs to be increased or decreased). Secondly, the torque gradient is position-sensitive, which means its value is not constant for a given time step, so the fixed adjustment of the previous angular acceleration is not reasonable and can increase the risk of divergence of the solution. Thirdly, their convergence criterion involving the magnitude of the absolute error may not be a good indicator of convergence because at some sensitive position, a small absolute error may cause the calculation to diverge. Hence, owing to these deficiencies, the methodology of Dumont et al. will require significant modification and optimization for use in the current application.

2.3 Multiphase FSI

Simulation of multiphase FSI problems is a relatively new research area that combines multiphase flow and FSI simulation techniques. It is essentially a FSI problem, in which the working fluid is multiphasic and (most likely) turbulent. The interactions occur not only between different phases of the fluid, but also between the (moving) structure and the multiphase flow. Examples include underwater implosions, pipeline explosions, and slit abrasive erosion in hydraulic turbines. Many of these problems have not yet been thoroughly analyzed owing to their inherent complexity. The slow development of accurate and robust multiphase FSI techniques directly hinders the advancement of related engineering fields.

To date, a very limited number of problems have been carefully analyzed by a strongly coupled multiphase FSI model, and as a result the related literature is very sparse. However, during the last decade, multiphase FSI research was utilized in many fields, indicating both the importance of and trend of advancing this technology.

Studying multiphase flows in pipelines was firstly reported in relation to oil transport systems. Wilkens and Jepson [112] conducted a set of experiments involving mixtures of oil, water, and gas in high- pressure horizontal and +5 degree inclined pipelines to research

potential corrosive effects of multiphase flows in pipelines. Their results showed that a specific ratio of gas, water, and oil could create slug flows, resulting in a highly corrosive environment for typical carbon steel pipelines.

Xie et al. [114] extended the multiphase model based on a modified ghost fluid method (MGFM) to solve compressible FSI problems, where the structure was assumed to be very thick. Xie et al. applied their model to simulate a close-in explosion problem, which was simplified as a highly pressurized spherical gas bubble immersed in a water-filled deformable cylinder. The interface between the water and the structure, as well as the interface between the water and the gas, were tracked in their simulation. The pressure fluctuations at the walls and the deformation of the cylinder subject to different initial pressures in the gas bubble were monitored and analyzed.

Rallu [88] used an in-house code based on the Arbitrary Lagrangian–Eulerian (ALE) method to develop a multiphase FSI modeling framework and to simulate underwater implosion problems in comparison with experimental results. Underwater implosion is a very complex problem that involves strong coupling among the liquid, gas, and structure. The simulation results generally agreed well with the experimental data.

Similar to Rallu's work, Wang [110] opted to develop an embedded boundary method to solve multiphase FSI problems. Wang applied his model to simulate the implosive collapse of an air-backed aluminum cylinder submerged in water, the explosion of an aluminum pipe, as well as underwater explosion problems. Only the first two cases were validated against experiments.

Overall, the preceding multiphase FSI models were developed based on in-house codes. Their physical problems are simple involving as such a clear interaction between the phases, so these models were able to track this interaction during the simulation. Unfortunately, the codes for these models are not available to the general public and will require substantial modification and enhancement if they are to be applied to solve very complex industrial problems, such as the present study of valve vibration and noise in fuel systems. Hence, another approach is needed to address this issue in the present work.

Several models for multiphase flows and different techniques for FSI problems will be reviewed in the following two sections. The specific combination of a multiphase model with an FSI technique will depend on the nature of the problem. The current problem will be addressed using commercial CFD software, as requested by our industry partner. This approach will require the utilization of two software platforms (one for the fluid flow and the other for structure) which, through in-house codes, will be coupled to provide a whole-system simulation.

2.4 Coolant Degassing

The coolant surge tank is a replaceable component of engine systems in vehicles. To date, it has not been researched thoroughly, much less using numerical methods.

Presently most of published literature dealing with design work is inspired by engineering practice and intuition. Their work focused on the design to coolant surge tank geometries or coolant system. Most of literature have been published only in the form of patent applications. For example, the first effort concerning a method for cooling and degassing an internal combustion engine was described in a patent issued in 1976 [19]. Since then, much research [18, 93, 69, 83] concerning the design of coolant surge tanks and cooling systems have been undertaken and patented. This effort indicates that the performance of a cooling system has always been important to the automotive industry. Specifically, the degassing (deaeration) capability of any engine cooling system is considered as critical [16].

Some research has been undertaken to improve the degassing capability of a vehicle cooling system. Garg et al. [37] proposed new instruments and analytical techniques to monitor the air content and performance of degas reservoirs in engine coolant systems based on electrical conductivity measurements of the flowing air or the coolant mixture. With embedded temperature compensation equations, measured system temperature, pressure,

flow rate, and instantaneous void fraction were used to display the air void fraction in real time.

Brahmasani et al. [16] proposed a secondary degassing circuit for an engine cooling system with an atmospheric recovery bottle to improve the degassing performance. In traditional cooling systems, degassing is not a continuous process. Thus, when the degassing process is stopped, there is chance of overheating under some critical conditions. The secondary degassing circuit enables a continuous degassing process to occur. Test results confirmed significant improvement of this proposed degassing capability.

For the automotive industry, degassing performance in a cooling system is not tested specifically to measure the degas rate. As a result, research is usually undertaken for the cooling system rather than the coolant surge tank. However, flow in the whole cooling system is too complex to be simulated in great detail. Currently, vehicle safety and comfort in the automotive industry has received unprecedented priority. The industry requires technical innovation at the component level. Hence, accurate multiphase modeling and simulation is of critical significance.

2.5 Valve Vibration and Noise

Nowadays, quality assurance and quality control (QA & QC) are required in production processes, and noise, vibration, and harshness (NVH) is one of most important issues that need to be solved during the final testing of automobiles. Many noise problems arise from valves, which are widely used in the fuel systems of a hybrid vehicle.

In fact, the vibration and noise problem of valves has been researched for several decades, almost since valves were first designed and constructed. Related literature can be traced back to the 1960s [59]. Over the past fifty years, researchers have gained more knowledge about noise generation and propagation processes by pursuing three research aims: (1) identification of the sources of valve noise, (2) reduction of valve noise by engi-

neering means as a short-term goal, and (3) understanding the fundamental mechanisms associated with valve noise and providing guidelines for the early design phase to eliminate future noise problems as a long-term goal. The third aim describes the one of the principal objectives of the present thesis.

Noise generated by a valve is believed to come from multiple sources, which can be classified into mechanical noise and flow dynamic noise [113]. Mechanical noise is associated with the instability of piping due to vibration, whereas flow dynamic noise is mainly generated by turbulence of the fluid. Huff [47] reported results from the careful monitoring of the noise in large butterfly valves, which involved both mechanical noise and flow dynamic noise.

Based on the sources of the noise, much research has been conducted around two main strategies for reducing the valve noise: namely, source control and path control. Source control seeks to reduce the mechanical noise by optimizing the structure and increasing the material rigidity [113]. Also, the structure of the flow channel can be optimized in such a way that the pressure drop can be varied gently over several stages in the flow channel. A smaller pressure difference between the inlet and the outlet reduces the possibility of cavitation, which can induce the noise. Another method, referred to as "flow division", has also been widely used for noise reduction in valves. In flow division, rather than having the flow pass through a single opening, the flow is made to traverse several openings in parallel. Owing to the viscosity of the fluid, the more solid surface that the fluid contacts with, the greater is the pressure drop is generated. Based on this method, noise suppressors have been designed since the 1960s [59]. To this purpose, a part with many orifices covers the fluid and divides its flow among many small streams in order to increase the noise frequency. This process attenuates the perceptibility of the noise to the human ear, which is more sensitive to the lower frequency noise [72].

Work related to the prediction of valve noise has also gone through a long development. As mentioned above, the pressure difference between the inlet and outlet is a key factor of the noise generation, so it is used as a reference to predict the noise level. The prediction

models for valve noise have been standardized by agencies, such as the Instrument Society of America (ISA) [48] and the International Electrotechnical Commission (IEC) [53].

However, due to the tiny dimensions and complex geometries of most valves, experimental research involving flow field measurements in valves is very limited. The lack of validation datasets poses challenges for numerical simulation research. In addition, multiphase turbulent flows are very difficult to model. To the author's best knowledge (which was also confirmed by engineers at Ford, Dearborn, USA), no literature has been found related to research on a dynamic valve involving liquid–gas flow with an in-depth explanation about the fundamental mechanisms associated with the valve noise generation. Hence, it is anticipated that development of an accurate numerical model to investigate the sources of noise in dynamic valves pertinent to the automotive industry will be both novel and challenging.

2.6 Chapter Summary

This chapter reviews previous research on the key techniques for the modeling and simulation of multiphase flows, FSI, as well as the simulation of multiphase flows involving FSI. Research on the coolant degassing and valve vibration and noise problems are also surveyed.

To date, modeling multiphase flow exactly is still very difficult due to its complexity. Compared with models using the Euler–Euler approach and the Euler–Lagrange approach, the two-fluid mode (called Eulerian model in FLUENT) is considered to be the most accurate model owing to its capability to separately model two phases as well as their interaction. In this approach, the proper selection of interfacial-force models is very important to obtaining accurate results in the simulation.

Most FSI problems solve for the fluid field and the structure field using separate solvers. It is extremely difficult to model a FSI problem in a single software package. Meanwhile,

data exchange between the fluid and structure solvers is the key to obtaining accurate results, especially for strong coupling problems.

Multiphase FSI problems are even more complicated than single-phase FSI. As a result, very few studies have been published so far, and most of them involve specialized software realized as in-house codes which are not publically available. Moreover, in-house coding solutions are too time consuming and limited in their modeling capabilities for the automotive industry. Hence, the objective of the present research, to solve multiphase FSI problems using ANSYS-FLUENT, will meet the requirements for efficiency, modeling capability and technology transfer in the automotive industry.

Published research results associated with the coolant degassing problem and valve vibration and noise problem are very limited, especially on the investigation of the underlying physical mechanisms that govern these problem. In consequence, a deeper understanding of the complex phenomenology associated with the multiphase-flow-induced noise and vibration in a dynamic valve is of critical importance to the automotive industry.

Chapter 3

Simulation Modeling

This chapter introduces models of key techniques used in the simulation: multiphase flow, interfacial force, turbulence model, dynamic mesh, and FSI. For most of these techniques, two different methodologies are described. The limitations and weaknesses of the model currently provided in ANSYS-FLUENT (version 13.0) are identified, and possible improvements and modifications of these models are described.

3.1 Multiphase Flow Models

As reviewed in Chapter 2, two main approaches have been used to simulate multiphase flows: namely, the Euler–Lagrange approach and the Euler–Euler approach. In the Euler–Lagrange approach, the two phases are divided into a (continuous) fluid phase, which is modeled in the Eulerian framework, and a (discrete) gas phase, which is modeled in the Lagrangian framework. In contrast, in the Euler–Euler approach, all phases of the flow are treated mathematically as interpenetrating continua and described in the Eulerian framework. As a result, the two approaches differ in their mass and momentum conservation equations and their post-processing of the simulation results.

As the discrete phase in the Euler–Lagrange approach is solved by tracking the positions of a large number of particles, bubbles or droplets using Newton's second law of motion, the forces exerted by the continuous phase on the dispersed phase can be calculated using a drag-force model similar to that used in the Euler–Euler approach. However, the volume of the discrete phase in the Euler–Lagrange approach is neglected because the continuity equation is solved only for the fluid phase. This approximation that is valid only for problems involving a low gas volume fraction (less than 10 %) which is not applicable to the physical problems to be solved in this work. In consequence, the Euler–Euler approach is utilized for the present study. The distribution of the volume fraction of gas is believed to be closely correlated with the noise generation in a dynamic valve.

In the Euler–Euler approach, the volume of a phase cannot be occupied by other phases, so the volume fraction of a phase in a given control volume is an important concept in representing the phase's mass, momentum and energy contributions. Taking a liquid–gas two-phase flow as an example, the volume of the liquid phase V_l (here the subscript l denotes the liquid phase) is defined as

$$V_l = \int_V \alpha_l dV, \tag{3.1}$$

and, similarly, the volume of the gas phase V_g (here the subscript g denotes the gas phase) is defined as

$$V_g = \int_V \alpha_g dV, \tag{3.2}$$

where α_l and α_g are the volume fraction of the liquid and the gas, respectively, with

$$\alpha_l + \alpha_g = 1. \tag{3.3}$$

ANSYS-FLUENT implements three multiphase models based on the Euler–Euler approach: namely, the VOF model, the mixture model, and the Eulerian model. The VOF model and the mixture model are based on a one-fluid model, whereby only one set of momentum transport equations is shared by the different phases. Obviously, the interfacial forces cannot be reflected in the solution for a one-fluid model. As a consequence, the

Eulerian model based on a two-fluid model is applied in the present work. The continuity and momentum transport equations for the Eulerian model [4] are summarized below.

3.1.1 Eulerian Model (Two-fluid Model)

Continuity Equation

The liquid and gas volume fractions α_l and α_g are obtained from continuity equations related to the mass conservation. The continuity equation for the liquid phase is

$$\frac{\partial}{\partial t}(\alpha_l \rho_l) + \nabla \cdot (\alpha_l \rho_l \mathbf{v}_l) = 0, \tag{3.4}$$

where ρ_l is the density of the liquid phase and $\mathbf{v}_l$ is the intrinsic velocity of the liquid phase. The intrinsic velocity is a hypothetical velocity assuming that both the liquid and the gas are continuum flow in the cross-section they occupy. Intrinsic velocity is usually used in the Euler approach and is defined as (for the liquid phase and the gas phase, respectively)

$$\mathbf{v}_l = \frac{Q_{V,l}}{A \cdot \alpha_l}, \tag{3.5}$$

$$\mathbf{v}_g = \frac{Q_{V,g}}{A \cdot \alpha_g}, \tag{3.6}$$

where $Q_{V,l}$ and $Q_{V,g}$ are the volume flow rates of the liquid and the gas, respectively, and A is the cross-sectional area.

Similarly, the continuity equation for the gas phase is

$$\frac{\partial}{\partial t}(\alpha_g \rho_g) + \nabla \cdot (\alpha_g \rho_g \mathbf{v}_g) = 0, \tag{3.7}$$

where ρ_g is the density of the gas phase and $\mathbf{v}_g$ is the intrinsic velocity of the gas phase.

Momentum Transport Equations

The momentum transport equation for the liquid phase is

$$\frac{\partial}{\partial t}(\alpha_l \rho_l \mathbf{v}_l) + \nabla \cdot (\alpha_l \rho_l \mathbf{v}_l \mathbf{v}_l) = -\alpha_l \nabla p + \nabla \cdot \bar{\bar{\tau}}_l + \alpha_l \rho_l \mathbf{g} + \mathbf{F}_{D,l} + \mathbf{F}_{L,l} + \mathbf{F}_{VM,l} + \mathbf{F}_{WL,l} + \mathbf{F}_{TD,l} + \mathbf{F}_{S,l}, \tag{3.8}$$

where $\bar{\bar{\tau}}_l$ is the stress-strain tensor of the liquid phase defined as

$$\bar{\bar{\tau}}_l = \alpha_l \mu_{e,l} \left(\nabla \mathbf{v}_l + \nabla \mathbf{v}_l{}^T \right) - \frac{2}{3} \alpha_l \mu_{e,l} \nabla \cdot \mathbf{v}_l \bar{\bar{I}}. \tag{3.9}$$

Here, $\mu_{e,l}$ is the effective viscosity (sum of the dynamic viscosity and the eddy viscosity) of the liquid and $\mathbf{F}_{D,l}$, $\mathbf{F}_{F,l}$, $\mathbf{F}_{VM,l}$, $\mathbf{F}_{WL,l}$, $\mathbf{F}_{TD,l}$ and $\mathbf{F}_{S,l}$ are the drag force, the lift force, the virtual mass force, the wall lubrication force, the turbulence dispersion force, and the surface tension force acting on the liquid phase as described (in greater detail) below. The force from surface tension in ANSYS-FLUENT is modeled based on Brackbill's [15] work.

Similarly, the momentum transport equation for the gas phase is

$$\frac{\partial}{\partial t}(\alpha_g \rho_g \mathbf{v}_g) + \nabla \cdot (\alpha_g \rho_g \mathbf{v}_g \mathbf{v}_g) = -\alpha_g \nabla p + \nabla \cdot \bar{\bar{\tau}}_g + \alpha_g \rho_g \mathbf{g} + \mathbf{F}_{D,g} + \mathbf{F}_{L,g} + \mathbf{F}_{VM,g} + \mathbf{F}_{WL,g} + \mathbf{F}_{TD,g} + \mathbf{F}_{S,g}, \tag{3.10}$$

where $\bar{\bar{\tau}}_g$ is the stress tensor of the gas phase given by

$$\bar{\bar{\tau}_g} = \alpha_g \mu_{e,g} (\nabla \mathbf{v}_g + \nabla \mathbf{v}_g{}^T) - \frac{2}{3} \alpha_g \mu_{e,g} \nabla \cdot \mathbf{v}_g. \tag{3.11}$$

Here, $\mu_{e,g}$ is the effective viscosity (the sum of the dynamic viscosity and the turbulent viscosity) of the gas and $\mathbf{F}_{D,g}$, $\mathbf{F}_{F,g}$, $\mathbf{F}_{VM,g}$, $\mathbf{F}_{WL,g}$, $\mathbf{F}_{TD,g}$ and $\mathbf{F}_{S,g}$ are the drag force, the lift force, the virtual mass force, the wall lubrication force, the turbulence dispersion force, and the surface tension force acting on the gas phase (defined in greater detail below).

Energy Transport Equations

The gas phase is considered to be a compressible fluid, so its density is calculated by

$$\rho_g = \frac{p_{\text{ope}} + p}{\frac{R}{M_w} T}, \tag{3.12}$$

where p_{ope} is the operating pressure (taken nominally to be 101325 Pa), R is the universal gas constant, and M_w is the molecular weight.

In ANSYS-FLUENT, only one phase can be treated as a compressible fluid. Hence, if compressibility of the liquid is also considered, it has to be performed using a user defined function (UDF). In the present study, the density change with temperature is very small, so the density of the liquid phase can be calculated using the following relationship:

$$\rho_l = \frac{\rho_{\text{ref},l}}{1 - \frac{p}{B}}, \tag{3.13}$$

where $\rho_{\text{ref},l}$ is the reference density for the liquid phase, and B is the bulk modulus of the liquid given by 2.2×10^{-9} Pa.

The energy transport equations are solved separately for each phase. For the liquid phase, the equation can be written as

$$\frac{\partial}{\partial t}(\alpha_l \rho_l h_l) + \nabla \cdot (\alpha_l \rho_l \mathbf{v}_l h_l) = \alpha_l \frac{\partial p}{\partial t} + \bar{\bar{\tau}}_l : \nabla \mathbf{v}_l - \nabla \cdot \mathbf{q}_l + Q_{gl}, \tag{3.14}$$

where h_l is the specific enthalpy of the liquid phase, $\mathbf{q}_l$ is the heat flux in the liquid, and Q_{gl} is the intensity of the heat exchange between the gas phase and the liquid phase.

For the gas phase, the energy transport equation is given similarly by

$$\frac{\partial}{\partial t}(\alpha_g \rho_g h_g) + \nabla \cdot (\alpha_g \rho_g \mathbf{v}_g h_g) = \alpha_g \frac{\partial p}{\partial t} + \bar{\bar{\tau}}_g : \nabla \mathbf{v}_g - \nabla \cdot \mathbf{q}_g + Q_{lg}, \tag{3.15}$$

where h_g is the specific enthalpy of the gas phase, $\mathbf{q}_g$ is the heat flux in the gas, and the intensity of the heat exchange between the gas phase and the liquid phase Q_{lg} is equal to Q_{gl}.

3.1.2 Eulerian Immiscible Fluid Model

The Eulerian immiscible fluid model is an additional function in the Eulerian model implemented in ANSYS-FLUENT. In addition to solving a separate set of momentum transport equations for each phase, the model allows the use of the Geo-reconstruct, compressive, and CICAM (compressive interface capturing scheme for arbitrary meshes) schemes with an explicit VOF option. Hence, with this model enabled, a sharp interface between phases can be obtained to reflect the physical interface in the multiphase flow of two immiscible fluids. The interface reconstruction method adopted in this present work is the Geo-reconstruct discretization scheme.

The term "Geo-reconstruct" refers to the fact that the interface between the two phases is reconstructed for each time step based on the volume fraction obtained in that time step. In ANSYS-FLUENT, the interface-capturing scheme is generalized for unstructured meshes from the work of Youngs [116]. The program assumes that the interface between the two phases has a linear slope within each cell.

The first step in this reconstruction scheme involves the calculation of the position of the linear interface relative to the center of each partially-filled cell, based on the information about the volume fraction and its derivatives in the cell. The second step involves the calculation of the advection of fluid through each face of the cell using the computed linear interface representation and the information about the normal and tangential velocity distribution on the face. The third step involves the calculation of the volume fraction in each cell using the balance of mass and momentum fluxes calculated from the previous time step [116, 4].

3.2 Interfacial Force Models for Liquid–Gas Flow

In liquid–gas flow, the pressure distribution around a bubble is non-uniform. Hence, the net pressure over the surface of a bubble is non-zero. The influence from a non-uniform pressure should be considered as the interface between the two phases is not tracked in the Eulerian model. According to these different effects, three components of the net pressure on the interface between the liquid and gas are defined: the drag force, lift force, and virtual mass force. The wall lubrication force and turbulence dispersion force observed in the experiments or obtained from an averaging procedure are considered as well. The models for these forces that have been adopted in the present work will be described in this section.

3.2.1 Literature Survey for Interfacial Force Models

The interfacial forces in a liquid–gas flow are viscous forces, pressure, and surface tension in real flow behaviors. They can be included in the momentum transport equations and need to be modeled for closure as the local volume average and time average are applied to these transport equations. modeling the interfacial forces accurately is very important to obtain correct flow results, especially for the motion of the secondary phase.

Five interfacial forces have been modeled and widely used: namely, the drag force, lift force, virtual mass force, wall lubrication force, and turbulent dispersion force. The drag force and lift force are of special importance to liquid–gas flow models since they determine the migration of bubbles in two main directions. The drag force contributes to a non-uniform pressure and to the viscous force (mainly produced within the boundary layer) which acts principally around the surface of the bubbles that are in relative motion with the liquid phase. The direction of the drag force always acts conversely to the relative motion direction by definition, while the lift force induced by the non-uniform velocity gradient acts orthogonally to the relative motion [as shown in Equation (3.25) below] and

contributes to the non-uniform pressure around bubbles. The virtual mass force (also called the added mass force) is modeled from the integration of the non-uniform pressure around bubbles. When bubbles are accelerated through the continuous phase, the continuous phase surrounding the bubbles is accelerated as well, at the expense of work done by the dispersed phase [22]. With the virtual mass force, the momentum transport equation for the secondary phase is influenced as if it has an added mass.

The concept of wall lubrication was proposed by Antal et al. [7]. In a liquid–gas flow, because the near-wall region has different drainage rates for liquids and gases, bubbles in this region will experience a net force pushing them away from the wall. This effect is consistent with the experimental phenomenon observed in reference [55]. The turbulent dispersion force is related to the influence of turbulent diffusion, which is the result of the fluctuating component of the forces acting on the bubbles. When a time averaging operation is applied to the momentum transport equations, the term in the drag force arising from the velocity fluctuations is defined as the turbulent dispersion force.

Presently, researchers are in general agreement on the form of the drag force model. In consequence, most recent research efforts have been focused on the development and formulation of a model for the drag coefficient. Among more than fifteen drag coefficient models that have been proposed in the literature, some are based on the bubble Reynolds number, which is related to the relative velocity of the two phases and the bubble's diameter [91, 24, 21, 5, 56, 58, 117, 95], whereas other models are related to the Eötvös number (also called the Bond number) (defined in Section 3.2.3), which characterize the shape of the bubbles [50, 40, 102], and some models combine the two approaches [104]. Pang and Wei [81] compared different drag coefficient models at low to medium Reynolds numbers by analyzing the drag coefficient vs. either the bubble Reynolds number or Eötvös number. Based on the continuity and smoothness of the resulting curves, the drag coefficient models reported by Schiller and Naumaan [91], Dalla Ville [24], Ahmadi and Ma [5], and Zhang and Vanderheyde [117] were considered to be the most reasonable and applicable for the calculation of the drag force in a bubbly flow. Tabib et al. [96] analyzed the effect of seven different drag coefficient models in a bubble column simulation. The results showed that

all the drag laws were able to predict the average gas hold-up and the centerline velocity very well. Models reported by Ishii and Zuber [50], Ahmadi and Ma [5], and Zhang and Vanderheyde [117] yield predictions closer to experimental values. Overall, the drag law of Zhang and Vanderheyde [117] gave generally better predictions for a wide range of relative velocity values. Zhang [118] simulated a liquid metal–air bubble problem using the Dalla Ville [24], Zhang and Vanderheyde [117], and universal drag models, which are all based on the drag model of Ahmadi and Ma [5]. The results indicate that the effect of drag models is very weak when the flow is turbulent (i.e., when the Reynolds number is above 3000), because the velocity fluctuations (acting through the turbulent dispersion force) are large enough to drive the motion of the bubbles.

Compared with the drag force, modeling of the lift force is more complicated. Key factors influencing the lift force are the bubble Reynolds number and the dimensionless shear rate [70, 60, 103]. It was found by Tabib et al. [96] that the value of the lift coefficient should be chosen depending on the bubble size, since the lift forces on different-diameter bubbles act in opposite directions (the coefficient could be positive or negative depending on the bubble diameter).Without this consideration, some researchers' models [119, 9, 90] are incorrect. Lucas and Frank et al. [67, 35] used the lift model proposed by Tomiyama et al. [103] to validate the multiphase model of ANSYS-CFX in bubbly pipe flow cases and achieved very good agreement with experimental results. Zhang [118] analyzed the results from different combinations of drag and lift models. The analysis shows that when used with a universal drag law, the use of different lift models makes no difference to the predictions for the multiphase flow.

Research into the virtual mass force is not as extensive as that concerning the drag and lift forces. Deen et al. [25] found only very small differences between the predicted results of the gas–liquid flow in a square cross-sectioned bubble column with and without the inclusion of a virtual mass force model. Lucas and Frank et al. [67, 35] considered the virtual mass force to be of minor importance in comparison with the other interfacial forces and neglected it. Zhang [118] obtained results similar to those of Deen et al. [25], showing that the virtual mass force has very limited influence on the predictions.

Researchers have begun to pay increasing attention to the wall lubrication force over the last decade, ever since it was first proposed. Antal et al. [7, 8], Tomiyama [101], and Frank [36] have proposed models for this force. Frank et al. [35] remarked that the model of Antal et al. [7] is too restricted to balance the lift force under certain flow conditions, while the model of Tomiyama [101] is limited only to pipe flow since it contains the pipe diameter as a geometry length scale. Frank et al. modified the wall lubrication force model and suggested using the coefficient values obtained from experiments done by Prasser et al. [86].

The turbulent dispersion force is generated from averaging procedures applied to the drag force and results in different models based on the form of averaging used. Ljus [62] and Johansson et al. [51] derived a turbulent force model based on time averaging. Gosman et al. [39] and Behzadi et al. [12] proposed a model derived from Favre-averaging drag (FAD). Burns et al. [17] compared the FAD model and the Rensselaer Polytechnic Institute (RPI) model [64] in a pipe flow simulation and showed that better results were obtained with the FAD model. Qian et al. [87] showed the obvious difference in bubble column simulation results with and without the turbulent dispersion force, verifying the importance of the turbulent dispersion force in a bubbly flow.

Although many research results have been applied to interfacial force models, due to our limited knowledge of multiphase flows, the complicated interaction between different phases still cannot be modeled accurately. In a liquid–gas flow at high velocities, especially in highly dispersed bubbly flow, the interfacial force models seriously deviate from experimental results. Furthermore, the development of methodologies that exhibit good convergence for the simulations is an extremely challenging problem.

3.2.2 Drag Force

The drag force is the most common force to include in the modeling of multiphase flows. The force always acts in the opposite direction to the relative motion. Its effect is to

weaken the relative motion between the bubble and the (surrounding) liquid.

The drag force acting on a single particle [55] is expressed as

$$\mathbf{f}_{D,l} = -\mathbf{f}_{D,g} = -\frac{1}{8}\pi C_D \rho_l d_g^2 \left|\mathbf{v}_l - \mathbf{v}_g\right| (\mathbf{v}_l - \mathbf{v}_g), \tag{3.16}$$

where C_D is the drag coefficient and is d_g the diameter of the bubble.

In the present work, the volume fraction of gas bubbles is lower than 50 %. The interactions among bubbles can be ignored if it is assumed that the bubbles are isolated when their volume fraction is low. Thus, the drag force acting on the gas phase in a control volume is equal to the drag force acting on a single bubble multiplied by the number of bubbles, assuming all the bubbles are spherical and of equal size, so:

$$\mathbf{F}_{D,l} = -\mathbf{F}_{D,g} = -\frac{3}{4} C_D \frac{\alpha_g \rho_l}{d_g} \left|\mathbf{v}_l - \mathbf{v}_g\right| (\mathbf{v}_l - \mathbf{v}_g). \tag{3.17}$$

The original causes of the drag force are the bubble's deformation and the viscosity of the liquid due to the relative motion. It is noted that the drag force consists of form drag and viscous drag, and each has a different weight under different relative velocity flow regimes. To differentiate them, two important concepts are introduced; namely, the bubble Reynolds number Re_b and the Rayleigh–Taylor instability wavelength λ_{RT}:

$$\mathrm{Re}_b = \frac{\left|\mathbf{v}_l - \mathbf{v}_g\right| d_g}{\upsilon_l}, \tag{3.18}$$

and

$$\lambda_{RT} = \left[\frac{\sigma}{g(\rho_l - \rho_g)}\right]^{0.5}, \tag{3.19}$$

where σ is the surface tension between the liquid and gas and g is the gravitational acceleration.

Using Re_b and λ_{RT} to distinguish between the different flow regimes and to condition the computation of the drag coefficient is called the universal drag law [4, 55], which is characterized as follows:

1) $\mathrm{Re}_b < 16$ (Stokes regime) The drag force on a single bubble depends linearly on its relative velocity. The coefficient is modeled by Stokes law:

$$C_{D,\mathrm{sto}} = \frac{24}{\mathrm{Re_b}}; \tag{3.20}$$

2) $\mathrm{Re}_b > 16$ (viscous regime) The drag force depends non-linearly on the velocity difference. For this regime, the Schiller–Naumann model is adopted:

$$C_{D,\mathrm{vis}} = \frac{24}{\mathrm{Re}_b}\left(1 + 0.1\mathrm{Re}_b{}^{0.75}\right); \tag{3.21}$$

3) $\frac{24}{\mathrm{Re}_b}\left(1 + 0.1\mathrm{Re}_b^{0.75}\right) \leq \frac{2}{3}\frac{d_g}{\lambda_{RT}} \leq \frac{8}{3}$ (distorted bubble regime) In this regime, the drag coefficient depends only on the bubble diameters and liquid properties, as follows:

$$C_{D,\mathrm{dis}} = \frac{2}{3}\left(\frac{d_g}{\lambda_{RT}}\right)\left[\frac{1 + 17.67(1-\alpha_g)^{\frac{9}{7}}}{18.67(1-\alpha_g)^{\frac{3}{2}}}\right]^2; \tag{3.22}$$

4) $\frac{d_g}{\lambda_{RT}} \geq 4$ (cap bubbles regime)

In this regime, bubbles are strongly deformed. The drag coefficient is computed as

$$C_{D,\mathrm{cap}} = \frac{8}{3}(1-\alpha_g)^2. \tag{3.23}$$

In the present work, the Stokes regime is absorbed into the viscous regime, so the drag coefficient can be expressed as

$$C_D = \min\left(\max\left\{\frac{24}{\mathrm{Re}_b}\left(1 + 0.1\mathrm{Re}_b^{0.75}\right), \frac{2}{3}\left(\frac{d_g}{\lambda_{RT}}\right)\left[\frac{1 + 17.67(1-\alpha_g)^{\frac{9}{7}}}{18.67(1-\alpha_g)^{\frac{3}{2}}}\right]^2\right\}, \frac{8}{3}(1-\alpha_g)^2\right). \tag{3.24}$$

3.2.3 Lift Force

The component of the net pressure acting perpendicular to the relative velocity is defined as the lift force. It results from a non-uniform gradient in the continuum velocity field over

the particle. Several researchers [55] have verified that rotating symmetric bubbles in a symmetric continuum flow, non-rotating symmetric bubbles in a non-symmetric continuum flow, and non-rotating asymmetric bubbles in a symmetric continuum flow; all experience a lift force. Its direction is always perpendicular to the relative velocity and the curl of the continuum velocity field. The general form of lift force acting on a single bubble, as defined by Drew and Lahey [29], is given by

$$\mathbf{f}_{L,l} = -\mathbf{f}_{L,g} = -C_L \rho_l \frac{\pi {d_g}^3}{6} (\mathbf{v}_l - \mathbf{v}_g) \times (\nabla \times \mathbf{v}_l). \tag{3.25}$$

where C_L is the lift coefficient. After multiplying by the bubble number per unit volume mixture, the lift force per unit volume is given by

$$\mathbf{F}_{L,l} = -\mathbf{F}_{L,g} = -C_L \rho_l \alpha_g (\mathbf{v}_l - \mathbf{v}_g) \times (\nabla \times \mathbf{v}_l). \tag{3.26}$$

The lift force is associated with the velocity field as well as the bubble parameters in a complex relationship. So far, the lift coefficient has been derived experimentally. Tomiyama et al. [101] modeled the lift coefficient, C_L, by measuring the trajectories of single bubbles in simple shear flows of a glycerol–water solution. The model proposed here has the following form:

$$C_L = \begin{cases} \min[0.288 \tanh(0.121 \mathrm{Re}_b), f(Eo_d)], & Eo_d < 4 \\ f(Eo_d), & 4 \le Eo_d \le 10 \\ -0.27, & Eo_d > 10 \end{cases}, \tag{3.27}$$

where

$$f(Eo_d) = 0.00105 {Eo_d}^3 - 0.0159 {Eo_d}^2 - 0.0204 Eo_d + 0.474, \tag{3.28}$$

$$Eo_d = \frac{g(\rho_l - \rho_g) d_H^2}{\sigma}, \tag{3.29}$$

$$d_H = d_g \left(1 + 0.163 Eo^{0.757}\right)^{1/3}, \tag{3.30}$$

$$Eo = \frac{g(\rho_l - \rho_g) d_g^2}{\sigma}. \tag{3.31}$$

This model considers the influence of the bubble diameter, an approach that consistent with the phenomena observed in experiments. Considering that the lift force model above changes the model's sign for large bubbles, and requires the addition of a correction term for deformed bubbles, Equation (3.27) is a more accurate model than others that have been proposed in the literature [55].

3.2.4 Virtual Mass Force

Another force component in a liquid–gas flow, the virtual mass force, was initially proposed by Prandtl [85] as

$$\mathbf{f}_{VM,l} = -\mathbf{f}_{VM,g} = -C_{VM}\rho_l \frac{\pi {d_g}^3}{6} \frac{d\left(\mathbf{v}_l - \mathbf{v}_g\right)}{dt}, \tag{3.32}$$

where C_{VM} is the coefficient of the virtual mass force.

The virtual mass force on a single bubble is multiplied by the number of bubbles per unit mixture volume to obtain the force acting per unit mixture volume:

$$\mathbf{F}_{VM,l} = -\mathbf{F}_{VM,g} = -C_{VM}\rho_l \alpha_g \frac{d\left(\mathbf{v}_l - \mathbf{v}_g\right)}{dt}. \tag{3.33}$$

The virtual mass force suggests that a bubble has additional mass because it moves relative to the liquid. This term is thus called the added mass force.

C_{VM} is a coefficient related to the volume fraction of the dispersed phase. For isolated bubbles or in a low bubble volume fraction where bubbles behave in isolation from one another, C_{VM} is generally equal to 0.5 [55]. For larger bubble volume fractions, C_{VM} is a function of the volume fraction of bubbles [107, 14, 79].

Researchers have different opinions about this force. Thakre and Joshi [99], Deen et al. [25], and Tabib [97] found that virtual mass force has no effect on simulation and can be neglected. However, Watanabe et al. [111] verified that the virtual mass force can

stabilize basic equations and numerical calculations. The present work also investigates this problem.

3.2.5 Wall Lubrication Force

To explain the observation that no bubbles appear near a wall, Antal et al. [7] proposed a wall lubrication force. They derived the form of this force from a flow analysis between a cylinder and a wall, as no analytical three-dimensional solution for this problem exists. Their wall lubrication force acting per unit mixture volume is

$$\mathbf{F}_{WL,l} = -\mathbf{F}_{WL,g} = C_{WL}\alpha_g\rho_l\Big|(\mathbf{v}_l - \mathbf{v}_g) - [(\mathbf{v}_l - \mathbf{v}_g)\cdot\mathbf{n}_W]\mathbf{n}_W\Big|^2\mathbf{n}_W, \tag{3.34}$$

where $\mathbf{n}_W$ is the wall's normal unit vector.

Obviously, the direction of this force is always normal to the wall. The coefficient C_{WL} is related to the distance to the wall, y_W, and the size of the bubbles. Frank [36] proposed a generalized model for the wall lubrication coefficient that considers the influence of geometry without the restriction to a specific geometry. It is expressed as

$$C_{WL} = C_{W3}\cdot\max\left[0, \frac{1}{C_{WD}}\cdot\frac{1-\frac{y_W}{C_{WC}d_g}}{y_W\cdot(\frac{y_W}{C_{WC}d_g})^{p-1}}\right], \tag{3.35}$$

where $C_{WC} = 10.0$, $C_{WD} = 6.8$, $p = 1.7$, and C_{W3} is given by

$$C_{W3} = \begin{cases} e^{-0.933Eo+0.179}, & 1 \le Eo \le 5 \\ 0.00599Eo - 0.0187, & 5 < Eo \le 33 \\ 0.179, & 33 < Eo \end{cases}. \tag{3.36}$$

and Eo was defined in Equation (3.31).

Multiphase flows are very difficult to model due to the complex interaction between the different phases. In the test case in Section 4.2, the geometry is a pipe, which simplifies the

interfacial models. In the following work, the multiphase flow model needs some further generalization.

In the formula for wall lubrication force, the distance to the wall y_W and the wall normal vector $\mathbf{n}_W$ are very important to the result. In the 2D test case in Section 4.2, due to the simple geometry of the pipe, y_W and $\mathbf{n}_W$ calculations could be simplified to

$$y_W = R_p - \sqrt{(x^2 + z^2)}, \tag{3.37}$$

$$\mathbf{n}_W = \begin{pmatrix} \frac{x}{\sqrt{(x^2+z^2)}} \\ 0 \\ \frac{z}{\sqrt{(x^2+z^2)}} \end{pmatrix}, \tag{3.38}$$

where (x, y, z) are the coordinates of the centroid of each cell and R_p is the radius of the pipe. However, for complex geometry, there could be multiple walls to each cell, as is shown in Figure 3.1. The calculations for y_W and $\mathbf{n}_W$ will be much more complicated and involved than those for the simple case involving a pipe.

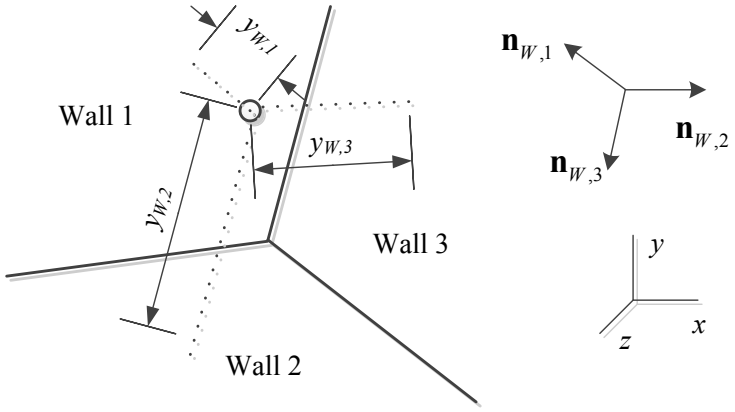

Figure 3.1: y_W and $\mathbf{n}_W$ in complex geometry.

One solution takes the maximum of three wall lubrication forces as the wall lubrication force acting on this cell. Another method takes the sum of three wall lubrication force vectors' values as the wall lubrication force acting on this cell. The former approach

can be used when the maximum value of wall lubrication forces is very dominant. The latter may be more accurate, however. To build an efficient model, the former approach is employed in the present work.

3.2.6 Turbulence Dispersion Force

The turbulence of a continuum flow has an effect on the dispersed phase that tends to smooth the volumetric concentrations of that phase. That is to say, the dispersed phase will tend to migrate from regions with a higher concentration field to ones with a lower concentration field by the effect of the turbulence dispersion force. Different averaging methods lead to different turbulence dispersion force models. Here, the model that for the turbulence dispersion force that we use in the present study is that described in ANSYS-FLUENT [63].

The turbulence dispersion force is derived from the drag force. When the time-averaging is performed, the drag force includes two parts:

$$\mathbf{F}_{D,l} = -\mathbf{F}_{D,g} = -\frac{3}{4} C_D \frac{\overline{\alpha_g} \rho_l}{d_g} \overline{\left|\mathbf{v}_l - \mathbf{v}_g\right|} (\overline{\mathbf{v}_l} - \overline{\mathbf{v}_g}) - \frac{3}{4} C_D \frac{\rho_l}{d_g} \overline{\left|\mathbf{v}_l - \mathbf{v}_g\right|} \cdot \overline{\alpha_g' \left(\mathbf{v}_l' - \mathbf{v}_g'\right)}, \tag{3.39}$$

where α_g', $\mathbf{v}_l'$, and $\mathbf{v}_l'$ are the fluctuation of α_g, $\mathbf{v}_l$, and $\mathbf{v}_g$, respectively. If these fluctuations are modeled using the eddy diffusivity hypothesis, then

$$\overline{\alpha_g' \mathbf{v}_l'} = -\frac{\mu_{t,l}}{\rho_l \sigma_{r,l}} \nabla \overline{\alpha_g}, \tag{3.40}$$

and

$$\overline{\alpha_g' \mathbf{v}_g'} = -\frac{\mu_{t,g}}{\rho_g \sigma_{r,g}} \nabla \overline{\alpha_g}, \tag{3.41}$$

where $\mu_{t,l}$ and$\mu_{t,g}$, are, respectively, the eddy viscosities of the liquid and gas, while $\sigma_{r,l}$ and $\sigma_{r,g}$, are the respective turbulent Prandtl numbers for volume fraction dispersion, whose values are generally taken to be 0.75.

In consequence, the component of drag force that is induced by turbulence is called the turbulent dispersion force and is determined using

$$\mathbf{F}_{TD,l} = -\mathbf{F}_{TD,g} = -\frac{3}{4} C_D \frac{\alpha_g \rho_l}{d_g} \overline{|\mathbf{v}_l - \mathbf{v}_g|} \left(\frac{\mu_{t,g}}{\rho_g \sigma_{r,g}} - \frac{\mu_{t,l}}{\rho_l \sigma_{r,l}} \right) \nabla \overline{\alpha_g}. \tag{3.42}$$

3.2.7 Improvements of Interfacial Force Models

Table 3.1: Interfacial force models in ANSYS-FLUENT.

Interfacial force name	Models in ANSYS-FLUENT	Examples of absent models
Drag	Schiller–Naumann (1935) [91] Morsi–Alexander (1972) [73] Symmetric [4] **Universal drag law** [4, 55] Constant coefficient	Ahmadi–Ma (1990) [5] Zhang–Vanderheyde (2002) [117] Tomiyama (2002) [103]
Lift	Constant coefficient	Auton (1987) [9]71] **Tomiyama (1998)** [101] Legendre and Magnaudet (1998) [60]
Virtual mass	**Constant coefficient**	Van Wijingaarden et al. (1976) [107] Biesheuvel and Spoelstra (1989) [14] Pan et al. (1999) [79]
Wall lubrication	None	Antal (1991) [7] Tomiyama (1998) [101] **Frank (2005)** [36]
Turbulence dispersion	**Constant coefficient**	RPI (1994) [63] FAD (2004) [17]

Note: bolds mean models adopted in the present work.

The range of interfacial force models in ANSYS-FLUENT (version 13.0), summarized in Table 3.1, is not complete. For drag coefficient models, five models are available in ANSYS-FLUENT, but these model are rather dated. Newer models are not included. For the lift

force, only the constant lift coefficient is available in the setup. The virtual mass force and turbulence dispersion force are modeled only with a constant coefficient and cannot be altered by users. Even worse, no turbulence dispersion force model is available on the software interface; rather, this force model needs to be enabled through a text command. Finally, the wall lubrication force is not even modeled in ANSYS-FLUENT.

To refine the multiphase model in ANSYS-FLUENT for the present study, models for lift coefficient and wall lubrication force need to be added by UDFs. Any relevant terms are added as source terms to the momentum transport equations. Details for calculation of the wall lubrication force are described in Section 3.2.5.

3.3 Turbulence Model

Turbulence models for multiphase flows are more complicated than single phase flows. In a multiphase flow, the effects of turbulent fluctuations of the velocities and other quantities in and among each phase need to be described by turbulence models. Since there are many terms in the momentum transport equations in a multiphase flow, three methods for modeling turbulence in a multiphase flow are generally available to simplify this problem during simulation. They are mixture turbulence model, the dispersed turbulence model and turbulence model for each phase.

In the mixture turbulence model, multiphase flow is considered as a mixture that has one set of turbulence equations. It is applicable with cases when the density ratio between the phases is close to 1 as the effect of turbulent fluctuations between the phases is offset. Under this condition, it is sufficient to use mixture properties and mixture velocities to capture important features of the turbulent multiphase flow.

The dispersed turbulence model is appropriate for the flow when the secondary phases are dilute and, therefore, the interaction among bubbles is negligible. The dominant process is the secondary phase's random motion under the influence of the primary phase's

turbulence. The turbulence quantities of the primary phase are solved from turbulence equations, whereas the turbulence quantities of the secondary phase are diagnosed from those of the primary phase.

The third method, used when the turbulence transfer among the phases is very important, solves a set of turbulence equations for each phase. Obviously, this method will require significantly more computational resources but results in the best accuracy.

Multiple turbulence models (Table 3.2) are used in validation and application cases in this thesis in reference to the specific requirements from each problem. For validation case of multiphase vertical pipe flow, the standard $k-\varepsilon$ model and the SST $k-\omega$ model with mixture method are employed so as to make a comparison. In the validation case of flow passing a square cylinder, the SST $k-\omega$ model is used in order to obtain a better result of vortex shedding. In the simulation of flow in a surge tank, the realizable $k-\varepsilon$ model is used for each phase to model the turbulence more accurately. In the most complex case of multiphase FSI problem, the SST $k-\omega$ model with mixture method is adopted in consideration of the whole model's realizability.

Turbulence models used in this thesis are introduced in following sections.

3.3.1 Standard $k-\varepsilon$ Model (for Mixture)

The standard $k-\varepsilon$ model with mixture method considers two phases as a mixture when modeling the turbulence. The turbulence equations for the mixture are as follows [4]:

$$\frac{\partial}{\partial t}(\rho_m k) + \nabla \cdot (\rho_m \mathbf{v}_m k) = \nabla \cdot (\frac{\mu_{t,m}}{\sigma_k}\nabla k) + G_{k,m} - \rho_m \varepsilon, \tag{3.43}$$

$$\frac{\partial}{\partial t}(\rho_m \varepsilon) + \nabla \cdot (\rho_m \mathbf{v}_m \varepsilon) = \nabla \cdot (\frac{\mu_{t,m}}{\sigma_\varepsilon}\nabla \varepsilon) + \frac{\varepsilon}{k}(C_{1\varepsilon}G_{k,m} - C_{2\varepsilon}\rho_m \varepsilon), \tag{3.44}$$

where the mixture density and velocity, ρ_m and $\mathbf{v}_m$, are computed from

$$\rho_m = \sum_{i=1}^{N} \alpha_i \rho_i, \tag{3.45}$$

Table 3.2: Multiple turbulence models used in this thesis.

Group	Case	Type	Turbulence model
Validation	Multiphase flow in a vertical pipe	Multiphase turbulence	Standard $k-\varepsilon$ model; mixture SST $k-\omega$ model; mixture
	Flow around a square cylinder	Single phase turbulence	SST $k-\omega$ model
	FSI in a flow-driven heart valve	Single phase laminar	–
Application	Multiphase flow in a coolant surge tank	Multiphase turbulence	Realizable $k-\varepsilon$ model; per phase
	Multiphase FSI in a dynamic valve	Multiphase turbulence	SST $k-\omega$ model; mixture

and

$$\mathbf{v}_m = \frac{\sum_{i=1}^{N} \alpha_i \rho_i \mathbf{v}_i}{\sum_{i=1}^{N} \alpha_i \rho_i}. \tag{3.46}$$

The mixture turbulent viscosity $\mu_{t,m}$ is computed from

$$\mu_{t,m} = \rho_m C_\mu \frac{k^2}{\varepsilon}. \tag{3.47}$$

The production of turbulence kinetic energy $G_{k,m}$ is computed from

$$G_{k,m} = -\rho_m \overline{v'_{i,m} v'_{j,m}} \frac{\partial v_{j,m}}{\partial x_i}. \tag{3.48}$$

The closure coefficients are set by same values as the standard $k-\varepsilon$ model

$$C_\mu = 0.09, \sigma_k = 1.0, \sigma_\varepsilon = 1.3, C_{1\varepsilon} = 1.44, C_{2\varepsilon} = 1.92. \tag{3.49}$$

3.3.2 Realizable $k-\varepsilon$ Model (for Each Phase)

The realizable $k-\varepsilon$ model for each phase means turbulence is modeled separately for each phase with a set of equations [4]. Turbulence equations for the liquid phase are as follows:

$$\begin{aligned}
\frac{\partial}{\partial t}(\alpha_l \rho_l k_l) + \nabla \cdot (\alpha_l \rho_l \mathbf{v}_l k_l) =& \nabla \cdot \left[\alpha_l \left(\mu_l + \frac{\mu_{t,l}}{\sigma_k} \right) \nabla k_l \right] + \alpha_l G_{k,l} - \alpha_l \rho_l \varepsilon_l + \\
& K_{gl}(C_{gl} k_g - C_{lg} k_l) - K_{gl} \left| \mathbf{v}_g - \mathbf{v}_l \right| \frac{\mu_{t,g}}{\alpha_g \sigma_g} \nabla k_g + \\
& K_{gl} \left| \mathbf{v}_g - \mathbf{v}_l \right| \frac{\mu_{t,l}}{\alpha_l \sigma_l} \nabla k_l,
\end{aligned} \tag{3.50}$$

$$\begin{aligned}
\frac{\partial}{\partial t}(\alpha_l \rho_l \varepsilon_l) + \nabla \cdot (\alpha_l \rho_l \mathbf{v}_l \varepsilon_l) =& \nabla \cdot \left[\alpha_l (\mu_l + \frac{\mu_{t,l}}{\sigma_\varepsilon}) \nabla \varepsilon_l \right] + \alpha_l \rho_l C_1 S_l \varepsilon_l - \\
& \alpha_l \rho_l C_2 \frac{\varepsilon_l^2}{k_l + \sqrt{\upsilon_l \varepsilon_l}} + C_{3\varepsilon} \frac{\varepsilon_l}{k_l} \left[K_{gl}(C_{gl} k_g - C_{lg} k_l) \right] - \\
& C_{3\varepsilon} \frac{\varepsilon_l}{k_l} \left[K_{gl} \left| \mathbf{v}_g - \mathbf{v}_l \right| \frac{\mu_{t,g}}{\alpha_g \sigma_g} \nabla k_g - K_{gl} \left| \mathbf{v}_g - \mathbf{v}_l \right| \frac{\mu_{t,l}}{\alpha_l \sigma_l} \nabla k_l \right],
\end{aligned} \tag{3.51}$$

where μ_l is the dynamic viscosity of the liquid phase.

The production of turbulence kinetic energy $G_{k,l}$ is computed from

$$G_{k,l} = -\rho_l \overline{v'_{i,l} v'_{j,l}} \frac{\partial v_{j,l}}{\partial x_i}. \tag{3.52}$$

S_l is calculated from

$$S_l = \sqrt{2 S_{ij,l} S_{ij,l}}, \tag{3.53}$$

where the strain-rate tensor of liquid $S_{ij,l}$ is given by

$$S_{ij,l} = \frac{1}{2}\left(\frac{\partial v_{i,l}}{\partial x_j} + \frac{\partial v_{j,l}}{\partial x_i}\right). \tag{3.54}$$

The terms C_{gl} and C_{lg} can be approximated as $C_{gl} = C_{lg}$ and

$$C_{lg} = 2\left(\frac{\eta_{gl}}{1+\eta_{gl}}\right), \tag{3.55}$$

where η_{gl} is a ratio between characteristic time based on the mean particle velocity and the mean relative velocity.

K_{gl} is the exchange coefficient which can be written as

$$K_{gl} = K_{lg} = \frac{\alpha_l \alpha_g \rho_g f}{\tau_{R,g}}, \tag{3.56}$$

where $\tau_{R,g}$ is the particulate relaxation time and defined as

$$\tau_{R,g} = \frac{\rho_g d_g^2}{18 \mu_{e,g}}. \tag{3.57}$$

The drag function f_D is defined as

$$f_D = \frac{C_D \mathrm{Re}}{24}. \tag{3.58}$$

The closure coefficients are set by

$$C_1 = 0.43, C_2 = 1.9, \sigma_k = 1.0, \sigma_\varepsilon = 1.2, C_{3\varepsilon} = \tanh\left|\frac{v_{\text{ver}}}{v_{\text{hor}}}\right|. \tag{3.59}$$

where v_{ver} is the component of the flow velocity parallel to the gravitational vector and v_{hor} is the component of the flow velocity perpendicular to the gravitational vector.

Turbulence equations for the gas phase are:

$$\begin{aligned}\frac{\partial}{\partial t}(\alpha_g\rho_g k_g) + \nabla\cdot(\alpha_g\rho_g \mathbf{v}_g k_g) =& \nabla\cdot\left[\alpha_g\left(\mu_g + \frac{\mu_{t,g}}{\sigma_k}\right)\nabla k_g\right] + \alpha_g G_{k,g} - \alpha_g\rho_g\varepsilon_g + \\ & K_{lg}\left(C_{lg}k_l - C_{gl}k_g\right) - K_{lg}(\mathbf{v}_l - \mathbf{v}_g)\cdot\frac{\mu_{t,l}}{\alpha_l\sigma_l}\nabla k_l + \\ & K_{lg}(\mathbf{v}_l - \mathbf{v}_g)\cdot\frac{\mu_{t,g}}{\alpha_g\sigma_g}\nabla k_g,\end{aligned} \tag{3.60}$$

$$\begin{aligned}\frac{\partial}{\partial t}(\alpha_g\rho_g\varepsilon_g) + \nabla\cdot(\alpha_g\rho_g \mathbf{v}_g\varepsilon_g) =& \nabla\cdot\left[\alpha_g(\mu_g + \frac{\mu_{t,g}}{\sigma_\varepsilon})\nabla\varepsilon_g\right] + \alpha_g\rho_g C_1 S_g\varepsilon_g - \\ & \alpha_g\rho_g C_2\frac{\varepsilon_g^2}{k_g + \sqrt{\upsilon_g\varepsilon_g}} + C_{3\varepsilon}\frac{\varepsilon_l}{k_l}\left[K_{gl}\left(C_{gl}k_g - C_{lg}k_l\right)\right] - \\ & C_{3\varepsilon}\frac{\varepsilon_l}{k_l}\left[K_{gl}\left(\mathbf{v}_g - \mathbf{v}_l\right)\cdot\frac{\mu_{t,g}}{\alpha_g\sigma_g}\nabla k_g\right] + \\ & C_{3\varepsilon}\frac{\varepsilon_l}{k_l}\left[K_{gl}\left(\mathbf{v}_g - \mathbf{v}_l\right)\cdot\frac{\mu_{t,l}}{\alpha_l\sigma_l}\nabla k_l\right],\end{aligned} \tag{3.61}$$

where μ_g is the dynamic viscosity of the gas phase.

The production of turbulence kinetic energy $G_{k,g}$ is computed from

$$G_{k,g} = -\rho_g\overline{v'_{i,g}v'_{j,g}}\frac{\partial v_{j,g}}{\partial x_i}. \tag{3.62}$$

S_g is calculated from

$$S_g = \sqrt{2S_{ij,g}S_{ij,g}}, \tag{3.63}$$

where the strain-rate tensor of gas $S_{ij,g}$ is given by

$$S_{ij,g} = \frac{1}{2}\left(\frac{\partial v_{i,g}}{\partial x_j} + \frac{\partial v_{j,g}}{\partial x_i}\right). \tag{3.64}$$

3.3.3 SST $k-\omega$ Model (for Single Phase or Mixture)

Equations of the SST $k-\omega$ model [71] for a single phase flow are

$$\frac{\partial}{\partial t}(\rho k) + \nabla \cdot (\rho \mathbf{v} k) = \nabla \cdot \left[\left(\mu + \frac{\mu_t}{\sigma_k} \right) \nabla k \right] + \widetilde{G_k} - Y_k, \tag{3.65}$$

$$\frac{\partial}{\partial t}(\rho \omega) + \nabla \cdot (\rho \mathbf{v} \omega) = \nabla \cdot \left[\left(\mu + \frac{\mu_t}{\sigma_\omega} \right) \nabla \omega \right] + G_\omega - Y_\omega + D_\omega, \tag{3.66}$$

where the turbulent viscosity μ_t is computed from

$$\mu_t = \frac{\rho a_1 k}{\max(a_1 \omega, S F_2)}, \tag{3.67}$$

with F_2 is given by

$$F_2 = \tanh \left\{ \left[\max\left(\frac{2\sqrt{k}}{0.09 \omega y_W}, \frac{500\mu}{\rho {y_W}^2 \omega} \right) \right]^2 \right\}, \tag{3.68}$$

where $\widetilde{G_k}$ represents the generation of turbulence kinetic energy due to mean velocity gradients, calculated as

$$\widetilde{G_k} = \min(G_k, 10\rho\beta^* k\omega), \tag{3.69}$$

and Y_k is the dissipation of k given by

$$Y_k = \rho\beta^* k\omega. \tag{3.70}$$

Furtheremore, G_ω represents the generation of turbulence kinetic energy due to mean velocity gradients, calculated as

$$G_\omega = \frac{\omega}{k} G_k, \tag{3.71}$$

and Y_ω is the dissipation of ω given by

$$Y_\omega = \rho\beta^* \omega^2. \tag{3.72}$$

The cross-diffusion term D_ω is defined by

$$D_\omega = 2(1 - F_1)\rho \frac{1}{\omega \sigma_{\omega,2}} \nabla k \nabla \omega. \tag{3.73}$$

The closure coefficients are set by

$$a_1 = 0.31, \beta^* = 0.09, \sigma_k = \frac{1}{D + \frac{1-F_1}{\sigma_{k,2}}}, \sigma_\varepsilon = \frac{1}{\frac{D}{\sigma_{\omega,1}} + \frac{1-F_1}{\sigma_{\omega,2}}}, \tag{3.74}$$

where F_1 is given by

$$F_1 = \tanh\left(\left[\min\left\{\max\left(\frac{\sqrt{k}}{0.09\omega y}, \frac{500\mu}{\rho y^2 \omega}\right), \frac{4\rho k}{\sigma_{\omega,2} D_\omega^+ y^2}\right\}\right]^4\right), \tag{3.75}$$

and D_ω^+ is calculated from

$$D_\omega^+ = \max\left(2\rho \frac{1}{\omega \sigma_{\omega,2}} \nabla k \nabla \omega, 10^{-10}\right). \tag{3.76}$$

Here, constant (closure) coefficients are

$$\sigma_{k,1} = 1.176, \sigma_{k,2} = 1.0, \sigma_{\omega,1} = 2.0, \sigma_{\omega,2} = 1.168. \tag{3.77}$$

The multiphase flow equations of the SST $k-\omega$ model with the mixture method are

$$\frac{\partial}{\partial t}(\rho_m k) + \nabla \cdot (\rho_m \mathbf{v}_m k) = \nabla \cdot \left(\frac{\mu_{t,m}}{\sigma_k} \nabla k\right) + \widetilde{G_{k.m}}, \tag{3.78}$$

$$\frac{\partial}{\partial t}(\rho_m \omega) + \nabla \cdot (\rho_m \mathbf{v}_m \omega) = \nabla \cdot \left(\frac{\mu_{t,m}}{\sigma_\omega} \nabla \omega\right) + G_{\omega,m}, \tag{3.79}$$

where ρ_m, $\mathbf{v}_m$, $\mu_{t,m}$, and $G_{k,m}$ are given in Section 3.3.1, and $\widetilde{G_{k,m}}$ is calculated from

$$\widetilde{G_{k,m}} = \min(G_{k,m}, 10\rho_m \beta^* k\omega). \tag{3.80}$$

Finally, $G_{\omega,m}$ is given by

$$G_{\omega,m} = \frac{\omega}{k} G_{k,m}. \tag{3.81}$$

3.4 Dynamic Mesh

When the simulation domain is deforming or the boundary of the domain is moving during the simulation, dynamic meshing can update the mesh automatically without stopping the simulation.

3.4.1 Methodologies of Dynamic Meshing

Three methods [4] for generating a dynamic mesh have generally been used for either a structured or non-structured mesh. One or more of these methods can be enabled to implement the dynamic mesh function.

Smoothing Methods

Spring-based, diffusion-based, or Laplacian smoothing methods update the mesh close to the boundary or create mesh motion without generating new nodes or cells. For small motions, this method uses a simple modification to keep almost the same mesh quality as before. For large motions, the method is generally used to aid adjustment of a new mesh that is updated by other methods. The Laplacian smoothing method is adopted in the present work (Section 4.4).

In the Laplacian smoothing method, the location of each mesh vertex is adjusted along the direction to the geometric center of its neighboring vertices. The node position is computed from

$$\overline{\mathbf{x}_i} = \frac{\sum_j^n \mathbf{x}_j}{n}, \tag{3.82}$$

where $\overline{\mathbf{x}_i}$ is the averaged nodal position of node i. Laplacian smoothing is the simplest and most-common mesh-smoothing method.

Re-meshing Methods

If the mesh is triangular or tetrahedral, the dynamic layering method is not applicable, and the smoothing method may generate a low quality mesh when applied to cases where there are large displacements (in the structure) relative to the sizes of the local cells. Re-meshing methods may generate new cells while retaining the quality of the mesh.

Four parameters control the generation of new cells in the re-meshing method: namely, the specified minimum length scale, the specified maximum length scale, the specified maximum cell skewness, and the specified maximum face skewness (the definition of the skewness is given in Section 3.4.2). If the boundary motion meets one or more of the following criteria, a re-meshing of the grid will be initiated: the boundary motion is smaller than the specified minimum length scale; the boundary motion is larger than the specified maximum length scale; the mesh has a skewness greater than the specified maximum cell or face skewness; or the height of a layer does not meet the specified length scale. The new mesh that results from re-meshing will satisfy the specified skewness, size and height as well.

Layering Methods

This method involves adding or removing layers of cells adjacent to a moving boundary, so it is applicable to hexahedral or wedge mesh zones.

The mesh layer will be split into two layers or merged with a neighboring layer, depending on its new height after addition to the boundary motion.

A layering method [4] is used in the application of the dynamic mesh. The strategy underpinning this method is to add or remove layers of cells adjacent to a moving boundary, with the result that the method is applicable to hexahedral or wedge mesh zones. To this purpose, a mesh layer will either be split into two layers or be merged with a neighboring

layer, depending on the nature of the boundary motion. More specifically, let $H_{\min}$ and $H_{\max}$ be the minimum and maximum cell height respectively in a cell layer, H_{ide} be the ideal cell height, and α_S be the layer split factor. If the current layer verifies $H_{\max} > (1+\alpha_S)H_{\text{ide}}$, then it will will split into two layers. For each cell in a height of H, the heights of these two layers will be H_{ide} and $H - H_{\text{ide}}$ if the height-based model is used or $H\Big/\Big(1+\alpha_S\Big)$ and $\alpha_S H\Big/\Big(1+\alpha_S\Big)$ if the ratio-based model is used. Furthermore, let α_C be the collapse factor. If the current layer verifies $H_{\min} < \alpha_C H_{\text{ide}}$, the layer of cells will be merged with the cells in the layer above it. A ratio-based model is used in the present work.

Conservation Equation of Dynamic Mesh

With dynamic meshing, the conservation equation for flow quantities corresponding to the newly generated or removed cells in the mesh will be added or removed (as the mesh is updated). Meanwhile, the conservation equation for cells whose volume have changed on the moving boundary (owing to the dynamic meshing) will need to account for this volume change in the conservation equations of the various quantities in the given cell. The conservation equation for a general scalar ϕ on an arbitrary control volume V whose boundary is moving can be written as [4]

$$\frac{d}{dt}\int_V \rho\phi dV + \int_{\partial V} \rho\phi\left(\mathbf{v}-\mathbf{v}_M\right) d\mathbf{A} = \int_{\partial V} \Gamma\nabla\phi \cdot d\mathbf{A} + \int_V S_\phi dV, \tag{3.83}$$

where ρ is the fluid density, $\mathbf{v}$ is the flow velocity vector, $\mathbf{v}_M$ is the mesh velocity of the moving mesh, Γ is the diffusion coefficient, and S_ϕ is the source term of ϕ. The volume V involved in this conservation equation will need to reflect the change in the volumes of those cells affected by the dynamic meshing.

3.4.2 Criteria of Mesh Quality

Many criteria can be used to access the quality of a mesh. Generally, in the process of mesh dynamics, the following criteria are used for this assessment.

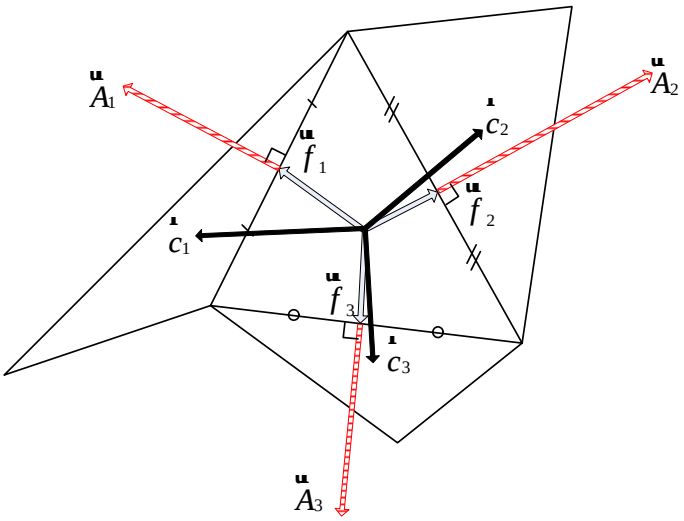

Figure 3.2: Vectors used to calculate mesh orthogonal quality.

The first criterion is the orthogonal quality. To determine the orthogonal quality of a given cell, three vectors are defined for each face, as shown in Figure 3.2. Here, $\mathbf{A}_i$ is the area vector of a face, $\mathbf{f}_i$ is a vector from the centroid of the cell to the centroid of the various faces that form the cell (or midpoint in a 2D problem), and $\mathbf{c}_i$ is a vector from the centroid of the cell to the centroid of the adjacent cell that shares that face. Two ratios are calculated for each face, as summarized in Equations (3.84) and (3.85):

$$\frac{\mathbf{A}_i \cdot \mathbf{f}_i}{|\mathbf{A}_i|\,|\mathbf{f}_i|}, \tag{3.84}$$

$$\frac{\mathbf{A}_i \cdot \mathbf{c}_i}{|\mathbf{A}_i|\,|\mathbf{c}_i|}. \tag{3.85}$$

The minimum value of the two ratios on each face in the cell is called the orthogonal quality for the cell. For good quality cells, this value should be close to 1.

The second criterion for mesh quality is the equivolume skew, which is a specific measure

of skewness. The skewness is a parameter that quantifies the deformation of a cell relative to its equilateral geometry of equivalent volume or in the same circumradius (a ratio of their volume, area, or angle). The equivolume skew S_e is a ratio of the cell volume difference, $V_{\text{opt}} - V$, and its equilateral cell volume with the same circumradius V_{opt}, defined as follows:

$$S_e = \frac{V_{\text{opt}} - V}{V_{\text{opt}}}. \tag{3.86}$$

Generally, the maximum skewness for a triangular/tetrahedral mesh in most flows should be kept below 0.95, with an average value that is significantly lower [4]. Both the orthogonal quality and the equivolume skew can be monitored during a simulation.

The third criterion is the aspect ratio, which is the ratio of the maximum value to the minimum value of any of the following distances: distance between the cell centroid and face centroids, or distance between the cell centroid and nodes. It is generally used to estimate the quality of a hexahedral mesh or a wedge mesh. The aspect ratio is reported by the mesh quality check procedure in ANSYS-FLUENT.

3.5 FSI Methods Based on Dynamic Mesh Model

In this work, the structure is considered to be a rigid body, with the result that the deformation of the structure is ignored. Only the motion of the structure is considered. As mentioned above, the motion of a structure is conducted through a dynamic mesh. In ANSYS-FLUENT, the motions of the dynamic mesh include translation and rotation, which are, respectively, controlled by the translational velocity and angular velocity for each degree of freedom. At the beginning of each time step, the mesh is updated based on the given translational velocities and angular velocities. These translational and angular velocities are constant during a given time step and are determined through a force balance analysis (including the force from fluid as well as other forces). As the mesh update occurs at the beginning of each time step, the force balance analysis is based on the result of the

fluid field at the end of the previous time step.

3.5.1 Explicit Method

In this work, the forces and moments acting on the moving structure (boundary) are used to compute the translational and angular motion of its center of gravity following the "Six DOF (degree of freedom)" method [71, 94]. The governing equation for the translational motion is

$$\dot{\mathbf{v}} = \frac{\sum \mathbf{F}}{m}, \tag{3.87}$$

where m is the mass of the moving structure, $\dot{\mathbf{v}}$ is the acceleration of the translational motion of the center of gravity, and $\mathbf{F}$ is the force vector acting on the moving structure.

The angular motion of the moving structure is computed using body coordinates as follows:

$$\dot{\omega}_{s,B} = \overline{\overline{L}}^{-1}\left(\sum \mathbf{M}_B - \omega_{s,B} \times \overline{\overline{L}}\omega_{s,B}\right), \tag{3.88}$$

where $\dot{\omega}_{s,B}$ is the angular acceleration of the moving structure in the body coordinates, $\overline{\overline{L}}$ is the inertia tensor, $\mathbf{M}_B$ is the moment vector in the body coordinates, and $\omega_{s,B}$ is the angular velocity.

The inertia tensor $\overline{\overline{L}}$ which is the second moment of mass with respect to distance from rotation axes is given by

$$\overline{\overline{L}} = \int_m r_i r_j dm, \tag{3.89}$$

where r is the distance to the axis of rotation.

The moments are transformed from the inertial to the body coordinates using

$$\mathbf{M}_B = R_t \times \mathbf{M}, \tag{3.90}$$

where R_t is a transformation (rotation) matrix calculated from the angles ϕ, θ, ψ, which represent rotations about the x, y, z axis, respectively:

$$R_t = \begin{bmatrix} \cos(\theta)\cos(\psi) & \cos(\theta)\sin(\psi) & -\sin(\theta) \\ \sin(\phi)\sin(\theta)\cos(\psi)-\cos(\phi)\sin(\psi) & \sin(\phi)\sin(\theta)\sin(\psi)+\cos(\phi)\cos(\psi) & \sin(\phi)\cos(\theta) \\ \cos(\phi)\sin(\theta)\cos(\psi)+\sin(\phi)\sin(\psi) & \cos(\phi)\sin(\theta)\sin(\psi)-\sin(\phi)\cos(\psi) & \cos(\phi)\cos(\theta) \end{bmatrix}. \tag{3.91}$$

With $\dot{\mathbf{v}}$ and $\dot{\omega}_{s,B}$ as well as $\mathbf{v}$ and $\omega_{s,B}$ from the last time step, the problem of solving for a new $\mathbf{v}$ and $\omega_{s,B}$ is transformed to finding a numerical solution for system of ordinary differential equations. Applying a one step Euler's method [38], $\mathbf{v}$ and $\omega_{s,B}$ are obtained by,

$$V_{n+1} = V_n + \Delta t \cdot \dot{V}_n, \tag{3.92}$$

where the subscript n implies that the quantity refers to the n^{th} time step, V represents either $\mathbf{v}$ or $\omega_{s,B}$, and $\dot{V}_{n+1}$ is obtained from

$$\dot{V}_{n+1} = \frac{F_n}{m}, \tag{3.93}$$

where m is the mass of a moving structure when V represents $\mathbf{v}$, and F represents the net force or m is the moment of inertia of the moving structure when V represents $\omega_{s,B}$ and F represents the net torque. Thus, $\dot{V}$ accordingly represents the acceleration of $\mathbf{v}$ or $\omega_{s,B}$.

The flow diagram of the explicit method used in the present work is displayed in Figure 3.3. The fluid–structure interaction is realized through the various forces that are transmitted between the fluid and the structure. In the dynamic mesh model, the mesh is updated at the beginning of each time step. An updated solution for the fluid flow will be obtained based on the updated configuration for the (valve) structure. In consequence, the forces transmitted from the structure to the fluid are modeled in this manner.

On the other hand, the forces transmitted from the fluid to the structure are obtained through a UDF. This function is used to determine the translational velocity and the angular velocity of the dynamic mesh. The net force acting on the poppet is calculated at the end of each time step, based on the updated solution. Then this solution is used to determine the dynamic mesh configuration for the next time step.

3.5.2 Implicit Method and Optimization

An explicit method does not work well with cases that involve sudden changes in forces or moments acting on a moving structure. In other words, the explicit method is not capable of solving strong coupling problems. One restriction of ANSYS-FLUENT is that a mesh update always occurs at the beginning of each time step. Mesh moving velocities are calculated from the previous flow field. An error can be calculated only when a new flow field is solved based on the updated mesh. However, calculations will proceed to the next time step, and an error correction is not possible. As a consequence, an error could lead to solution divergence when a sudden change in the forces or moments is acting on a moving structure. To avoid this problem, an implicit method, which rearranges the ANSYS-FLUENT solution procedure through use of a Scheme file was firstly proposed by Dumont et al. [71, 94] in a simulation of a heart valve. Updates of values for or in the implicit method is are obtained as follows:

$$V_{n+1} = V_n + \Delta t \cdot \dot{V}_{n+1}, \tag{3.94}$$

where the subscript n refers to the n^{th} time step, V represents either $\mathbf{v}$ or $\omega_{s,B}$, and $\dot{V}_{n+1}$ is obtained from

$$\dot{V}_{n+1} = \frac{F_{n+1}}{m}, \tag{3.95}$$

where m is the mass of a moving structure when V represents $\mathbf{v}$ and F represents the net force, or m is the moment of inertia of the moving structure when V represents $\omega_{s,B}$ and F represents the net torque. Thus, $\dot{V}$ accordingly represents the acceleration of $\mathbf{v}$ or $\omega_{s,B}$.

This equation is realized through iterations as F_{n+1} is obtained at the end of each iteration, but V_{n+1} is set up at the beginning of each iteration. So Equation (3.95) is solved iteratively, which is the reason that a Scheme command file is used to rearrange the ANSYS-FLUENT solution procedure.

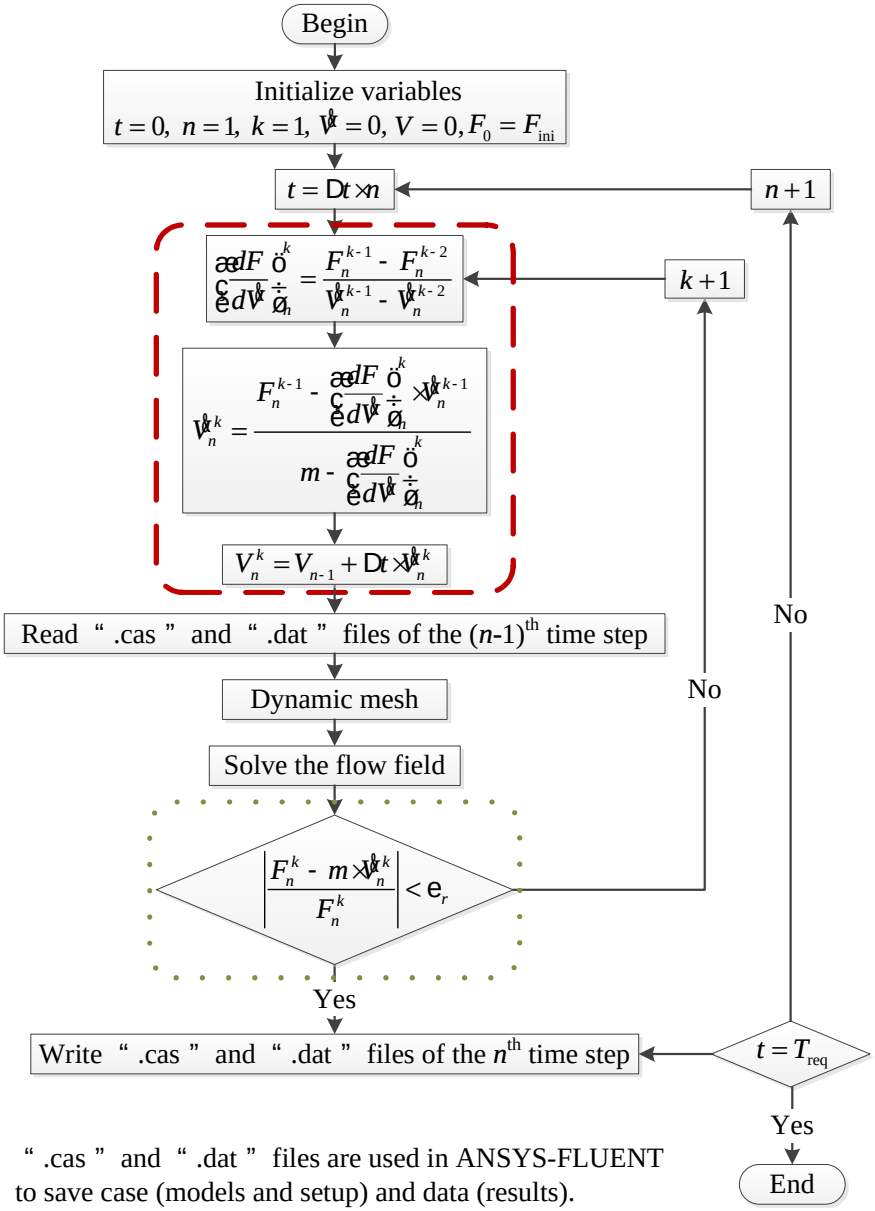

Figure 3.3: Flow diagram summarizing the computational procedure of an explicit method.

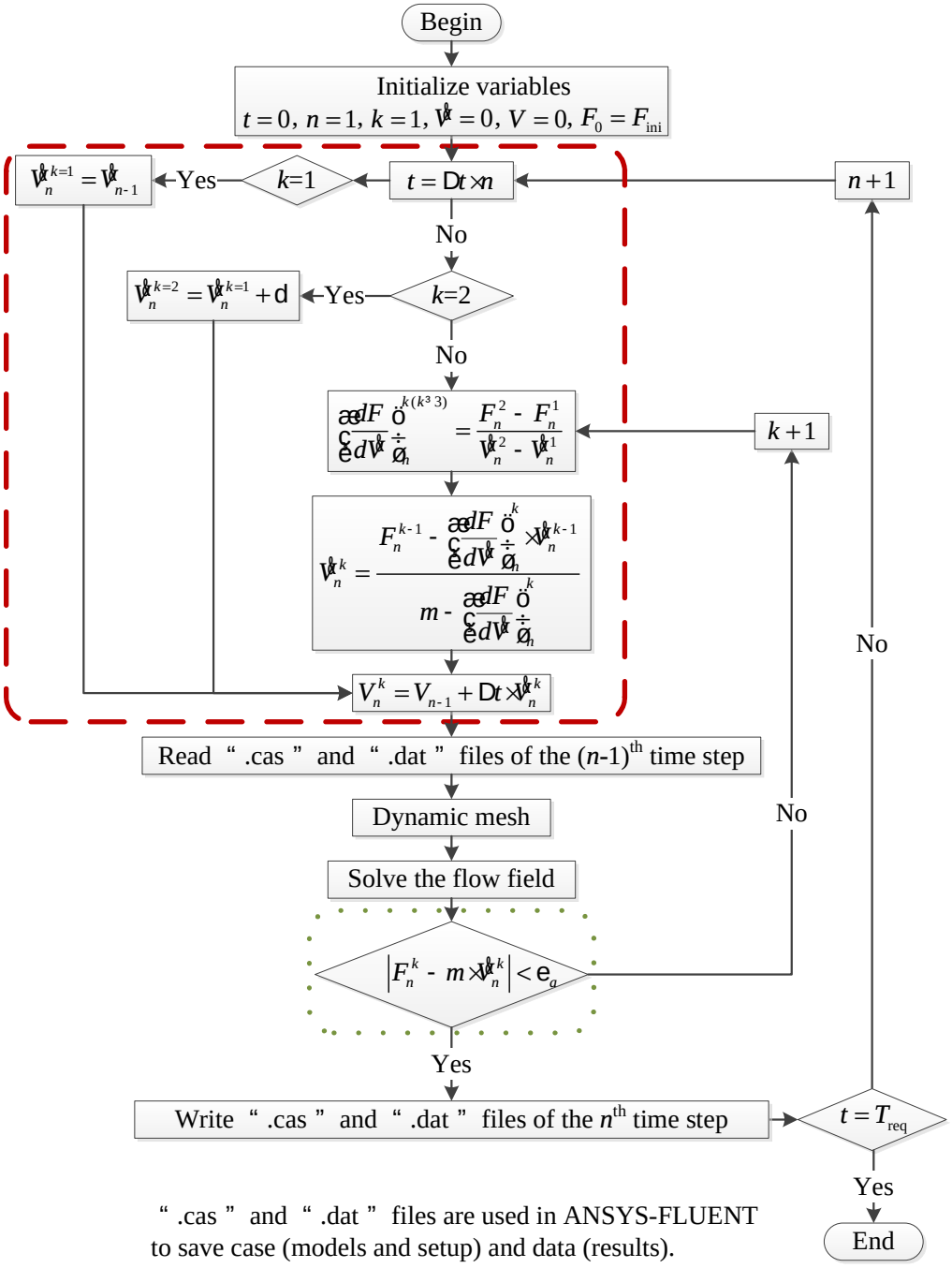

Figure 3.4: Flow diagram summarizing the computational procedure used by Dumont et al. [30] for the iterative method.

Figure 3.4 summarizes the work of Dumont et al. [71, 94]. In the first iteration of a new time step when time is $(n+1)\cdot\Delta t$, if $\mathbf{v}$ or $\omega_{s,B}$ (represented by V) is assigned the value of this quantity from the previous time step, then

$$\dot{V}_{n+1}^{k=1} = \dot{V}_n, \tag{3.96}$$

where k is the iteration counter (and $k = 1$ corresponds to the first iteration of a time step). Obviously Equation (3.95) will not be satisfied as $F_{n+1} \neq F_n$ in strong-coupling problems, so the calculation proceed with the second iteration. Note, at the beginning of each iteration, the mesh is the result of the previous time step, rather than the previous iteration of the current time step.

In the second iteration, an assumed variation is added to $\dot{V}$:

$$\begin{aligned} \dot{V}_{n+1}^{k=2} &= \dot{V}_n + \delta \\ &= \dot{V}_{n+1}^{k=1} + \delta, \end{aligned} \tag{3.97}$$

where the assumed variation δ is an empirical constant value.

In the third or later iteration, the derivative $\frac{dF}{d\dot{V}}$ can be calculated as

$$\left(\frac{dF}{d\dot{V}}\right)_{n+1}^{k+1(k\geq 2)} = \frac{F_{n+1}^2 - F_{n+1}^1}{\dot{V}_{n+1}^2 - \dot{V}_{n+1}^1}. \tag{3.98}$$

This derivative can be used to provide a correction for the angular acceleration for the next iteration as follows:

$$F_{n+1}^{k-1} + \left(\frac{dF}{d\dot{V}}\right)_{n+1}^{k} \cdot \left(\dot{V}_{n+1}^{k} - \dot{V}_{n+1}^{k-1}\right) = m \cdot \dot{V}_{n+1}^{k}, \tag{3.99}$$

or

$$\dot{V}_{n+1}^{k} = \frac{F_{n+1}^{k-1} - \left(\frac{dF}{d\dot{V}}\right)_{n+1}^{k} \cdot \dot{V}_{n+1}^{k-1}}{m - \left(\frac{dF}{d\dot{V}}\right)_{n+1}^{k}}. \tag{3.100}$$

At the end of each iteration, the absolute error will be checked to judge whether the result has converged for the current time step. If the result has not converged, more

iterations will need to be undertaken. The derivative $\frac{dF}{d\dot{V}}$ will need to be calculated at every time step because F is in fact non-linear with respect to $\dot{V}$, so updating its value for each iteration can accelerate the convergence. The iteration has converged when the following condition is satisfied:

$$\left|F_{n+1}^{k} - m \cdot \dot{V}_{n+1}^{k}\right| < \varepsilon_a, \tag{3.101}$$

for a user prescribed value of ε_a.

The implicit method described herein features high accuracy and robustness, both of which are necessary for obtaining a solution for strong-coupling problems. However, the computational efficiency of the implicit method is lower than that of the explicit method. To improve its efficiency, two modifications have been made. The first one is in how the calculation of the derivative $\frac{dF}{d\dot{V}}$ is undertaken. In Dumont et al.'s work, this derivative is firstly calculated in the third iteration for each time step. In other words, the first two iterations are just used to initialize the iterative procedure. It is thus impossible to obtain a converged solution for the iterative procedure within the first two iterations. Furthermore, the "correct" assignment of δ is difficult in the iterative procedure. Its value depends on the nature of the physical problem that is addressed. Therefore, it is extremely difficult to guess an appropriate value for δ, and furthermore it is not reasonable for the value of δ to be constant for the entire iterative process. The second disadvantage is the need for a better convergence criterion to be used at each time step. In Dumont et al.'s work, an absolute error value is used to determine the convergence of the iterative procedure. This method does not always work as there may be some sensitive positions in the computational domain where even a small absolute error may cause the calculation to diverge. In addition, it is really difficult to prescribe a priori an appropriate value for ε_a before a solution is known. These deficiencies in the current iterative procedure that need to be addressed are shown within the dashed box in Figure 3.4.

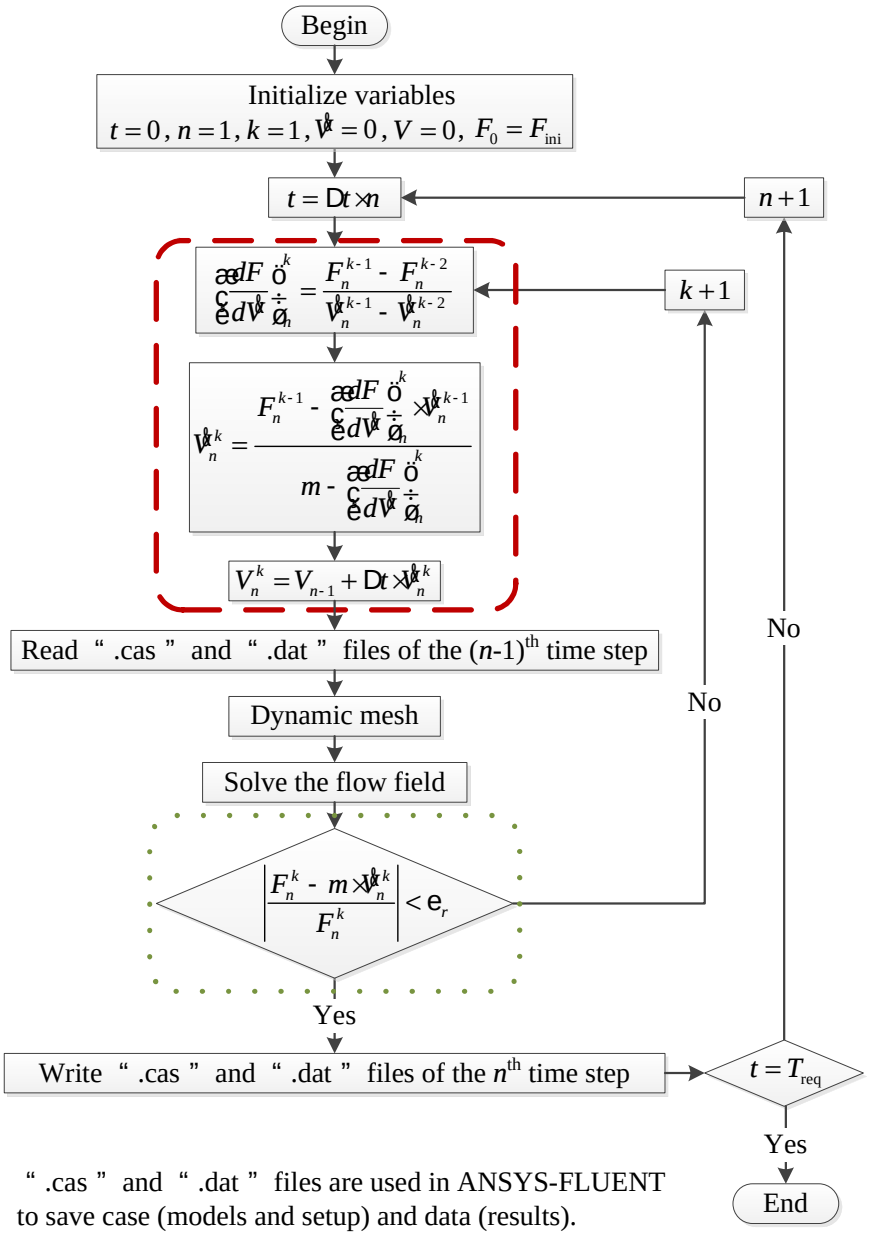

Figure 3.5: Flow diagram summarizing the computational procedure of the proposed implicit method.

The improvements we propose are based on the above two consideration. A new flow diagram summarizing the proposed iterative method is shown in Figure 3.5, with the improvement incorporated (shown within the dashed box). Firstly, the calculation of $\frac{dF}{d\dot{V}}$ is optimized as follows. In the present work, $\frac{dF}{d\dot{V}}$ is a variable and always calculated from the two previous iterations as follows:

$$\left(\frac{dF}{d\dot{V}}\right)_{n+1}^{k} = \frac{F_{n+1}^{k-1} - F_{n+1}^{k-2}}{\dot{V}_{n+1}^{k-1} - \dot{V}_{n+1}^{k-2}}. \tag{3.102}$$

When $k = 1$ or 2, the two previous iterations may involve iterations in the previous time step. Therefore, both $\frac{dF}{d\dot{V}}$ and $\dot{V}$ are corrected to more precise values in each time step. As a result, the convergence of the iterative procedure, which usually cannot be obtained in the first three iterations in the algorithm proposed by Dumont et al., can now be obtained in the first three iterations of the (proposed) optimized iterative methodology. That is to say, the time to convergence is reduced. Secondly, the relative error (the percentage of the error in the absolute torque to the absolute torque) is used to determine whether the solution has converged:

$$\left|\frac{F_{n+1}^{k} - m\dot{V}_{n+1}^{k}}{F_{n+1}^{k}}\right| < \varepsilon_r. \tag{3.103}$$

This approach avoids the risk of divergence due to a large relative error that can be associated with a small absolute value.

With the modifications above, which results in a reduction in iterations and in the continuous correction of $\frac{dF}{d\dot{V}}$, computational efficiency is expected to be increased. In addition, the relative error provides a better criterion for convergence and, as a result, will lead potentially to improvements in the accuracy of the solution obtained by the proposed implicit method.

3.6 Chapter Summary

This chapter has introduced methodologies for each of the key techniques used in the simulations: namely, the multiphase flow model, the specification of the relevant interfacial forces, the selection of the appropriate turbulence models, the use of a dynamic mesh, and the FSI methodology.

The Eulerian model (the name used in ANSYS-FLUENT), also known as a two-fluid model, is employed in this research owing to its accuracy. An immiscible model that can be enabled within the Eulerian model has also been advocated. Interfacial force models are a very important part of the Eulerian model, as accurate phase interaction is reflected through the interfacial forces. Multiple turbulence models has been adopted in this research. For the dynamic mesh model, a smoothing method for unstructured meshes and a layering method for structured meshes have been adopted and described in detail. Various criteria of mesh quality have been defined for the two types of meshes, followed by a description of an explicit method for addressing the FSI based on a dynamic mesh model. Because this method is not suitable for the solution of strong coupling problems, a new implicit method has been proposed and its use for obtaining flow solutions through a Scheme file and UDFs is described.

Improvements and modifications to the interfacial force models currently available in ANSYS-FLUENT (version 13.0) have also been proposed in this chapter. A lift force coefficient model and a wall lubrication force model are added to ANSYS-FLUENT using UDFs. An explicit method for FSI modeling based on the dynamic mesh model in ANSYS-FLUENT is realized through a UDF that launches the force analysis and dynamic motion. A Scheme file is used to rearrange the solution process in order to allow an implicit method to be used for FSI modeling.

Chapter 4

Validation Cases and Results

This chapter applies the models introduced in Chapter 3 to various test cases designed to validate the feasibility and accuracy of the components in the integrated modeling system. Methods for realizing the improvements and modifications proposed in the previous chapter are also described. In the validations, different methodologies for each technique are compared and evaluated, thereby creating a solid foundation for selection and utilization of model components in actual applications.

4.1 Validation Plan

Validation is of crucial importance to making numerical research credible and reliable, as the accuracy of a new model can be assessed by comparing model predictions with experimental results. As mentioned previously, due to the limitations of small geometry and complex flow in the problems of interest in this research, there are currently no experimental data on coolant degassing problems and dynamic valve vibration and noise problem that can be used for direct validation of the entire integrated modeling system. Therefore, the validation focuses on other (related) cases with experimental results, rather than directly

on cases involving these challenging problems. However, it has been very difficult to find a case that includes all key techniques (multiphase flow, dynamic mesh, and FSI). Hence, the validation undertaken here will attempt to validate each of the key techniques (or, model components) separately.

As different methodologies are proposed for each key technique, an additional objective of this validation effort is to determine the strengths and weaknesses of these various methodologies. For the multiphase model, a vertical pipe bubble flow has been selected as a benchmark case because of the existence of a great deal of numerical and experimental results for this case. The simulation for this case is undertaken with the Eulerian model, both with and without the incorporation of the immiscible model. For the dynamic mesh model, two different methodologies, smoothing and layering, are validated using the case of flow over an prescribed oscillating square cylinder. For FSI, two methodologies are again proposed, but based on different physical problems. As a result, two cases are selected for the validation.

Figure 4.1 provides a plan of the validation work undertaken herein.

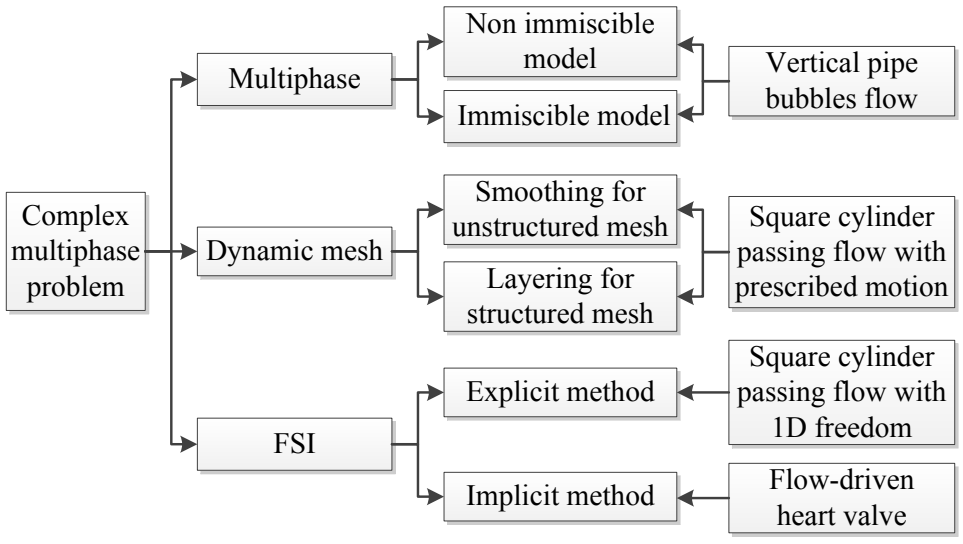

Figure 4.1: Flow diagram of the validation plan.

4.2 Pipe Bubble Flow: Model Validation of Multiphase Flow

The simulation in this case is done to validate the multiphase flow model in ANSYS-FLUENT against a database of extensive experimental results for water–air bubbly flows [66] in a vertical pipe test section. The prediction of the volume fraction of air bubbles will be compared with the data of the experiments as well as others' simulation results. The volume fraction, which is determined by the interfacial forces, is an important variable used to reflect the distribution of each phase. That is to say, the fidelity in the prediction of the volume fraction can be used to test the accuracy of the multiphase model.

4.2.1 Problem Description

The test setup of the benchmark experiment is shown in Figure 4.2 [66]. It is comprised of a circular pipe system through which water with air bubbles flows at a constant temperature (30 °C). The test section is a vertical pipe with a length of 4 m and a diameter of 0.0512 m. Various combinations of water and air velocities are used to validate the prediction for the diameters of air bubbles under different flow conditions.

4.2.2 Validation of Eulerian Model without Immiscible Model

CFD Simulation

To be consistent with the experiment, the computational domain for the simulation has the same diameter as the test section, which is a cylinder with a length of 4 m and with a diameter of 0.0512 m, as shown in Figure 4.2, except that the cross-section is a sector of 20°. The densities of water and air are constants. Break-up and coalescence of the bubbles are ignored. The energy equation is not enabled as the temperature in the experiment is

kept constant at 30 °C at the beginning of each cycle, and the temperature fluctuations in the test section are small and can be neglected.

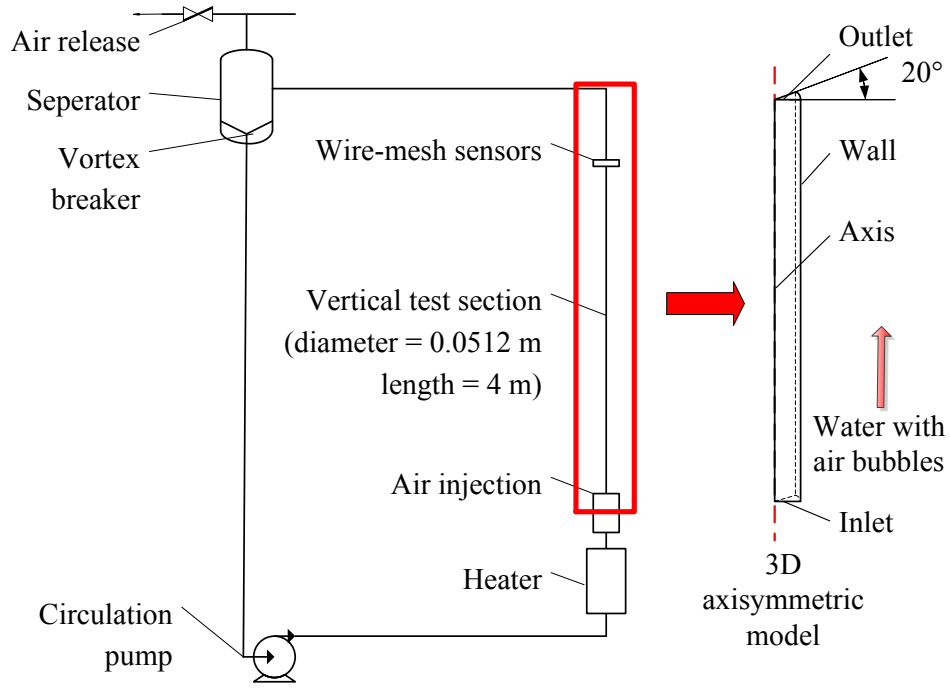

Figure 4.2: Sketch of the test case in the Eulerian multiphase model validation: the left portion shows the MT-Loop test facilities at the Research Center Dresden-Rossendorf [65]; the right portion shows a general view of the 3D computational domain.

Three cases are simulated here, as shown in Table 4.1. All three cases are in the bubbly flow regime [as shown in Figures 2.1 (a) and (b)]. Case 038 and 039 are for bubbly flow with the gas volume fraction peak located near the wall. The velocities of liquid and gas for Case 039 are higher than those for Case 038. Case 036 is for bubbly flow with the gas volume fraction peak located in the core region. In consequence, these three cases are very representative [10, 92].

In Table 4.1, $\mathbf{v}_{\text{sup},l}$ and $\mathbf{v}_{\text{sup},g}$ are the superficial velocity of the liquid and gas, respec-

tively defined as

$$\mathbf{v}_{\text{sup},l} = \frac{Q_{V,l}}{A}, \tag{4.1}$$

and

$$\mathbf{v}_{\text{sup},g} = \frac{Q_{V,g}}{A}, \tag{4.2}$$

where $Q_{V,l}$ and $Q_{V,g}$ are the volume flow rates of the liquid and gas, respectively, and A is the area of the cross-section (of the pipe) as defined in Section 3.1.1. The quantities v_l and v_g are the intrinsic velocities of the liquid and gas, respectively, which are defined in Equations (3.1) and (3.2). In consequence, $\mathbf{v}_{\text{sup},l}$ and $\mathbf{v}_{\text{sup},g}$ are related to the intrinsic velocities v_l and v_g as follows:

$$\mathbf{v}_{\text{sup},l} = \mathbf{v}_l \alpha_l, \tag{4.3}$$

and

$$\mathbf{v}_{\text{sup},g} = \mathbf{v}_g \alpha_g. \tag{4.4}$$

Table 4.1: Simulated conditions in the multiphase model validation.

No.	d_g (m)	$\mathbf{v}_{\text{sup},l}$ (m s^{-1})	$\mathbf{v}_l$ (m s^{-1})	$\mathbf{v}_{\text{sup},g}$ (m s^{-1})	$\mathbf{v}_g$ (m s^{-1})	α_g	Re_l	Flow regime
038	0.0043	0.2250	0.2346	0.0096	0.2346	0.0409	11,976	Bubbly flow: wall peak
039	0.0045	0.4050	0.4146	0.0096	0.4146	0.0232	21,164	Bubbly flow: wall peak
036	0.0043	0.1000	0.1096	0.0096	0.1096	0.0876	5,595	Bubbly flow: core peak

First, grid independence and turbulence models testing was done on Case 038. A hierarchy of three numerical grids was constructed, where the number of grid elements was increased by a factor of 3 from a coarser to a finer mesh (using a scaling factor of $3^{1/3}$ in each coordinate, see Table 4.2). The type of mesh used for the simulations was unstructured. This type of mesh is generally applicable to complex geometry (e.g., which

is a basic characteristic of the dynamic valve in the present work). The mesh was wedge-shaped with respect to the long, narrow geometry. The minimum orthogonal quality was larger than 0.4, and the maximum aspect ratio was less than 500; these values show that the quality of the mesh was reasonably good.

Table 4.2: Hierarchy of numerical meshes in the multiphase model validation.

Level	No. of cells	No. of cells in pipe cross-section	No. of cells along the axis	Mesh quality	
				Minimum orthogonal quality	Maximum aspect ratio
1	9514	142	67	5.08582e-01	2.42149e+02
2	31400	314	100	4.95326e-01	2.62069e+02
3	92960	581	160	4.80736e-01	2.49596e+02

Details of the CFD simulations setup are summarized in Table 4.3. For the inlet boundary conditions, constant values were assumed for the intrinsic water and air velocity and the air volume fraction, in accordance with the experimental setup conditions. For the air phase, a mean bubble diameter, determined from the test case wire-mesh sensor data, was prescribed for the simulation. At the outlet cross-section, an averaged static pressure outlet boundary condition was used. The non-slip condition set up as wall boundary conditions for water and gas were. The symmetric condition was adopted on the two sides of the radial sector. Both the standard $k-\varepsilon$ model and SST $k-\omega$ model with the mixture interphase turbulence model were tested in the present work. The physical time step was 0.001 s to satisfy the Courant-Friedrichs-Lewy (CFL). The CFL condition uses the Courant number C as the criterion, where C defined as

$$C = \frac{|\mathbf{v}|\,\Delta t}{\Delta l}, \tag{4.5}$$

where $\mathbf{v}$ is the local velocity, Δt is the time step, and Δl is the cell length. In this case, Δl was calculated as the square root of the cell area on cross-sections, as the cells are long narrow wedges. If an explicit solver is used, then typically $C_{\max} \leq 1$; implicit solvers are usually less sensitive to numerical instability and so larger values of the Courant number

can be tolerated (or used). In this case, the average Courant number ranged between 1 and 5.

Table 4.3: Simulation setup details in the multiphase model validation.

Setup	Details
Mesh	Three levels, with a factor of 3; mesh type: wedge, unstructured;
Boundary conditions	Inlet: velocity inlet for air and bubble, volume fraction of air; outlet: pressure outlet (0 Pa); wall: non-slip condition for water and gas; symmetric: flow rotating along the axis is ignored
Turbulence model	$k-\varepsilon$ model; SST $k-\omega$ model; mixture
Time step	0.001 s

The differences (with respect to the details given in Table 4.3) in the simulation setup of Lucas et al.'s model [67] are shown in Table 4.4. His work was performed on a 60° radial sector of the pipe with the same boundary conditions as in the present work, and he used five grid levels, with an increasing factor of 2. The SST $k-\omega$ model with the Sato interphase turbulence model uses a different turbulence calculation (see Section 2.1.1). The time step used in Lucas et al.'s simulations was 0.005 s.

Table 4.4: Differences on simulation setup details of Lucas et al.'s model [67].

Setup	Details
Geometry	Five levels, with a factor of 2
Mesh	A 60° radial sector of the pipe
Turbulence model	SST model; Sato
Time step	0.005 s

Results and Analysis

A physical time of 30 s was simulated for the flow field. After the first 10 s, the inlet volume rates were equal to those at the outlet, as both the water and air had fully flowed through the whole pipe length. All the results were time-averaged, using the simulation data between 10 to 30 seconds. Figures 4.2–4.6 present the normalized volume fraction of the air on the horizontal cross section at $Z = 3.03$ m along the axial direction. Normalization was performed by dividing the local volume fraction by its average value (i.e., weighted by the cell area):

$$\alpha_{g,i}^{\text{nor}} = \frac{\alpha_{g,i}}{\langle \alpha_{g,i} \rangle} = \frac{\alpha_{g,i}}{\frac{\sum \alpha_{g,i} A_i}{\sum A_i}}, \tag{4.6}$$

where A_i is the area of cell in the cross section at $Z = 3.03$ m location. This form of averaging of the volume frame is equivalent to the one defined by Lucas (2007) [67]

$$\alpha_{g,x/R}^{\text{nor}} = \frac{\alpha_{g,x}}{\frac{\sum \alpha_{g,i} A_i}{\sum A_i}} = \frac{\alpha_{g,x}}{2\int_0^1 \alpha_{g,x} x dx}. \tag{4.7}$$

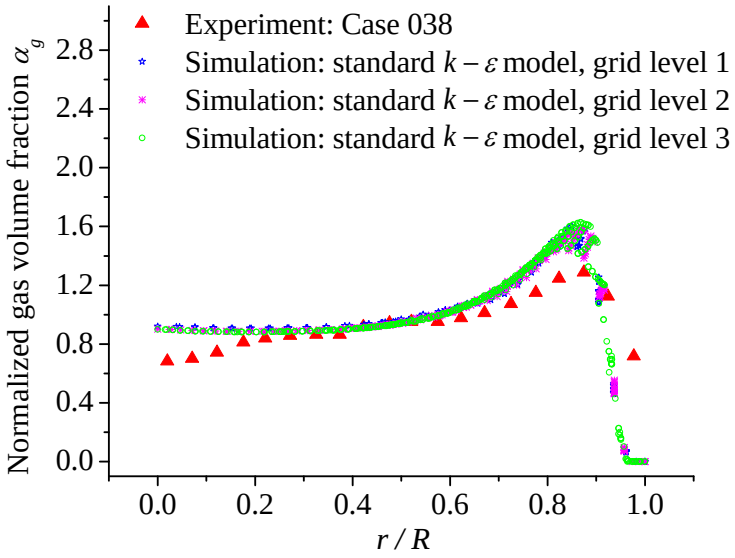

Figure 4.3: Grid independence test results for Case 038 using the standard $k - \varepsilon$ model.

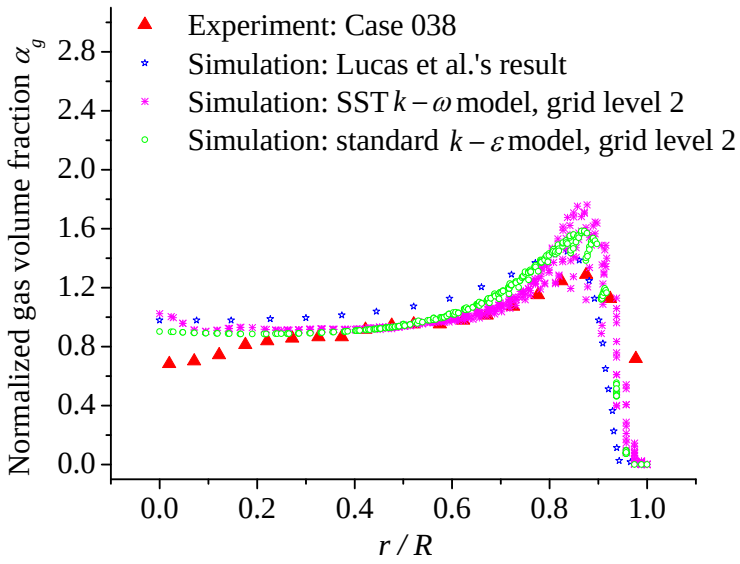

Figure 4.4: Comparison of predictions of the volume fraction using the SST $k-\omega$ model and standard $k-\varepsilon$ model at grid level 2.

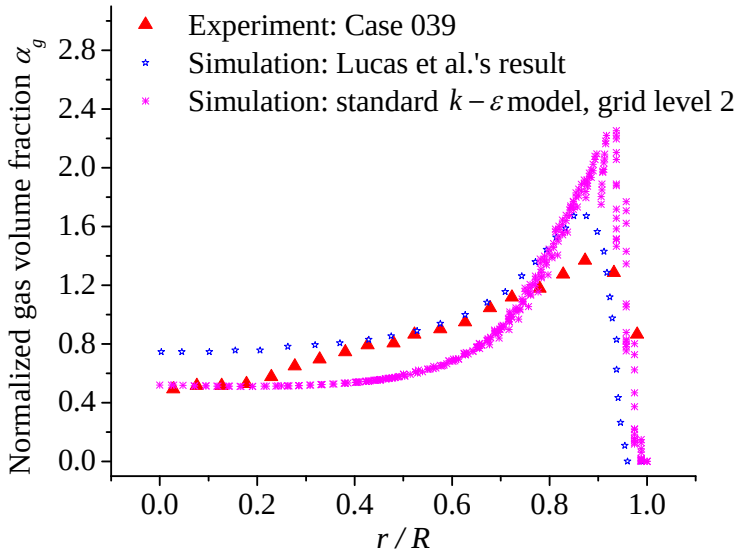

Figure 4.5: Volume fraction profiles for Case 039 using the standard $k-\varepsilon$ model at grid level 2.

The results of the grid independence test for Case 038 are shown in Figure 4.3. All the predicted results show consistent trends with the experimental measurements. As the number of cells in the computational domain increases, the discrepancy between the experimental and simulation results decrease. The results for grid level 2 and grid level 3 show almost no difference. To minimize computational resources, grid level 2 was used to do the following simulations.

Figure 4.4 compares the SST $k-\omega$ model and standard $k-\varepsilon$ model predictions for Case 038 for grid level 2. The standard $k-\varepsilon$ model yields better results throughout most of the region. Hence, in the following work the $k-\varepsilon$ model was used. Compared with Lucas et al.'s [67] numerical simulations, the current model predictions are in better conformance with the experimental measurements over a larger radial range through the pipe cross section.

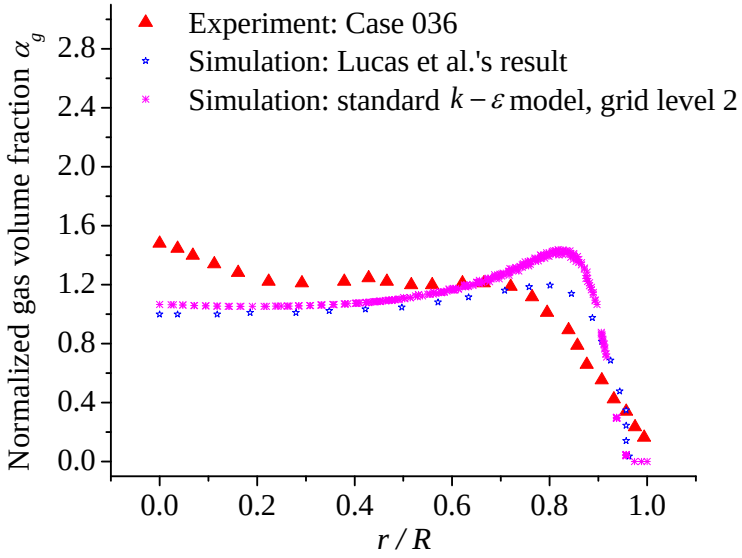

Figure 4.6: Volume fraction profiles for Case 036 using the standard $k-\varepsilon$ model at grid level 2.

Figures 4.5 and 4.6 show the results of the simulations for Cases 039 and 036, respectively. From Cases 039 to 036, the peak air volume fraction at near-wall regions becomes

weaker and tends to concentrate more and more in the core region, which is consistent with the experimental measurements. The results for Case 039 are good in both the core and near-wall regions, and are in better conformance with the experimental measurements than Lucas et al.'s numerical results, perhaps because the lift force and the wall lubrication force are too strong or the turbulent dispersion force is too weak in the model used by Lucas. The result for Case 036 does not show enough of a "core peak" feature owing to the limitations of the lift force model. More specifically, the direction of the lift force is changed only when the diameter of a bubble is sufficiently large.

Next, comparison and analysis of the different models will focus on ways to better optimize the interfacial force models.

4.2.3 Validation of Eulerian Model with Immiscible Model

CFD Simulation

With the immiscible model, the location of the interface between the liquid and gas phases is solved at each time step, which requires necessarily the utilization of a fine mesh, of a time step, and of a stringent convergence criterion. To solve a complex problem with realizable computational resource, some simplifications have been used for the application of the immiscible model. Firstly, the problem has been simplified to a 2D axi-symmetric model, as shown in Figure 4.7. Secondly, only the drag and lift forces are considered in the simulations.

Combining the Eulerian model with an immiscible model requires a high quality mesh with an especially low aspect ratio in order to avoid the grid shape influencing the interface shape. Details of the mesh adopted in this work are summarized in Table 4.5.

The boundary conditions and turbulence model used in this validation are same as in the previous validation of the Eulerian model without an immiscible model. However, to

ensure good convergence in the simulation, a smaller time step of 0.0005 s was used.

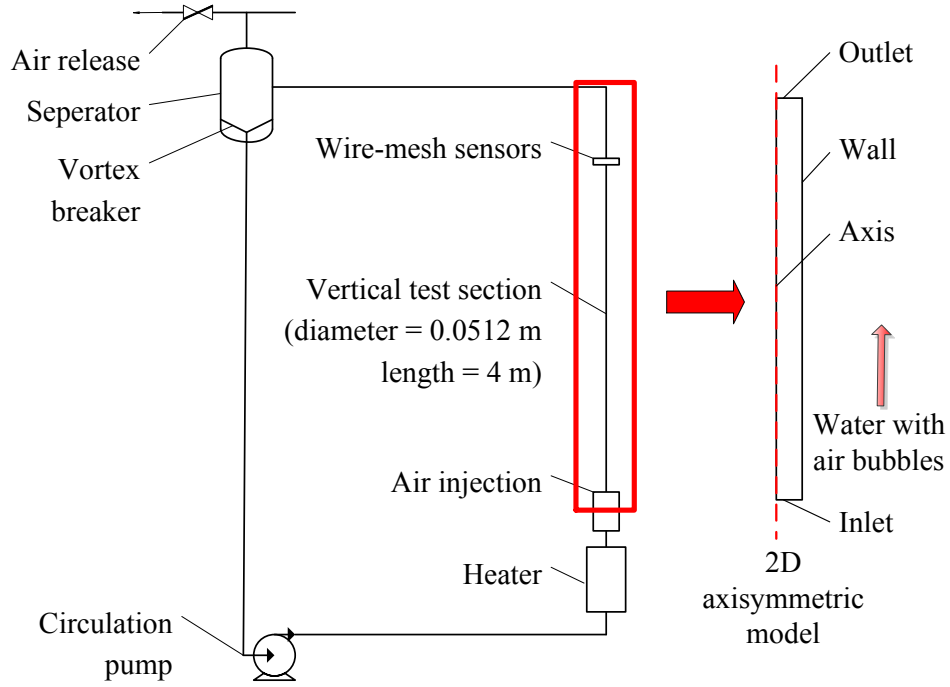

Figure 4.7: Sketch of the test case in the Eulerian immiscible multiphase model validation: the left portion shows the MT-Loop test facilities at the Research Center Dresden-Rossendorf [65]; the right portion shows a general view of the 2D computational domain.

Table 4.5: Details of mesh adopted in the Eulerian immiscible model validation.

Level	No. of cells	No. of cells in pipe cross-section	No. of cells along the axis	Mesh quality	
				Minimum orthogonal quality	Maximum aspect ratio
1	148,000	37	4,000	1	1.95

Results and Analysis

A physical time of 12 s was simulated for the flow field. After the first 8 s, the outlet time-averaged volume rates were equal to the inlet, as both water and air had fully flowed through the whole pipe length. All the results were time-averaged values using data between 8 to 12 seconds. Figure 4.8 present the normalized volume fraction of gas on the horizontal cross section at $Z = 3.03$ m along the axial direction.

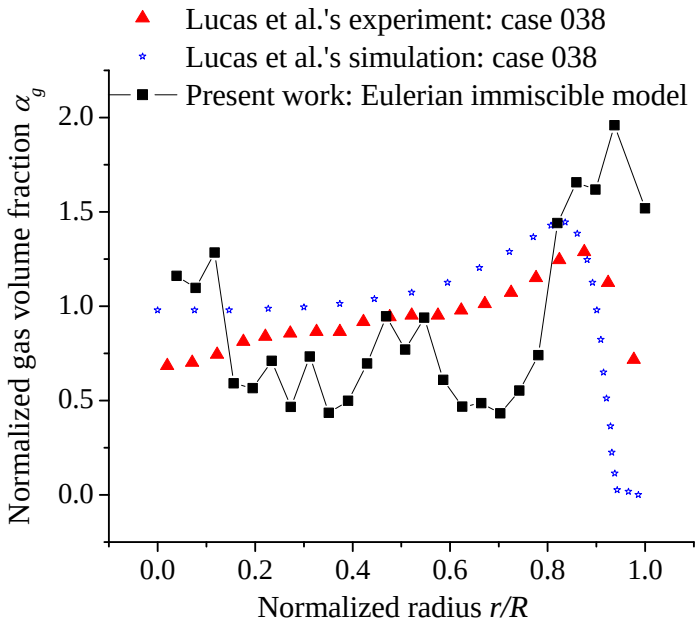

Figure 4.8: Predictions of the gas volume fraction using Eulerian immiscible model and comparison with other results.

In Figure 4.8, the trend of the gas volume fraction along the radial direction is broadly consistent with Lucas et al.'s experimental and simulation results. Indeed, it shows a wall peak, which is the primary flow characteristic of bubbly flow for Case 38.

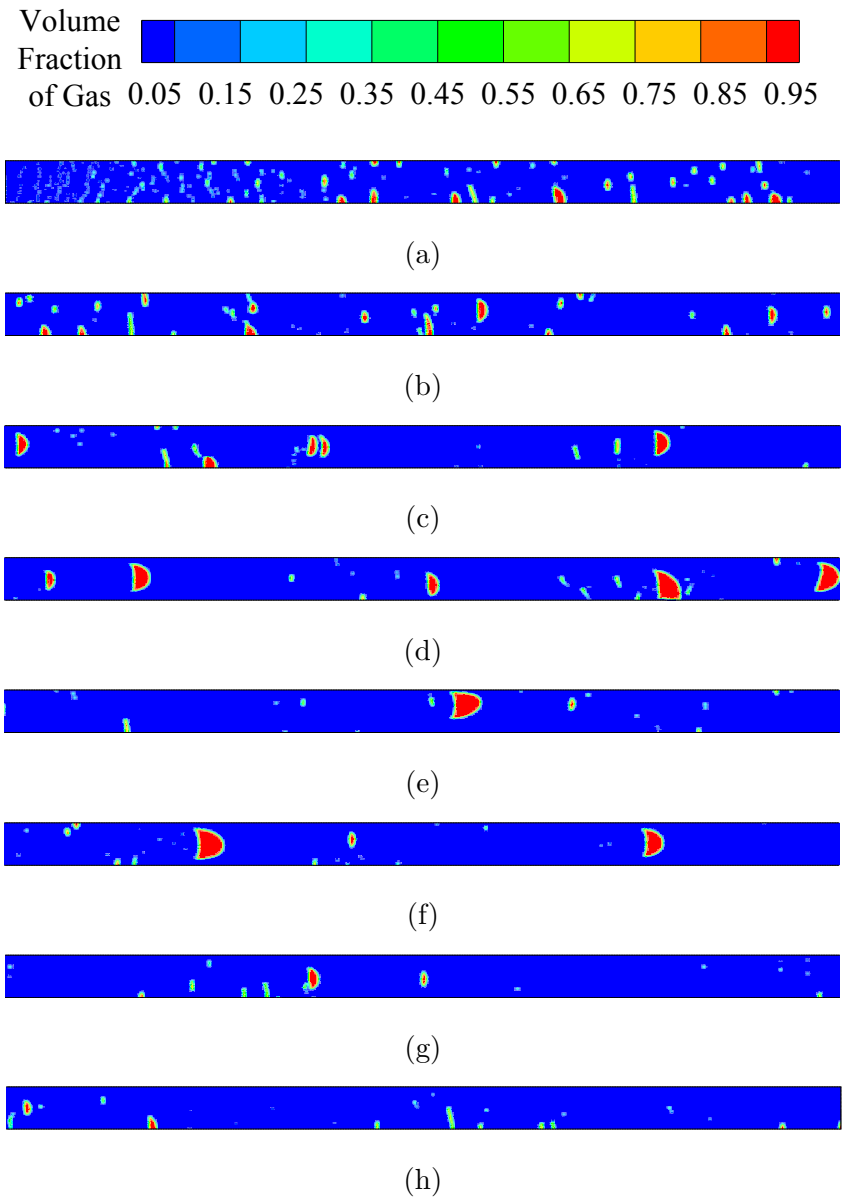

Figure 4.9: Contours of gas volume fraction at $t = 12$ s: (a) 0–0.5 m; (b) 0.5–1.0 m; (c) 1.0–1.5 m; (d) 1.5–2.0 m; (e) 2.0–2.5 m; (f) 2.5–3.0 m; (g) 3–3.5 m; and, (h) 3.5–4.0 m.

As shown in Figure 4.9, the gas distributes throughout the liquid volume, unlike in the

case of the Eulerian model in which the interface is not determined. As a result, it will take a much longer averaging time to obtain a smooth curve for the normalized gas volume fraction (in which the statistical fluctuations are negligible), and indeed, a curve as smooth as that in Lucas et al.'s simulation result. Limited by the current computational resources, the present simulation cannot be conducted for a sufficiently long averaging time such that the statistical fluctuations in the gas volume fraction curve are negligible. However, based on the underlying physics, the statistical fluctuations in the gas volume fraction curve arise primarily from the instabilities in the flow.

4.3 Flow Passing a Square Cylinder with Prescribed Oscillation: Model Validation of Dynamic Mesh Model

The Karman vortex shedding phenomenon behind a square cylinder (stationary or moving) has been widely researched. This case will be simulated in this section and used for validation of the fluid-structure interaction component of the proposed integrated modeling system. This is a transient (time-dependent) problem that requires the careful simulation of a wide range of length and time scales of the turbulent flow (viz., the turbulent motions that make the most significant contributions to the energetics of the flow). Furthermore, the simulation necessarily involves a detailed consideration of the fluid-structure interaction which, in turn, requires an appropriate application of a dynamic mesh procedure. This case can be used to test not only the quality of the dynamic mesh in the simulation, but also the ability of the whole simulation model to respond to the dynamic mesh. As such, it is an excellent test case for the validation of the one-way fluid–structure interaction and dynamic meshing procedures used in the proposed numerical methodology.

4.3.1 Problem Description

Both simulations and experimental measurements are available for the case of turbulent flow past a square cylinder with a prescribed motion. The Karman vortex street will show up behind the square cylinder [76]. It is observed that the Karman vortex sheds from the square cylinder at a steady frequency. The prediction of the properties of the Karman vortex street over the oscillating square cylinder and comparison of these predictions with experimental measurements provides validation for the FSI and dynamic meshing components of this proposed numerical procedure.

Generally, the hydrodynamical quantities of interest for flow over a square cylinder include the mean drag and lift coefficients C_L and C_D, and their root mean square (RMS) values $C_{L,\mathrm{rms}}$ and $C_{D,\mathrm{rms}}$ [100]. These coefficients are given by the following expressions:

$$\overline{C_L} = \overline{\frac{f_{\mathrm{ver}}}{\frac{1}{2}\rho {u_\infty}^2}}, \tag{4.8}$$

$$\overline{C_D} = \overline{\frac{f_{\mathrm{hor}}}{\frac{1}{2}\rho {u_\infty}^2}}, \tag{4.9}$$

$$C_{L,\mathrm{rms}} = \sqrt{\frac{\sum_1^n \left(C_L^i - \overline{C_L}\right)^2}{n}}, \tag{4.10}$$

$$C_{D,\mathrm{rms}} = \sqrt{\frac{\sum_1^n \left(C_D^i - \overline{C_D}\right)^2}{n}}. \tag{4.11}$$

where u_∞ is the far field flow velocity and n is the number of data, so this formulation renders the force dimensionless and facilitates the comparison; f_{ver} and f_{hor} are components of the net force acting per unit surface area in the vertical and horizontal directions, respectively. In CFD, they are obtained from calculating the surface integrals of the stresses and pressure force on each side of the square cylinder as follows:

$$\mathbf{F} = \int_S \mathbf{n}_W \cdot \left(\overline{\overline{\tau}} + p\right) ds, \tag{4.12}$$

where $\mathbf{n}_W$ is the wall normal vector, $\overline{\overline{\tau}}$ is the stress tensor and p is the pressure force.

The Strouhal number is another important parameter used in the analysis of the simulation result. It is a dimensionless vortex-shedding frequency, and is calculated as

$$\mathrm{St} = \frac{f_v D}{u_\infty}, \tag{4.13}$$

where D is the square cylinder side and f_v is the vortex shedding frequency.

If a prescribed motion is applied to the square cylinder, the vortex shedding frequency will be influenced by the frequency at which the cylinder motion induces the shedding. When the difference between these two frequencies is large, they remain independent of one another. When the difference between the two frequencies is small, the vortex shedding frequency will be influenced by the frequency associated with the motion of the square cylinder; in other words, the vortex-shedding frequency and the frequency of the cylinder motion synchronize. This is the famous phenomenon known as "lock-in". When the frequency of the cylinder motion is less than the natural vortex-shedding frequency, the system is defined as being above the lock-in region. When the frequency of the cylinder motion exceeds the natural vortex-shedding frequency, the system is defined as being below the lock-in region.

In the present work, the lock-in phenomenon is simulated, and the results are compared with experimental measurements and simulation results obtained by other investigators.

4.3.2 CFD Simulation

The dynamic mesh model utilizes a 2D rectangular computational domain, whose dimensions are $20.5D \times 14D$ in the streamwise (x) and spanwise (y) directions, respectively, as shown in Figure 4.10. The left edge of the domain is the inlet, the right side is the outlet, and the other two edges are set up as walls.

The prescribed motion of the cylinder is defined as

$$y = A \sin\left(2\pi f_{\text{dri}} t\right), \tag{4.14}$$

where A is the amplitude of the cylinder motion and f_{dri} is the driving frequency of the cylinder motion.

To facilitate the analysis, the frequency of the cylinder motion will be expressed in terms of the reduced velocity u_r defined as follows:

$$u_r = \frac{u_\infty}{f_{dr} D}, \tag{4.15}$$

where u_∞ is the far-field flow velocity.

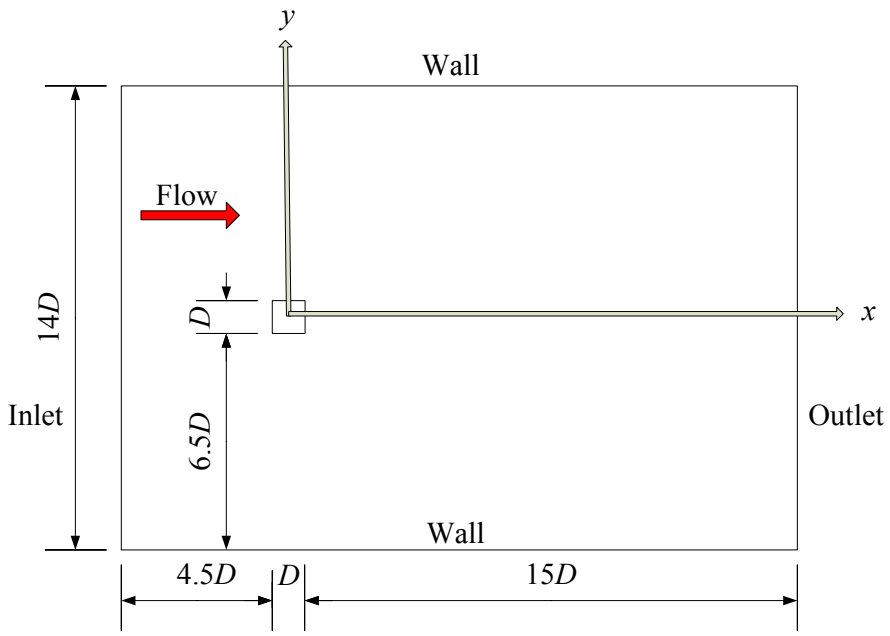

Figure 4.10: General view of the computational domain in the dynamic mesh model validation.

In the present work, Re=21,400, the value of the (non-dimensional) kinematic viscosity of the material is 1/Re, and A and u_∞ take the values of $0.1D$ and $1D$, respectively.

This case will involve simulations of the oscillatory square cylinder whose frequency of motion is summarized in terms of the reduced velocity in Table 4.6 as well as simulations for a stationary square cylinder. Fifteen test frequencies of the cylinder motion are chosen around the Karman vortex shedding frequency (0.132 Hz), the latter of which is available from experimental measurements [68].

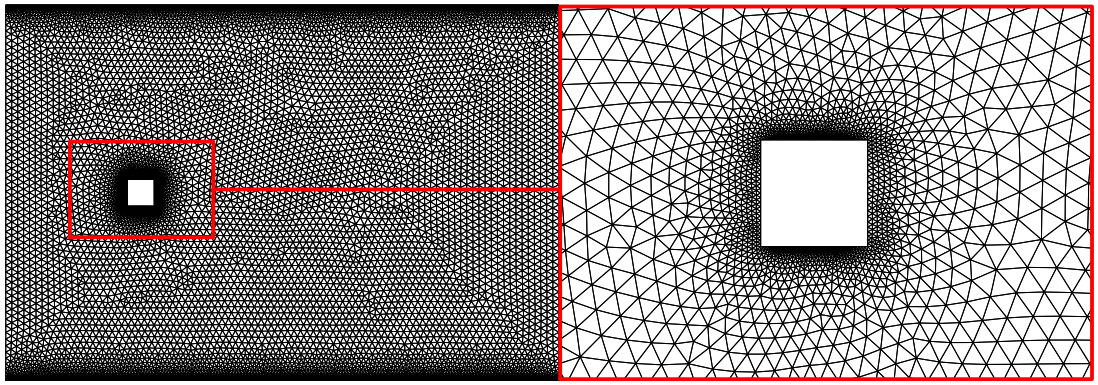

(a)

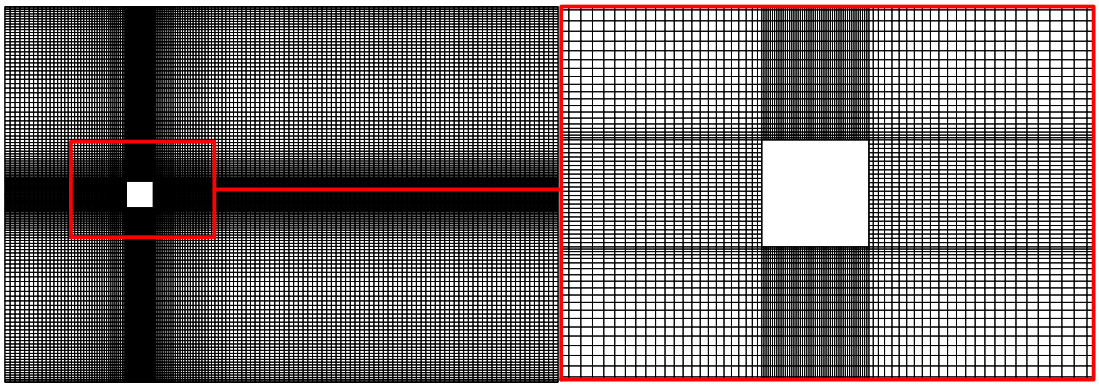

(b)

Figure 4.11: Initial mesh of the dynamic mesh model test case: (a) unstructured mesh; and, (b) structured mesh.

Detailed information about the CFD simulation and setup is summarized in Table 4.7. For an unstructured mesh as show in Figure 4.11 (a), (b), the initial orthogonal quality of

the mesh is about 0.77, and the maximum equivolume skew is about 0.46. The cell size surrounding the square cylinder is about $0.03\boldsymbol{D}$. The dynamic mesh re-meshing process is controlled by the following parameters: namely, the minimum length scale $0.03\boldsymbol{D}$, the maximum length scale $0.035\boldsymbol{D}$, the maximum cell equivolume skewness 0.7 and the maximum face skewness 0.7. These parameter values show that the mesh quality is acceptable with respect to the criteria mentioned in Section 3.4.2. For a structured mesh [shown in Figure 4.11 (c), (d)], a ratio-based model, with 0.5 set for both of the split factor and the collapse factor, is used in the present work. The aspect ratio defined in Section 3.4.2 is considered as the criterion of mesh quality. The initial aspect ratio is 4.79; hence its value during calculation is controlled under 9.58.

Table 4.6: Simulated conditions in the dynamic mesh model validation.

Test No.	f_{dri} (Hz)	u_r
1	0.35	2.86
2	0.30	3.33
3	0.25	4.00
4	0.20	5.00
5	0.18	5.55
6	0.16	6.26
7	0.15	6.67
8	0.14	7.14
9	0.13	7.69
10	0.12	8.33
11	0.11	9.09
12	0.10	10.00
13	0.07	14.29
14	0.05	20.00
15	0.04	25.00

Table 4.7: Simulation setup details in the dynamic mesh model validation.

Setup	Details
Unstructured mesh	Smoothing method; No. of cells: 19810; mesh type: wedge; minimum orthogonal quality: 0.772
Structured mesh	Layering method; No. of cells: 26300; mesh type: quadrilateral; maximum aspect ratio: 9.58
Boundary conditions	Inlet: velocity inlet; outlet: outflow; wall: non-slip condition
Turbulence model	SST $k-\omega$ model
Time step	0.005 s ($C < 12$)

4.3.3 Results and Analysis

As mentioned above, fifteen values of drive frequency f_{dri} for the oscillating square cylinder, as well as the case of a stationary square cylinder, were simulated in the present work. When the cylinder is moving, the vortex shedding adds a component induced by the cylinder motion, so the frequency of this component has the same value as the cylinder motion frequency. This frequency cannot be obtained directly, so the lift coefficient, which has a linear relation with the surface integral of the pressure on the horizontal sides of the square cylinder, is monitored. Here, a Fast Fourier Transform (FFT) is used in obtaining the frequency information. Then the weights of vortex shedding induced by the cylinder motion and the natural shedding can be compared using the amplitude of the frequency corresponding to the source.

Table 4.8: Comparison of time-averaged square cylinder data.

Group	Reference	$\overline{C_L}$	$C_{L,\mathrm{rms}}$	$\overline{C_D}$	$C_{D,\mathrm{rms}}$	St
Numerical data	Verstappen and Veldman [108]	0.005	1.45	2.09	0.178	0.133
	Porquie et al. [84]	-0.02	1.01	2.2	0.14	0.13
		-0.04	1.12	2.3	0.14	0.13
		-0.05	1.02	2.23	0.13	0.13
	Murakami and Mochida [74]	-0.05	1.39	2.05	0.12	0.131
	Wang and Vanka [109]	0.04	1.29	2.03	0.18	0.13
	Nozawa and Tamura [75]	0.0093	1.39	2.62	0.23	0.131
	Kawashima and Kawamura [54]	0.01	1.26	2.72	0.28	0.16
		0.009	1.38	2.78	0.28	0.161
	Ochoa and Fueyo [76]	0.03	1.4	2.01	0.22	0.139
		0.000421	1.09	2.51	0.048	0.141
	Thompson [100]	0.00171	1.45	2.29	0.118	0.143
Experimental data	Lyn et al. [68]	–	–	2.1	–	0.132
The present work	Unstructured mesh; smoothing method	0.0032	1.09	2.02	0.04	0.13
	Structured mesh; layering method	0.0026	1.27	2.09	0.07	0.13

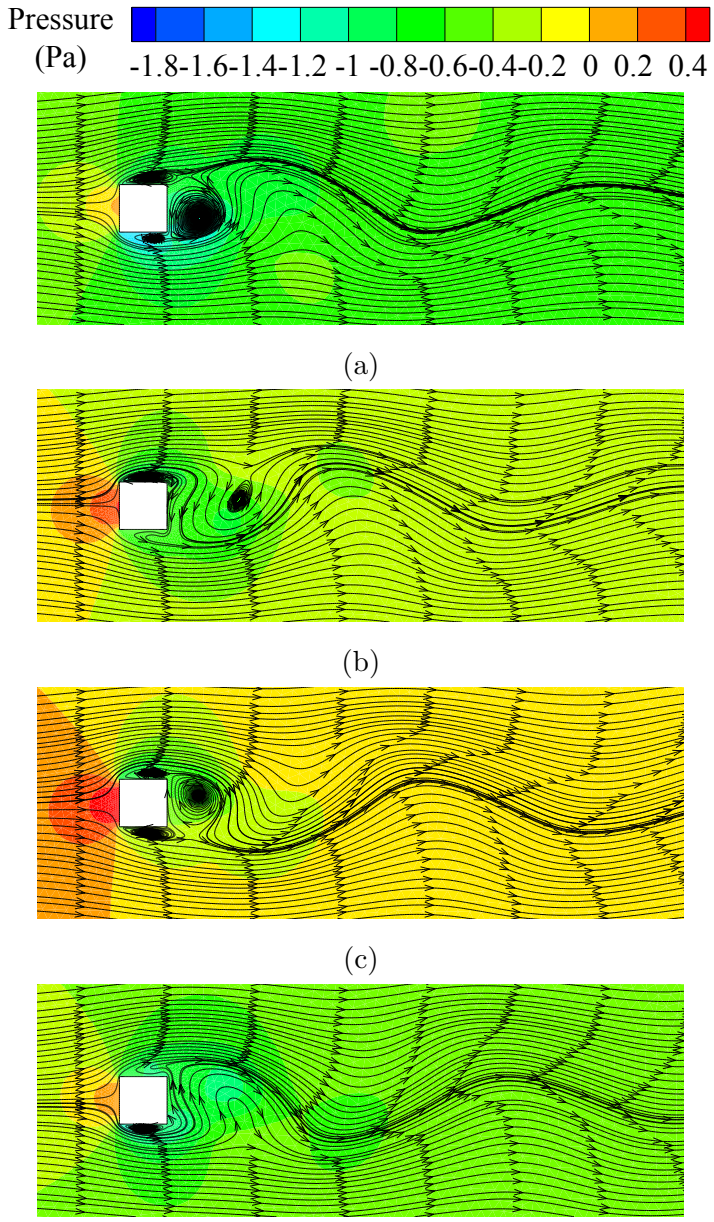

Figure 4.12: Streamlines and pressure contours for flow near the stationary square cylinder in a vortex shedding cycle: (a) $t = 244$ s; (b) $t = 246$ s; (c) $t = 248$ s; and, (d) $t = 250$ s.

The result of the stationary cylinder case (Table 4.8) is compared with other researchers' results, which are quoted from Ochoa and Fueyo [76].

The results shown Table 4.8 agree well with other researchers' numerical and experimental results. These encouraging results form a good foundation for the validation of the dynamic meshing in the next step.

The mesh adopted for this test case is unstructured and triangular, so re-meshing and smoothing methods are used for the dynamic mesh procedure. The streamlines and pressure contours in the region near the stationary square cylinder are shown in Figure 4.12 at the times $t = nT$, $(1/4 + n)T$, $(2/4 + n)T$ $(n = 0, 1, 2, \ldots)$.

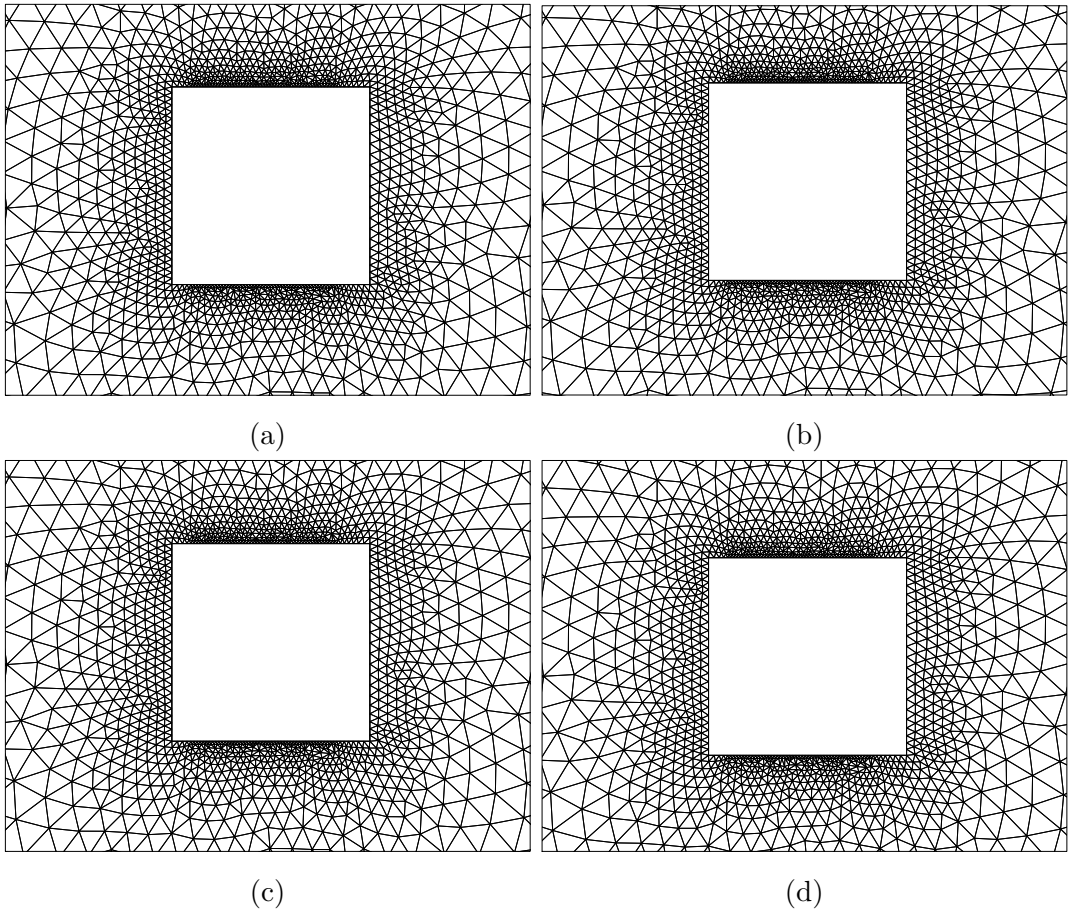

(a) (b)

(c) (d)

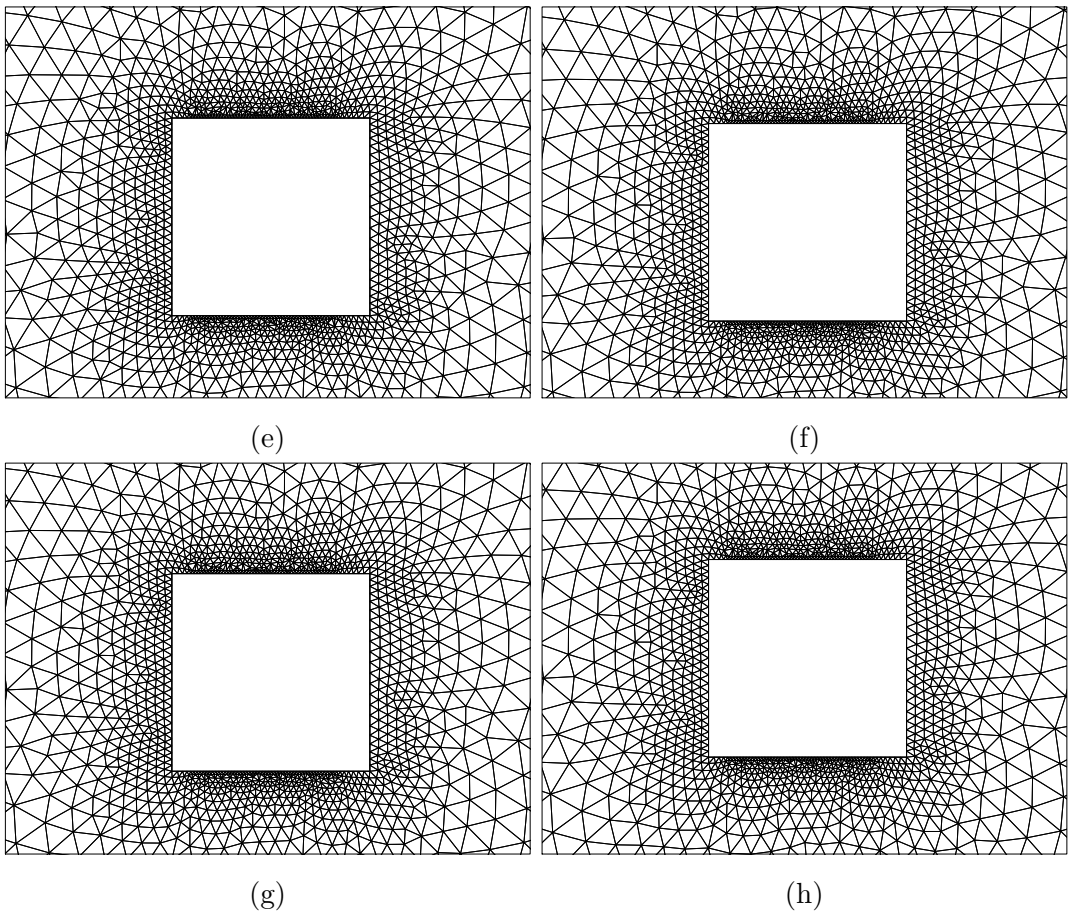

Figure 4.13: Dynamic mesh in a cylinder motion cycle ($u_r = 10$): (a) $t = 251.25$ s; (b) $t = 252.5$ s; (c) $t = 253.75$ s; (d) $t = 255s$; (e) $t = 256.25$ s; (f) $t = 257.5$ s; (g) $t = 258.75$ s; and, (h) $t = 260$ s.

The simulation lasts from $t = 0$ s to $t = 450$ s. The cylinder is stationary between $t = 0$ s and $t = 250$ s and begins to move at $t = 250$ s. The dynamic mesh in a motion cycle is shown in Figure 4.13. The dynamic mesh after 50 s, 100 s, 150 s, 200 s of cylinder motion (i.e., $t = 300$, 350, 400, 450 s) is shown in Figure 4.14.

As is evident from a perusal of Figures 4.13 and 4.14, the dynamic mesh retains a good

quality during the entire coarse of the simulation. The transition from a refined mesh to a coarse mesh (and vice-versa) is smooth. The minimum orthogonal quality and maximum cell equivolume skew are monitored after the cylinder motion begins (Figure 4.15). The minimum orthogonal quality remains above 0.6, and the maximum cell equivolume skew stays under 0.8.

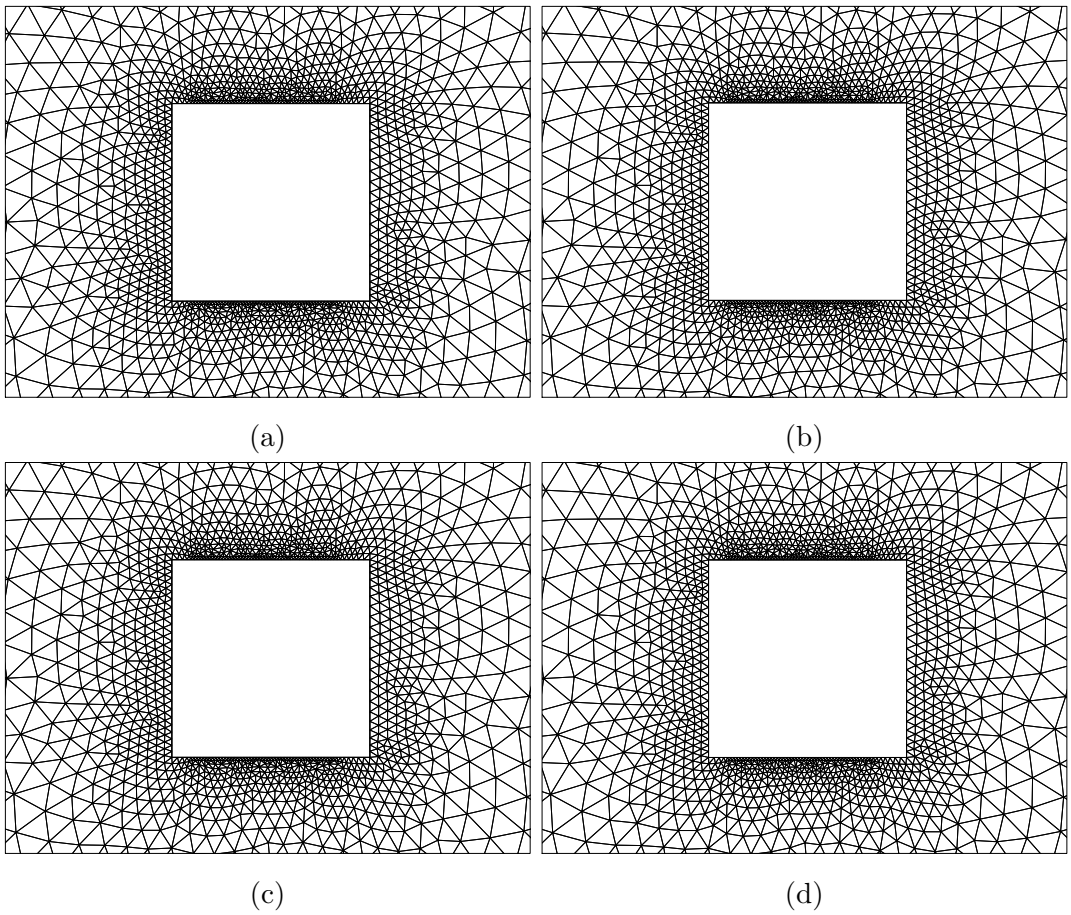

Figure 4.14: Dynamic mesh during simulation ($u_r = 10$): (a) $t = 50$ s; (b) $t = 100$ s; (c) $t = 150$ s; and, (d) $t = 200$ s after cylinder motion begins.

Figure 4.16 shows the results of a stationary cylinder and a moving cylinder in the lock-in, below lock-in, and above lock-in ranges. The peaks in the amplitude spectra of

the lift coefficient shown in Figure 4.16 correspond to the vortex shedding frequency.

The result shown in Figure 4.16 (a) is for a stationary cylinder; the vortex shedding results from its natural properties. The main frequency is compared with other results in Table 4.8.

Figure 4.16 (b) shows the result for $u_r = 9.09$. The driving frequency f_{dri} is 0.11 Hz, which is different from the vortex-shedding natural frequency of 0.13 Hz. However, the vortex shedding occurs at a single main frequency, which is the same as the motion driven frequency of the square cylinder. This indicates that this case corresponds to the lock-in range.

Figure 4.16 (c) plots the result for $u_r = 5$, which is below the lock-in range. The lift coefficient has two frequency peaks. The one at the natural vortex-shedding frequency is lower than the one at the cylinder motion frequency, which is consistent with the result of Hines [42].

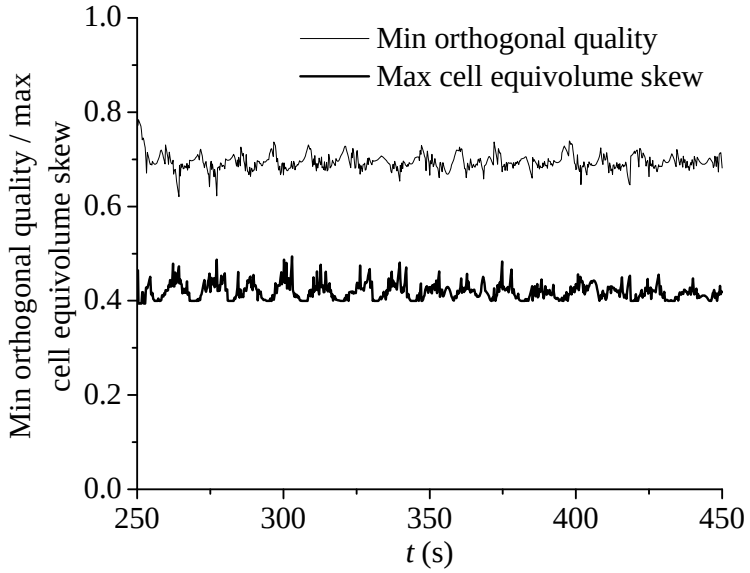

Figure 4.15: The minimum orthogonal quality and maximum cell equivolume skew during simulation.

Figure 4.16 (d) shows the result for $u_r = 14.29$, above lock-in range. As in the case below lock-in range, the frequencies of natural vortex shedding and cylinder motion are easily distinguishable.

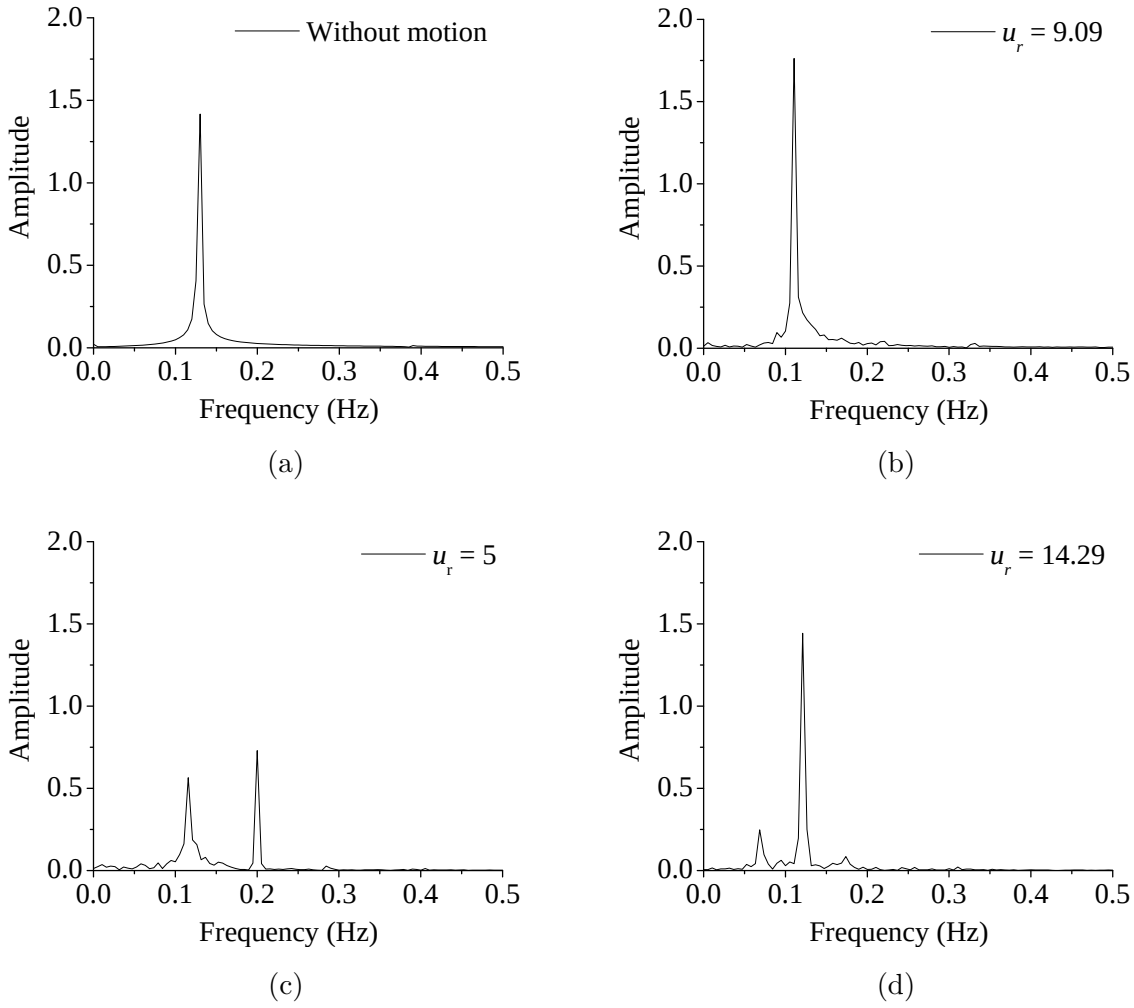

Figure 4.16: Amplitude spectra of the lift coefficient: (a) without cylinder motion; (b) $u_r = 9.09$ (within lock-in range); (c) $u_r = 5$ (below lock-in range); and, (d) $u_r = 14.29$ (above lock-in range).

By transforming the vortex-shedding main frequency at every reduced velocity, the relation between the vortex-shedding frequency and the cylinder-motion frequency can be determined as shown in Figure 4.17. The region of the plot where the ratio of the vortex-shedding frequency to the cylinder-motion frequency is equal to unity corresponds to the lock-in range. In this range, resonance occurs (viz., the vortex-shedding frequency is synchronized with the cylinder-motion frequency). This result corresponds well with the results reported in references [78, 11, 98], indicating that the dynamic mesh model and the SST $k-\omega$ turbulence model can provide reasonable good predictions for this case.

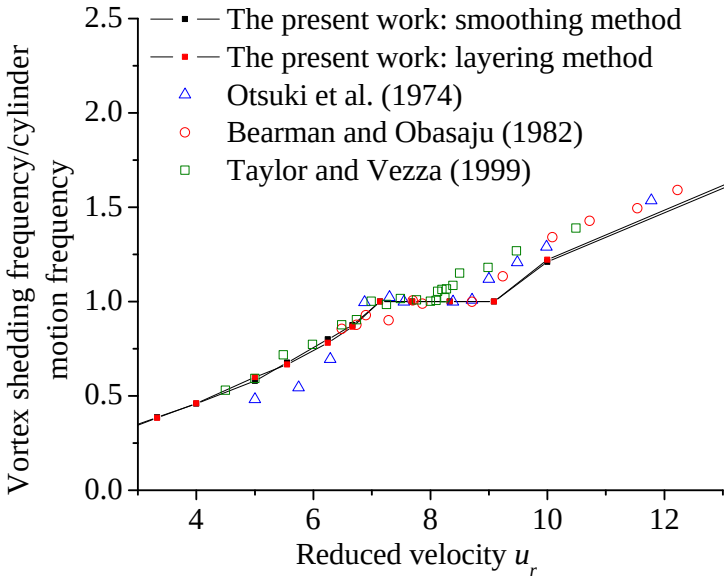

Figure 4.17: Comparison of the present work and previously published results on the relation between reduced velocity and the ratio of vortex shedding to cylinder motion frequency [106]–[108].

In this test case, the turbulent simulation system with a dynamic mesh is verified. The simulation reasonably predicts the lock-in phenomenon, indicating that the dynamic mesh maintains high quality and that the whole system responds well to this dynamic mesh.

4.4 Flow Passing Square Cylinder with Autonomous Oscillation: Model Validation of FSI (Explicit Method)

4.4.1 Problem Description

For a flow past a moving cylinder with one degree of freedom, there exists an interaction between the flow and the cylinder. The vibration that is induced on the moving cylinder by the vortex shedding is commonly referred to as vortex-induced vibration (VIV). This situation corresponds to a two-way coupling FSI problem. As in the case in Section 4.3, the "lock-in" phenomenon can occur for this situation also. In the present work, this lock-in phenomenon has been simulation and the results are compared to some experimental measurements as well as to simulation results obtained by other researchers.

4.4.2 CFD Process

In this case, the same 2D rectangular computational domain as Section 4.3 is utilized, as shown in Figure 4.18. The left edge of the domain is the inlet, the right side is the outlet, and the other two edges are set up as walls.

The cylinder is modeled as a limited-cycle oscillator, implying that when the cylinder experiences vortex-shedding oscillations, its response $y(t)$ exhibits stable amplitude after an initial transient regime. In two dimensional configurations, the motion of the cylinder satisfies the following equation:

$$\ddot{y} + 2\eta(2\pi f_0)\dot{y} + (2\pi f_0)^2 y = \frac{F}{m}, \tag{4.16}$$

where m is the mass of the cylinder; F is the time-dependent flow dynamic force resulting

from the vortex shedding; and f_0 is the under-damped natural frequency of the system:

$$f_0 = \frac{1}{2\pi}\sqrt{\frac{k_S}{m}}, \tag{4.17}$$

and the damping ratio is

$$\eta = \frac{c}{2\sqrt{k_S m}}, \tag{4.18}$$

where c is the damping coefficient and k_S is the spring constant (or, stiffness). With reference to the simulation of the experiment of Amandolese and Hemon [6], the values of the relevant parameters are summarized in Table 4.9.

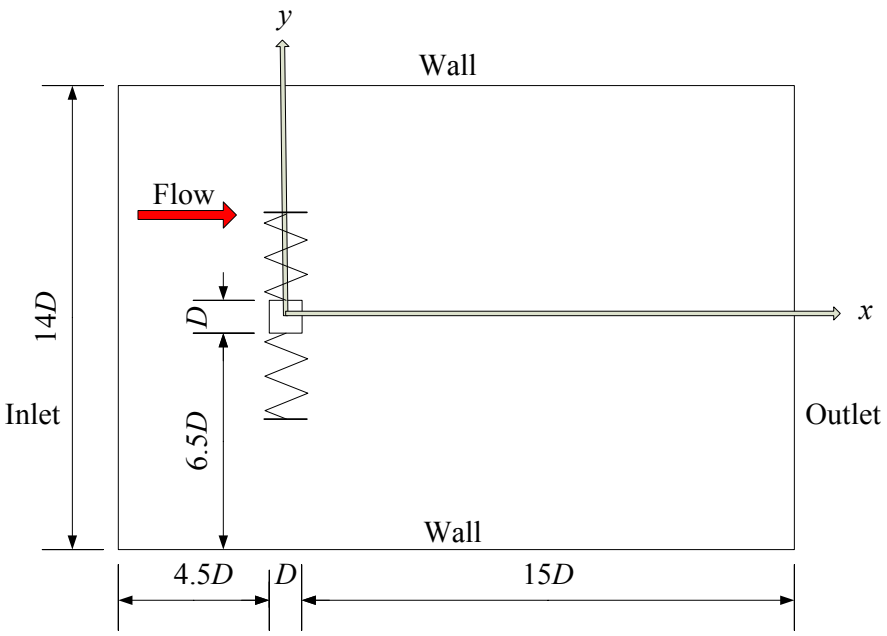

Figure 4.18: General view of the simulation domain in the explicit FSI model validation.

This case is tested under varying reduced velocities by changing the inlet velocity (see Table 4.10). Eight inlet velocities have been chosen to make a vortex frequency range covering the structure's natural frequency (15.22 Hz). The vortex frequency f_v^* is estimated based on a Strouhal number of 0.127 [77].

Table 4.9: System physical parameters.

Variable	Symbol	Value	Unit or formula
Side length	D	0.02	m
Stiffness	k_S	3987	N m-1
Mass of the cylinder	m	0.436	kg
Structural damping	c	0.069	Ns m-1
Natural frequency	f_0	15.22	Hz
Inlet velocity	u_{inl}	0.6–6.0	m s^{-1}
Fluid density	ρ	1.205	kg m^{-3}
Kinematic viscosity	ν	1.5×10^{-5}	m^2 s^{-1}
Damping ratio	η	8.28×10^{-4}	$c/(2\sqrt{k_S m})$
Reduced velocity	u_r	2–10	$u_{\text{inl}}/(f_0 D)$

The CFD simulation and setup are summarized in Table 4.11. Cells having a maximum aspect ratio of 9.58 occur at or near the walls. During the dynamic mesh process, the mesh only deforms at the upper and lower walls with a split factor and a collapse factor of 0.5. Hence, the maximum aspect ratio in the domain will vary in a range from 9.58 to 19.16 during the updating of the dynamic mesh, confirming that the mesh quality is acceptable.

4.4.3 Result and Analysis

Firstly, simulations for the flow over a stationary square cylinder were conducted. As shown in Figure 4.19, the variation of the Strouhal numbers obtained is consistent with Okajima's [77] experimental measurements Within the expected experimental scatter, the agreement of the numerical predictions with the data is judged to be satisfactory. More specifically, the current simulation results agree with the experimental measurements with a maximum discrepancy of about 11 %.

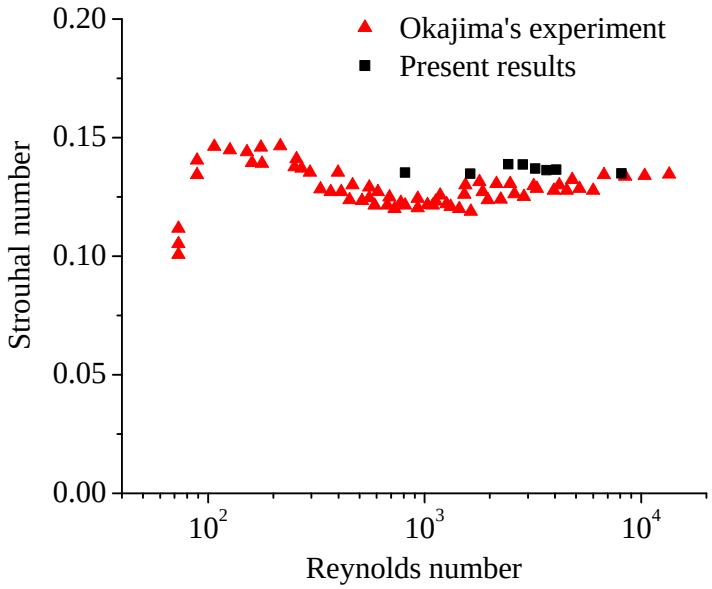

Figure 4.19: Variation of Strouhal number with Reynolds number compared with experimental results.

Simulations of flow through a square cylinder with one degree of freedom were undertaken subsequently. From $u_r = 7$ to 10, it was observed that the vortex shedding frequency stayed the same as the system's natural frequency. This lock-in regime is also shown in Figure 4.16.

Figure 4.20 shows the time history of the normalized cylinder displacement and lift coefficient for the case $u_r = 10$. It is difficult to obtain the vortex-shedding frequency directly, so the lift coefficient, which has a linear relation with the surface integral of the pressure on the horizontal sides of the square cylinder, is monitored. When lock-in occurs, the oscillation of the lift coefficient is in lock step with normalized cylinder displacement.

Table 4.10: Simulated conditions in the explicit FSI model validation.

Test No.	u_{inl} (m s^{-1})	u_r	f_v^* (Hz)
1	0.61	2	3.87
2	1.22	4	7.73
3	1.83	6	11.60
4	2.13	7	13.53
5	2.44	8	15.46
6	2.74	9	17.40
7	3.04	10	19.33
8	6.09	20	38.66

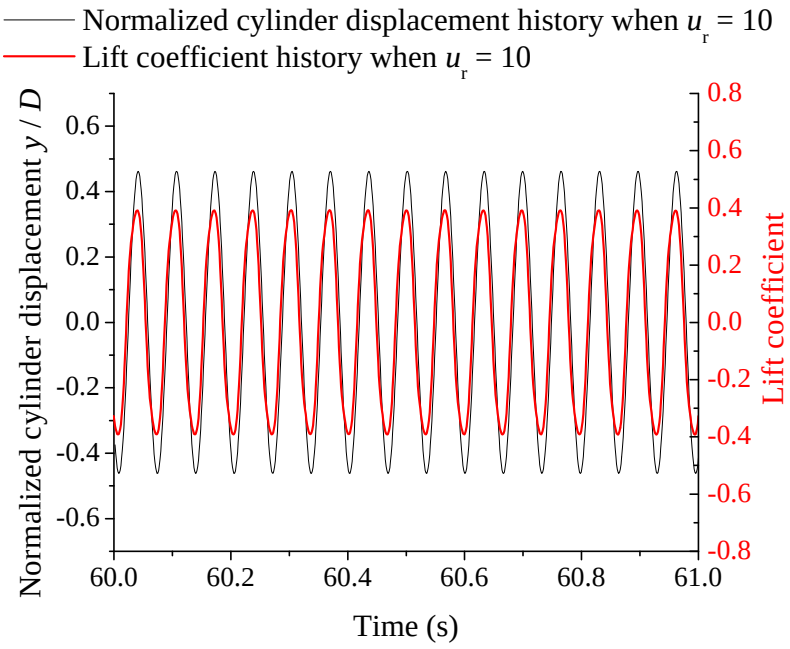

Figure 4.20: Time history of cylinder displacement and lift coefficient for case with $u_r = 10$.

Table 4.11: Simulation setup details in the explicit FSI model validation.

Setup	Details
Mesh	Structured mesh; layering method; cell amount: 26300; mesh type: quadrilateral; maximum aspect ratio: 9.58
Boundary conditions	Inlet: velocity inlet; outlet: outflow; wall: non-slip condition
Turbulence model	SST $k-\omega$ model
Time step	0.005 s ($C < 12$)

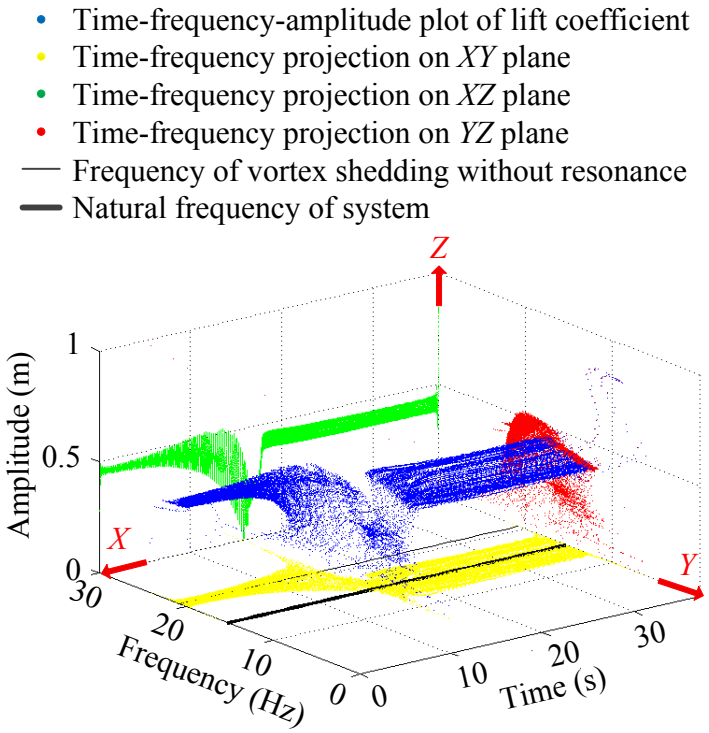

Figure 4.21: Time-frequency-amplitude plot for the case with $u_r = 10$.

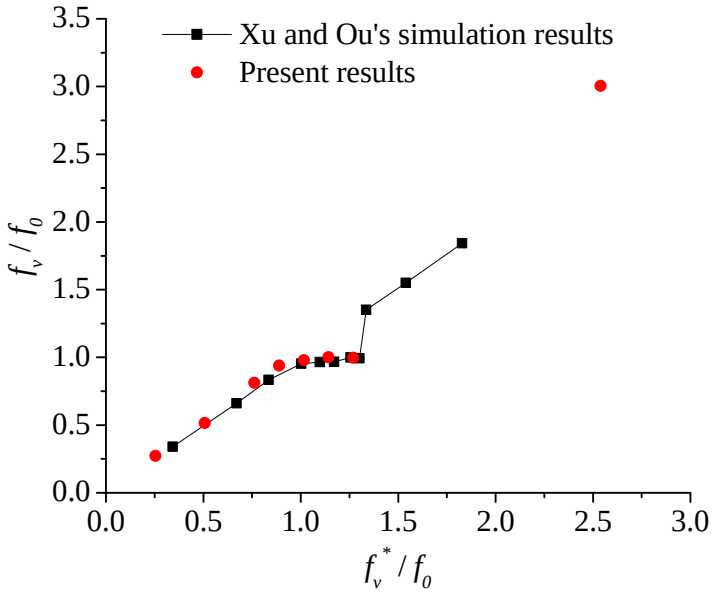

Figure 4.22: Variation of vortex shedding frequency of square cylinder with autonomous oscillation versus stationary square cylinder.

Applying the Hilbert Huang Transform [46] (see Appendix A.1) to the time history of the lift coefficient, the relation of time, frequency, and amplitude can be observed in Figure 4.21. From the projection of data on to the ***XY*** plane, referring to the black lines, it is evident that the vortex-shedding frequency switches from the vortex-shedding frequency associated with the case of a stationary cylinder (about 20 Hz) to that of the system natural frequency (15 Hz), signaling that resonance has occurred.

In comparison with Xu and Ou's [115] work as summarized in Figure 4.22 where f_v^* is the vortex shedding frequency in the case of stationary cylinder, the present simulations have captured the lock-in phenomenon successfully.

4.5 Flow Driven Heart Valve: Model Validation of FSI (Implicit Method)

This section validates the approach of solving a FSI two-way coupling problem by dynamic mesh in ANSYS-FLUENT. The physical model is an artificial heart valve, which is very popular in the biomechanics and the biomedical fields. The heart valve has one leaflet on it. This leaflet can rotate freely around its axis as driven by the cyclical inlet velocity. Both its angular velocity and acceleration vary with the inlet velocity. The heart valve is a classic FSI problem due to the strong interaction between the fluid and the structure.

4.5.1 Problem Description

An artificial heart valve has a structure similar to a real heart valve. The opening and closing of the valve are driven by the cyclical inlet velocity, just like the relationship between a real heart and a pulse. In an experiment conducted at the Eindhoven University of Technology [30] on a heart valve, the geometry of the heart valve is simplified to a regular shape with only one leaflet (Figure 4.23). The leaflet can rotate along its upper edge. Due to its symmetry along the rotating axis, the geometry can be simplified to the 2D domain, as shown in Figure 4.24. Here, due to the limitation in the dynamic mesh model in ANSYS-FLUENT, at least one cell is required to cover the gap between the valve leaflet and the wall. The length of the leaflet in the CFD model is 0.0001 m shorter than its real length (0.02 m). Its thickness (0.001 m) is ignored in the geometry but is still calculated in its mass. Its mass and moment of inertia with respect to the rotational axis along the edge of the leaflet are 0.0242 kg and 3.9×10^{-6} kg m^2, respectively.

The liquid flows from left to right. The inlet velocity, assumed to be uniform across

the section, is normal to the inlet and varies over time in accordance with

$$V_{\text{inl}} = \begin{cases} 0.4 + 0.11 \cdot \sin\left(\frac{2\pi \frac{t}{T_P}}{0.74}\right), & 0 \le t \le 0.37T_P \\ 0.4 + 0.055 \cdot \sin\left[\frac{2\pi\left(\frac{t}{T_P}+0.26\right)}{1.26}\right], & 0.37T_P \le t \le T_P \end{cases}, \tag{4.19}$$

where T_P is the period of the inlet velocity and has a value of 2.45 s. The liquid in the experiment is a mixture of glycerol and water, which has similar properties to blood, with a dynamic viscosity of 0.004 Pas and a density of 1090 kg m^{-3}.

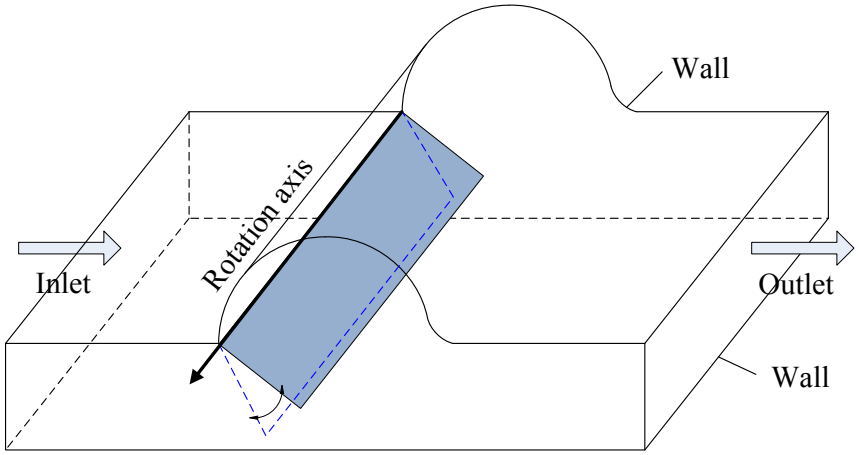

Figure 4.23: Schematic representation of the geometry of the heart valve in an experiment conducted at Eindhoven University of Technology [30].

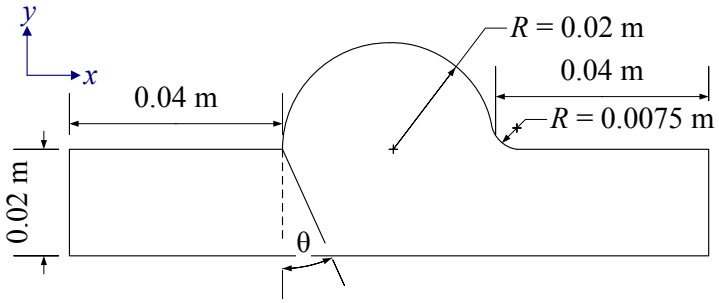

Figure 4.24: General view of the computational domain in the implicit FSI model validation.

The rotation of the leaflet is driven by the torque due to the gravity, the buoyancy force, and the pressure and viscous forces. Here, the friction from structures is neglected. The relation of the torque M and the angular acceleration $\ddot{\theta}$ at a given time is

$$\ddot{\theta} = \frac{M}{L}, \tag{4.20}$$

where L is the moment of inertia given by

$$L = \sum_{i=1}^{n} m_i r_i^2. \tag{4.21}$$

In ANSYS-FLUENT M is calculated as

$$M = \sum_{i=1}^{n} f_{n,i} r_i, \tag{4.22}$$

where i is the index of cells on the leaflet surface, r_i is the distance from the centroid of cell i to the rotating axis, and $f_{n,i}$ is the net force acting on cell i normal to the surface, as shown in Figure 4.25.

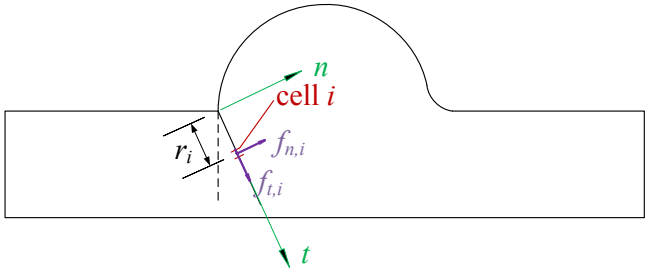

Figure 4.25: Forces analysis on a cell of the leaflet surface.

4.5.2 CFD Simulation

The mesh is triangular and refined in the region near the leaflet to maintain good quality when the dynamic mesh is activated, as shown in Figure 4.26.

The Reynolds number for this problem varies in the range from 0 to 817.5, which is in the laminar regime. The boundary conditions are set to the inlet velocity defined by the UDF, the outlet pressure is assigned the value of 101,325 Pa, and along the solid walls a non-slip boundary condition is applied.

The issue in the model is how to implement the coupling between the fluid and the structure. In ANSYS-FLUENT, for unsteady calculation, the motion of the leaflet is discrete as well. In a time step, the torque from the fluid and the angular acceleration, velocity, and displacement are constant. These quantities are related for the $(n+1)^{\text{th}}$ time step as follows:

$$\ddot{\theta}_{n+1} = \frac{M_{n+1}}{L}, \tag{4.23}$$

$$\Delta\dot{\theta}_{n+1} = \ddot{\theta}_{n+1} \cdot \Delta t, \tag{4.24}$$

$$\dot{\theta}_{n+1} = \dot{\theta}_n + \ddot{\theta}_{n+1} \cdot \Delta t. \tag{4.25}$$

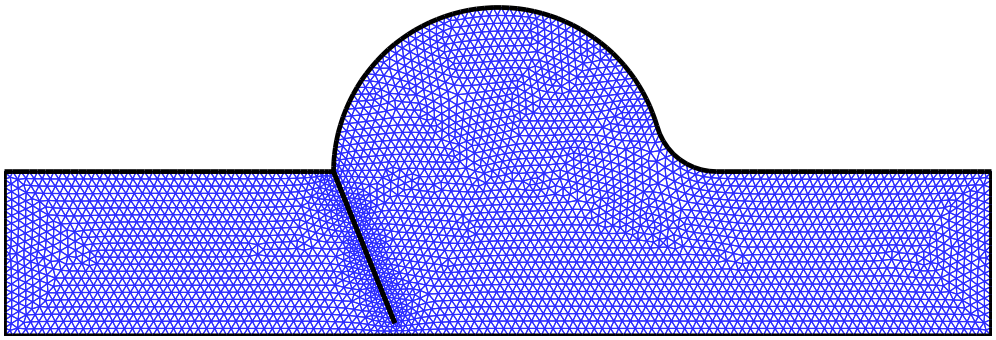

Figure 4.26: Mesh of the 2D heart valve model.

All of these dynamical variables vary (change) significantly with time. When using an explicit algorithm, the angular acceleration is obtained from the net torque calculated from the flow field of the previous time step. This approach can result in a large correction in the angular velocity which can induce numerical instabilities in the calculation and cannot be tolerated. Consequently, such a large-displacement FSI problem must be solved by an

implicit algorithm. To reduce the calculation time, the leaflet motion equations and flow equations are not coupled in the solution, but instead the value of the angular acceleration is corrected at each iteration until the equation $\ddot{\theta}_{n+1} = \frac{M_{n+1}}{L}$ is satisfied. In the first iteration of the $(n+1)^{\text{th}}$ time step, if the angular acceleration is initialized with the value of the angular acceleration at the previous time step, so

$$\ddot{\theta}_{n+1}^{k=1} = \dot{\theta}_n, \tag{4.26}$$

Obviously the relationship of $\ddot{\theta}_{n+1} = \frac{M_{n+1}}{L}$ will not be satisfied with this initialization, so a correction needs to be applied. Towards this purpose, the derivative $dM/d\ddot{\theta}$ is first determined as follows:

$$\left(\frac{dM}{d\ddot{\theta}}\right)_{n+1}^{k+1} = \frac{M_{n+1}^{k} - M_{n+1}^{k-1}}{\ddot{\theta}_{n+1}^{k} - \ddot{\theta}_{n+1}^{k-1}}, \tag{4.27}$$

which can then be used to calculate a more correct angular acceleration in the next iteration. This correction is obtained from

$$M_{n+1}^{k} + \left(\frac{dM}{d\ddot{\theta}}\right)_{n+1}^{k+1} \cdot \left(\ddot{\theta}_{n+1}^{k+1} - \ddot{\theta}_{n+1}^{k}\right) = L \cdot \ddot{\theta}_{n+1}^{k+1}, \tag{4.28}$$

or, equivalently, form

$$\ddot{\theta}_{n+1}^{k+1} = \frac{M_{n+1}^{k} - \left(\frac{dM}{d\ddot{\theta}}\right)_{n+1}^{k+1} \cdot \ddot{\theta}_{n+1}^{k}}{L - \left(\frac{dM}{d\ddot{\theta}}\right)_{n+1}^{k+1}}. \tag{4.29}$$

At the end of each iteration, the relative error is monitored to determine if the result has converged for this time step. If the result has not converged, additional iterations will need to be conducted. The derivative $dM/d\ddot{\theta}$ is calculated at every iteration because M is in fact non-linear about $\ddot{\theta}$, so updating its value at each iteration can accelerate the convergence. The iterative process has converged when the following condition is satisfied:

$$\left|\frac{M_{n+1}^{k} - L \cdot \ddot{\theta}_{n+1}^{k}}{M_{n+1}^{k}}\right| < \varepsilon_r, \tag{4.30}$$

where ε_r is the acceptable error tolerance. The value used in this work for the error tolerance is 1×10^{-3}.

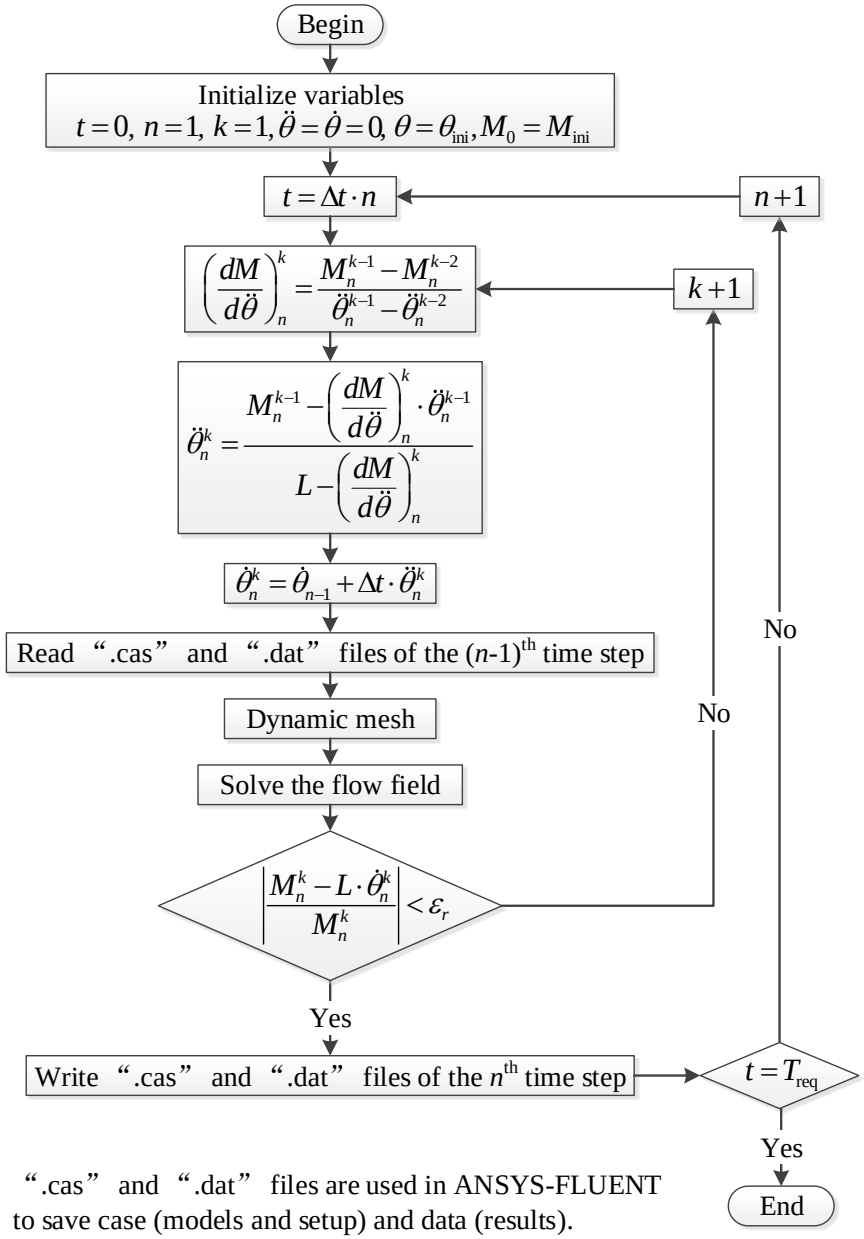

Figure 4.27: Flow diagram of the calculation loop for heart valve case.

In the dynamic mesh model of ANSYS-FLUENT, the mesh is updated at the be-

ginning of every time step, but not at every iteration within a given time step, so the calculation loop for the iterations described above needs to run outside ANSYS-FLUENT. The calculation in ANSYS-FLUENT is only a step in this loop. In the present work, the various steps in the iterative process are controlled using a Scheme file (see Appendix A). Scheme is a dialect of the List Processor language (LISP). A Scheme file can interact with ANSYS-FLUENT to automate various processes. In addition to the basic functions of a programming language, such as the if-command and do-loops, Scheme can exchange data with ANSYS-FLUENT and execute any text commands of ANSYS-FLUENT. These commands cover almost all functions embodied in the Graphical User Interface. This functionality is very important in rearranging the ANSYS-FLUENT calculation procedures.

The calculation begins at $t = 2.05T_P$, corresponding to $V_{\text{inl}} = 0$, and the initial angle is 0.384 rad, corresponding to the beginning (start) of the opening of the leaflet in the experiment.

As described in Section 3.5.3, some steps of the calculational procedure have been significantly improved in the present work (see Figure 4.27 for a summary of the iterative scheme used herein). The first concerns how to calculate the value of the angular acceleration $dM/d\ddot{\theta}$, which is required for the correction of $\ddot{\theta}$, and therefore also for the calculation of $\dot{\theta}$ [see Equations (4.25) and (4.29)]. In Dumont et al.'s model, at the beginning of each time step ($t = n \cdot \Delta t$), Equation (4.29) is not applied to the first ($k = 1$) and second ($k = 2$) iterations of the process. In these two iterations, $\ddot{\theta}$ is determined using the previous value for $\ddot{\theta}$ for $k = 1$ and using the previous plus a certain value for $k = 2$. The quantity $t = n \cdot \Delta t$ can be calculated till the third iteration when two sets of M and are already obtained to calculate dM and $d\ddot{\theta}$. Note, in Dumont et al.'s work, the quantity $dM/d\ddot{\theta}$ is calculated only once in a given time step since it is considered no change during a time step and no correction needed. Actually, $dM/d\ddot{\theta}$ is not constant in a time step, especially when the leaflet is accelerating or decelerating. In consequence, in the second iteration $\ddot{\theta}$ needs to be corrected by an appropriate δ value, and this correction will depend on the leaflet's motion (both the direction and absolute magnitude of the acceleration). In the present work, $dM/d\ddot{\theta}$ is to be time varying (even in a single time step) and this quantity is always

calculated from the information available about this quantity from the previous two time steps. Both $dM/d\ddot{\theta}$ and $\ddot{\theta}$ are corrected in order to provide to more precise estimates for these quantities.

The second improvement of the iterative process concerns is how to assess the convergence in the iteration. In Dumont et al.'s work, an absolute error was used to compare with an error tolerance to determine convergence. Unfortunately, this method is not very effective, owing to the fact that at some sensitive position in the computational domain, a small absolute error does not necessarily imply convergence and, indeed the calculation in the iterative scheme may diverge even though the absolute error is small. In the present work, the relative error (the percentage of the absolute torque error with respect to the torque) is used instead to determine whether the iterative solution has converged. This approach avoids the risk of divergence owing to the fact that a large relative error invariably signals a divergence of the iterative scheme, even though the more conventional absolute error is small.

4.5.3 Results and Analysis

After two cycles of motion, the solution becomes independent of the cycle's number. The following results are taken from the third cycle of motion.

Figure 4.28 shows the inlet velocity and relative pressure in a period (a cycle) or motion. In contrast to the velocity which exhibits two inflection points, the pressure difference between the inlet and the outlet Δp (defined as the inlet pressure minus the outlet pressure) has two jump points in each period which lead to points of discontinuity in the angular acceleration.

The angular opening (or, opening degree) of the leaflet during a cycle is shown in Figure 4.29 and compared with some experimental measurements. The opening and closing loop during a pulse is very consistent with the experimental measurements, indicating that

the simulation model is performing well. The general features of the angular opening as a function of the normalized time over a cycle (t/T_p) are reproduced well by the simulation. However, because all frictional forces are ignored in the simulations in this research, the magnitude of the leaflet's displacement in the simulation is larger than that obtained in the experiment.

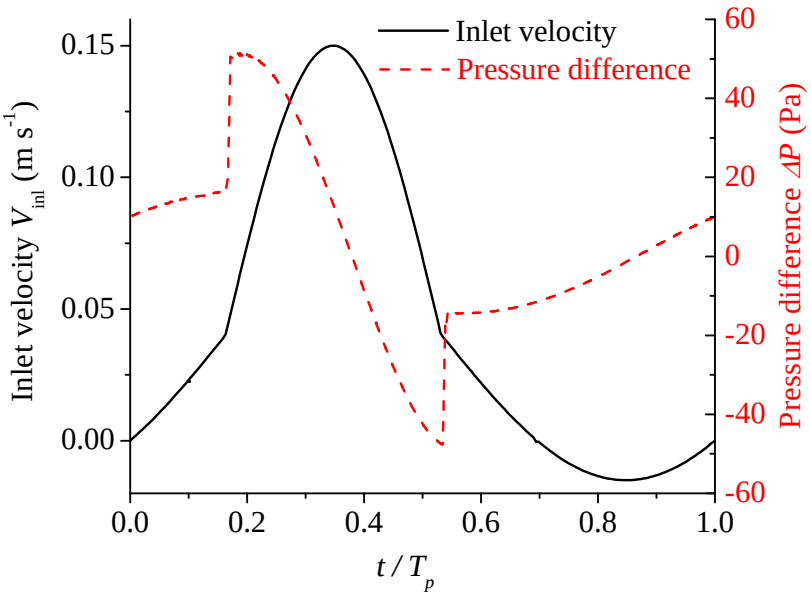

Figure 4.28: Inlet velocity and pressure difference during a period.

In Figure 4.30, the velocity vectors at five different times in a cycle of motion of the leaflet are shown and compared with the photographs taken during experiment [32]. The five different instants of time corresponding to the start of the opening of the leaflet, the two points associated with a zero pressure difference, and the two discontinuous points of the pressure are representative of the leaflet motion in a cycle. In Figure 4.30 (a), the leaflet is almost closed since the inlet velocity is nearly zero. A large vortex exists in the sinus cavity, and small ones exist downstream. From Figure 4.30 (a) corresponding to $t = 0$ to Figure 4.30 (c) corresponding to $t = 0.38T_p$, the leaflet is pushed up by the increasing

fluid velocity. All the vortex sizes are reduced and moved in the forward direction to the outlet. In Figure 4.30 (c), the opening degree (or angular opening) just passes its peak, and the vortex in the sinus cavity becomes very small. From Figure 4.30 (c) to Figure 4.30 (e), the leaflet is closing. The vortex in the sinus cavity is growing, and small downstream vortices are generated again.

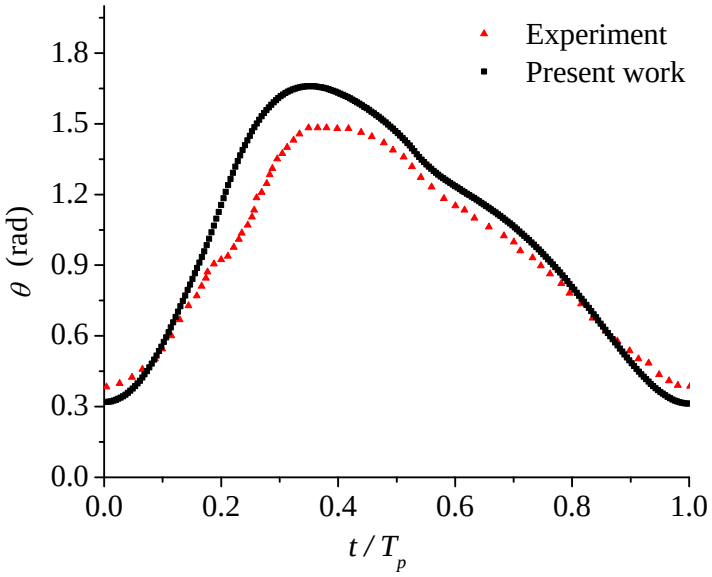

Figure 4.29: Comparison between simulation and experimental results [30] of the opening degree over a period.

In this section, a 2D FSI model of a heart valve was constructed based on the dynamic mesh technique in ANSYS-FLUENT. The phenomenon of the leaflet driven by a periodic inlet velocity was monitored in the simulation. It was found that the simulation correctly captured the complex formation and movement of the fluid vortices in the heart valve. Compared with the results captured by a CCD (charged-coupled device) camera during an experiment [32], the simulation results provide reasonable predictions of most of the flow field details. It can be concluded that the FSI model in this work can provide predictions for large-displacement strong coupling FSI problems with reasonable accuracy.

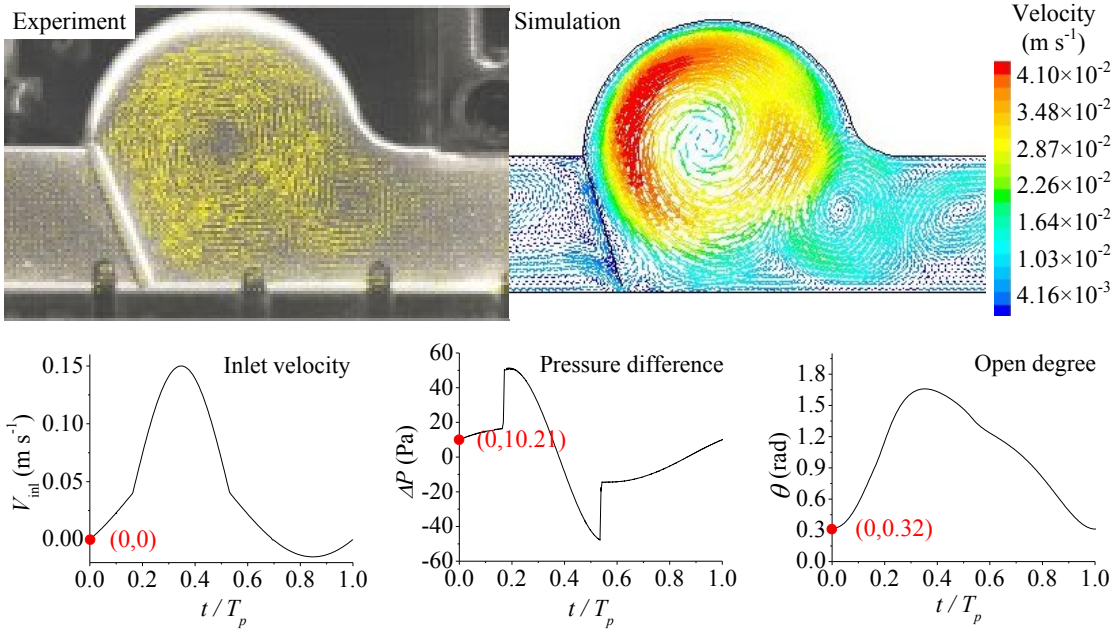
Experiment
Simulation
Velocity
(m s-1)
4.10×10-2
3.48×10-2
2.87×10-2
2.26×10-2
1.64×10-2
1.03×10-2
4.16×10-3
Inlet velocity
Vinl (m s-1)
(0,0)
t / Tp
Pressure difference
ΔP (Pa)
(0,10.21)
t / Tp
Open degree
θ (rad)
(0,0.32)
t / Tp

(a)

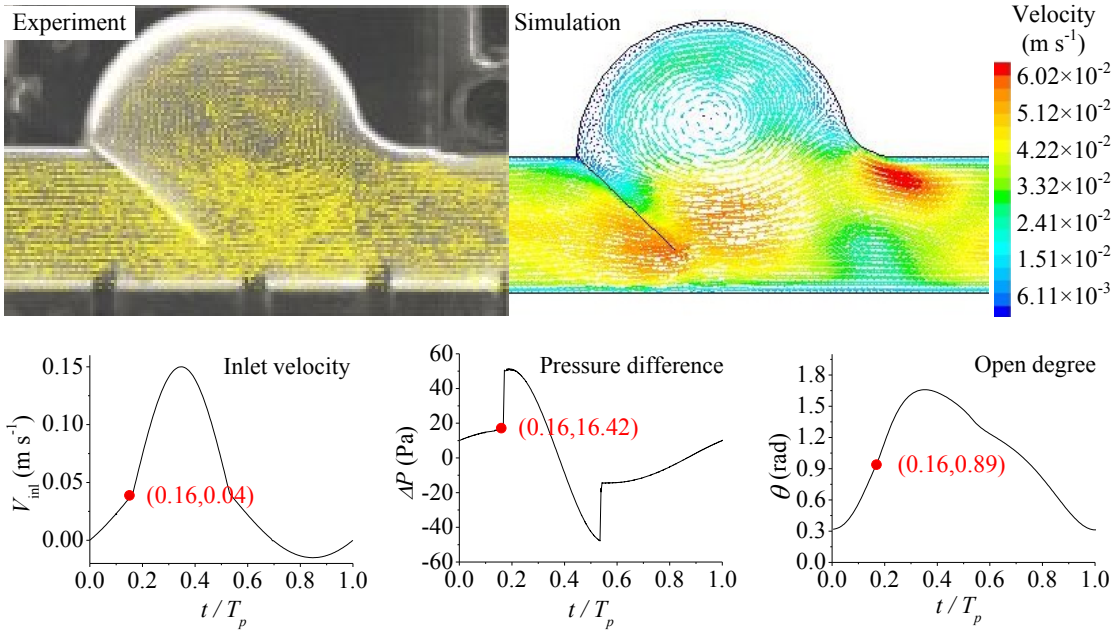
Experiment
Simulation
Velocity
(m s-1)
6.02×10-2
5.12×10-2
4.22×10-2
3.32×10-2
2.41×10-2
1.51×10-2
6.11×10-3
Inlet velocity
Vinl (m s-1)
(0.16,0.04)
t / Tp
Pressure difference
ΔP (Pa)
(0.16,16.42)
t / Tp
Open degree
θ (rad)
(0.16,0.89)
t / Tp

(b)

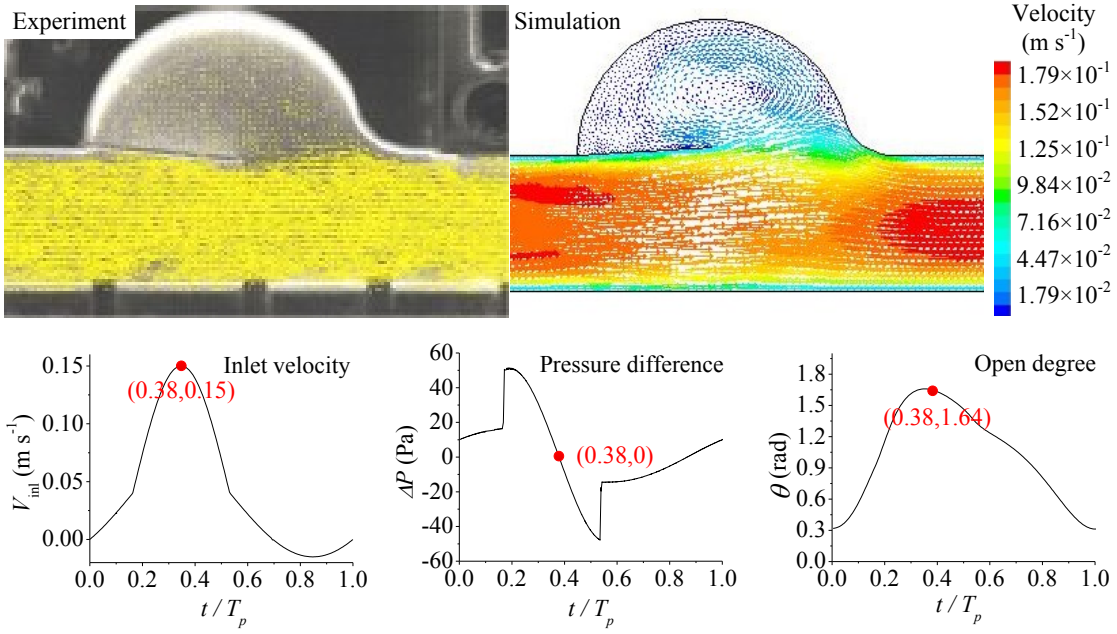
Experiment
Simulation
Velocity
(m s-1)
1.79×10-1
1.52×10-1
1.25×10-1
9.84×10-2
7.16×10-2
4.47×10-2
1.79×10-2
Inlet velocity
(0.38,0.15)
Vinl (m s-1)
Pressure difference
(0.38,0)
ΔP (Pa)
Open degree
(0.38,1.64)
θ (rad)
t / Tp

(c)

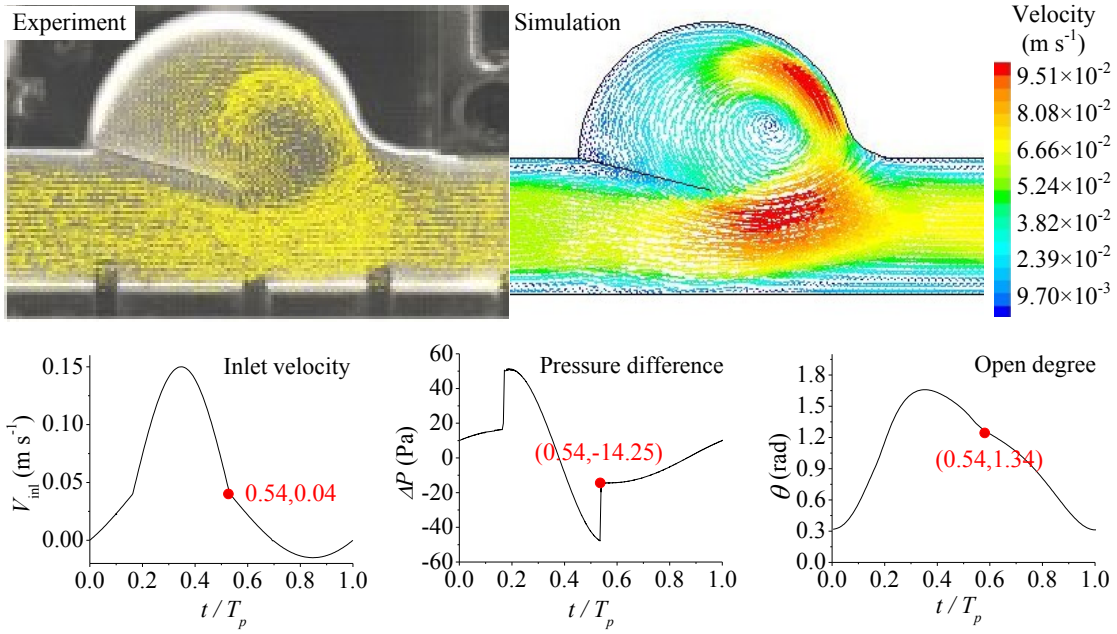
Experiment
Simulation
Velocity
(m s-1)
9.51×10-2
8.08×10-2
6.66×10-2
5.24×10-2
3.82×10-2
2.39×10-2
9.70×10-3
Inlet velocity
0.54,0.04
Vinl (m s-1)
Pressure difference
(0.54,-14.25)
ΔP (Pa)
Open degree
(0.54,1.34)
θ (rad)
t / Tp

(d)

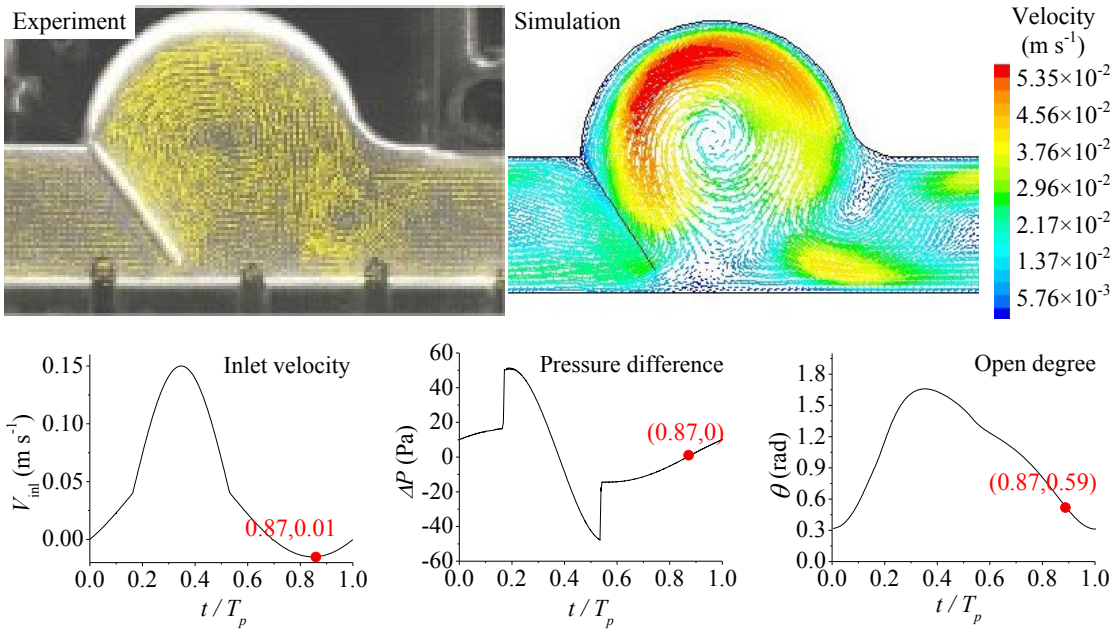

(e)

Figure 4.30: Velocity vectors compared with experiment [32] at different instances of time in a cycle of the leaflet motion: namely, at (a) $t = nT_p$; (b) $t = (0.16{+}n)T_p$; (c) $t = (0.38{+}n)T_p$; (d) $t = (0.54 + n)T_p$; and, (e) $t = (0.87 + n)T_p$.

4.6 Chapter Summary

In this chapter, validations of key methodologies for multiphase flow, dynamic mesh, and FSI modeling have been carried out separately before these new models were applied to the complex problems of interest in this research.

A bubbly turbulent flow in a vertical pipe was firstly simulated and then compared with the experimental data to validate the proposed multiphase model. The new multiphase model is based on the original Eulerian model (sometimes referred to the two-fluid model in

the literature) in ANSYS-FLUENT, but includes new interfacial force models implemented through a user-defined function (UDF). The model correctly captured both the "wall peak" observed in the radial distribution of the air volume fraction, and the shift of this "wall peak" towards the towards the core region of the pipe (to give a "core peak") as the volume fraction of air increases. This feature in the simulations is in accordance with experimental measurements and simulation results reported by other researchers. The immiscible model was also tested and was found also to be capable of capturing the features of a flow regime, although the distribution curve was not as smooth as in the results obtained without the immiscible model included, largely due to a lack of clear interfaces.

A turbulent flow over a square cylinder with a prescribed motion was selected as the second benchmark test case. The purpose of this test was to verify the capability and accuracy of the dynamic (or moving) mesh model in ANSYS-FLUENT. Two methods, smoothing and layering, were utilized to generate the dynamic mesh in order to compare with experimental results. Both methods had good performance on mesh quality. The predicted shedding of the Karman vortex street behind the cylinder and the "lock-in" phenomena over a small range of reduced velocities agrees well with the experimental results. The layering method was found to give a higher computational efficiency than the smoothing method for the dynamic mesh generation.

Validations of the FSI model were more complicated as models for FSI depend strongly on a problem's physical features: namely, whether the fluid-structure interaction is weakly-coupling or strongly-coupling. To model a weak-coupling FSI problem, a turbulent flow over a square cylinder autonomously oscillating in the flows' normal direction was conducted as a validation case. In this case, the vortex-induced vibration (VIV) occurring to the square cylinder is a classic weak-coupling FSI problem. A UDF was created to simulate FSI through a dynamic mesh. The purpose of this test was to verify the capability and accuracy of the FSI method based on the dynamic mesh model in ANSYS-FLUENT. A layering method was adopted to generate the dynamic mesh. The predicted shedding of the Karman vortex street behind the cylinder and the "lock-in" phenomena over a small range of reduced velocities agrees well with the experimental results.

Finally, validation of the strong-coupling FSI component of the integrated modeling system was undertaken using as a benchmark test case that of a laminar flow in a heart valve. This heart valve is modeled as a freely rotating leaflet controlled by the periodic variations of the unsteady inlet velocity. A new implicit solution method was proposed and implemented for this problem using a command file (written in Scheme) within ANSYS-FLUENT in order to solve this large-displacement problem. Simulation results indicate that the periodic motion of the leaflet was predicted fairly accurately even though frictional forces were ignored. The resulting implicit FSI model demonstrates the capability of the present modeling tool to solve strongly coupled FSI problems similar to the simulation of a dynamic valve, where a vibration model will be required to determine the displacement of the poppet valve.

The validation work in this chapter indicates that the model components developed in Chapter 3 feature are feasible for the simulation of complex multiphase flows involving fluid-structure interaction, and that these components individually provide predictions with reasonable accuracy. This validation effort provides a sound basis for applications of the proposed integrated modeling scheme to practical problems of interest to the automotive industry.

Chapter 5

Application Case I: Coolant Degassing Process in a Surge Tank

This chapter presents an application of the proposed integrated modeling procedure to the coolant degassing problem. Details of modeling this multiphase flow are introduced in this chapter. Based on requirements from the automotive industry[1], qualitative conclusions from a parametric study of the degas rate (based on the simulations conducted) are analyzed and summarized, providing an important reference for the design of coolant surge tanks.

5.1 Simulation Plan

A pressurized coolant surge tank is used to separate gas bubbles generated within the engine water jacket during the main coolant flow. This process recovers coolant performance and

[1]This chapter is based on the research work done on an NSERC Engage project entitled "CFD Modeling of Surge Tank Degassing Process" in collaboration with ABC Group Tech Center in Toronto.

protects the pump from cavitation. The gas/liquid separation process, referred to as degas, is affected by many factors, such as the tank's internal structure, the flow conditions (e.g., velocity, coolant physical properties, etc.), and most importantly the bubbly flow characteristics (e.g., gas volume fraction). A deep understanding of this process is greatly required by certain entities in the automotive industry, such as ABC Group, who is a major supplier of surge tanks. Therefore, the main objective of this research is to investigate the underlying transport mechanisms of bubbly flow within a surge tank, and to correlate the degas performance to some parameters, which can provide valuable insights for future surge tank designs.

Modeling this problem involves multiple challenges. Firstly, the multiphase flow including bubble dynamics is extremely difficult to model, as the physical mechanism is very complicated. Secondly, the numerical methodology is difficult to realize. Although an improved multiphase model is developed and described in the previous chapters, many modeling details still need optimization with consideration of computational effort , the stability of the calculations, etc. Last but not least, no experimental results and very little literature are available as references.

In view of the objectives and challenges above, modeling this problem will be simplified on the basis of geometry and physics. For the geometry, a single chamber and three connected chambers are designed as typical geometries in surge tanks. A structured mesh is used for our simulations for this case in order to achieve better accuracy. The degas rate is proposed as a metric to facilitate analysis and comparison of cases. Calculation of the degas rate requires a high accuracy from the multiphase modeling. Thus, a grid size sensitivity test, time step sensitivity test, and interfacial force effects test are carried out to eliminate effects from these factors. Parametric studies are undertaken on three typical factors of importance to the automotive industry.

5.2 CFD Modeling

5.2.1 Simplifications and Assumptions

Geometry Simplification

Coolant surge tanks have various external geometries. Although they are replaceable, vehicles of different brands or models require different surge tanks. Figure 5.1 shows coolant surge tanks used by Cadillac, Ford, and Kia, respectively. Their internal geometries are also varied and complex. As shown in Figure 1.2, most surge tanks are designed with a multi-chamber structure in order to separate liquid and air in the coolant. Therefore, a chamber is the basic structural unit of a surge tank.

(a) (b) (c)

Figure 5.1: Exteriors of coolant surge tanks for: (a) Cadillac [1]; (b) Ford [2]; and, (c) Kia [3].

In this work, a multiphase flow will be simulated with a focus on accuracy. In view of the computational resource requirements of the multiphase flow model, simulations including parametric tests in a 3D domain containing the whole geometry are beyond the capability of our computers and software license constraint. Thus, a simple 2D geometry representing a single chamber is used in this work.

The dimensions and initial interface position shown in Figure 5.2 were recommended by engineers from the ABC Group who are familiar with surge tank design. An initial

interface between the air and coolant is assumed according to a typical coolant level. The coolant, containing bubbles, flows into the tank from the inlet.

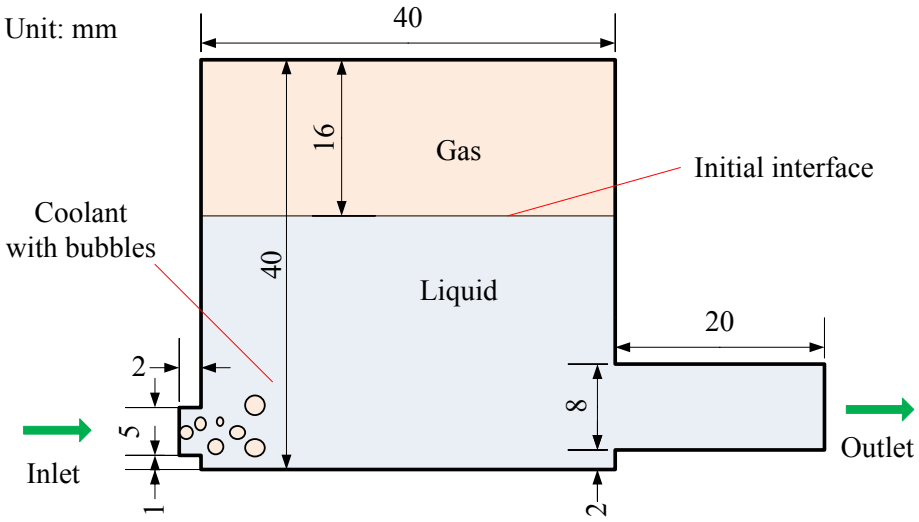

Figure 5.2: Geometry of a single chamber of a surge tank.

In addition, a 2D domain of three connected chambers is simulated to analyze the continuous degas effect in a surge tank. Dimensions are shown in Figure 5.3. The three chambers have the same dimensions except for the inlet and the outlet. Passages connect the chambers, both in the gas region and liquid region. Initial interfaces are also given at the same height as in single chamber cases.

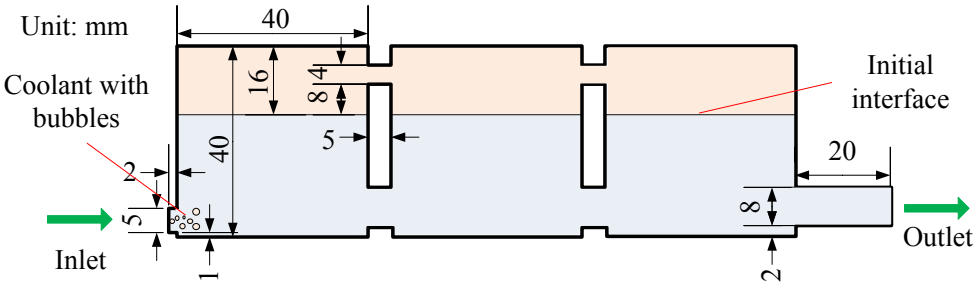

Figure 5.3: Geometry of three connected chambers of a surge tank.

Other Simplifications and Assumptions

Degas in a pressurized surge tank also includes a process of pressure release. The pressure control valve on the top of a surge tank will release gas when pressure is large enough as large amount of gas accumulated. The present work focuses on the process of degas, so the pressure release is not studied. However, variations of the pressure in the gas region during degas could be monitored.

The fluid in the valve is assumed to be a mixture of coolant and air with physical properties at 20 ° as shown in Table 5.1. Here, the properties of the coolant are assumed to be based on common coolants, but not specified by brand and type. The phase transformation between the coolant and its vapor is ignored.

The gas phase is modeled as a compressible fluid, but the liquid phase is assumed to be incompressible.

The surface tension coefficient for the coolant is assumed to be constant.

Table 5.1: Physical properties of coolant and air at 20 °C.

Physical property	Units	Coolant	Air
Density	kg m^{-3}	1064	1.225
Viscosity	Pa s	3×10^{-3}	1.79×10^{-5}
Surface tension	N m^{-1}	6×10^{-2}	—

5.2.2 Boundary Conditions

As the mixture of coolant and air enters through the inlet, the velocity of each phase and the volume fraction of gas are specified as boundary conditions. The outlet is controlled by pressure. For the walls, no-slip conditions are applied for both phases.

5.2.3 Data Monitoring

Degassing is a multifaceted process, as the phase distribution is complex and dynamic. It is very important to identify a parametric variable that reflects the degassing process for comparison with the experimental data.

In this work, the area-averaged velocity and the gas volume fraction at the outlet will be monitored. The volume flow rate difference between the inlet and outlet represents gas that has been degassed. A degas rate is defined as

$$R_d = 1 - \frac{V_{\text{out}}\alpha_{\text{inl},g}A_{\text{out}}}{V_{\text{inl}}\alpha_{\text{out},g}A_{\text{inl}}}, \tag{5.1}$$

where V_{inl} and V_{out} are the area-averaged velocities at the inlet and outlet, $\alpha_{\text{inl},g}$ and $\alpha_{\text{out},g}$ are the area-averaged gas volume fractions at the inlet and outlet, A_{inl} and A_{out} are the cross-sectional areas of the inlet and outlet.

5.2.4 Grid Sensitivity Test

Details of Grid Size

A square mesh is used in the present work because the computational domain is simple and regular. A hierarchy of three numerical grids is constructed as shown in Table 5.2, where the number of grid elements has been increased by a factor of about 4 from one grid hierarchy to the next. Three grid levels with cells numbering 15,930 (grid level 1), 44,250 (grid level 2) and 177,000 (grid level 3) were tested with the same model setup. For all the numerical meshes, the minimum orthogonal quality and maximum aspect ratio are optimal when square meshes are used in the whole domain.

A case with the setup shown in Table 5.3 has been investigated on the established grid hierarchy in order to study the grid sensitivity of the numerical solution; the time step for

each grid level is provided. For comparison, the area-averaged gas volume fraction at the outlet was monitored during the simulations.

Table 5.2: Hierarchy of numerical grids for the grid independence test in simulation of surge tank.

Level	No. of cells	No. of cells in pipe cross-section	No. of cells along the axis	Mesh quality	
				Minimum orthogonal quality	Maximum aspect ratio
1	15,930	3,000	3,000	1	1
2	44,250	5,000	5,000	1	1
3	177,000	10,000	10,000	1	1

Table 5.3: Simulation setup for grid sensitivity test in a surge tank.

Setup	Value	Units
Liquid inlet velocity	1	m s^{-1}
Gas inlet velocity	1	m s^{-1}
Gas volume fraction	0.1	–
Outlet gauge pressure	0	Pa
Time step	10.0 (level 1) 5.0 (level 2) 2.5 (level 3)	μs

Results and Discussion

Contours of the gas volume fraction and stream traces at $t = 1$ s for each of the grid levels are shown in Figure 5.4. The results from the three grid levels are very similar. Due to a high inlet velocity, the main interface between the gas and liquid has migrated from its initial position. A large vortex was formed owing to the strong shear force from

inflow which features a high horizontal velocity acting on stationary fluids in the chamber. Some gas is accordingly dissolved in the coolant. At the higher (finer) grid levels, the main interface is more clearly displayed (viz., more highly resolved), and more details are captured.

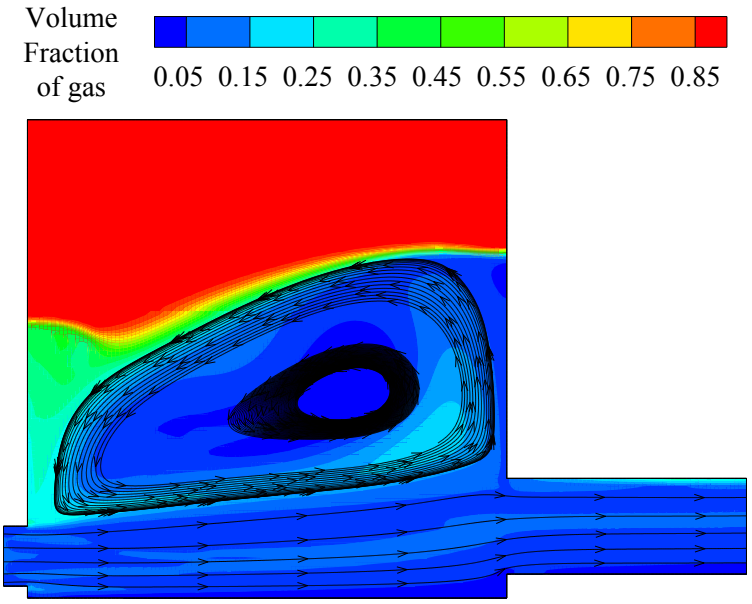

(a)

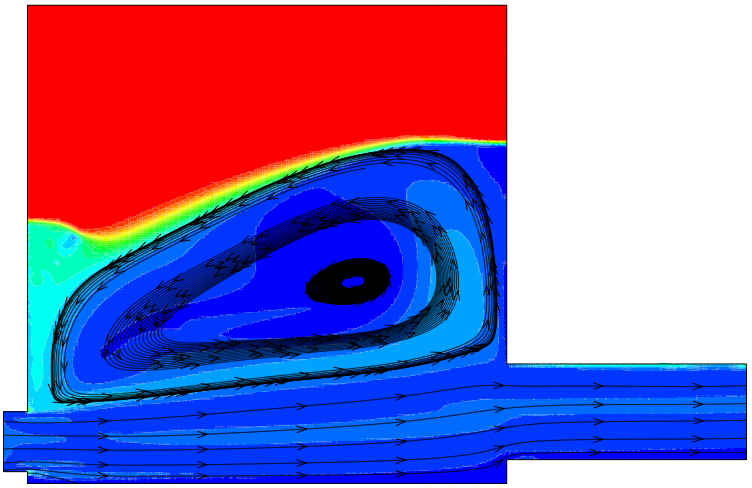

(b)

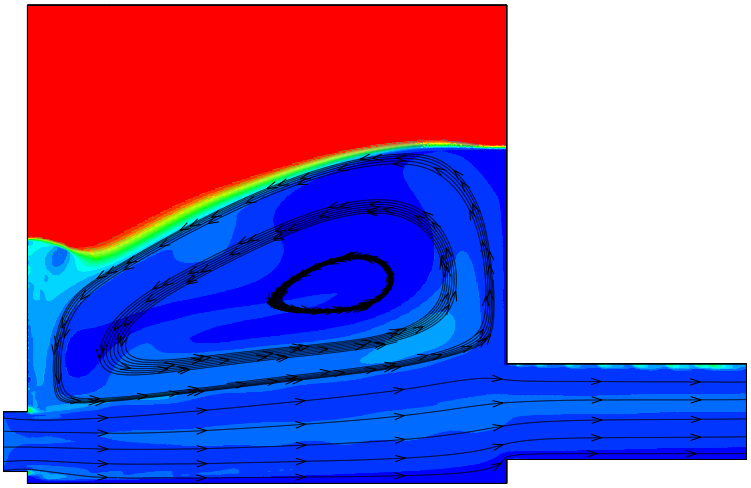

(c)

Figure 5.4: Contours of the gas volume fraction and stream traces at $t = 1$ s for the three cases in the grid sensitivity test: (a) grid level 1; (b) grid level 2; and, (c) grid level 3.

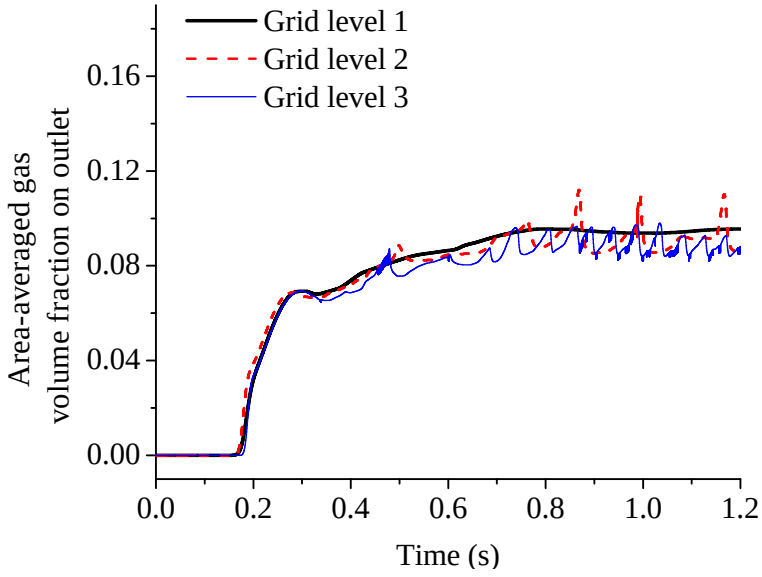

Figure 5.5: Time history of area-averaged gas volume fraction at the outlet for the three different grid levels.

Figure 5.5 shows monitored data for cases from the different grid levels. As the fluid flows through the tank, the area-averaged gas volume fraction at the outlet increases from zero and then approaches an approximately constant level. At the higher grid level, the curve representing volume fraction looks less smooth. In other words, the higher grid level (viz., finer spatial resolution) results in a higher temporal resolution (see Table 5.3) allowing the resolution of fluctuations in the volume fraction. Nevertheless, the general trends in volume fraction variation for the three grid levels are very consistent with each other.

Overall, the results of the simulation exhibited low sensitivity to the grid refinements. For computational efficiency, grid level 1 will be used for the subsequent work.

5.2.5 Time Step Sensitivity Test

Description

A hierarchy of four time step levels is constructed, where the time step is increased by a factor of 10 from one level to the next. The four time step levels—1×10^{-2} s (time step level 1), 1×10^{-3} s (time step level 2), 1×10^{-4} s (time step level 3) and 1×10^{-5} s (time step level 4)—were tested with grid level 1 (from Table 5.2) and the model setup.

The time step test case was setup differently from the benchmark setup as shown in Table 5.3. To test across a larger range of time steps, the inlet velocity was set to 0.5 m s^{-1} instead of 1.0 m s^{-1}. Other setup parameters were the same as in the grid sensitivity test. This case was conducted over a hierarchy of time steps in order to study the time-step sensitivity of the numerical solution. For comparison, the area-averaged gas volume fraction at the outlet was monitored during simulation.

Results and Discussion

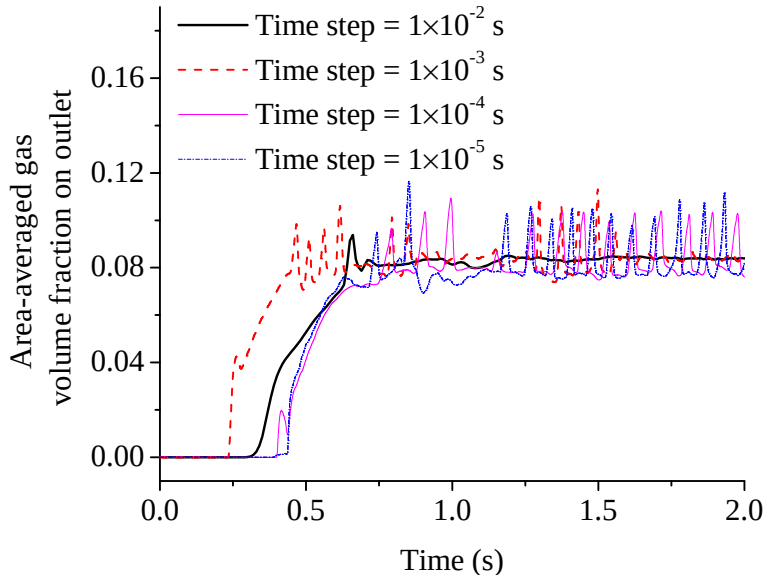

Figure 5.6: Time history of area-averaged gas volume fraction at the outlet under different time step levels.

Figure 5.6 shows the area-averaged gas volume fraction at the outlet for the four time step levels. The traces show the same trend, rising from zero and then reaching a quasi-steady value.

Of primary concern in this case is the degas rate, which is determined from a time average of the outlet gas volume fraction during the time interval in which this quantity has reached its quasi-steady value. Based on this consideration, a time-averaged outlet gas volume fraction for each time step level is calculated for the interval from $t = 1.5$ to 2.0 s. The results are shown in Table 5.4. Here, the coefficient of variation is defined as:

$$C_{\text{var}} = \frac{\sqrt{\sum_{i=1}^{n} \left(S_i - \overline{S}\right)^2}}{n \cdot \overline{S}}, \tag{5.2}$$

where S_i is a sample value, $i = 0, 1, 2\ldots$ is the sample index, n is the number of samples. The coefficient of variation is a measure of the dispersion of the samples. In this case, the coefficient of variation is only 1.47 % for the four sample values of the time-averaged gas volume fraction shown in Table 5.4. Although the data for each time step level exhibit different fluctuation levels, there is very little difference in the time-averaged value outlet gas volume fraction for each of the four cases.

Table 5.4: Results of time-averaged outlet gas volume fraction for all time step levels.

Hierarchy	Value
Time step level 1	0.0841
Time step level 2	0.0838
Time step level 3	0.0840
Time step level 4	0.0826
Coefficient of variation	1.47 %

At the higher time step levels (with greater temporal resolution), more details were captured naturally. Also, the higher time step levels facilitate a more robust and stable calculation. However, using a small time step incurs a greater computation cost. In consideration of these factors, a time step level 2 is used in the subsequent work.

5.3 Flow in a Single Chamber

5.3.1 Effect of Interfacial Forces

Drag Force Model Tests

Drag is the force most commonly included in the modeling of multiphase flows. This force always acts in a direction opposite to that of the relative motion. Its effect is to weaken the

relative motion between the bubble and the liquid. The drag force is especially important to the degassing process.

The definition of the drag force in a liquid–gas flow was introduced in Section 3.2.2. Recent research on the drag force focuses on modeling the drag coefficient. There exist many models for the drag coefficient in a multiphase flow. An appropriate drag coefficient model should be chosen based on the materials involved, the flow regime, and the Reynolds number. Here, we will study the effect of different drag coefficient models on the predictions.

Three drag coefficient models are tested here: the Universal Drag Law, the Schiller–Naumann drag model, and the symmetric drag model. As described in Section 3.2.2, the universal drag laws are suitable for the calculation of the drag coefficients in a variety of gas–liquid flow regimes.

The Schiller–Naumann model, which was proposed originally in 1935 [51], is acceptable for general use for all fluid–fluid pairs of phases. The drag coefficient in the Schiller–Naumann model is defined as

$$C_D = \begin{cases} \frac{24\left(1+0.15\mathrm{Re}^{0.687}\right)}{\mathrm{Re}}, & \mathrm{Re} \leq 1000 \\ 0.44, & \mathrm{Re} > 1000 \end{cases}. \tag{5.3}$$

The symmetric model averages the drag effect from liquid to gas and from gas to liquid. In this model, the drag coefficient has the same definition as in the Schiller–Naumann model. However the formula for the drag force is modified as follows:

$$\mathbf{F}_{D,l} = -\mathbf{F}_{D,g} = -\frac{3}{4} C_D \frac{\alpha_g \rho_m}{d_m} \left|\mathbf{v}_l - \mathbf{v}_g\right| (\mathbf{v}_l - \mathbf{v}_g). \tag{5.4}$$

where and are calculated from

$$\rho_m = \alpha_l \rho_l + \alpha_g \rho_g, \tag{5.5}$$

$$d_m = \frac{1}{2}(d_l + d_g). \tag{5.6}$$

With only the drag force enabled as interfacial forces in this test, the effect of the

different drag force models on the predictions can be clearly seen. The other relevant parameters in the simulations are the same as in the time step test. The results are shown in Figure 5.7. Based on averaging the gas volume fraction over time interval of 2–4 s, the time-averaged gas volume fraction at the outlet for the three drag force models were found to be 0.0532, 0.0513 and 0.0839, respectively. Similar results were obtained using the Universal Drag Law and Schiller–Naumann drag model. However, the symmetric drag model predicted a higher gas volume fraction due to the averaging of the drag force between the liquid and gas phases. In the degassing process, the drag force from the liquid phase helps gas to escape from the liquid before flowing to the outlet. In bubbly flow, the drag force acts from the liquid to the gas phase, which implies that the velocity of the gas is slowed down by the liquid phase. However, because the drag force from the liquid to the gas is weakened by the averaging process, more bubbles flowing to the outlet increase the gas volume fraction there. In consequence, the symmetric drag model is not reasonable for the simulation of the degassing process. From these results, we choose the Universal Drag Law for the subsequent simulations.

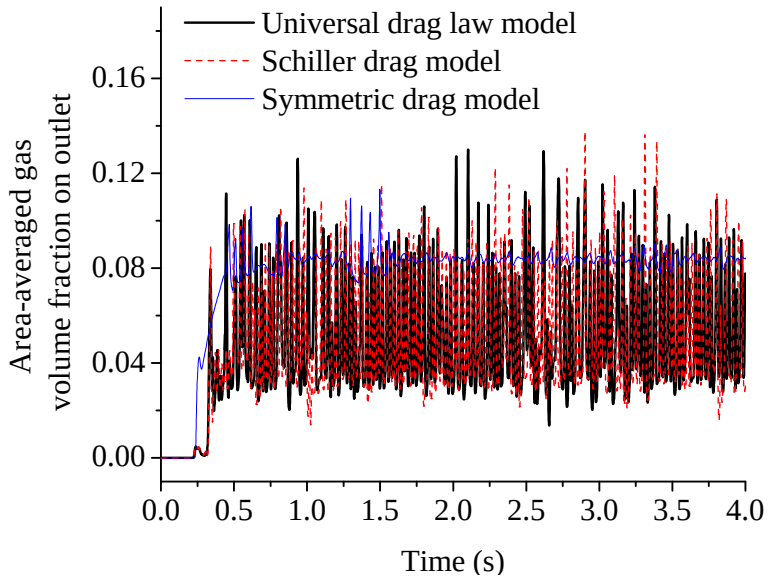

Figure 5.7: Drag force models comparison.

Lift Force Model Tests

The component of the net pressure acting perpendicular to the relative velocity is modeled as the lift force. Its direction is always perpendicular to the curl of the continuum velocity field. As discussed in Section 3.2.3, researchers are in agreement as to the correct form for the lift force, but there have been many proposals for models for the lift coefficient.

Both the drag force and the lift force are considered essential interfacial forces. Selection of the lift coefficient model could seriously influence the results obtained from the numerical simulation. Hence, it is very important to test different lift coefficient models. Three lift coefficient models are tested here and compared with a no-lift case. Setting the lift coefficient to 0.5 is the crudest method for simulation of the lift force. The Tomiyama model [76] (described in Section 3.2.3) is applicable to the lift force for larger-scale deformable bubbles in the ellipsoidal and spherical cap regimes. The Legendre–Magnaudet model [67] is applicable primarily to small-diameter spherical fluid particles, though it can be applied to non-distorted liquid drops and bubbles. In the Legendre–Magnaudet model, the lift coefficient is given by

$$C_L = \sqrt{\left(C_{L,\mathrm{lowRe}}\right)^2 + \left(C_{L,\mathrm{highRe}}\right)^2}, \tag{5.7}$$

where $C_{L,\mathrm{lowRe}}$ and $C_{L,\mathrm{highRe}}$ are defined as

$$C_{L,\mathrm{lowRe}} = \frac{6}{\pi^2}\left(\mathrm{Re}_b \mathrm{Sr}\right)^{-0.5} \frac{2.55}{\left(1 + 0.2\frac{\mathrm{Re}_b}{\mathrm{Sr}}\right)^{1.5}}, \tag{5.8}$$

$$C_{L,\mathrm{highRe}} = \frac{1 + 16\mathrm{Re}_b^{-1}}{2\left(1 + 29\mathrm{Re}_b^{-1}\right)}. \tag{5.9}$$

Re_b is the bubble Reynolds number which is defined in Equation (3.22). Sr is the ratio of the vorticity Reynolds number and the bubble Reynolds number, which are defined as:

$$\mathrm{Sr} = \frac{\mathrm{Re}_\omega}{\mathrm{Re}_b}, \tag{5.10}$$

$$\mathrm{Re}_\omega = \frac{\rho_l \left|\nabla \times \mathbf{v}_l\right| d_g^2}{\mu_l}. \tag{5.11}$$

The results of the simulations are shown in Figure 5.8. The averaged gas volume fraction at the outlet for 1 s < t < 3 s for the four models are: 0.411401, 0.393852, 0.392769 and 0.399248. All the cases, including the no-lift case, gave similar results, which implies that the lift force is not very important. The main direction of two phases' motion as well as their relative motion is horizontal from inlet to outlet, especially in the region near to the inlet. Therefore, the direction of the lift force is vertical (perpendicular to the relative motion) according to its definition. However, in the vertical direction, the buoyancy force which is much larger than the lift force strongly dominates bubbles' motion and the degas rate.

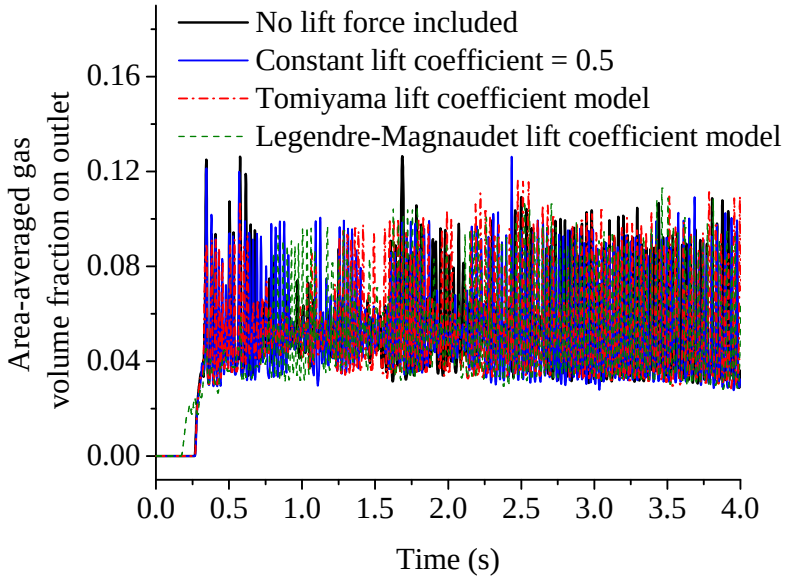

Figure 5.8: Lift coefficient models comparison.

5.3.2 Parametric Analysis

This section will focus on flow analysis in a single chamber, as well as the effect of input parameters.

The parametric test conducted herein is very important to revealing how the degassing process is affected. From this information, conclusions obtained can be easily extended to other different working conditions.

Factor 1: Inlet Velocity

Coolant is normally pumped into the system at such a rate so as to attain a specific circulation speed needed for a particular task. The inlet velocity should be considered as an important parameter to the degassing process.

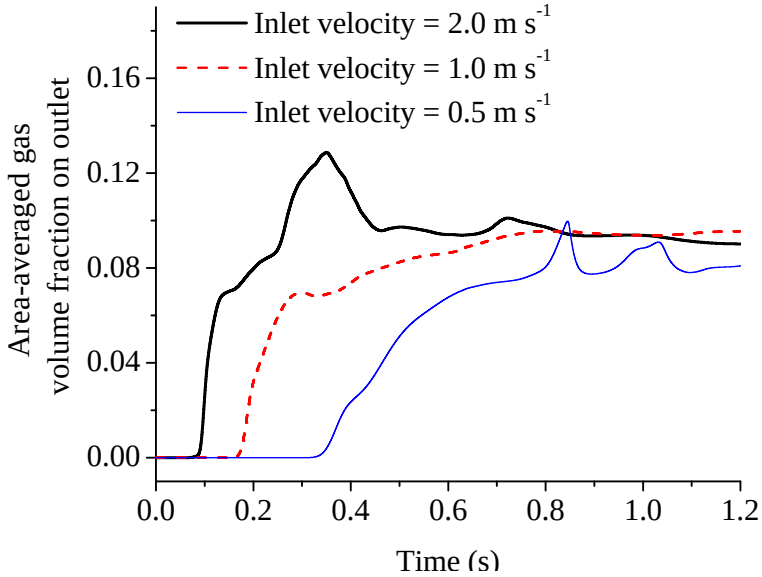

Figure 5.9: Effect of inlet velocity on the area-averaged volume fraction at the outlet.

Three cases with inlet velocities of 2.0 m s^{-1}, 1.0 m s^{-1} and 0.5 m s^{-1} were tested, and results are shown in Figure 5.9. With the higher inlet velocity, bubbles appear at the outlet sooner as compared with cases at the lower inlet velocity. During the period 0.6 s $<$ t $<$ 1.2 s, the average volume fraction is larger when the inlet velocity is larger. When the velocity is large, bubbles are easily dissolved in the liquid downstream, which in turn

implies that the degas rate will be lower. Further analysis based on more results will be discussed in Section 5.4.3.

Factor 2: Bubble Size

A bubble diameter test is helpful for optimizing the structure of the surge tanks. Three cases with bubble diameters of 0.0001 m, 0.0005 m and 0.0025 m were tested. Generally speaking, small bubbles tend to be carried by the liquid, resulting in a lower degas rate. On the other hand, larger bubbles bearing higher drag (opposite direction to the outlet) are easily degassed.

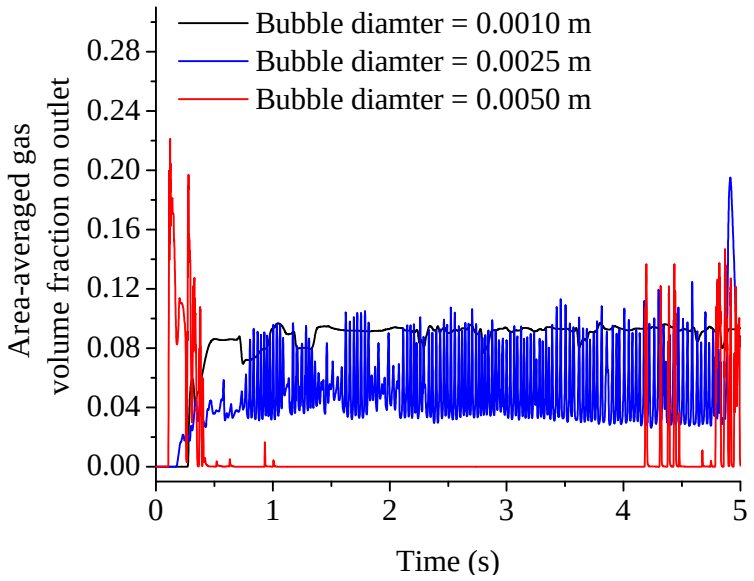

Figure 5.10: Effect of bubble diameter on the area-averaged volume fraction at the outlet.

The results shown in Figure 5.10 are consistent with the above reasoning. During the period 3 s $<$ t $<$ 5 s, the average gas volume fractions at the outlet for three cases were 0.0922, 0.0553 and 0.00957 for the bubble diameters of 0.0001 m, 0.0005 m and 0.0025m, respectively The case with the largest bubble diameter exhibits the largest degas rate.

Meanwhile, larger-diameter bubbles yield greater outlet volume fraction fluctuations, indicating that the bubbles generally exhibit a large diameter throughout the outlet. Therefore, the case with large bubble diameter will exhibit a larger degas rate if a liquid–gas mixture flows through the multiple chambers.

Factor 3: Coolant Viscosity

In operating cooling system, the coolant experiences a very large temperature variation. This leads to coolant viscosity also varies in large range. A liquid viscosity test was also conducted in order to determine how the degas rate is affected by this material property.

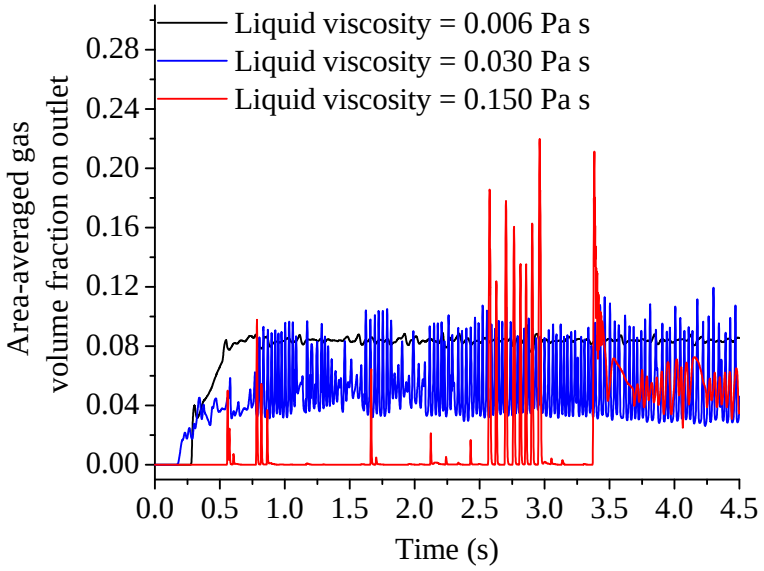

Figure 5.11: Effect of coolant viscosity on the area-averaged volume fraction at the outlet.

The results in Figure 5.11 show that a higher viscosity induces a lower degas rate. The reason is that a liquid with a larger viscosity retains more bubbles and is therefore difficult to degas. In consequence, a coolant with smaller viscosity is more effective for degassing, as the coolant system will exhibit generally a better degassing performance.

Under certain conditions (e.g., longer working time), a coolant loses its effectiveness as its viscosity increases.

5.4 Flow in Three Connected Chambers

5.4.1 Geometry

Multiple chambers are used in a surge tank in order to degas bubbles from stage to stage. To analyze this process, we simulate the flow through a geometry consisting three connected chambers (Figure 5.3).

5.4.2 Variation of Gas Volume Fraction at Outlet

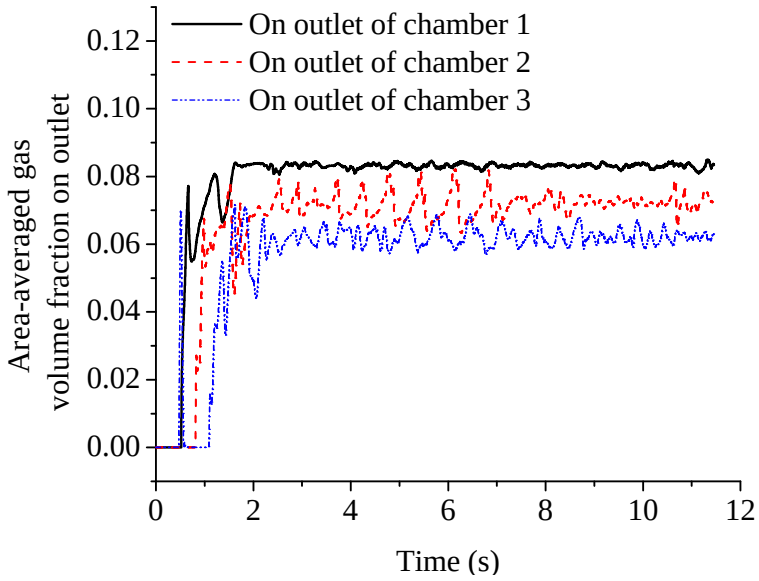

Figure 5.12: Result of flow in three connected chambers with an inlet velocity 0.5 m s^{-1}.

Figure 5.12 shows the area-averaged gas volume fraction at the outlet of each stage of the surge tank for an inlet velocity of 0.5 m s^{-1}. Clearly the area-averaged gas volume fraction decreases from one stage to next stage in the surge tank. The time-averaged (3–12 s) degas rate is 15.3 % for the first chamber, 12.9 % for the second chamber, and 13.7 % for the third chamber.

5.4.3 Inlet Velocity Test

Figure 5.13 shows the area-averaged gas volume fraction at the outlet of each stage of the surge tank for an inlet velocity of 1.0 m s^{-1}. Here, the time-averaged (3–12 s) degas rate is 8.2 % for the first chamber, 6.8 % for the second chamber, and 5.8 % for the third chamber.

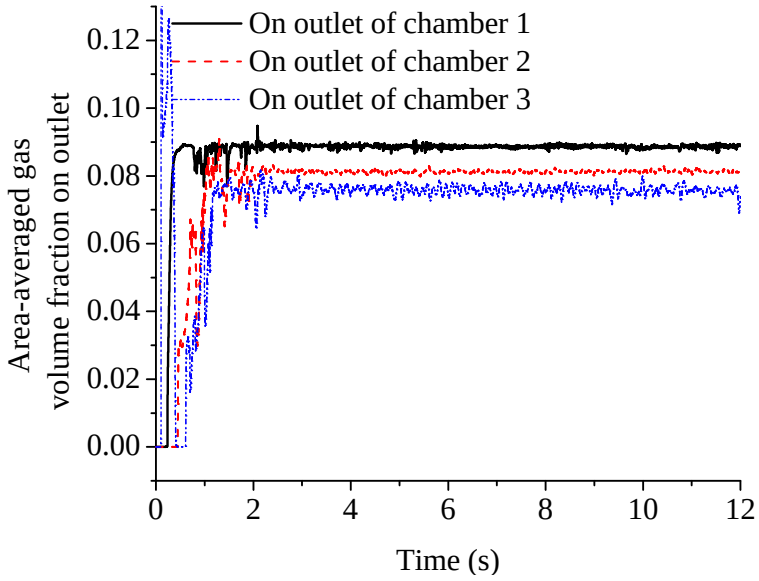

Figure 5.13: Result of flow in three connected chambers in a surge with inlet velocity 1.0 m s^{-1}.

Compare the two cases, a total time-averaged degas rate is 42.0 % for the case with an inlet velocity 0.5 m s^{-1}, 20.8 % for the case with an inlet velocity 1.0 m s^{-1}. This is

consistent with the conclusion in cases for a single chamber that low inlet velocity is helpful to degas.

The variation of the degas rate among chambers is much more complicated. The result for the case with an inlet velocity of 1.0 m s^{-1} indicates that the lower the gas volume fraction, the lower is the degas rate. However, in case with an inlet velocity of 0.5 m s^{-1}, the degas rate of the chamber 3 whose gas inlet volume fraction is the lowest in the three chambers is even higher than the chamber 2. This result indicates that the factors affecting the degas rate also interact to each other. In the case with 0.5 m s^{-1}, the lower velocity is helpful to form larger bubbles and than increase the degas rate. Therefore, the degas rate of the chamber 3 is higher than the chamber 2 as the factor of inlet gas volume fraction dominates the result. In Figures 5.12 and 5.13, fluctuations of the gas volume fraction from chamber 1 to chamber 3 becomes more and more "'violent". This phenomenon was a result of gas concentrating which indicates larger bubbles formed owing to bubbles coalescence.

In consequence, incorporation of a vertical structure which is helpful to bubbles coalescence and floating is very important to facilitate the degassing, as bubbles get more of a chance to move upward instead of laterally towards the outlet.

5.5 Chapter Summary

A refined and validated multiphase model was applied to the simulation of the degassing problem in a coolant surge tank. Grid sensitivity and time step sensitivity were tested to optimize the parameters to use for simulation of this problem. The drag force is very important for simulation of the interaction between the two phases. Bubbles are degassed stage by stage in a surge tank due to the buoyancy effect. Degassing is important in preventing a liquid–gas flow downstream. The degassing rate is a dynamic variable related to many elements, such as the inlet velocity, the liquid viscosity, and the bubble size. A larger inlet velocity, a lower gas volume fraction, a greater liquid viscosity, and a smaller

bubble size all lead to a lower degas rate. Meanwhile, owing to the complication of bubble dynamics(coalescence and/or breakup) interactions among these factors also affect the degas rate depending on which factor is dominant.

The CFD model used in the current study provides good results for the simulation of the degassing process in a surge tank. In future work, this physical problem could be extended to a real situation existing in operating vehicles. The motion of a vehicle should be considered and factored into the simulation of the degassing process. Meanwhile, more interfacial forces should be added into the current multiphase flow model in order to obtain a more accurate result.

Chapter 6

Application Case II: Multiphase Flow Induced Noise and Vibration Problem in a Dynamic Valve

In this chapter, a complex multiphase FSI problem is solved using new models. Specifically, the vibration and noise problem in a dynamic valve is modeled and solved in FLUENT. Together, this clarification of the mechanism underlying the vibration and noise generation and the conclusions from parametric tests should help the automotive industry to eliminate or reduce this problem.

6.1 Simulation Plan

The noise arising from operation of a dynamic valve in the fuel system is a critical issue contributing to the overall noise, vibration and harshness (NVH) in vehicle performance. Thus, understanding the various phenomena associated with this problem and ways to

eliminate or reduce it are of enormous interest within the automotive industry. Automotive engineers always want the various dynamic components (e.g., dynamic valves) within a vehicle to operate stably so as to reduce the NVH in vehicle performance. Consequently, dynamic valves should be designed so as to avoid the presence of multiphase flow in their routine operation. Otherwise, the formation of bubbles in the flow through the valve can easily induce cavitation, which is known to be very harmful to its stable operation. However, it may not be possible to remove multiphase flows in a dynamic valve altogether because operating fluids such as gasoline and various coolants are volatile. Moreover, air has the tendency to dissolve into these fluids as they are mixed together during normal vehicle operation.

An observed phenomenon within the automotive industry is that vibration exists generally in a dynamic valve involving necessarily a liquid–gas flow. This classical problem in automotive engineering has received enormous attention as the noise from vibrating valves disturbs the quiet expected from the operation of hybrid vehicles when the engine is disengaged. Experiments have shown that this noise disappears if the multiphase flow through the dynamic valve is replaced by a single-phase flow. However, the complex relationship between the vibration in the valve and the nature of the liquid–gas flow through the valve is not yet understood. Moreover, experimental studies undertaken to address this problem are constrained by the small dimension of the valve. In view of these difficulties, numerical studies employing computational fluid dynamics (CFD) may be usefully applied to provide some deeper understanding of this problem.

Simulation of the noise problem in a dynamic valve necessarily involves two main components: (1) simulation of the liquid–gas flow through the valve and (2) consideration of the fluid–structure interaction (FSI) between the valve and the fluid flowing through the valve. In consequence of the complexity, the simulation of this multiphase flow problem is very computationally expensive. Indeed, the solution of the FSI component requires the application (coupling) of a number of different software components. The most attractive computational solution to the noise problem in a dynamic valve would be the development of a capability to simulate the entire problem within a single software plat-

form. Unfortunately, this comprehensive software platform does not exist as yet, requiring at present the innovative coupling of a number of different (disparate) software components to obtain a solution. To simplify the problem, this current analysis ignores the deformation of the valve structure as it is not critical for analyzing the noise. To this purpose, a two-dimensional axi-symmetric numerical model has been developed within the ANSYS-FLUENT framework to simulate the complex phenomenology associated with noise generation in a dynamic valve. This undertaking required the development and use of a user-defined function (UDF) to couple the multiphase flow model with the dynamic mesh, resulting in an innovative non-standard application of ANSYS-FLUENT.

As introduced above, flow in a dynamic valve is a multiphase FSI problem which is extremely hard to model and computationally expensive to solve. In addition, both multiphase model and FSI model can easily diverge. To overcome these weaknesses, two points must be given sufficient attention: improving the computational efficiency and keeping the model stability. Towards this objective, the geometry, physical properties, and models have been simplified. Details are shown in Section 6.2.2.

For the multiphase model, an immiscible model will be enabled based on its physical material properties. Because of this model's clear interfaces between the phases, the effect of multiphase flow is reflected more clearly than it would be through averaging. Gas distribution and migration are not key points requiring simulation. Therefore, only drag force is considered. This approach also saves computational resources.

A structured mesh and layering method is adopted to generate the dynamic mesh in view of its high accuracy and speed of operation. However, the structured mesh cannot fit the complex geometry of a dynamic valve, so an unstructured mesh is combined with the structured mesh to generate a grid for this complex shape (shown in Figures 6.1 and 6.2).

For the FSI model, the implicit method is more accurate than the explicit method but, as a result of the small time steps required by the multiphase flow in this problem, it is also more computationally expensive. Hence, the explicit method is the first choice unless it is not suitable for this problem.

The simulation is undertaken from a single phase flow to a multiphase flow, and from a single bubble to multiple bubbles step by step.

6.2 CFD Model

6.2.1 Physical Problem

The dynamic valve considered in current study is unique as the gap is controlled automatically by the flow condition and the spring of the valve. The structure of this valve is shown in Figure 1.5. The poppet is a movable component with a spring that presses it onto the valve seat. The fluid flowing through the valve exerts an upward pressure on the poppet seal. The gap size is determined by the position of the poppet, which is controlled by the balance between the pressure and the spring force. Obviously, the flow field in a dynamic valve is unsteady owing to the dynamic motion of the poppet. Moreover, when a liquid–gas (or, two-phase) flow is involved, the liquid–gas flow interacting with the poppet can potentially generate more pressure fluctuations. As a result, noise can be generated from the dynamic valve operation and propagate subsequently into the cabin of the vehicle.

This problem has never been carefully researched before, but was first encountered by the automotive industry during the development of hybrid vehicles. A whistle noise problem that was audible in certain hybrid vehicles was confirmed by automotive engineers at the Ford Motor Company to be associated with the noise generated by a dynamic valve in the fuel system [28].

Generally, the dynamic valve works over a temperature range from -10 °C to 60 °C. As shown in Figure 1.5, the inlet diameter is 4.90×10^{-3} m and the maximum diameter of this valve is 1.25×10^{-2} m. For this small-sized valve with its restrictive geometry, it is extremely difficult to observe the complex flow field through the valve using an experimental methodology. The fluid in this valve is a mixture of diesel and air or diesel vapor.

Depending on the operation of the vehicle, the volume flow rate for the inlet can vary from 6.94 $m^3\ s^{-1}$ to 36.11 $m^3\ s^{-1}$ (which is equivalent to an inlet velocity of 0.37 m s^{-1} to 1.91 m s^{-1} [28]).

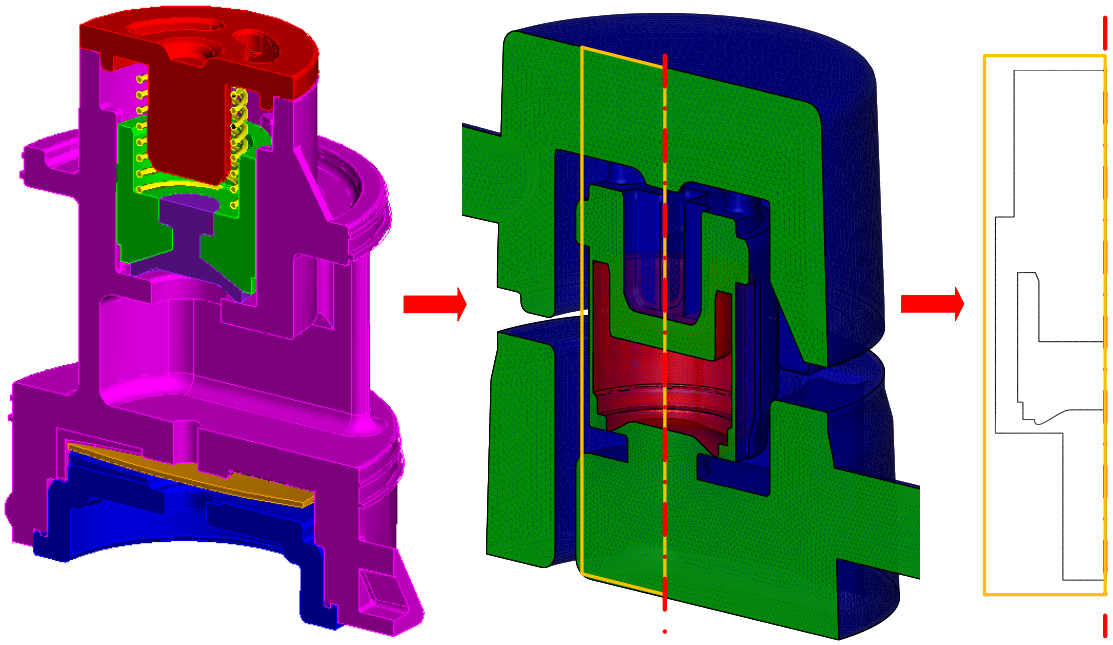

Figure 6.1: Geometry of the dynamic valve.

It has been found by Ford automotive engineers that the noise from the dynamic valve shown in Figure 6.1 persists for 5 to 90 seconds and is associated with a certain frequency range. This noise was found to mainly occur when idling after the vehicle has been parked for an extended period of time (e.g., overnight), but has also been found to occur when the vehicle is driven or when the vehicle is performing at high engine speeds when idling. However, the noise observed in this valve does not appear to be reproducible [28]. In laboratory experiments conducted by Ford engineers on this dynamic valve, it was found that no noise was generated by the dynamic valve when only a liquid flow through the valve was involved.

6.2.2 Simplifications and Assumptions

Noise generation in a dynamic valve is very complex owing to the varying flow conditions, the movable structural components that comprise the valve and the multiphase flow through valve. There may be multiple sources for the noise generation in the valve. If the noise is induced by flow through the valve, then the primary cause would be from the pressure fluctuations in the fluid. The fluctuating pressure due to the varying operating conditions of the vehicle can result in a vibration of the poppet. Generally, this vibration is expected to be slow and associated with a low frequency in the noise spectrum. However, if the liquid–gas flow is involved directly in the noise generation, the vibration is expected to occur at a high frequency in the noise spectrum. Cavitation is also a common source of noise. Given the complexity of the problem and to ensure a high computational efficiency in the simulation, the following simplifications and assumptions have been made in the development of the numerical model.

In order to improve the computational efficiency for our complex multiphase fluid flow problem with fluid–structure interaction, we simplified the problem by focusing only on a two-dimensional axi-symmetric model. The geometry has been simplified to a straight pipe inlet and outlet with an extension to their actual lengths. The volume that the spring and the outlet cap occupies has been ignored. The geometries of the valve before and after the simplifications are shown in Figure 6.1. Note that in reality the *instantaneous* distribution of bubbles will not have a ring-like shape as implied by the use of an axi-symmetric model. In our simulations, we do not deal with the instantaneous distribution of bubbles, but rather we interpret the ring-like shape distribution of bubbles here to be simply an ensemble average of the instantaneous distribution of spherical bubbles in the angular direction.

The fluid in the valve is assumed to be a mixture of diesel and air (whose physical properties at 20 °C are shown in Table 6.1) and we have ignored the phase transformations between the diesel and its vapor. Cavitation has not been modeled in the problem, as it has never been observed to occur in our situation.

The gas phase is modeled as a compressible fluid, but the liquid is assumed to be incompressible.

The surface tension coefficient of the liquid is assumed to be a constant.

Table 6.1: Physical properties of diesel and air at 20 °C.

Physical property	Unit	Diesel	Air
Density	kg m^{-3}	852.3	1.225
Viscosity	Pa s	3.98×10^{-3}	1.79×10^{-5}
Surface tension	N m^{-1}	2.639×10^{-2}	–

6.2.3 CFD Model Details

A detailed multiphase flow model has been developed with the purpose of describing the interaction between the two fluid phases more completely. In FLUENT, an Eulerian model [4] is used in the present work. This model is based on an Euler–Euler approach which is generally considered to be the most accurate and complete model for multiphase flows. For each phase, an exclusive set of continuity and momentum transport equations is solved. The interaction between the two phases is modeled using interfacial forces. At the same time, an immiscible fluid model (VOF model) that is consistent with the physical problem is used to ensure that there is clear-cut interface between the two phases (liquid and gas) of the fluid. Setup details are shown in Table 6.2.

Dynamic Mesh

A structured mesh generally has a high mesh quality, but unfortunately this type of mesh is much less flexible for the representation of complex geometry than an unstructured mesh. In present work, a structured mesh is used to represent the valve in most parts of the domain, with a small portion of the domain gridded using an unstructured mesh in order

Table 6.2: Simulation setup details of the multiphase FSI model application in a dynamic valve.

Setup	Details
Mesh	No. of cells: 20,248; mesh type: quadrilateral and triangle, unstructured and structured; minimum orthogonal quality: 0.80; maximum aspect ratio: 5.09
Boundary conditions	Inlet: velocity inlet for air and bubble, volume fraction of air; outlet: pressure outlet (0 Pa); wall: no-slip condition for water and for gas; axi-symmetric: flow on angular direction is not modeled
Turbulence model	SST $k-\omega$ model; mixture
Time step	5×10^{-7} s

to better represent the irregular shapes in the valve. The mesh consists of 20,248 cells and is shown in Figure 6.2.

The motion of the poppet in the computational domain is represented using a dynamic (or, dynamically evolving) mesh. This allows the boundaries of the poppet to move when it is driven (moved) by the fluid. As a result, a new solution is calculated after the (dynamic) mesh has been updated at the beginning of the computational time step.

A layering method [4] is used in the application of the dynamic mesh. A ratio-based model with 0.5 set for both the split factor and the collapse factor is used in the present work.

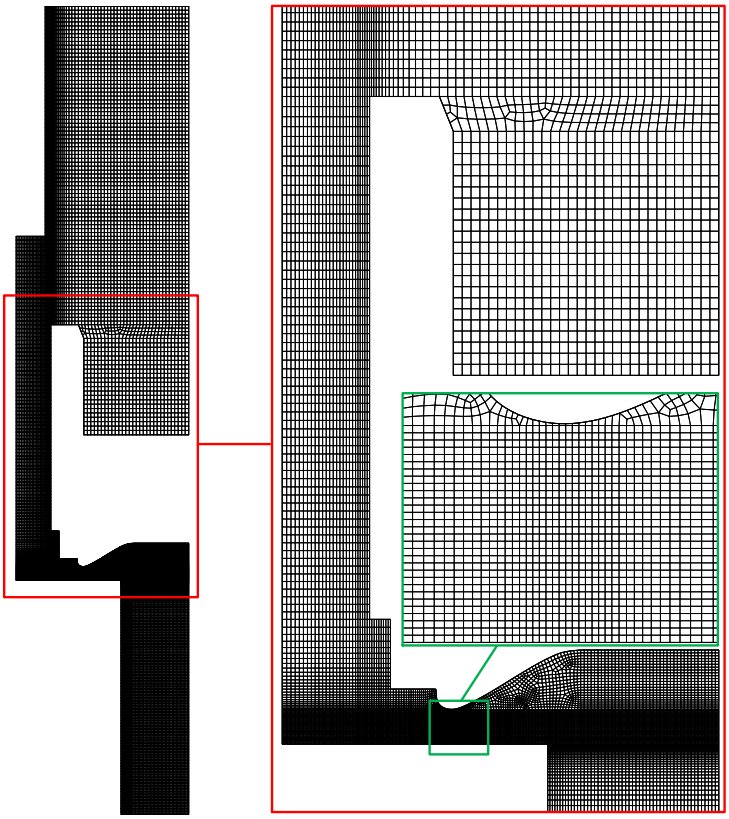

Figure 6.2: Mesh used to represent the two-dimensional axi-symmetric dynamic valve model.

Force Balance

Forces acting on the poppet include the gravitational force, the spring force $\mathbf{F}_s$ and the force exerted on the spring by the liquid. The gravitational force is a constant and can be calculated from a knowledge of the mass of the spring and poppet. In the current simulations, the mass of the spring and poppet is 5×10^{-3} kg. The spring force $\mathbf{F}_s$ is calculated from Hooke's law given by

$$\mathbf{F}_s = k_s \mathbf{x}, \tag{6.1}$$

where k_s is the spring stiffness (taken to be 600 N m^{-1} here), and $\mathbf{x}$ is the (vector) displacement of the spring from its relaxed position. The direction of $\mathbf{x}$ is opposite the positive direction of the y axis in our case because the spring is always compressed. The force from the liquid on the poppet can be divided into a viscous force and a pressure force contribution, depending on the poppet lift. The viscous force is very small owing to the fact that the viscosity of diesel is only 3.98×10^{-3} Pa s (at 20 °C). Taken together, the viscous and pressure forces can be interpreted as a drag force on the poppet. In accordance to Newton's second law of motion, the force balance on the poppet is given by the following relationship:

$$c\mathbf{v} + m\mathbf{a} = \mathbf{F}_f + m\mathbf{g} + \mathbf{F}_s, \tag{6.2}$$

where c is the structural damping coefficient, $\mathbf{v}$ is the poppet velocity, $\mathbf{a}$ is the poppet acceleration, $\mathbf{F}_f$ is the force exerted by the fluid (which includes the buoyancy, pressure and viscosity forces) on the poppet and $\mathbf{g}$ is the acceleration due to gravity (whose magnitude is 9.81 m s^{-2}). In this study, the structural damping is ignored. Therefore, the first term is zero. The terms on the right-hand-side of Eq. (6.1) provide the net force $\mathbf{F}_{\text{net}}$ which results in an acceleration $\mathbf{a}$ given by:

$$\mathbf{a} = \frac{\mathbf{F}_{\text{net}}}{m}. \tag{6.3}$$

The poppet and spring with the diesel flowing through it form an under-damped vibration system. If the poppet is not balanced, it will begin to vibrate until its energy is consumed by the viscous friction from the (operating) fluid. Note that the effects of the damping, resulting from the fluid surrounding the poppet, is included implicitly when the resultant aerodynamic forces (including the pressure and friction forces) are calculated in our CFD solution. It should be noted that other research teams {e.g., Panagiotopoulos and Kyparissis (2010) [80], Snyder and Anttonen (2003) [94]} have employed such an approach in addressing similar FSI problems.

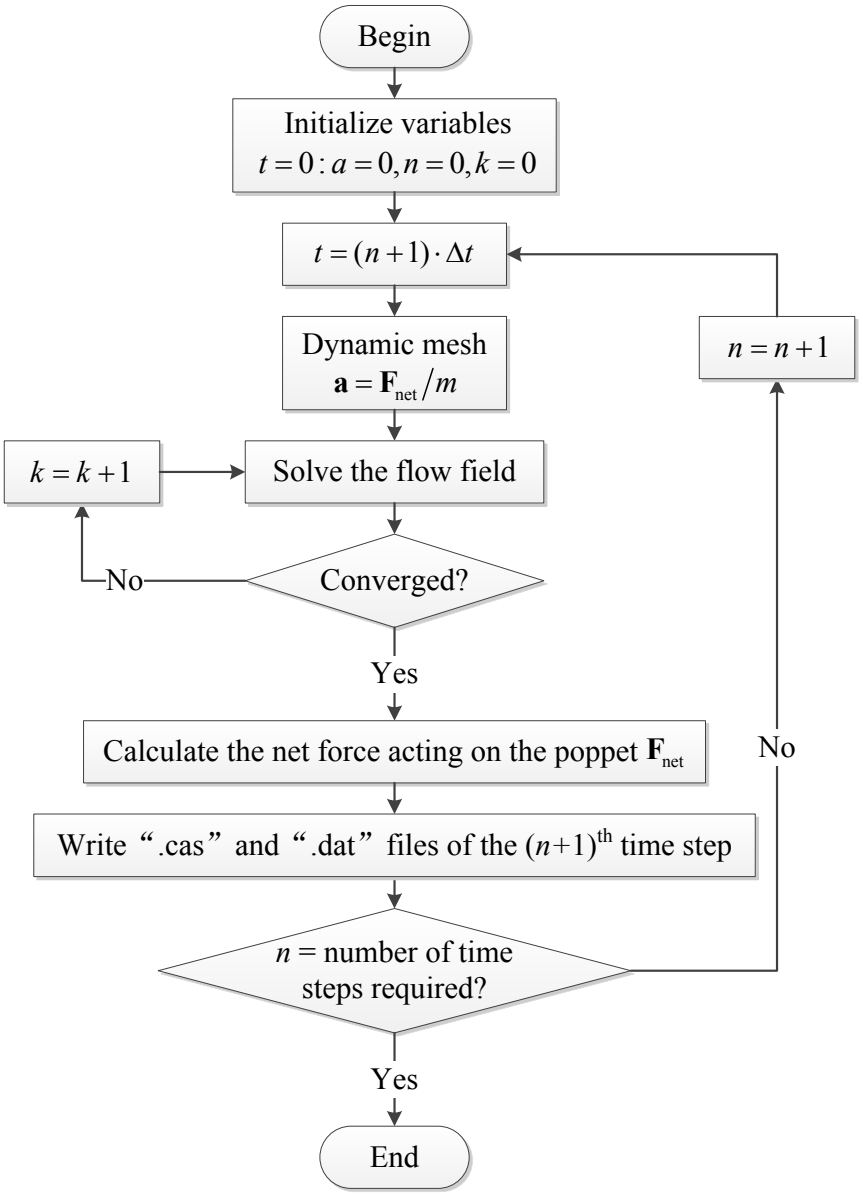

Figure 6.3: Flow diagram summarizing the computational procedure used in the present work.

Force Transmission

The flow diagram summarizing the computational procedure used in the present work is displayed in Figure 6.3. The fluid–structure interaction is realized through the various forces that are transmitted between the fluid and the structure. In our dynamic mesh model, the mesh is updated at the beginning of each computational time step. An updated solution for the fluid flow is obtained based on the updated configuration for the valve structure (viz., the current position of the poppet in the valve). In consequence, the forces transmitted from the structure to the fluid are accounted for using this sequence of updates.

On the other hand, the forces transmitted from the fluid to the structure are obtained through a user-defined function. This function is used to determine the translational and rotational velocities of the dynamic mesh. The net force acting on the poppet is calculated at the end of each time step, based on the updated solution and this solution is used to determine the dynamic mesh configuration for the next time step (see Figure 6.3).

6.3 Simulation of a Single Bubble

The computational procedure that combines a dynamic mesh, the Eulerian multiphase flow model and user-defined functions was found not to be computationally stable for the simulation of multiphase flows (although the procedure was stable for the simulation of a single phase flow).

To avoid potential computational divergences, the simulation was divided into two main steps, one involving a single phase flow for a temporal duration long enough so that the poppet moves into a position where it is balanced (viz., is in equilibrium) and the second involving the injection of bubbles which signals the start of the multiphase flow.

For future reference, the poppet lift is defined as the distance from the lowest point of poppet to the valve seat (as shown in Figure 6.8). The initial poppet lift is 0.50×10^{-3} m.

6.3.1 Single Phase Flow with FSI

A case with an inlet velocity 1.0 m s^{-1} is used as a reference base case for comparison. The variation of the poppet lift is shown in Figure 6.4. The initial poppet location is not a balanced location (viz., equilibrium position) for the poppet. Driven by the net force acting on it, the poppet begins to exhibit a damped vibration. Finally, the poppet vibration stops and the poppet achieves a new equilibrium position in which the poppet lift is 2.50×10^{-4} m.

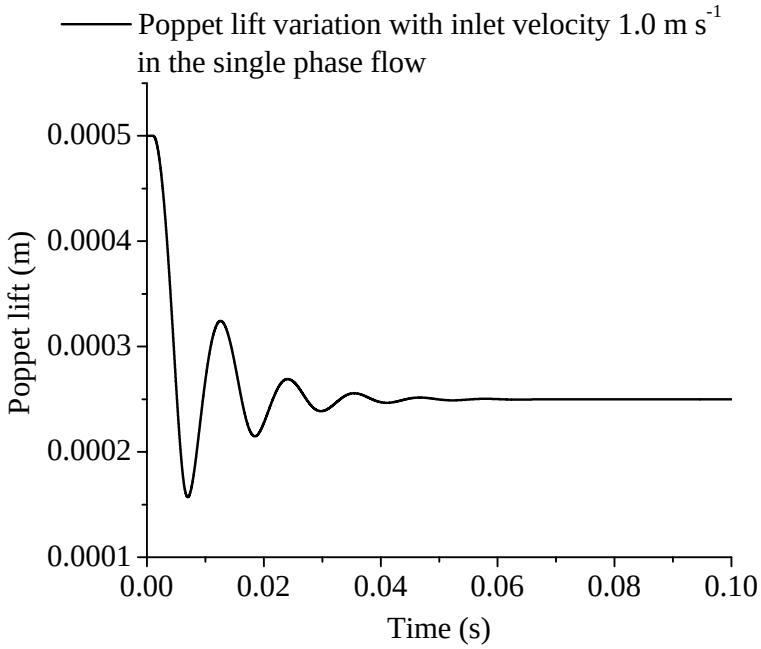

Figure 6.4: Poppet lift time variation for a single phase flow.

A Fast Fourier Transform (FFT) was used to analyze the poppet vibrations. The amplitude spectrum of these vibrations is shown in Figure 6.5. A perusal of this spectrum indicates that there is a dominant (peak) frequency at about 87 Hz. This frequency depends on the properties of the system undergoing the vibrations, such as the poppet mass, the spring stiffness and the pressure force variations that determine the poppet lift. In our

case, the spring stiffness is a constant. The pressure force variations that determine the poppet lift is unknown and will be studied further in the following section.

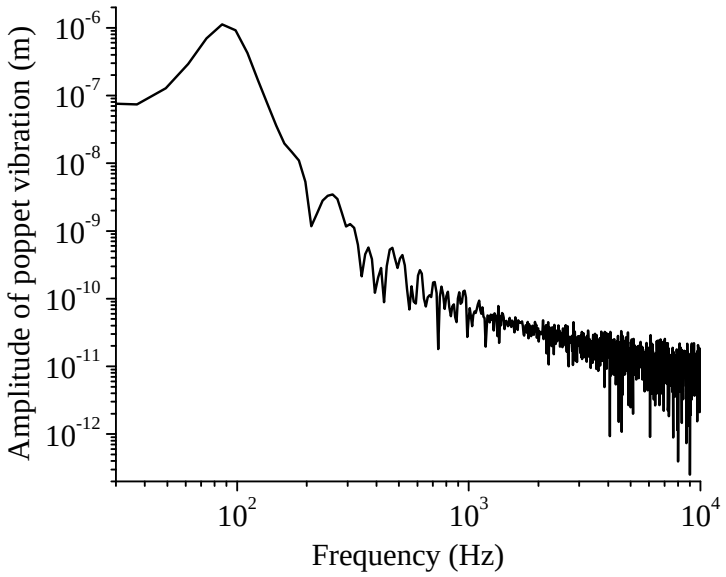

Figure 6.5: Amplitude spectrum of the poppet vibrations for a single phase flow.

Figure 6.6 shows the pressure in and velocity of the flow field inside the valve after the poppet relaxes to its equilibrium position. Generally, the flow inside the valve is very complex. It can be seen that there is a region with high velocity and low pressure between the poppet and valve seat. Furthermore, from a visualization provided by various stream traces in the flow, it can be seen that many vortical structures exist in the flow within the valve. More specifically, at the top of poppet, a large vortex is observed in the flow simulations. The presence of these vortices suggests that the flow field in the valve is highly unsteady, even although the poppet position is fixed (viz., in equilibrium).

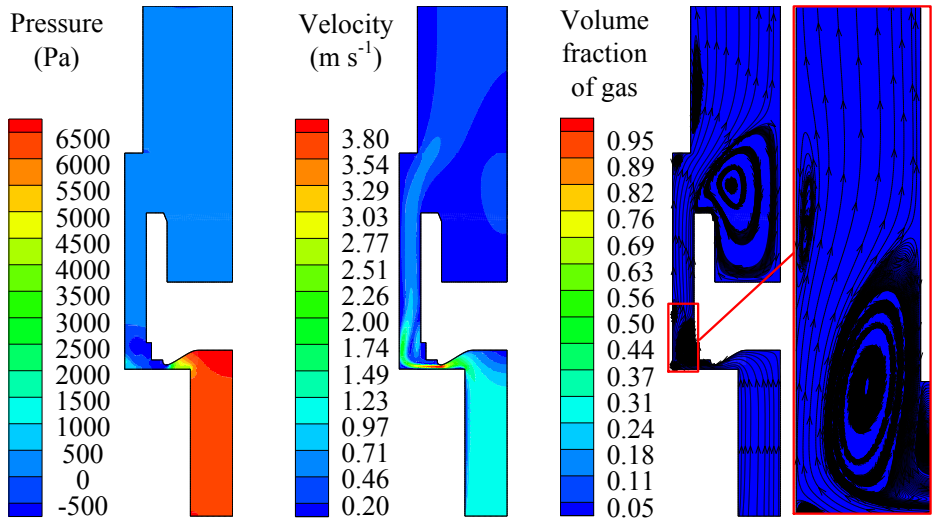

Figure 6.6: Flow field in the valve after the poppet relaxes to its equilibrium position: (a) pressure; (b) velocity; and, (c) stream traces.

6.3.2 Single Phase Flow with Prescribed Velocity

An analysis of the variations in the force balance under a number of different poppet lift conditions was undertaken. A prescribed motion with constant velocity is applied to the poppet and the resulting pressure force on the poppet is monitored for this single phase flow simulation. The equilibrium solution for the poppet lift in Figure 6.4 is taken as the initial conditions for these simulations.

Cases involving different velocities and directions for the poppet motion were compared in order to ensure that the simulation results are independent of these factors. Furthermore, small poppet velocities were used in the simulations to ensure that the poppet can relax to an equilibrium position. The results of these various simulations are exhibited in Figure 6.7. A perusal of Figure 6.7 shows that pressure variations as a function of the poppet lift is

not linear. When the poppet is moving towards the valve seat, the pressure force increases very sharply as seen in the figure. Indeed, this pressure force can be more than 700 times that of the spring force.

The straight line in Figure 6.7 represents the combined spring, buoyancy and gravitational forces which vary linearly with the poppet lift. The intersection of this line with the pressure force curve corresponds to the equilibrium position of the poppet. This equilibrium poppet lift position is shown also in Figure 6.4, where it is seen to be 2.5×10^{-4} m.

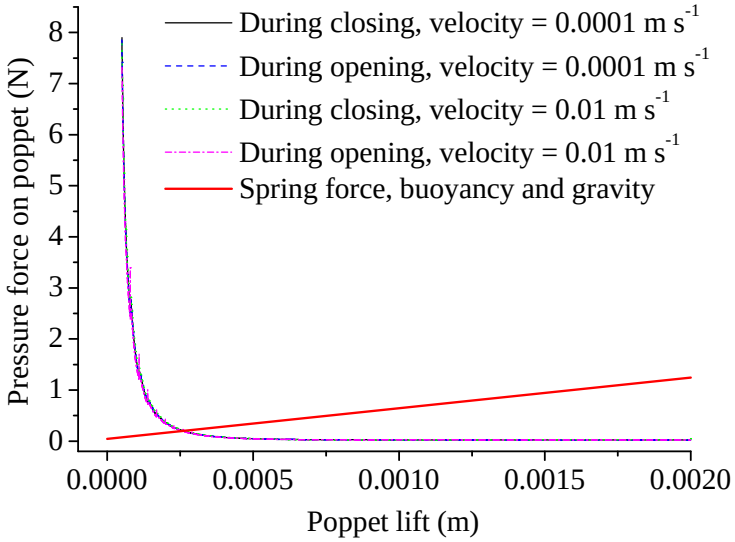

Figure 6.7: Pressure variations as a function of the poppet lift under different velocities and directions of motion for the poppet.

6.3.3 Multiphase Flow with FSI

Using the simulation result for the single phase flow, a bubble with a diameter of 0.003 m was injected in the liquid phase [the bubble location is show in Figure 6.10 (a)] for

this simulation and then a liquid–gas flow through the valve was simulated subsequently. As shown in the sketch of Figure 6.8, a number of parameters were monitored in this simulation. These included the poppet lift variation rate, the volume fraction of the gas in a cross-section at poppet lift and the pressure force on the poppet. The flow corresponding to a physical time from $t = 0.1$ to 0.2 s (viz., from 0–0.1 s after the bubble was injected into the single phase flow) was simulated until the poppet relaxed to its equilibrium position.

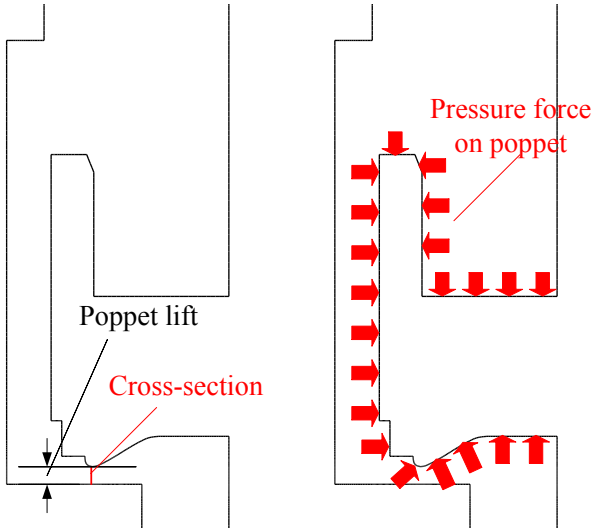

Figure 6.8: Sketch of the various parameters monitored in the multiphase flow simulations.

The poppet lift variation is defined as the displacement of the poppet in a non-equilibrium position relative to the poppet lift in the equilibrium position. The volume fraction is the area-averaged volume fraction of the gas in a cross-section as shown in Figure 6.8. These two parameters, as well as the pressure force on the poppet, are shown in Figure 6.9. The time axis has not been non-dimensionalized here in order to allow the reader to assess how quickly in real (or, actual) time the poppet takes to relax to its equilibrium position. The curve corresponding to the volume fraction of the gas indicates that the time period taken by the gas to pass through the cross-section is from $t = 0.1028$ s to $t = 0.1044$ s. Over this short time period, it can be inferred from an examination of the curve of the poppet lift variation rate that the poppet keeps moving downwards and

then begins to undergo a damped vibration. At $t = 0.2$ s, the amplitude of this vibration has damped to about 1.5 % of the maximum of the amplitude variation. The fluctuations of the pressure force on the poppet are generated over the time period corresponding to the passage of the gas bubble through the cross-section, after which these fluctuations are damped (gradually).

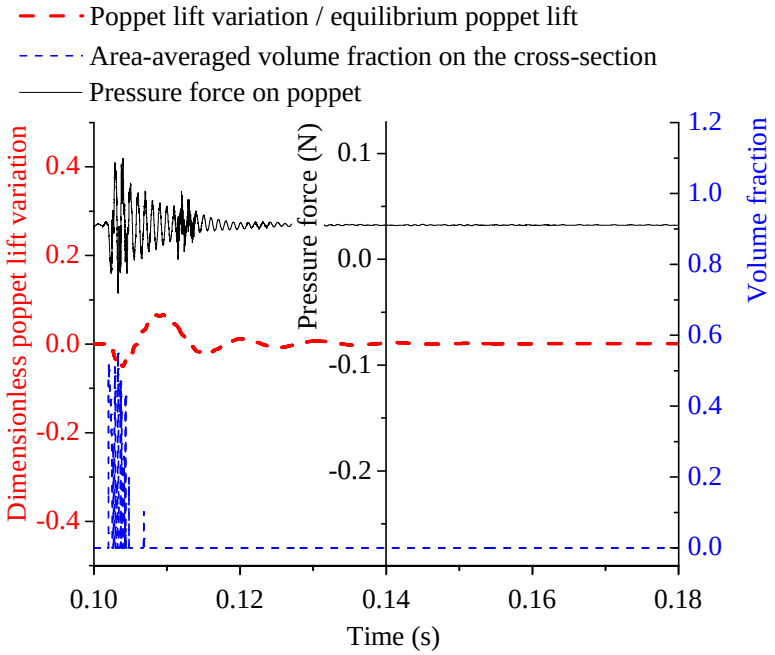

Figure 6.9: Time variation of three parameters monitored in a multiphase flow for an inlet velocity of 1.0 m s^{-1} and an injected bubble diameter of 0.003 m.

The contours of the gas volume fraction in Figure 6.10 summarize the evolution of the gas bubble as it passes through the cross-section. Here, the poppet is at its lowest position at $t = 0.104$ s and at its highest position at a time of $t = 0.109$ s. The bubble injected into the single phase flow deforms and breaks up as it passes through the cross section. This causes the poppet to move downward until all the gas has passed through the section and the liquid has refilled the gap between the poppet and the valve seat.

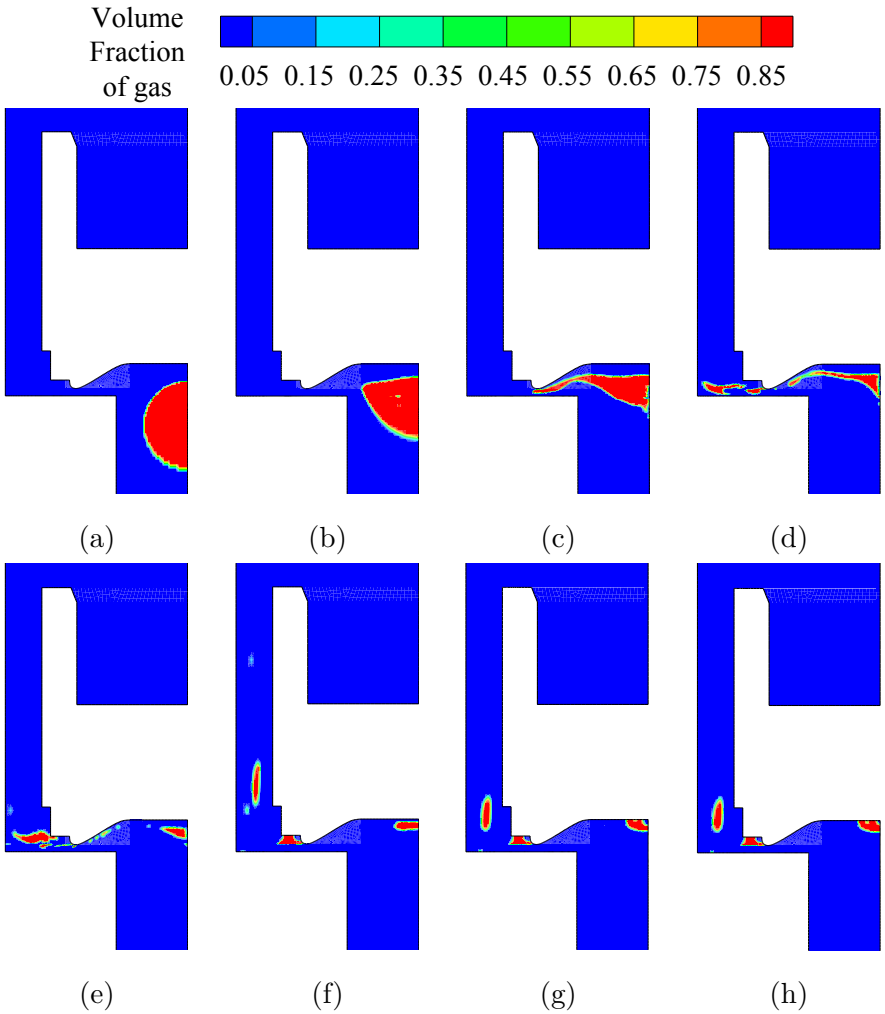

Figure 6.10: Contours of the volume fraction of gas at different times: namely, at (a) $t = 0.100$ s; (b) $t = 0.101$ s; (c) $t = 0.102$ s; (d) $t = 0.103$ s; (e) $t = 0.104$ s; (f) $t = 0.109$ s; (g) $t = 0.115$ s; and, (h) $t = 0.120$ s.

From Figure 6.7, it is seen that when the poppet lift is less than its equilibrium position, a much larger pressure force than the spring force is acting on it. This pressure force provides the energy to the poppet that induces the poppet vibration. The poppet returns to an equilibrium position as a result of the damping from the liquid.

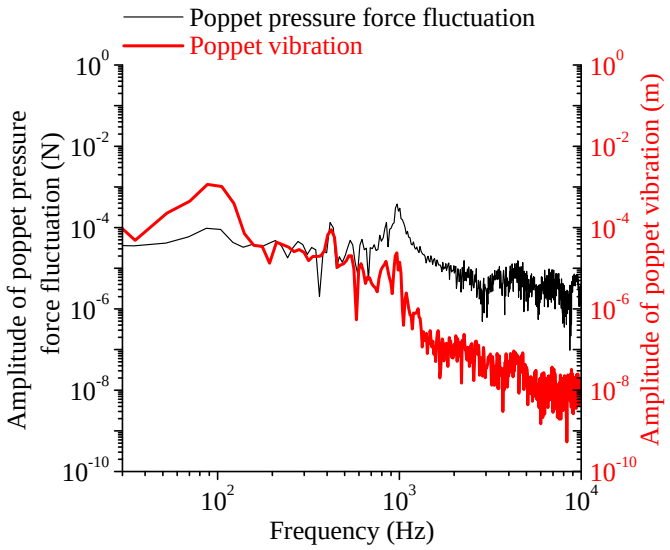

Figure 6.11: Amplitude spectra of the pressure force fluctuations and of the poppet vibration in a multiphase flow for an inlet velocity of 1.0 m s^{-1} and an injected bubble diameter of 0.003 m.

The amplitude spectra of the pressure force on the poppet and of the poppet vibration were obtained using FFT, and are displayed in Figure 6.11. An examination of these spectra shows that there are two dominant frequencies. Firstly, there is a low-frequency peak at about 87 Hz. This is consistent with the dominant frequency in the amplitude spectrum of the poppet vibration observed for the single phase flow (see Figure 6.5). This frequency is associated with the vibrations in the poppet and spring structure in the dynamic valve.

Secondly, in the two amplitude spectra shown in Figure 6.11, there is high frequency peak at about 970 Hz. This peak is associated with the largest amplitude for the pressure fluctuations. Comparing this with the result for the poppet vibration for the single phase flow shown in Figure 6.5, it is inferred that the high frequency peak is induced by (or the result of) the multiphase flow. It is observed from the flow field that the center of the vortex above the poppet exhibits the same dominant high frequency in its motion.

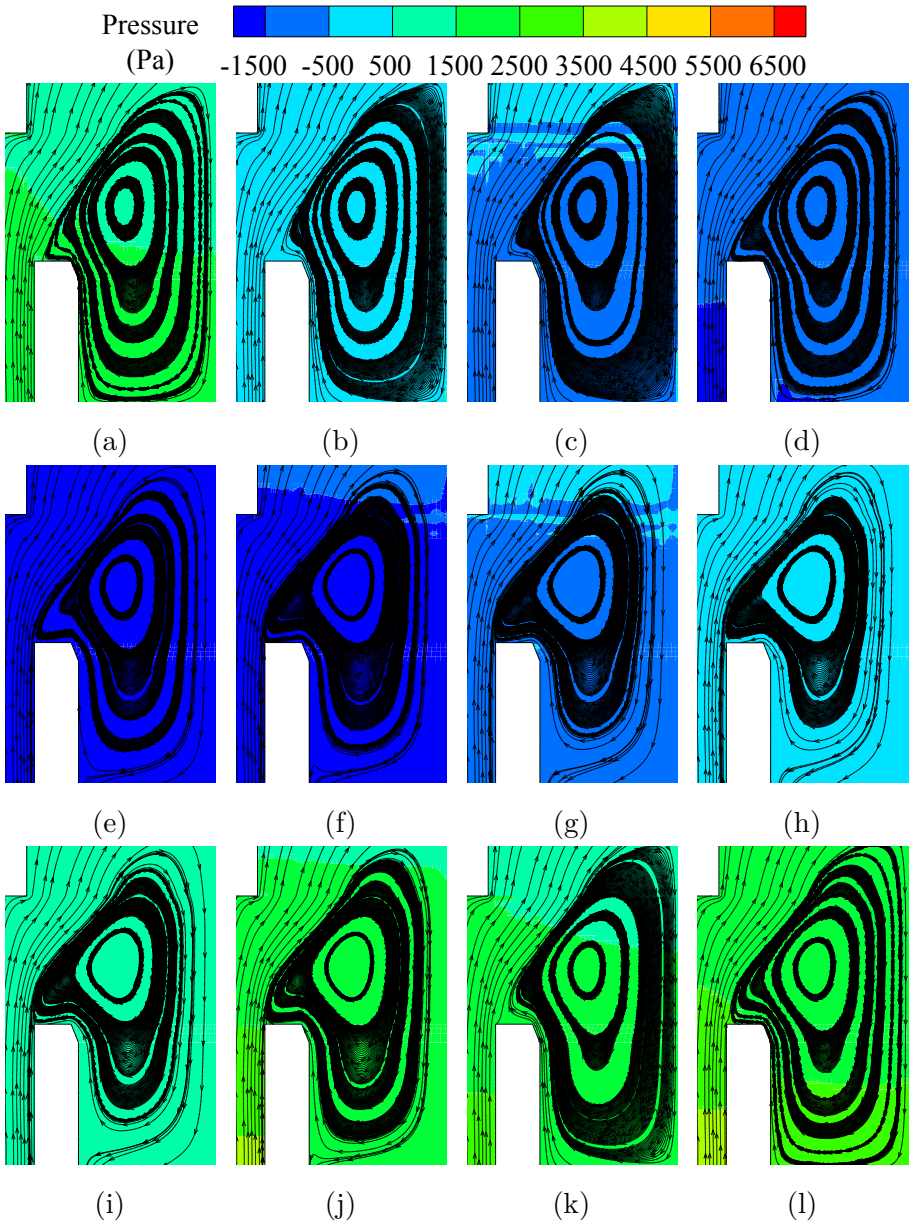

Figure 6.12: Stream traces of the vortex above the poppet in a single cycle at the following times: (a) $t = 0.1030$ s; (b) $t = 0.1031$ s; (c) $t = 0.1032$ s; (d) $t = 0.1033$ s; (e) $t = 0.1034$ s; (f) $t = 0.1035$ s; (g) $t = 0.1036$ s; (h) $t = 0.1037$ s; (i) $t = 0.1038$ s; (j) $t = 0.1039$ s; (k) $t = 0.1040$ s; and, (l) $t = 0.1041$ s.

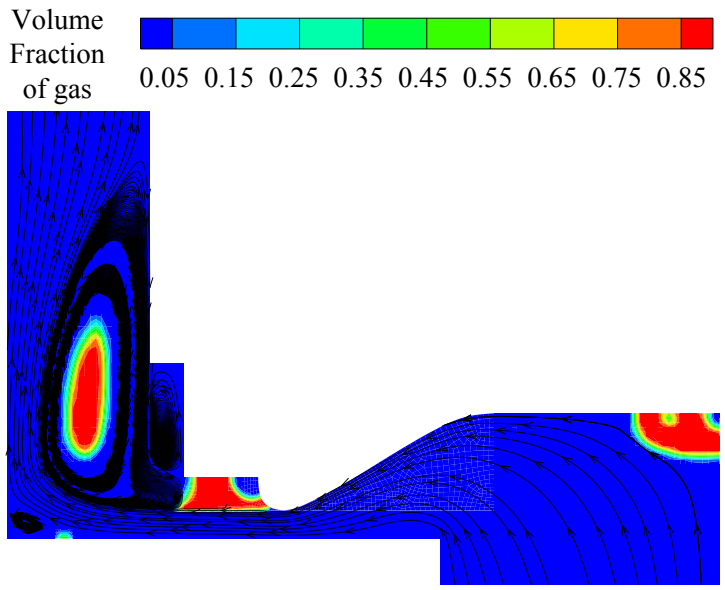

(a)

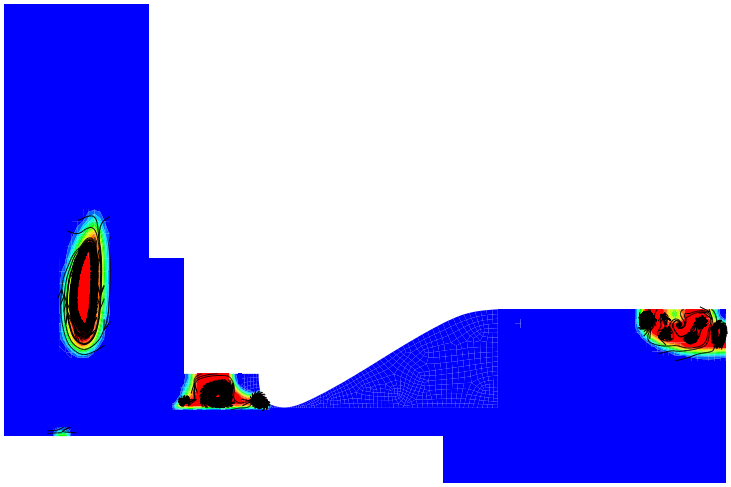

(b)

Figure 6.13: Stream traces of the liquid and gas flow in the valve close to the valve seat at $t = 0.20$ s: (a) stream traces of the flow in the liquid phase; and, (b) stream traces of the flow in the gas phase.

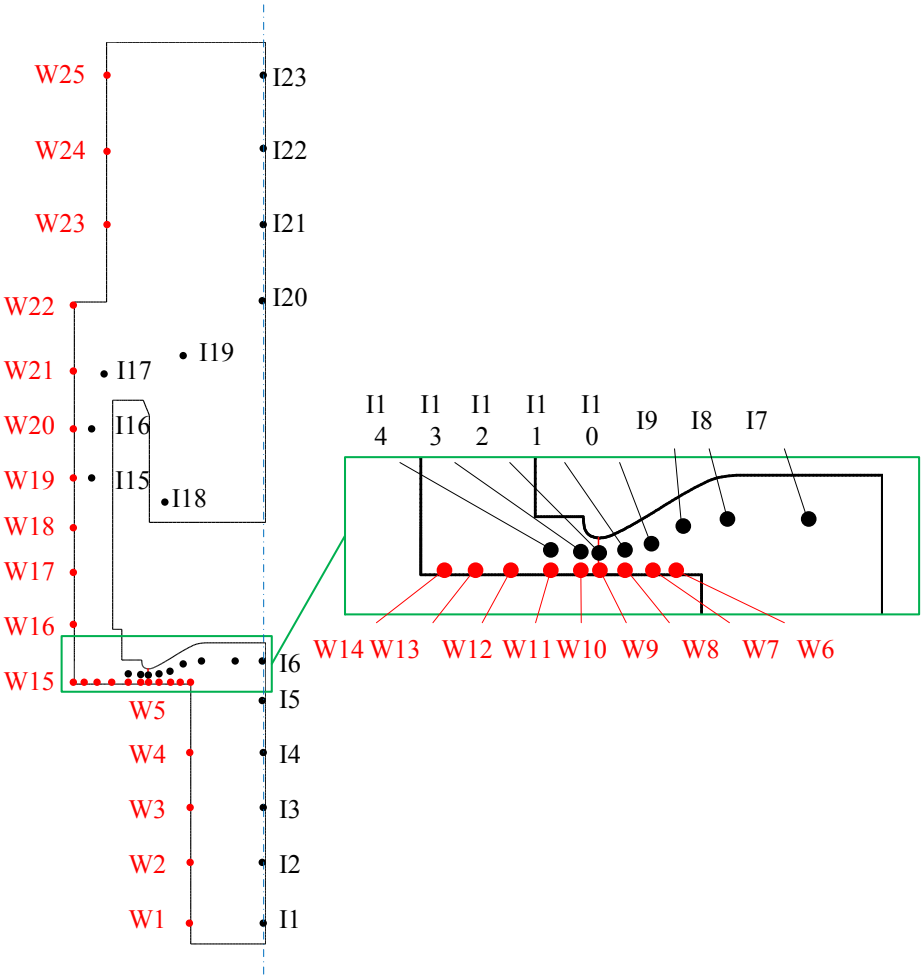

Figure 6.14: Pressure monitoring locations.

Figure 6.12 shows the stream traces of this vortex motion in a single cycle. Both the size and center of the vortex vary with time in a periodic manner. It is believed that instabilities in the chamber vortices shown in Figure 6.12 is related to the moving bubbles passing through the gap between the poppet and valve seat. Some residual bubbles are entrained into these vortices and trapped under the poppet valve as illustrated in Figure 6.13.

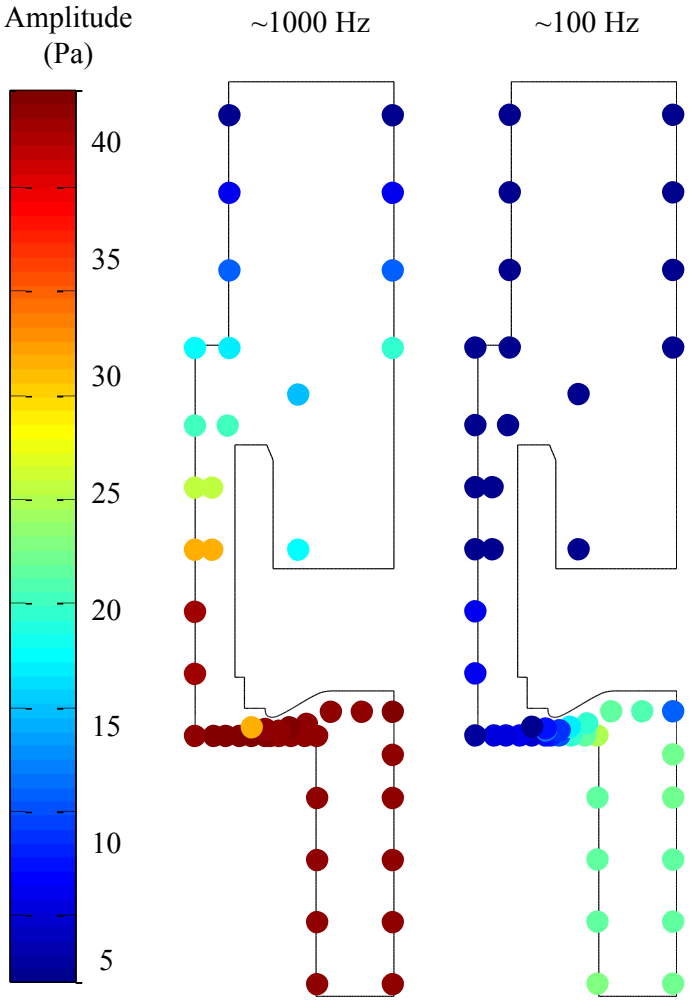

Figure 6.15: Amplitudes of the pressure fluctuations for the two principal peak frequencies at the monitored locations: left side of figure shows the amplitude associated with the higher peak frequency and the right side of the figure shows the amplitudes associated with the lower frequency.

The vibration of the pressure force on the poppet suggests that the pressure field in the valve exhibits unstable fluctuations. To analyze the strength and distribution of these fluctuations, the pressure at 48 specified locations was monitored, as shown in Figure 6.14.

The "W" series of monitored pressure locations is located near the walls of the valve body in order to observe the pressure fluctuation near the walls. The "I" series of monitored pressure locations is located on an internal streamline in order to observe the pressure fluctuations in the channel. Pressure monitoring locations are concentrated near the valve lift, as this region is of more concern in this research.

The pressure time history data at all of the monitored locations were analyzed using a FFT. Two principal peak frequencies are observed in the amplitude spectra for the temporal pressure variations (which are consistent with the amplitude spectra obtained for the pressure force on the poppet). The amplitudes of the pressure fluctuations at these two peak frequencies are summarized in Figure 6.15. Generally, amplitudes corresponding to the higher frequency (about 1000 Hz) are larger than amplitudes associated with the lower frequency (about 100 Hz). More specifically, the locations near the inlet and valve lift exhibit generally higher amplitudes in the pressure fluctuations than those locations near the outlet.

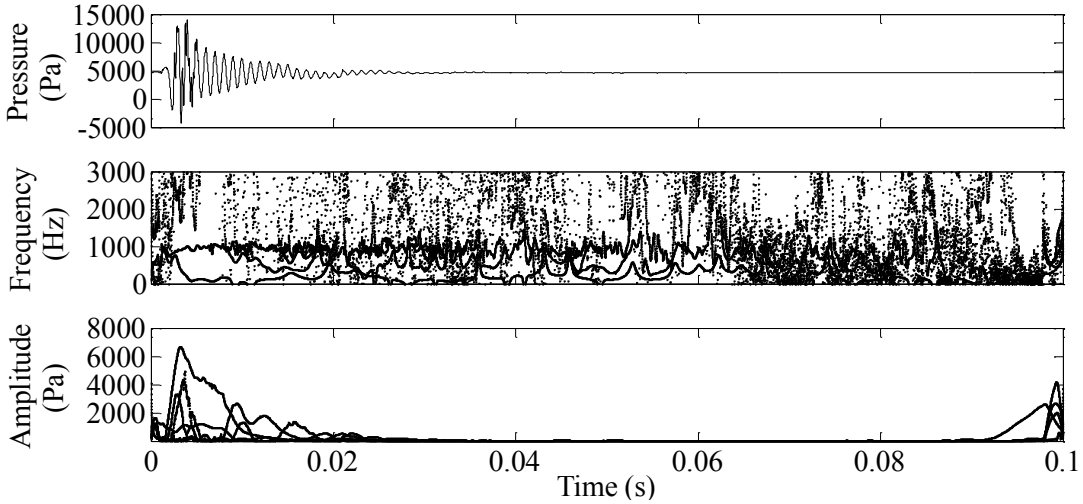

Figure 6.16: Time–frequency–amplitude plot of pressure fluctuation at W5 (obtained using a HHT).

The amplitudes exhibited in Figure 6.15 (obtained using an FFT) are not able to encapsulate the time-varying history of these amplitudes. From Figure 6.9, it is evident that the time variation of the pressure fluctuations is a non-stationary process, rather than a stationary process (the latter assumption of which is implicit in the spectral analysis based on the FFT). To capture the non-stationarity of the pressure fluctuations, we apply a HHT to the data (used earlier in this thesis with reference to the pressure fluctuation data obtained for the vortex-induced vibrations arising from flow past an oscillating square cylinder). To this purpose, the pressure fluctuation data at location W5 (see Figure 6.14) was analyzed using HHT. The time–frequency–amplitude plot of the pressure fluctuations for this location is exhibited in Figure 6.16.

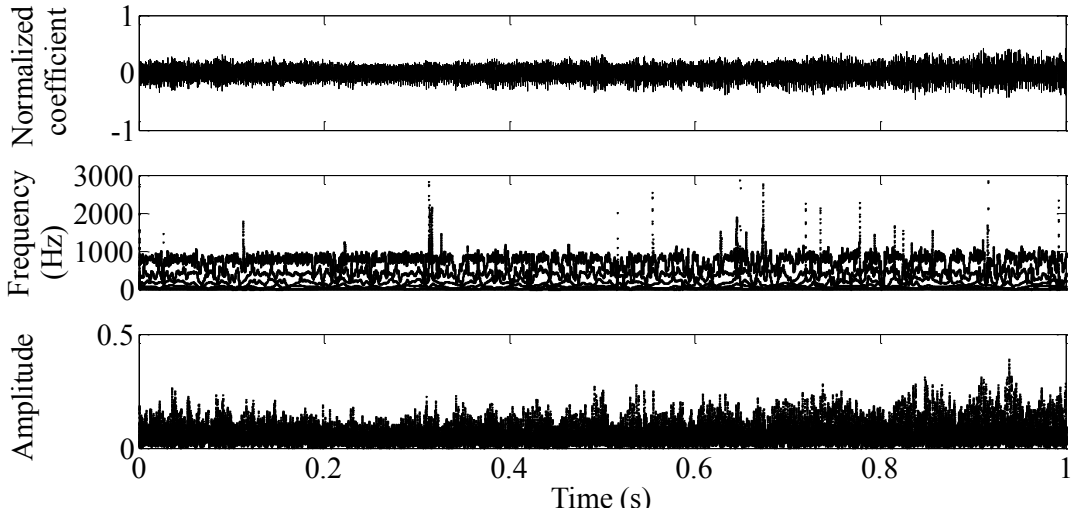

Figure 6.17: Time–frequency–amplitude plot of a measured valve noise signal (obtained using a HHT).

In the upper panel of Figure 6.16, the time history of the pressure fluctuation data clearly shows that the variations in the pressure are not stationary over time. An examination of the time–frequency plot (middle panel) shows that a frequency of about 1000 Hz is the dominant frequency in the pressure variations and that this dominant frequency does not appear to vary with time. However, a variation of the amplitude (of the domi-

nant frequency) over time is observed in the time–amplitude plot shown in the lower panel of Figure 6.16. These features of the HHT analysis of the pressure fluctuation data are consistent with the non-stationarity in the pressure fluctuation time series.

Similarly, we apply the HHT to analyze a noise signal measured in an experiment involving the poppet valve (shown in Figure 6.17). This measurement was conducted by Ford engineers [28]. The results of the HHT analysis of a noise signal of one second duration are displayed in Figure 6.17. The dominant or peak frequency for this measured noise signal varies with time, but this frequency lies principally in a range about from 800–1000 Hz. The experimental data obtained from the Ford Motor Company shows that the dominant frequency for the noise measured in the poppet appears to be confined to the range from about 500 to 1000 Hz in all their tests. The valve used in the experiment by Ford engineers is slightly different from the present simplified valve geometry.

Both low-frequency and high-frequency pressure fluctuations provide contributions to the noise generation in the valve. The low-frequency pressure fluctuation contribution to the noise is associated with the mechanical noise arising from the poppet vibration. In our simulations, the high-frequency pressure fluctuation contribution to the valve noise has a larger amplitude than that associated with the low-frequency contribution. This aspect of our simulations is consistent with the principal noise frequency observed in the extensive measurements of noise in the poppet valve conducted by the Ford Motor Company [28]. As a consequence, our current simulations suggest that the high-frequency pressure fluctuations in the flow is the main source of the valve noise.

The valve noise is influenced by a number of factors. One category of factors relates to the material properties and the components that make up the dynamic valve itself. These factors include the spring stiffness, the poppet mass and the geometry of valve. Another category of factors is related to the flow conditions through the valve. The inlet velocity, the bubble size, the fuel type, and the operating temperature can be considered to belong to this category of factors. Fuel type and operating temperatures influence the physical properties of the fluids. Higher viscosity and higher surface tension in the fluid tend to

promote the poppet vibration and noise.

Factor 1: Bubble Size

6.3.4 Parametric Analysis

To verify the influence of bubble size on the noise generation, a case with a larger bubble passing through the valve lift was conducted using the same simulation procedure. After the poppet reached its equilibrium position in the single phase flow, a bubble with a diameter of 0.004 m was injected into the flow.

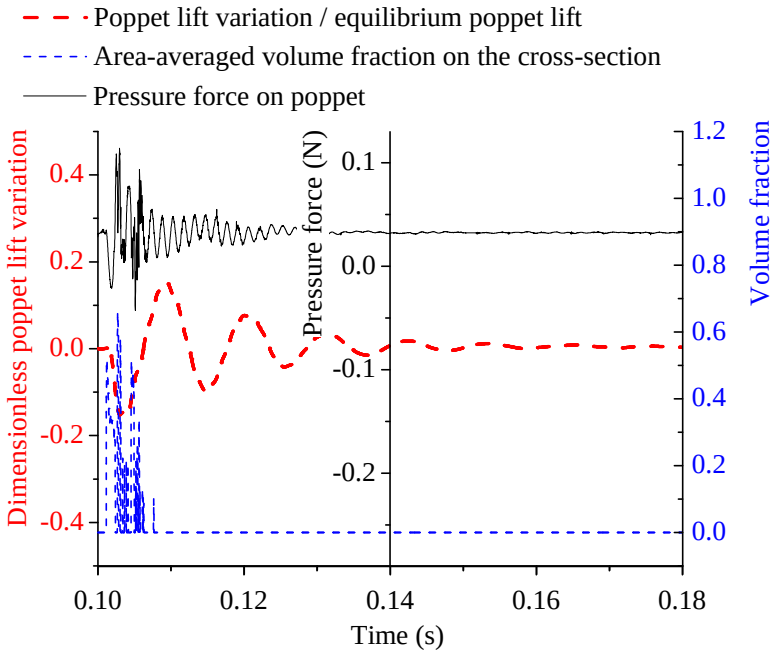

Figure 6.18: Time variation of three parameters monitored in a multiphase flow for an inlet velocity of 1.0 m s^{-1} and an injected bubble diameter of 0.004 m.

In Figure 6.18, it can be seen that the maximum poppet lift during this period is larger

than that for the case involving the injection of a 0.003 m bubble into the flow. From the time–volume fraction plot, it can be deduced that the larger bubble took more time to completely pass though the cross-section.

As in the case for the smaller injected bubble, the current case involving the larger injected bubble also exhibits two dominant peak frequencies in the amplitude spectra of the pressure fluctuation data and of the poppet vibrations (see Figure 6.19). Depending on the characteristics of the spring system, a low frequency peak is also seen to occur at about 100 Hz. However, the high frequency peak is at about 700 Hz for this case, which is lower than that obtained for the case with the smaller bubble. Amplitudes corresponding to the low and high frequency peaks are both larger for the case with the larger bubble than those with the smaller bubble.

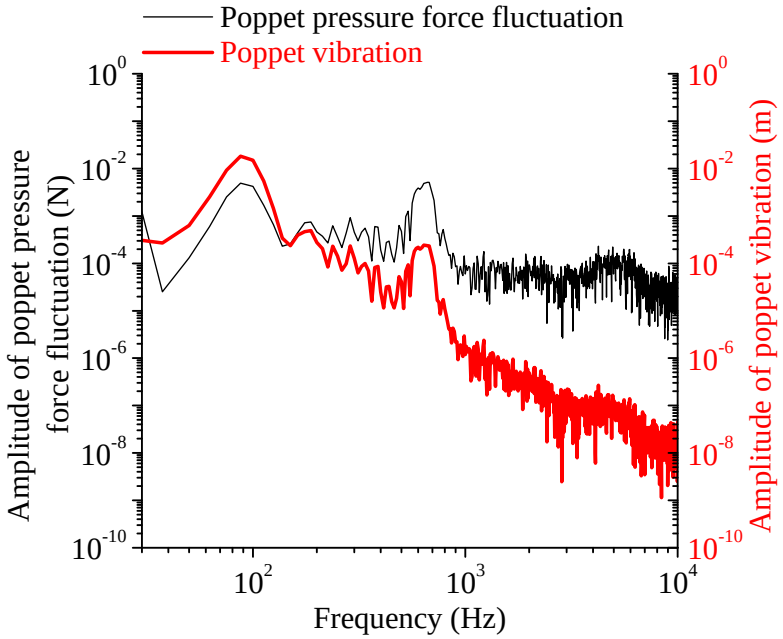

Figure 6.19: Amplitude spectra of the pressure force fluctuations and the poppet vibration in a multiphase flow for an inlet velocity of 1.0 m s^{-1} and an injected bubble diameter of 0.004 m.

Factor 2: Inlet Velocity

The inlet velocity is another key parameter in this problem. To analyze its effect on the noise generation, a case with an inlet velocity of 0.5 m s^{-1} was simulated and these results were compared to the case with an inlet velocity of 1.0 m s^{-1}.

Firstly, a single phase flow through the valve was simulated. Figure 6.20 shows that the balanced poppet lift for the case with the lower inlet velocity is smaller than that for the case with the higher inlet velocity. As fluid with a lower velocity produces a lower pressure on a poppet, the equilibrium position of the poppet is expected to be lower than that in the case with a larger inlet velocity.

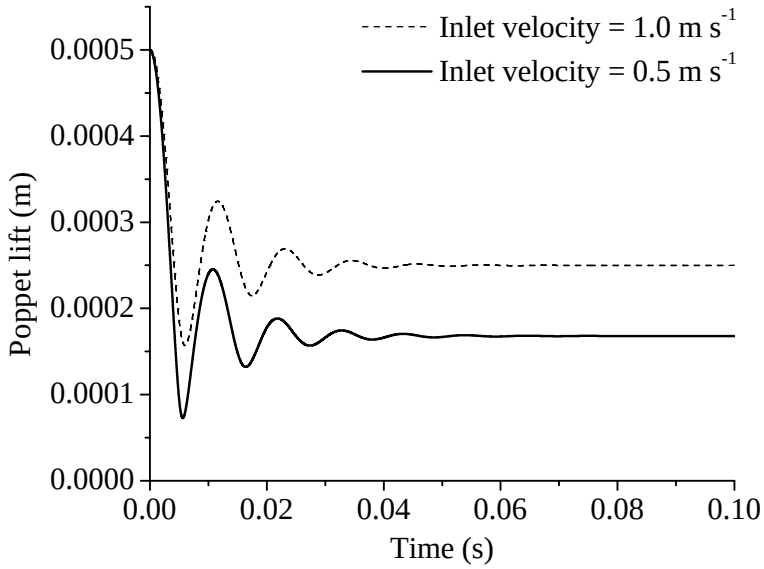

Figure 6.20: Comparison of the poppet lift variation of a single phase flow with an inlet velocity of 0.5 and 1.0 m s^{-1}.

In the multiphase flow simulation, a bubble of 0.004 m was injected into this flow (viz. the flow with an inlet velocity of 0.5 m s^{-1}). The poppet lift variation, volume fraction on the cross-section, and pressure force on the poppet are exhibited in Figure 6.21. In this

case, the pressure force fluctuation and the poppet vibration are much more "violent" than in the benchmark case. The effect of a lower inlet velocity coupled with the effect from a larger bubble size is responsible for these more "violent" fluctuations. Furthermore, the time required for the value of the volume fraction in the cross-section to return to zero is longer than in any of the cases simulated previously.

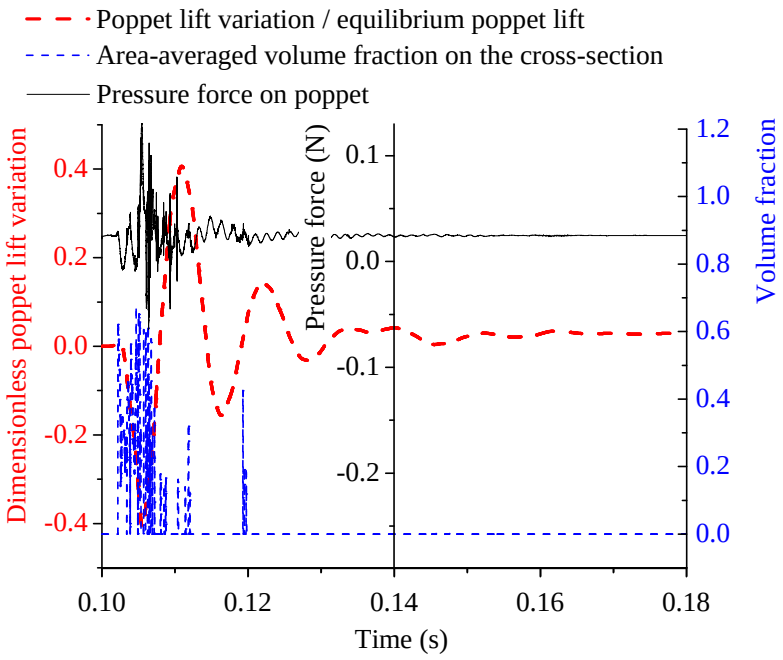

Figure 6.21: Time variation of three parameters monitored in a multiphase flow for an inlet velocity of 0.5 m s^{-1} and an injected bubble diameter of 0.004 m.

The amplitude spectra of the pressure fluctuation and the poppet vibration data in Figure 6.21 is exhibited in Figure 6.22. In conformance with the results of Figure 6.21, it can be seen that the spectral amplitudes for both the pressure force fluctuations and the poppet vibrations are larger than those associated with any of the cases simulated previously. The low frequency peak representing the natural frequency of the system (valve) is still at about 100 Hz. However, the higher frequency peak has shifted downwards to about 650 Hz which is even lower than that for the case with an injected bubble diameter

of 0.004 m and an inlet velocity of 1.0 m s^{-1}.

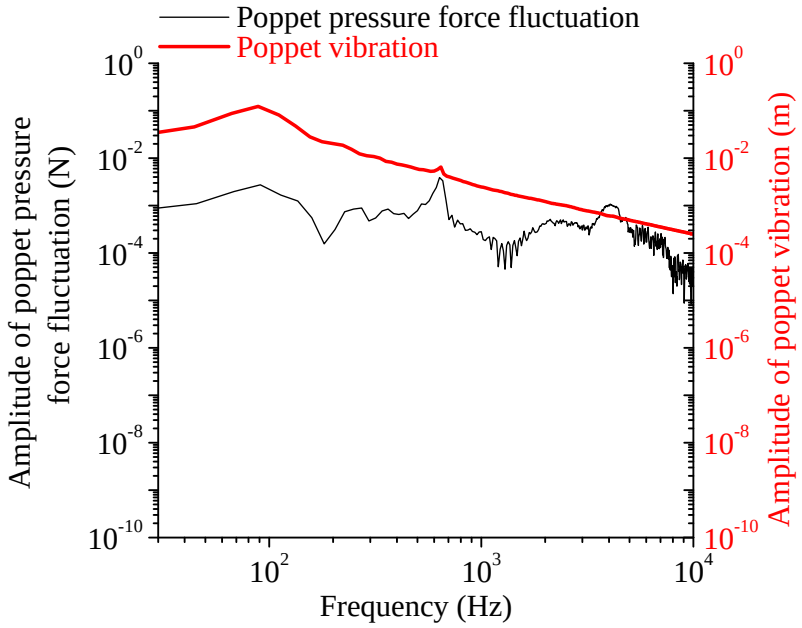

Figure 6.22: Amplitude spectra of the pressure force fluctuations and the poppet vibration in a multiphase flow for an inlet velocity of 0.5 m s^{-1} and an injected bubble diameter of 0.004 m.

6.4 Simulation of Multiple Bubbles

In this case, two bubbles with a diameter of 0.004 m were injected into the flow to show the effect of multiple bubbles on the vibration of the valve. The poppet lift variation, volume fraction on the cross-section, and pressure force on the poppet were monitored in the simulations (Figure 6.23). In this case, the pressure force fluctuations and the poppet vibrations are much more "volatile" than for cases involving the single bubble, as the effect from two bubbles last much longer than that from a single bubble. It is also evident that it takes the longest time in all cases for the value of the volume fraction on the cross-section

to return to zero.

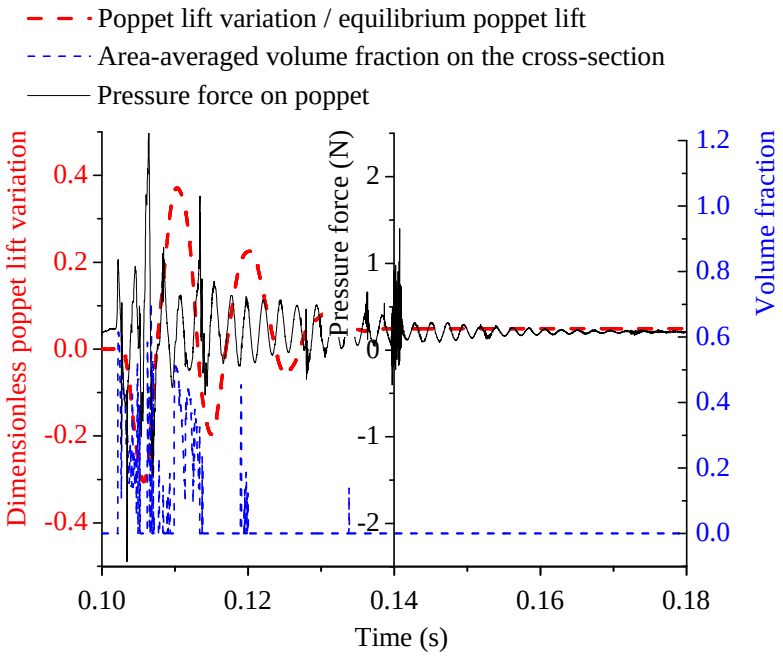

Figure 6.23: Time variation of three parameters monitored in a multiphase flow with two bubbles.

The contours of the gas volume fraction in Figure 6.24 summarize the evolution of the gas bubble as it passes through a cross-section in the valve. Here, the poppet is at its lowest position at $t = 0.106$ s and at its highest location at $t = 0.110$ s which are seen to occur at later times than for the cases. Bubbles injected into the single phase flow deform and break up as they pass through the cross section. As it takes more time for two bubbles to pass through the cross-section, the poppet must move downward further before the gas phase can pass through the cross-section and the liquid phase has refilled the gap between the poppet and the valve seat. After two bubbles passing through the cross section some gas was trapped in the vortex close to the corner of poppet shown in Figures 6.24 (e) to (h).

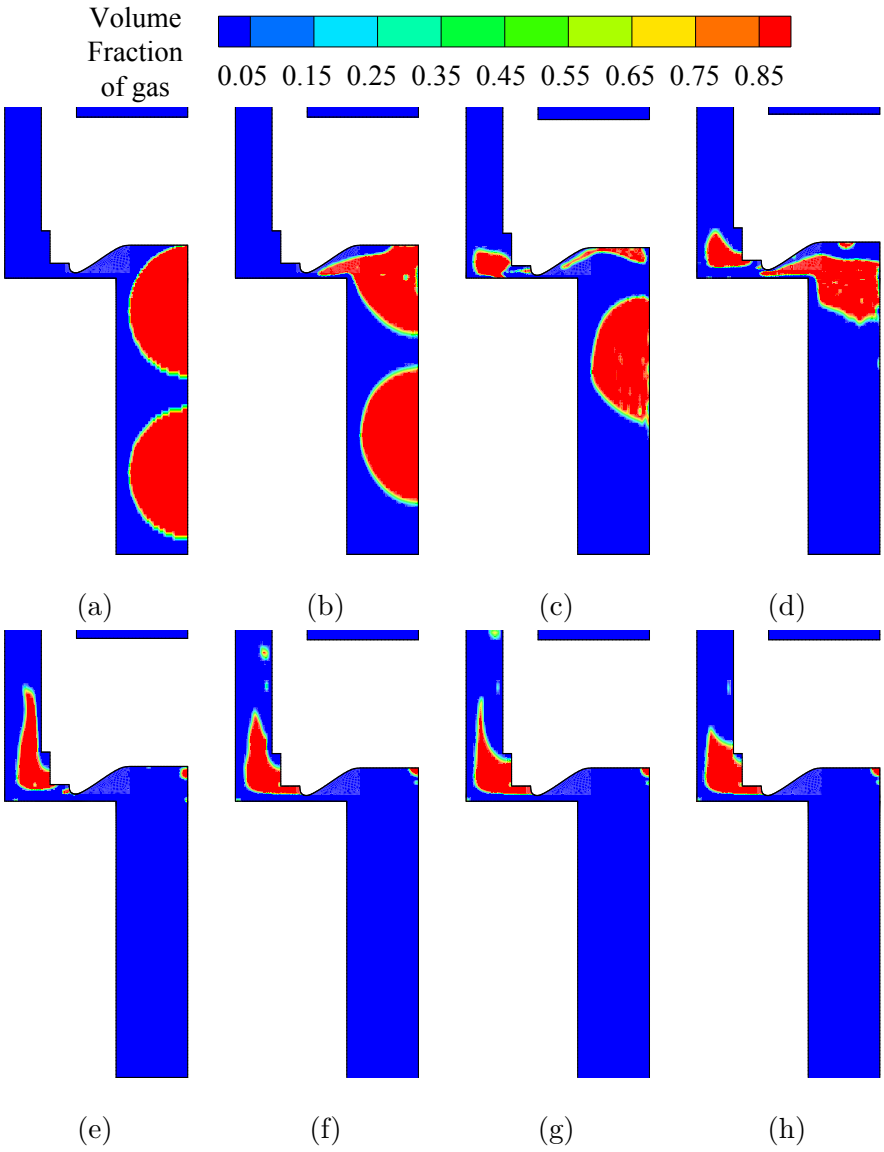

Figure 6.24: Contours of the volume fraction of gas at different times: (a) $t = 0.100$ s; (b) $t = 0.102$ s; (c) $t = 0.106$ s; (d) $t = 0.110$ s; (e) $t = 0.120$ s; (f) $t = 0.140$ s; (g) $t = 0.150$ s; and, (h) $t = 0.200$ s.

Consistent with the finding above, in the frequency analysis shown in Figure 6.25, it

can be seen that the amplitudes of both the pressure force fluctuations and the poppet vibrations are larger. The low frequency which is associated with the system natural frequency is still at about 100 Hz. However, the higher frequency in this case is at about 450 Hz, which is lower than all cases investigated with a single bubble passing through the cross-section.

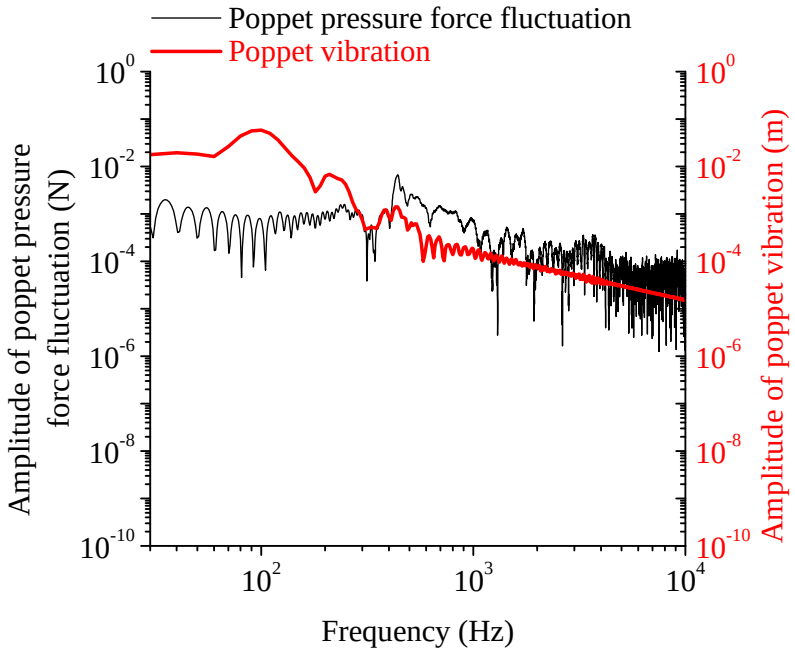

Figure 6.25: Amplitude spectra of the pressure force fluctuations and the poppet vibration in a multiphase flow with two bubbles.

6.5 Chapter Summary

A two-dimensional axi-symmetric numerical model has been developed to simulate the complicated two-phase fluid–structure interaction processes that are responsible for the noise and vibration in a poppet valve (or poppet).

An Eulerian multiphase flow model, a dynamic mesh and user-defined functions are utilized within the ANSYS-FLUENT software system in order to provide a computationally efficient methodology for conducting the simulations of the noise generation in the dynamic valve. In this strongly coupled simulation framework, the poppet valve which is driven by the spring and various dynamical fluid forces (e.g., viscous and pressure forces), is modeled as an under-damped vibration system. The dynamical motions of this system are controlled by a user defined function in our simulations, involving the application of Newton's second law of motion in the context of an unsteady oscillatory flow field.

It was found that the poppet vibrations and pressure fluctuations are induced by the liquid–gas flow through the valve. In a liquid–gas flow, the deformation and breakup of the gas bubbles in the gap between the poppet and the valve seat forces the poppet into a non-equilibrium (unbalanced) condition. When liquid refills the gap after the bubbles pass through it, the high pressure acting on the poppet forces it to undergo an under-damped vibration. Furthermore, when a multiphase flow is involved, the vortices in the flow become unstable and induce pressure fluctuations in the flow field.

A spectral analysis of the transient wall pressure at a specific locations of the valve seat showed the presence of a strong cyclical behavior that consists of two major components. There is a low-frequency peak at about 87 Hz which is associated with the frequency of the poppet vibration (and which we interpret to be the source of the mechanical noise). Furthermore, there is a high-frequency peak at about 970 Hz which is associated with compressibility effects and the unsteady vortex motions in the spring chamber.

Finally, it was found that the frequency, amplitude, and rate of decay of the poppet vibrations are influenced by numerous factors such as the flow condition (e.g., gas volume fraction, inlet velocity, fuel type, and temperature), the properties of the spring system, and the geometry of the valve. Larger bubbles result in larger displacements in the poppet in a non-equilibrium condition and induce stronger forcing of the spring due to the higher pressures, which in turn amplify the poppet vibration and noise. With a lower inlet velocity, the poppet reaches an equilibrium condition for a smaller poppet lift. At the same time,

a larger displacement is associated with a non-equilibrium configuration in the poppet. Hence, a higher inlet velocity and smaller bubble size could potentially reduce the noise in the valve.

The detailed simulations and subsequent analysis of the complex interaction of the turbulent multiphase fluid motion through the moving poppet valve allowed deeper physical insights and an improved understanding to be obtained concerning both the source and properties of the noise and vibrations generated in this complicated dynamical system.

Chapter 7

Conclusions and Future Work

The multiphase model in ANSYS-FLUENT has been further developed to improve its accuracy and capability for the solution of certain complex problems that the automotive industry has been confronted with recently. The application of UDFs and a Scheme file was used to include the effects of various interfacial-force models and to extend an FSI model based on a dynamic meshing procedure in FLUENT. After the initial validation studies had verified the new integrated model's effectiveness, the dynamic valve vibration and noise problem and the coolant surge tank degassing problem were solved and analyzed. A summary of the findings from the present study and recommendations for future work for the integrated multiphase and FSI models are provided in this chapter.

7.1 Conclusions

7.1.1 Summary of the Present Work

Most multiphase models in commercial software cannot meet the requirements from the automotive industry to solve pressing problems involving the presence of multiphase flow in complex structures which are characteristic of this field of endeavor. To solve these real-world industrial problems, the present work has further developed the existing multiphase models available in ANSYS-FLUENT and verified the improved model's efficiency and accuracy. UDFs and Scheme file have been the main development tools used in the implementation of the proposed integrated modeling system. The new developments consist of the incorporation of additional interfacial-force models in the simulation and the coupling of the solution process for multiphase flows with fluid–structure interaction. Validation had been undertaken to test the predictive accuracy of the new model components in the integrated modeling scheme. To compensate for the lack of experimental data for problems that incorporate all the key methodologies in the integrated modeling scheme, the individual components of the scheme (e.g., multiphase flow, dynamic mesh, and FSI) had to be validated individually. Additionally, for each key methodology (or component), different models were compared to obtain further understanding of their features.

Within the multiphase model component, various interfacial-force models, which were not included in FLUENT had to be incorporated in the integrated model procedure using UDFs. Models with or without an immiscible model were compared. Through comparison with experimental results, it was found that the inclusion of the additional interfacial-force models within the multiphase model allowed the liquid–gas flow to be simulated more accurately. With the immiscible model enabled, the interface between the liquid and gas phases could be clearly captured. The time-averaged gas distribution tended to coincide with the results without the immiscible model enabled. However, it was found that predictions of the time-averaged gas distribution were in better conformance with the experimental measurements without the inclusion of the immiscible model. Unfortunately,

these results without the inclusion of the immiscible model did not capture the unsteady (non-stationary) evolution of the gas volume fraction distribution. In consequence, the multiphase flow model without the inclusion of the immiscible model is only applicable to those problems (applications) where only time-averaged quantities are of interest (e.g., the degassing problem in a coolant surge tank). For problems where the unsteady aspects of the phenomenology are of critical importance (e.g., the vibration and noise problem in the operation of a dynamic valve), it is necessary to include the immiscible model within the multiphase flow modeling framework.

Two methods for generating a dynamic mesh, namely the smoothing and layering methodologies, were applied and compared in a validation case study. Maintaining acceptable mesh quality and high computational efficiency are highly important when using a dynamic mesh. The results show that both these methods ensured the generation of meshes of good quality and resulted in a high accuracy in the simulations, but the layering methodology was found to give a higher computational efficiency than the smoothing methodology.

Developing an effective FSI model has been the most challenging part of the research reported herein. The current version of FLUENT offers no established models for these types of multiphysics problems. The dynamic mesh procedure has been employed within the FSI model. However, due to restrictions from the dynamic mesh model in FLUENT, the data transference between the fluid and the structure is only weakly coupled, implying that the procedure is incapable of solving strongly coupled problems. To overcome this weakness, a Scheme file was programmed to implement an implicit method through the strategic rearrangement of the solution process. This implicit method was then applied to the simulation of the complex flow in a heart valve. This validation provided evidence that the proposed solution procedure is capable of solving strongly coupled fluid–structure interaction problems.

The refined and validated multiphase model was applied to the simulation of a degassing problem in a coolant surge tank. The degassing rate, which is a critical parameter

in automotive design, needs to be simulated accurately. Therefore, research on the effects of interfacial forces in the Eulerian models on the accuracy of the predictions is very important. Grid sensitivity testing and time step sensitivity testing were investigated in order to determine the optimal set of parameters to use for the simulations. Parametric tests, including inlet velocity tests, bubble diameter tests, and liquid viscosity tests, were carried out. A degassing rate was proposed and defined to assess the degassing process. Geometries for a surge tank consisting of a single chamber and and three connected chambers were simulated. It was found that the bubbles in the flow were degassed stage by stage due to the buoyancy effect. The degassing rate is a dynamic variable that is determined by a number of flow characteristics, such as the inlet velocity, the liquid viscosity, and the bubble size. A larger inlet velocity, a greater liquid viscosity, and a smaller bubble size result in a lower degassing rate. The drag force is an important interfacial force that influences the interaction between the two phases. The effect of the lift force is not as important as the drag force for the modeling of the interaction between the two phases. It is concluded that the CFD model used in this thesis is a reasonable tool for studying the degassing process in a surge tank.

Finally, as the validation results also confirmed that the model proposed in the study can be used to reliably solve complex flow problems, such as the multiphase flow-induced vibration and noise problem in a dynamic valve. For a two-phase flow through a dynamic valve, the simulations showed that the deformation and breakup of gas bubbles in the gap between the poppet and the valve seat generate a vibration that arises primarily from the force imbalance between the spring and the two-phase fluid-flow-induced forces on the poppet. A spectral analysis of the transient pressure force on the poppet revealed the presence of a strong cyclical behavior consisting of two major components. There was a low-frequency peak located at about 87 Hz, which was associated with the frequency of the poppet vibration (and which we interpret to be the source of the mechanical noise), and a high-frequency peak located at 450–970 Hz, which is associated with compressibility effects and unsteady vortex motions in the spring chamber. The poppet vibration and noise is influenced by numerous factors such as the flow condition, the spring system properties,

and the geometry of the valve. Larger bubbles and lower inlet velocity result in larger displacements in the poppet in a non-equilibrium condition and induce stronger forcing of the spring due to the higher pressures, which in turn amplify the poppet vibration and noise. The detailed simulations and subsequent analysis of the complex interactions of the turbulent multiphase fluid motion through the moving poppet valve have provided deeper physical insights and improved understanding of both the source and properties of the noise and vibrations generated in this complicated dynamic system.

7.1.2 Contributions

With regard to the CFD methods, the present work improves the multiphase models in ANSYS-FLUENT by implementing different interfacial force models through the use of UDFs and optimizes the FSI methodology by using a dynamic mesh in conjunction with a Scheme command file. The new model has been validated and shown to be both accurate and capable of solving complex multiphase FSI problems.

The coolant degassing problem was the first application for the new accurate multiphase model. After research on the effect of each interfacial force, an accurate and realizable CFD model for multiphase flow was applied to this problem. Parameter test results showed that the degassing process is influenced by inlet velocity, bubble size, viscosity, etc.

To date, the vibration and noise problems arising from turbulent multiphase FSI are still very new and challenging. To the author's best knowledge, only very limited related research has been reported in the open literature. An accurate and robust CFD model to solve turbulent multiphase FSI problems has been developed to investigate the vibration and noise problems associated with a dynamic valve in fuel systems of a hybrid vehicle. This problem was first suggested by our industrial partner, the Ford Motor Company, in Dearborn, Michigan, USA. Although several remedies or quick fixes were proposed by Ford engineers to solve this problem in an "engineering" fashion (e.g., by introducing a better damper to prevent noise propagating into the cabin), the fundamental noise generation

and propagation mechanisms were never understood. The results of the present numerical study provide better insight about where, when, and how this noise is generated inside a dynamic valve under turbulent multiphase flow conditions. These results can therefore form the basis for proposing guidelines and best practices to the automotive industry for eliminating the sources of noise during the early design phase.

7.2 Future Work

An Eulerian model is the most accurate multiphase model for the interaction between two fluid phases in which this interaction is modeled using interfacial forces. Drag force models and lift force models have matured for these types of application after having undergone a long research process. The virtual mass force, turbulence dispersion force, and wall lubrication force were proposed much later than the drag and lift forces. Therefore, models for these forces still need improvement. However, the development and improvement of these type of models will depend critically on the availability of new experimental data involving ever more complex multiphase flows. In consequence, experimental research should be undertaken to obtain high-quality and reliable experimental data.

For the automotive industry, computational accuracy and efficiency are always important criteria for the evaluation of a CFD model. The present research has explored these criteria in some depth. However, when a model is focused on accuracy and efficiency, other issues such as stability may be sacrificed. Further custom development of commercial software is extremely difficult for users because permissions and the ability to access the source code for such purposes it is not available. Therefore, substantial improvements in the modeling capabilities for commercial code are difficult to achieve by the end user. Further work should be considered by the development teams of commercial software to improve these modeling capabilities.

More research should be undertaken to improve the structural dynamics of the FSI

model. In this current study, the structure is rigid, without any deformation. The FSI model should be improved to allow the modeling of more complex problems involving structural deformations.

To further improve simulation results, improved methodologies for the simulation of turbulence (e.g., an LES model) should be tested in order to further investigate the role of turbulence models in multiphase flows.

APPENDICES

Appendix A

Spectral Analysis Method

A.1 Hilbert-Huang Transform

A.1.1 Introduction

The Hilbert-Huang Transform (HHT) was firstly proposed by Huang in 1996 [45]. Its advantages include high resolution on a time-frequency-amplitude characteristic, good adaptability to nonlinear and non-stationary processes and high computational efficiency.

In conventional spectral analysis methods (e.g., those based on a conventional Fast-Fourier Transform), only a frequency-amplitude decomposition of the underlying signal can be obtained. Applications of these methods are all based on an assumption that the frequency or amplitude characteristics of a signal do not vary with time. However, this assumption is not true as in many cases of signal analysis which involve intrinsically time-varying frequencies and amplitudes in the decomposition of the signal. In consequence, new signal analysis methods (e.g., Short-Time-Fourier Transform, Wavelet Transform) have been proposed in recent years to deal with such non-stationary signals. The Hilbert-

Huang Transform has become a *de facto* standard for the analysis of nonlinear and/or non-stationary signals.

A.1.2 Main Steps

The HHT involves the implementation of two main steps: namely, (1) an empirical mode decomposition (EMD) and (2) a Hilbert spectral analysis (HSA). The principal concept underpinning the HHT is the decomposition of a signal into several intrinsic mode functions (IMFs) followed subsequently by the application of the HSA to each of these IMF components in order to obtain their time-frequency-amplitude characteristics.

EMD

An EMD is the process of decomposing a signal into a number of empirical mode functions. This process is based on two conditions: namely, (1) the signal $x(t)$ should have at least two extrema (viz., a minimum and a maximum) and (2) the characteristic time scale is determined by the time interval between two extrema. With respect to the first condition, if the signal does not have extrema, the derivative of the function will be used instead in order to satisfy this condition (with integration to be undertaken after EMD in order to recover the original signal).

For a signal $x(t)$, an upper envelope (curve) $x_{\max}(t)$ connecting all the maxima and an lower envelope (curve) $x_{\min}(t)$ connecting all the minima of the signal are constructed using cubic spline interpolation. A mean function $m(t)$ of upper and lower envelopes of the signal is then obtained in accordance to

$$m(t) = [x_{\max}(t) + x_{\min}(t)] \Big/ 2. \tag{A.1}$$

This mean function is used for the identification of an IMF. The criteria which is used to determine whether a function is an IMF consists of the following: (1) the number of

extrema and the number of zero-crossings of the signal are equal or differ at most by one, and (2) $m(t)$ is always zero for the entire signal (whole dataset). Obviously, most signals are not IMFs and, therefore, need to be decomposed into a superposition of IMFs. If a signal $x(t)$ is not an IMF, then a new (transformed) signal is obtained from the following prescription:

$$h(t) = x(t) - m(t). \tag{A.2}$$

If $h(t)$ is not an IMF, then the preceding steps are repeated for $h(t)$ until an IMF is obtained. After the first IMF component $I_1(t)$ is determined, a residual signal is computed from

$$r_1(t) = x(t) - I_1(t). \tag{A.3}$$

The procedure is applied to the residual signal to obtained other IMF components $I_2(t)$, $I_3(t)$, ..., $I_k(t)$ until the residual signal no longer contains any periodic components. The stopping criterion for the EMD process is when the normalized squared difference between the two consecutive residual signals determined as

$$SD_k = \frac{\sum_{t=0}^{T} \left| r_{k-1}(t) - r_k(t) \right|}{\sum_{t=0}^{T} r_{k-1}^2(t)}, \tag{A.4}$$

is less than some prescribed tolerance. Generally, this tolerance is usually chosen to be smaller than about 0.3. When all the k IMFs have been extracted from the original signal, the final residual signal $r_k(t)$ is either a constant or a monotonic function which contains little energy of the original signal and, hence, can be ignored.

Hilbert Spectral Analysis

After the EMD process is completed, the following steps are applied to each of the IMF components. Firstly, a Hilbert transform to applied to each IMF component. For a signal $y(t)$, the Hilbert transform involves the calculation of the convolution of $y(t)$ and $1/(\pi\tau)$,

i.e. ,

$$z(t) = \frac{1}{\pi} PV\left[\int_{-\infty}^{\infty} \frac{y(\tau)}{t-\tau} d\tau\right]. \tag{A.5}$$

Secondly, a new complex signal $W(t)$ is constructed, consisting of the original signal and its Hilbert transform, as follows:

$$W(t) = y(t) + iz(t) = a(t)e^{i\theta(t)}, \tag{A.6}$$

The time-amplitude function $a(t)$ is defined as

$$\begin{cases} a(t) = [y^2(t) + z^2(t)]^{1/2} \\ \theta(t) = \arctan\left[\frac{z(t)}{y(t)}\right]. \end{cases} \tag{A.7}$$

Finally, the derivative of $\theta(t)$ determines the time-frequency function $\omega(t)$ as follows:

$$\omega(t) = \frac{d\theta(t)}{dt}. \tag{A.8}$$

Each IMF component $I_j(t)$ $(j = 1, 2, \ldots, k)$ obtained from the original signal has an time-amplitude function $a_j(t)$ and a time-frequency function $\omega_j(t)$ associated with it. Therefore, the time-frequency-amplitude function of a signal is obtained through the compositing of $a_j(t)$ and $\omega_j(t)$ for $j = 1, 2, \ldots, k$.

In the present work, the HHT has been programmed in MATLAB.

Appendix B

User-Defined Function Examples

B.1 The UDF for Interfacial Forces Models

```
#include "udf.h"
#include "sg.h"
#include "sg_mphase.h"
#include "flow.h"
#include "mem.h"
#include "math.h"
#define GG 9.81 /*gravity acceleration, m/s^2*/
#define DIAMP 0.0043 /*particle diameter, m*/
#define SIGMA 0.0716 /*surface tension, N/m*/
#define CWC 10.0 /*cut-off coefficient in wall lubrication force*/
#define CWD 6.8 /*damping coefficient in wall lubrication force*/
#define PW 1.7 /*power coefficient in wall lubrication force*/
#define RADIUS 0.0256 /*radius of the pipe*/
#define SIGMA_ra 0.9
```

```
/* turbulent Prantle number in turbulence dispersion force*/

DEFINE_SOURCE(wx,c,t,dS,eqn)
{
Thread *tm = THREAD_SUPER_THREAD(t);
Thread **pt = THREAD_SUB_THREADS(tm);
int w[4];
Domain *domain;
int i=1,p=1;
face_t f;
Thread *tf;
real dm;
real d[ND_ND],d_old[ND_ND],x[ND_ND],y[ND_ND],e_n[ND_ND],vel_w[ND_ND],
vel_a[ND_ND],vel_slip[ND_ND],FWL[ND_ND],FL[ND_ND],vel_g[ND_ND][ND_ND],
aa[ND_ND],gg[ND_ND],bb,ff,dd[ND_ND],ee;
real source,abs_v,reyp,dH,Eod,fEod,VOF_a,R,CL_wa,yW,CWL,CW3,CDdis,CDvis,
CDcap,CD,VOF_w,lambtRT,fterm,NUT,rho_w,rho_a,mu_w,Eo;
/*WallDistance*/
domain=Get_Domain(1);
d[0]=1000;
d[1]=1000;
d[2]=1000;
w[0]=6;
C_CENTROID(x,c,t);
for (i=1; i<=1; i++)
{
p=w[i-1];
tf=Lookup_Thread(domain,p);
begin_f_loop(f,tf)
{
```

```
F_CENTROID(y,f,tf);
NV_V(d_old,=,d);
NV_VV(d,=,x,-,y);
if (NV_MAG(d)>=NV_MAG(d_old))
{NV_V(d,=,d_old);}
dm=NV_MAG(d);
NV_VS(e_n,=,d,/,dm);
}
end_f_loop(f,tf)
}
yW=NV_MAG(d);
vel_w[0]=C_U(c,pt[0]);
vel_w[1]=C_V(c,pt[0]);
vel_w[2]=C_W(c,pt[0]);
vel_a[0]=C_U(c,pt[1]);
vel_a[1]=C_V(c,pt[1]);
vel_a[2]=C_W(c,pt[1]);
NV_VV(vel_slip,=,vel_w,-,vel_a);
abs_v=NV_MAG(vel_slip);
rho_w=C_R(c,pt[0]);
rho_a=C_R(c,pt[1]);
mu_w=C_MU_L(c,pt[0]);
/*Lift Force*/
Eo=GG*(rho_w-rho_a)*DIAMP*DIAMP/SIGMA;
reyp=rho_w*abs_v*DIAMP/mu_w;
dH=DIAMP*pow((1+0.163*pow(Eo,0.757)),1/3);
Eod=GG*(rho_w-rho_a)*dH*dH/SIGMA;
fEod=0.00105*pow(Eod,3)-0.0159*pow(Eod,2)-0.0204*Eod+0.474;
if (Eod>10)
CL_wa=-0.27;
```

```
else if (Eod<4)
CL_wa=MIN(0.288*tanh(0.121*reyp),fEod);
else
CL_wa=fEod;
VOF_a=C_VOF(c,pt[1]);
VOF_w=C_VOF(c,pt[0]);
ff=-CL_wa*VOF_a*rho_w;
FL[0]=ff*(vel_slip[1]*(C_V_G(c,pt[0])[0]-C_U_G(c,pt[0])[1])-vel_slip[2]*
(C_U_G(c,pt[0])[2]-C_W_G(c,pt[0])[0]));
FL[1]=ff*(vel_slip[2]*(C_W_G(c,pt[0])[1]-C_V_G(c,pt[0])[2])-vel_slip[0]*
(C_V_G(c,pt[0])[0]-C_U_G(c,pt[0])[1]));
FL[2]=ff*(vel_slip[0]*(C_U_G(c,pt[0])[2]-C_W_G(c,pt[0])[0])-vel_slip[1]*
(C_W_G(c,pt[0])[1]-C_V_G(c,pt[0])[2]));
/*Wall Lubrication Force*/
if (Eo<=5)
CW3=exp(-0.933*Eo+0.179);
else if (Eo<=33)
CW3=0.00599*Eo-0.0187;
else
CW3=0.179;
CWL=CW3*MAX(0,(1-yW/CWC/DIAMP)/(CWD*yW*pow(yW/CWC/DIAMP,
(PW-1.0))));
NV_V_VS(dd,=,vel_slip,-,vel_slip,*,NV_DOT(e_n,vel_slip));
ee=CWL*VOF_a*rho_w*NV_MAG2(dd);
NV_VS(FWL,=,e_n,*,ee);
C_UDMI(c,tm,0)=FL[0];
C_UDMI(c,tm,1)=FL[1];
C_UDMI(c,tm,2)=FL[2];
C_UDMI(c,tm,3)=FWL[0];
C_UDMI(c,tm,4)=FWL[1];
```

```
C_UDMI(c,tm,5)=FWL[2];
return C_UDMI(c,tm,0);}

DEFINE_SOURCE(wy,c,t,dS,eqn)
{
Thread *tm = THREAD_SUPER_THREAD(t);
return C_UDMI(c,tm,1);
}
DEFINE_SOURCE(wz,c,t,dS,eqn)
{
Thread *tm = THREAD_SUPER_THREAD(t);
return C_UDMI(c,tm,2);
}
DEFINE_SOURCE(ax,c,t,dS,eqn)
{
Thread *tm = THREAD_SUPER_THREAD(t);
return -C_UDMI(c,t,0);
}
DEFINE_SOURCE(ay,c,t,dS,eqn)
{
Thread *tm = THREAD_SUPER_THREAD(t);
return -C_UDMI(c,tm,1);
}
DEFINE_SOURCE(az,c,t,dS,eqn)
{
Thread *tm = THREAD_SUPER_THREAD(t);
return -C_UDMI(c,tm,2);
}
```

B.2 UDF for FSI

```
# include "udf.h"
# include "mem.h"
# include "dynamesh_tools.h"
# define DEBUG 1
# define NO_OF_VALVES 1
# define NO_OF_ZONES 11
# define INITIAL_LIFT 1.68e-4
# define BMODULUS 2.2e9
# define rho_ref 852.3
static int valveid[NO_OF_VALVES][NO_OF_ZONES]={{50056,-1}};
static real lift_min[NO_OF_VALVES]={1e-5};
static real lift_max[NO_OF_VALVES]={3e-3};
static real mass[NO_OF_VALVES]={0.005};
static real volume[NO_OF_VALVES]={5e-7};
static real stiffness[NO_OF_VALVES]={-600};
static real stretch_at_closed[NO_OF_VALVES]={0};
static real rest_conts[NO_OF_VALVES]={0};
static real current_vel_mag[NO_OF_VALVES]={0};
static real axis[NO_OF_VALVES][ND_ND]={{1, 0}}; /* normalized */
static real gravity_direction[ND_ND]={-1, 0}; /* normalized */
static real r_rp_closed[NO_OF_VALVES][ND_ND]={{0,0}};
static real cur_r_rp[NO_OF_VALVES][ND_ND]={{INITIAL_LIFT, 0}};
static real previous_time[NO_OF_VALVES]={0};

DEFINE_PROPERTY(water_density,c,t)
{
real rho;
real p, dp, p_operating;
```

```
p_operating = RP_Get_Real("operating-pressure");
p = C_P(c,t);
dp = p-p_operating;
rho = rho_ref/(1.0-dp/BMODULUS);
return rho;
}
static void f_valve(int valveNo, void *dt, real *cg_vel, real *cg_omega,
real time, real dtime)
{
#if !RP_HOST
real tmp[ND_ND], dv, current_vel[ND_ND], CG[ND_ND], force[ND_ND],
moment[ND_ND], stretch;
real aero_force[ND_ND], aero_force_axis, spring_force, gravity_force,
net_force,
r_rp_new[NO_OF_VALVES][ND_ND];
int i;
Thread * tf;
Domain * domain;
face_t f;
real NV_VEC(A);
real NV_VEC(x);
real NV_VEC(Force_viscous);
static real cg_vel_saved[NO_OF_VALVES][ND_ND];
static FILE *fposi;
/* Do the calculation if the new time step */
if(fabs(previous_time[valveNo]-time)>0.2*dtime)
{
fposi=fopen("position.dat","a");
/* reset velocities */
NV_S (cg_vel, =, 0.0);
```

```
NV_S (cg_omega, =, 0.0);
/* Check to see if there is data */
if (!Data_Valid_P ())
{
Message0("\n\nNo data->No mesh motion!!!\n\n");
return;
}
/*Calculate force*/
domain = THREAD_DOMAIN (DT_THREAD ((Dynamic_Thread *)dt));
i=0;
NV_S(aero_force,=,0);
while(valveid[valveNo][i]>=0)
{
tf=Lookup_Thread(domain, valveid[valveNo][i]);
NV_S (CG, =, 0.0);
begin_f_loop(f,tf)
{
F_AREA(A,f,tf);
/*Message0("\nA0=%10.4e,A1=%10.4e,x0=%10.4e,x1=%10.4e\n",
A[0],A[1],x[0],x[1]);*/
NV_S(A,*=,F_P(f,tf));
NV_V(force,+=,A);
}
end_f_loop(f,tf);
Compute_Force_And_Moment (domain, tf, CG, aero_force, moment, 1);
i++;
}
aero_force_axis=NV_DOT(aero_force, axis[valveNo]);
NV_VV(tmp,=,r_rp_closed[valveNo],+,cur_r_rp[valveNo]);
stretch = stretch_at_closed[valveNo]+NV_DOT(tmp,axis[valveNo]);
```

```
spring_force=stiffness[valveNo]*stretch;
gravity_force = 9.81*mass[valveNo]*NV_DOT(gravity_direction,
axis[valveNo]);
net_force=spring_force+aero_force_axis+gravity_force;
dv=net_force/mass[valveNo]*dtime;
/* Update velocity */
current_vel_mag[valveNo]+=dv;
/* Calculate the C.G location and velocity if it does not hit the boundary */
NV_VS(current_vel,=,axis[valveNo],*,current_vel_mag[valveNo]);
NV_VS(tmp,=,current_vel,*,dtime);
NV_VV(r_rp_new[valveNo],=,cur_r_rp[valveNo],+,tmp);
NV_VV(tmp,=,r_rp_new[valveNo],-,r_rp_closed[valveNo]);
if((NV_DOT(tmp,axis[valveNo]))<1.0000001*(lift_min[valveNo]))
{
cg_vel[0]=0;
NV_V(r_rp_new[valveNo],=,cur_r_rp[valveNo]);
current_vel_mag[valveNo]=0;
current_vel[0]=0;
Message0("\n Valve hits the min valve lift\n");
}
else if((NV_DOT(tmp,axis[valveNo]))>0.99999999*(lift_max[valveNo]))
{
cg_vel[0]=0;
NV_V(r_rp_new[valveNo],=,cur_r_rp[valveNo]);
current_vel_mag[valveNo]=0;
current_vel[0]=0;
Message0("\n Valve hits the max valve lift\n");
}
else
{
```

```
NV_VV(tmp,=,r_rp_new[valveNo],-,cur_r_rp[valveNo]);
NV_VS(cg_vel,=,tmp,/,dtime);
NV_V(cur_r_rp[valveNo],=,r_rp_new[valveNo]);
NV_V(cg_vel_saved[valveNo],=,cg_vel);
}
previous_time[valveNo]=time;
/* debug info */
if DEBUG
{
Message0("\nCurrent valve lift =%10.3e\n", NV_DOT(cur_r_rp[valveNo],
axis[valveNo]));
Message0("\nCurrent valve velocity (negative if pointing to positive x) =
%10.3e\n", current_vel_mag[valveNo]-dv);
Message0("\naero force =%10.3e\n", aero_force[0]);
Message0("\n(stretching at closed, stretching, force)=(%10.3e, %10.3e,
%10.3e)\n",stretch_at_closed[valveNo], stretch, spring_force);
Message0("\n(net_force, spring force, aero force, gravity_force)=(%10.3e,
%10.3e, %10.3e, %10.3e)\n",net_force, spring_force, aero_force_axis,
gravity_force);
Message0("\nNext valve velocity (negative if pointing to positive x)=
%11.3e\n", current_vel_mag[valveNo]);
Message0("\nNext valve lift =%10.3e\n", NV_DOT(r_rp_new[valveNo],
axis[valveNo]));
fprintf(fposi,"\n%14.5e,%14.5e,%14.5e,%14.5e,%14.5e",time,
net_force,aero_force[0],force[0],NV_DOT(cur_r_rp[valveNo], axis[valveNo]));
fclose(fposi);
}
}
else
{
```

```
NV_V(cg_vel,=,cg_vel_saved[valveNo]);
}
node_to_host_real(current_vel_mag, NO_OF_VALVES);
node_to_host_real(cur_r_rp[0], NO_OF_VALVES*ND_ND);
node_to_host_real(previous_time, NO_OF_VALVES);
}
DEFINE_CG_MOTION(valve, dt, cg_vel, cg_omega, time, dtime)
{
f_valve(0, dt, cg_vel, cg_omega, time, dtime);
node_to_host_real(cg_vel,ND_ND);
node_to_host_real(cg_omega,ND_ND);
}
static void write_data(FILE *fp)
{
int i, j;
for(i=0; i<NO_OF_VALVES; i++)
{
fprintf(fp, "%e  ", current_vel_mag[i]);
}
fprintf(fp, "\n");
for(i=0; i<NO_OF_VALVES; i++)
{
for(j=0; j<ND_ND; j++)
{
fprintf(fp, "%e  ", cur_r_rp[i][j]);
}
fprintf(fp, "\n");
}
fprintf(fp, "\n");
for(i=0; i<NO_OF_VALVES; i++)
```

```
{
fprintf(fp, "%e  ", previous_time[i]);
}
}
static void read_data(FILE * fp)
{
int i, j;
for(i=0; i<NO_OF_VALVES; i++)
{
if RP_DOUBLE
fscanf(fp, "%le", current_vel_mag+i);
else
fscanf(fp, "%e", current_vel_mag+i);
endif
}
for(i=0; i<NO_OF_VALVES; i++)
{
for(j=0; j<ND_ND; j++)
{
if RP_DOUBLE
fscanf(fp, "%le", cur_r_rp[i]+j);
else
fscanf(fp, "%e", cur_r_rp[i]+j);
endif
}
}
 for(i=0; i<NO_OF_VALVES; i++)
{
if RP_DOUBLE
fscanf(fp, "%le", previous_time+i);
```

```
else
fscanf(fp, "%e", previous_time+i);
endif
}
}

DEFINE_RW_FILE(writer, fp)
{
Message0("Writing UDF data to data file...\n");
if PARALLEL
if RP_HOST
write_data(fp);
else
write_data(fp);
}

DEFINE_RW_FILE(reader, fp)
{
Message0("Reading UDF data from data file...\n");
if PARALLEL
if RP_HOST
read_data(fp);
else
read_data(fp);
host_to_node_real(current_vel_mag, NO_OF_VALVES);
host_to_node_real(cur_r_rp[0], NO_OF_VALVES*ND_ND);
host_to_node_real(previous_time, NO_OF_VALVES);
}
```

Appendix C

Scheme File Example

C.1 The Scheme File for FSI

```
(rp-var-define 'timeb 2.05 'real #f)
(rp-var-define 'mlcg 0 'real #f)
(rp-var-define 'klcg 0 'real #f)
(rp-var-define 'nlcg 0 'real #f)
(rp-var-define 'setao 0 'real #f)
(rp-var-define 'omegao 0 'real #f)
(rp-var-define 'domegao 0 'real #f)
(rp-var-define 'mo 0 'real #f)
(rp-var-define 'domegaoi 0 'real #f)
(rp-var-define 'moi 0 'real #f)
(rp-var-define 'mi 0 'real #f)
(rp-var-define 'dmo 0 'real #f)
(rp-var-define 'el 0.01 'real #f)
(define x 1)
```

```
(define y 1)
(define mg 1)
(define kg 0)
(define ng 1)
(set! ng y)
(define setag 5.67911e-001)
(define omegag 1.97157e+000)
(define domegag 6.42030e-002)
(define mog 2.50325e-005)
(define domegagi 6.78603e-002)
(define mogi -1.89504e-005)
(define mgi 2.50325e-005)
(define dmog -1.20281e-004)
(do ((x 1 (+ x 1)) ) ((> x 6000))
(ti-menu-load-string  (format #f "file/read-case-data heartvalve~05d" y))
(rpsetvar 'mlcg mg)
(rpsetvar 'klcg kg)
(rpsetvar 'nlcg ng)
(rpsetvar 'setao setag)
(rpsetvar 'omegao omegag)
(rpsetvar 'domegao domegag)
(rpsetvar 'mo mog)
(rpsetvar 'domegaoi domegagi)
(rpsetvar 'moi mogi)
(rpsetvar 'mi mgi)
(rpsetvar 'dmo dmog)
(ti-menu-load-string "solve/set/time-step 0.0049")
(ti-menu-load-string "solve/dual-time-iterate 1")
(ti-menu-load-string  (format #f "file/write-case-data ~05d-~07d" y x))
(set! mg (rpgetvar 'mlcg))
```

```
(set! kg (rpgetvar 'klcg))
(set! ng (rpgetvar 'nlcg))
(set! setag (rpgetvar 'setao))
(set! omegag (rpgetvar 'omegao))
(set! domegag (rpgetvar 'domegao))
(set! mog (rpgetvar 'mo))
(set! domegagi (rpgetvar 'domegaoi))
(set! mogi (rpgetvar 'moi))
(set! mgi (rpgetvar 'mi))
(set! dmog (rpgetvar 'dmo))
(if (> (rpgetvar 'mlcg) 0)
(begin
(set! y (+ y 1))
(ti-menu-load-string (format #f "file/write-case-data heartvalve~05d" y)))))
```

References

[1] Google images. http://goo.gl/s8yAJM. [Online; accessed Mar. 11, 2015].

[2] Google images. http://goo.gl/3ijNLK. [Online; accessed Mar. 11, 2015].

[3] Google images. http://goo.gl/uUJv7H. [Online; accessed Mar. 11, 2015].

[4] *ANSYS-FLUENT Theory Guide*. Number November. ANSYS Inc., 2011.

[5] G. Ahmadi and D. Ma. A thermal-dynamical formulation for dispersed multiphase turbulent flows—1 Basic theory. *Multiphase Flow*, 16(2):323–340, 1990.

[6] X. Amandolèse and P. Hémon. Vortex-induced vibration of a square cylinder in wind tunnel. *Comptes Rendus - Mecanique*, 338:12–17, 2010.

[7] S. P. Antal, R. T. Lahey, and J. E. Flaherty. Analysis of phase distribution in fully developed laminar bubbly two-phase flow. *International Journal of Multiphase Flow*, 17(5):635–652, Sept. 1991.

[8] S. P. Antal, M. Z. Podowski, R. T. J. Lahey, D. Barber, and C. Delfino. Multidimensional modeling of developing two-phase flows in a large adiabatic riser channel. In *Proceedings NURETH-11*, Avignon, France, 2005.

[9] T. R. Auton. The lift force on a spherical body in a rotational flow. *Journal of Fluid Mechanics*, 183:199–218, 1987.

[10] R. Bannari, F. Kerdouss, B. Selma, A. Bannari, and P. Proulx. Three-dimensional mathematical modeling of dispersed two-phase flow using class method of population balance in bubble columns. *Computers and Chemical Engineering*, 32(12):3224–3237, Dec. 2008.

[11] P. Bearman and E. Obasaju. An experimental study of pressure fluctuations on fixed and oscillating square-section cylinders. *Journal of Fluid Mechanics*, 119:297–321, 1982.

[12] A. Behzadi, R. I. Issa, and H. Rusche. Effects of turbulence on inter-phase forces in dispersed flow. In *the 4th International Conference of Multiphase Flow*, New Orleans, USA, 2001.

[13] F. K. Benra, H. J. Dohmen, J. Pei, S. Schuster, and B. Wan. A comparison of one-way and two-way coupling methods for numerical analysis of fluid-structure interactions. *Journal of Applied Mathematics*, 2011.

[14] A. Biesheuvel and S. Spoelstra. The added mass coefficient of a dispersion of spherial gas bubbles in liquid. *International Journal of Multiphase Flow*, 15(6):911–924, 1989.

[15] J. Brackbill, D. Kothe, and C. Zemach. A continuum method for modeling surface tension. *Journal of Computational Physics*, 100:335–354, 1992.

[16] L. Brahmasani, S. Solomon, and P. Khan. A secondary de-aeration circuit for an engine cooling system with atmospheric recovery bottle to improve de-aeration. *SAE Technical Paper*, pages 2014–01–2342, 2014.

[17] A. D. Burns, T. Frank, I. Hamill, and J. Shi. The Favre averaged drag model for turbulent dispersion in Eulerian multi-phase flows. In *5th International Conference on Multiphase Flow*, number 392, page 392, Yokohama, Japan, 2004.

[18] D. R. Caldwell. Degas tank for engine cooling system, US Patent No. 5,329,899, 1994.

[19] J. T. Cieszko and C. L. Moon. Method and apparatus for cooling and deaerating internal combustion engine coolant, US Patent No. 3,939,901, 1976.

[20] J. Clements. Working of hybrid cars. http://www.circuitstoday.com/working-of-hybrid-cars, 2010. [Online; accessed Mar. 11, 2015].

[21] R. Clift, J. R. Grace, and M. E. Weber. *Bubbles, Drops and Particles*. Aademic Press, Orlando, 1978.

[22] C. T. Crowe, J. D. Schwarzkopf, M. Sommerfeld, and Y. Tsuji. *Multiphase Flows with Droplets and Particles*. CRC Press, Boca Raton, 2nd edition, 2011.

[23] S. K. Dahl, J. Vierendeels, J. Degroote, S. Annerel, L. R. Hellevik, and B. Skallerud. FSI simulation of asymmetric mitral valve dynamics during diastolic filling. *Computer Methods in Biomechanics and Biomedical Engineering*, 15(2):121–130, 2012.

[24] J. M. Dalla Ville. *Micrometrics*. Pitman Publishing Co., New York, 1948.

[25] N. G. Deen, T. Solberg, and B. H. Hjertager. Large eddy simulation of the gas–liquid flow in a square cross-sectioned bubble column. *Chemical Engineering Science*, 56:6341–6349, 2001.

[26] M. E. Díaz, A. Iranzo, D. Cuadra, R. Barbero, F. J. Montes, and M. A. Galán. Numerical simulation of the gas–liquid flow in a laboratory scale bubble column. *Chemical Engineering Journal*, 139(2):363–379, June 2008.

[27] M. Dong. V34x StV diesel filter fuel flow paths. Technical report, Ford Motor Company, 2011.

[28] M. Dong. Personal communication, 2012.

[29] D. A. Drew and R. T. Lahey JR. The virtual mass and lift force on a sphere in rotating and straining inviscid flow. *International Journal of Multiphase Flow*, 13(I):113–121, 1987.

[30] K. Dumont, J. M. A. Stijnen, J. Vierendeels, F. N. Van De Vosse, and P. R. Verdonck. Validation of a fluid-structure interaction model of a heart valve using the dynamic mesh method in FLUENT. *Computer Methods in Biomechanics and Biomedical Engineering*, 7(3):139–146, June 2004.

[31] K. Dumont, J. Vierendeels, R. Kaminsky, G. van Nooten, P. Verdonck, and D. Bluestein. Comparison of the hemodynamic and thrombogenic performance of two bileaflet mechanical heart valves using a CFD/FSI model. *Journal of Biomechanical Engineering*, 129(4):558–65, Aug. 2007.

[32] N. Forsythe and J.-D. Muller. Simulation of flexible and mechanical heart valves. In *the 4th Physiological Flow Meeting*, April 2007.

[33] T. Frank. Advances in computational fluid dynamics (CFD) of 3-dimensional gas-liquid multiphase flows. In *NAFEMS Seminar "Simulation of Complex Flows (CFD)"*, pages 1–18, Wiesbaden, Germany, 2005.

[34] T. Frank, C. Lifante, H.-M. Prasser, and F. Menter. Simulation of turbulent and thermal mixing in T-junctions using URANS and scale-resolving turbulence models in ANSYS-CFX. *Nuclear Engineering and Design*, 240(9):2313–2328, Sept. 2010.

[35] T. Frank, P. Zwart, E. Krepper, H.-M. Prasser, and D. Lucas. Validation of CFD models for mono- and polydisperse air–water two-phase flows in pipes. *Nuclear Engineering and Design*, 238(3):647–659, Mar. 2008.

[36] T. Frank, P. J. Zwart, J. Shi, E. Krepper, D. Lucas, and U. Rohde. Inhomogeneous MUSIG model – a population balance approach for poly-dispersed bubbly flows. In *International Conference of Nuclear Energy for New Europe 2005*, Sept. 2005.

[37] A. Garg, R. S. Marano, A. D. Colvin, and J. M. Jakupco. In-vehicle engine coolant void fraction and de-aeration monitoring using a computerized electrical conductivity method. In *SAE Technical Paper*, number 970938, 1997.

[38] J. Gong, Z. Zhou, and B. Liu. Using the unstructured dynamic mesh to simulate multi-store separating from aircraft. *Procedia Engineering*, 16:572–580, 2011.

[39] A. D. Gosman, C. Lekakou, S. Politis, R. I. Issa, and M. K. Looney. Multidimensional modeling of turbulent two-phase flows in stirred vessels. *AIChE Journal*, 38(12):1946–1956, Dec. 1992.

[40] S. Grevskott, M. P. Dudukovid, and H. F. Svendsen. Liquid circulation, bubble size distributions, and solids movement in two- and three-phase bubble columns. *Chemical Engineering Science*, 51(10):1703–1713, 1996.

[41] A. Gupta and S. Roy. Euler-Euler simulation of bubbly flow in a rectangular bubble column: experimental validation with radioactive particle tracking. *Chemical Engineering Journal*, 225:818–836, Nov. 2013.

[42] J. Hines, G. P. Thompson, and F. S. Lien. A turbulent flow over a square cylinder with prescribed and autonomous motions. *Engineering Applications of Computational Fluid Mechanics*, 3(4):573–586, 2009.

[43] C. Hirt and B. Nichols. Volume of fluid (VOF) method for the dynamics of free boundaries. *Journal of Computational Physics*, 39(1):201–225, Jan. 1981.

[44] B. P. B. Hoomans, J. A. M. Kuipers, W. J. Briels, and W. P. M. Van Swaaij. Discrete particle simulation of bubble and slug formation in a two-dimensional gas-fluidised bed: a hard-sphere approach. *Chemical Engineering Science*, 51(1):99–118, Jan. 1996.

[45] N. E. Huang, S. R. Long, and Z. Shen. The mechanism for frequency downshift in nonlinear wave evolution. *Advances in Applied Mechanics*, 32:59–117, 1996.

[46] N. E. Huang and S. S. P. Shen. *Hilbert Huang Transform and Its Applications*. World Scientific Publishing Co. Pte. Ltd., Singapore, 2005.

[47] R. G. Huff. Noise generated by flow through large butterfly valves. *NASA Technical Memorandum*, 88911:1–16, 1987.

[48] J. W. Huthison. *ISA Handbook of Control Valves*. Instrument Society of America, 1971.

[49] M. Iguchi and O. J. Ilegbusi. *Modeling Multiphase Materials Processes: Gas-Liquid Systems*. Springer, New York, USA, 2011.

[50] M. Ishii and N. Zuber. Drag coefficient and relative velocity in bubbly, droplet or particulate flows. *AIChE Journal*, 25(5):843–855, 1979.

[51] K. Johansson, A. Magnesson, R. Rundqbist, and A. E. Almstedt. Study of two gas-particle flows using Eulerian/Eulerian and two-fluid models. In *the 4th International Conference of Multiphase Flow*, New Orleans, USA, 2001.

[52] J. E. Juliá, Y. Liu, S. Paranjape, and M. Ishii. Upward vertical two-phase flow local flow regime identification using neural network techniques. *Nuclear Engineering and Design*, 238(1):156–169, Jan. 2008.

[53] F. D. Jury. Understanding IEC Aerodynamic Noise Prediction for Control Valves. http://www.documentation.emersonprocess.com/groups/public/documents/tech_bulletin_monograph/d350489x012.pdf. [Online; accessed Mar. 8, 2015].

[54] N. Kawashima and H. Kawamura. Numerical analysis of LES of flow past a long square cylinder. In *the ERCOFTAC Workshop*, pages 413–422, Grenoble, France, 1996.

[55] N. I. Kolev. *Multiphase Flow Dynamics*. Springer, 3rd edition, 2007.

[56] R. Kurose, R. Misumi, and S. Komori. Drag and lift forces acting on a spherical bubble in a linear shear flow. *International Journal of Multiphase Flow*, 27:1247–1258, 2001.

[57] K. Kzuk. OEM coolant header tank. http://www.nsxcb.co.uk/entry.php?1321-OEM-Coolant-Header-Tank, 2014. [Online; accessed Mar. 11, 2015].

[58] S. Lain, D. Broder, M. Sommerfeld, and M. F. Goz. Modelling hydrodynamics and turbulence in a bubble column using the Euler-Lagrange procedure. *International Journal of Multiphase Flow*, 28:1381–1407, 2002.

[59] L. W. Lassiter. Fluid valve noise suppressor, US Patent No. 3,238,955, 1966.

[60] D. Legendre and J. Magnaudet. The lift force on a spherical bubble in a viscous linear shear flow. *Journal of Fluid Mechanics*, 368:81–126, 1998.

[61] M. Li. Introduction to cooling system. Technical report, ABC Group Inc., 2013.

[62] C. Ljus. *On Particle Transport and Turbulence Modification in Air-Particle Flows*. Ph.D. thesis, Chalmers University of Technology, 2000.

[63] M. Lopez de Bertodano, R. Lahey, and O. Jones. Turbulent bubbly two-phase flow data in a triangular duct. *Nuclear Engineering and Design*, 146:43–52, 1994.

[64] M. Lopez de Bertodano, F. J. Moraga, D. A. Drew, and R. T. Lahey. The modeling of lift and dispersion forces in two-fluid model simulations of a bubbly jet. *Journal of Fluids Engineering*, 126(4):573, 2004.

[65] D. Lucas, M. Beyer, L. Szalinski, and P. Schütz. A new database on the evolution of air–water flows along a large vertical pipe. *International Journal of Thermal Sciences*, 49(4):664–674, Apr. 2010.

[66] D. Lucas, E. Krepper, and H.-M. Prasser. Development of co-current air–water flow in a vertical pipe. *International Journal of Multiphase Flow*, 31(12):1304–1328, Dec. 2005.

[67] D. Lucas, E. Krepper, and H.-M. Prasser. Use of models for lift, wall and turbulent dispersion forces acting on bubbles for poly-disperse flows. *Chemical Engineering Science*, 62(15):4146–4157, Aug. 2007.

[68] D. A. Lyn, S. Einav, W. Rodi, and P. H. J. A laser-doppler velocimetry study of ensemble-averaged characteristics of the turbulent near wake of a square cylinder. *J. Fluid Mech.*, 304:285–319, 1995.

[69] A. McLane and W. D. Kramer. Automotive coolant control valve, US Patent No. 6,688,333, 2004.

[70] R. Mei and J. F. Klausnert. Shear lift force on spherical bubbles. *International Journal of Heat and Fluid Flow*, 15(1):62–65, 1994.

[71] F. R. Menter. Two-equation eddy-viscosity turbulence models for engineering applications. *AIAA Journal*, 32:1598–1605, 1994.

[72] J. Monsen. Valve noise reduction strategies. http://www.valin.com/blog/14-fluid-management-/311-valve-noise-reduction-strategies, 2011. [Online; accessed Mar. 11, 2015].

[73] S. A. Morsi and A. J. Alexander. An investigation of particle trajectories in two-phase flow systems. *Journal of Fluid Mechanics*, 55:193–208, 1972.

[74] S. Murakami and A. Mochida. On turbulent vortex shedding flow past 2D square cylinder predicted by CFD. *Journal of Wind Engineering and Industrial Aerodynamics*, 54-55:191–211, Feb. 1995.

[75] K. Nozawa and T. Tamura. (LES of flow past a square cylinder using embedded meshes. In *the ERCOFTAC Workshop*, pages 409–412, Grenoble, France.

[76] J. S. Ochoa and N. Fueyo. Large-eddy simulation of the flow past a square cylinder. In *PHOENICS 10th International User Conference*, Melbourne, Australia, 2004.

[77] A. Okajima. Strouhal numbers of rectangular cylinders. *Journal of Fluid Mechanics*, 123:379, 1982.

[78] Y. Otsuki, K. Washizu, H. Tomizawa, and A. Ohya. A note on the aeroelastic instability of a prismatic bar with square section. *Journal of Sound and Vibration*, 34(2):233–248, 1974.

[79] Y. Pan, M. P. Dudukovic, and M. Chang. Dynamic simulation of bubbly flow in bubble columns. *Chemical Engineering Science*, 54:2481–2489, 1999.

[80] E. E. Panagiotopoulos and S. D. Kyparissis. CFD transonic store separation trajectory predictions with comparison to wind tunnel investigations. *International Journal of Engineering*, 6(3):538–553.

[81] M. J. Pang and J. J. Wei. Analysis of drag and lift coefficient expressions of bubbly flow system for low to medium Reynolds number. *Nuclear Engineering and Design*, 241(6):2204–2213, June 2011.

[82] D. Pfleger, S. Gomes, N. Gilbert, and H.-G. Wagner. Hydrodynamic simulations of laboratory scale bubble columns: Fundamental studies of the Eulerian–Eulerian modelling approach. *Chemical Engineering Science*, 54(21):5091–5099, Nov. 1999.

[83] M. Piddock, I. Pegg, and L. Routledge. Internal combustion engine coolant flow, US Patent No. 7,263,954, 2007.

[84] M. Pourquie, M. Breuer, and W. Rodi. Computed test case: square cylinder. In *the ERCOFTAC Workshop*, pages 375–379, Grenoble, France, 1996.

[85] L. Prandtl. Essentials of fluid dynamics. *Quarterly Journal of the Royal Meteorological Society*, 79(342):570, 1952.

[86] H.-M. Prasser, M. Beyer, H. Carl, S. Gregor, D. Lucas, H. Pietruske, P. Schütz, and F. Weiss. Evolution of the structure of a gas–liquid two-phase flow in a large vertical pipe. *Nuclear Engineering and Design*, 237(15-17):1848–1861, Sept. 2007.

[87] W. Qian, X. Wang, and Z. Sha. Effect of non-drag forces on the numerical simulation of bubbly flow in a bubble column. *Chemical Engineering transations*, 17:573–578, 2009.

[88] S. D. Rallu. *A Multiphase Fluid-Structure Computational Framework for Underwater Implosion Problems*. Ph.D. thesis, Stanford University, 2009.

[89] W. J. Rider and D. B. Kothe. Reconstructing volume tracking. *Journal of Computational Physics*, 141(2):112–152, Apr. 1998.

[90] P. G. Saffman. The lift on a small sphere in a slow shear flow. *Journal of Fluid Mechanics*, 22(02):385, Mar. 2006.

[91] L. Schiller and A. Nauman. A drag oefficient correlation. *Ver. Deutsch. Ing.*, 77:318–320, 1935.

[92] B. Selma, R. Bannari, and P. Proulx. Simulation of bubbly flows: Comparison between direct quadrature method of moments (DQMOM) and method of classes (CM). *Chemical Engineering Science*, 65(6):1925–1941, Mar. 2010.

[93] G. M. Smith, R. A. Reese, L. S. Lubaczewski, P. A. Varma, G. J. DeNyse, and C. J. Hauer. Deaeration bottle for liquid cooling systems for automotive vehicle engines, US Patent No. 6,216,646, 2001.

[94] D. O. Snyder, E. K. Koutsavdis, and J. S. R. Anttonen. Transonic store separation using unstructured CFD with dynamic meshing. In *33rd AIAA Fluid Dynamics Conference and Exhibit*, pages AIAA 2003–3919, Orlando, USA, 2003.

[95] M. R. Snyder, O. M. Knio, J. Katz, and O. P. Le Maitre. Statistical analysis of small bubble dynamics in isotropic turbulence. *Physics of Fluids*, 19:065108, 2007.

[96] M. V. Tabib, S. A. Roy, and J. B. Joshi. CFD simulation of bubble column—An analysis of interphase forces and turbulence models. *Chemical Engineering Journal*, 139(3):589–614, June 2008.

[97] M. V. Tabib and P. Schwarz. Quantifying sub-grid scale (SGS) turbulent dispersion force and its effect using one-equation SGS large eddy simulation (LES) model in a gas–liquid and a liquid–liquid system. *Chemical Engineering Science*, 66(14):3071–3086, July 2011.

[98] I. Taylor and M. Vezza. Calculation of the flow field around a square section cylinder undergoing forced transverse oscillations using a discrete vortex method. *Journal of Wind Engineering and Industrial Aerodynamics*, 82:271–291, 1999.

[99] S. Thakre and J. Joshi. CFD simulation of bubble column reactors: Importance of drag force formulation. *Chemical Engineering Science*, 54(21):5055–5060, Nov. 1999.

[100] G. P. Thompson. *A Numerical Study of the Vortex Shedding from a Square Cylinder in a Uniform Cross-Flow*. Master thesis, University of Waterloo, 2003.

[101] A. Tomiyama. Struggle with computaional bubble dynamcs. *Multiphase Science and Technology*, 10(4):369–405, 1998.

[102] A. Tomiyama. Drag, lift and virtual mass forces acting on a single bubble. In *3rd International Symposium on Two-Phase Flow Modelling and Experimentation*, Pisa, 2004.

[103] A. Tomiyama, G. Celata, S. Hosokawa, and S. Yoshida. Terminal velocity of single bubbles in surface tension force dominant regime. *International Journal of Multiphase Flow*, 28(9):1497–1519, Sept. 2002.

[104] K. Tsuchiya, A. Furumoto, L.-S. Fan, and J. Zhang. Suspension viscosity and bubble rise velocity in liquid-solid fluidized beds. *Chemical Engineering Science*, 52(18):3053–3066, Sept. 1997.

[105] Y. Tsuji, T. Kawaguchi, and T. Tanaka. Discrete particle simulation of two-dimensional fluidized bed. *Powder Technology*, 77(1):79–87, Oct. 1993.

[106] J.-M. Vaassen, P. De Vincenzo, C. Hirsch, and B. Leonard. Strong coupling algorithm to solve fluid-structure-interaction problems with a staggered approach. In *11th International Workshop on Simulation and EGSE Facilities for Space Programmes*, number 117, Noordwijk, Netherlands, 2010.

[107] L. V. Van Wijngaarden and D. J. Jeffrey. Hydrodynamics interaction between gas bubbles in liquid. *Journal of Fluid Mechanics*, 77:27–44, 1976.

[108] R. W. C. P. Verstappen and A. E. P. Veldman. Fourth-order DNS of flow past a square cylinder: First results. In *the ERCOFTAC Workshop*, pages 381–384, Grenoble, France, 1996.

[109] G. Wang and S. P. Vanka. Les of flow over a square cylinder. In *the ERCOFTAC Workshop*, pages 397–400, Grenoble, France, 1996.

[110] G. Y. Wang. *A Computational Framwork Based on an Embedded Boundary Method for Nonlinear Multi-phase Fluid-Structure Interactions*. Ph.D. thesis, Stanford University, 2011.

[111] T. Watanabe, M. Hirano, F. Tanabe, and H. Kamo. The effect of the virtual mass force term on the numerical stability. *Nuclear Engineering and Design*, 120:181–192, 1990.

[112] R. Wilkens and W. P. Jepson. Studies of multiphase flow in high pressure horizontal and +5 degree inclined pipelines. In *Proceedings of the 6th International Offshore and Polar Engineering Conference*, volume 11, pages 139–146, Los Angeles, USA, 1996.

[113] G. Wu. *Regulating Valve Use and Maintenance*. Chemical Industry Press, 1999.

[114] W. F. Xie, Y. L. Young, and T. G. Liu. Multiphase modeling of dynamic fluid-structure interaction during close-in explosion. *International Journal for Numerical Methods in Engineering*, 74:1019–1043, 2008.

[115] F. Xu and J. Ou. Numerical simulation of unsteady flow around square cylinder and vortex-induced vibration. *Journal of Southest University*, 35(Sup(I)):35–39, 2005.

[116] D. L. Youngs. Time-dependent multi-material flow with large fluid distortion. In *Numerical Methods For Fluid Dynamics*, pages 273–285. Academic Press, New York, 1982.

[117] D. Z. Zhang and W. B. VanderHeyden. The effects of mesoscale structures on the macroscopic momentum equations for two-phase flows. *International Journal of Multiphase Flow*, 28(5):805–822, May 2002.

[118] T. Zhang. *Examination and Numerical Simulation of Interphase Forces in Metal Melt-Bubble Two-Phase Flow*. Master thesis, Dalian University of Technology, 2012.

[119] I. Zun. The transverse migration of bubbles influenced by walls in vertical bubbly flow. *Multiphase Flow*, 6:583–588, 1980.